

## Optimal Design of Structures and Variable Stiffness Laminates with Strength and Manufacturing Constraints

Hong, Zhi

**DOI**

[10.4233/uuid:94c8973e-bf3d-4a12-86e2-24801ed008c9](https://doi.org/10.4233/uuid:94c8973e-bf3d-4a12-86e2-24801ed008c9)

**Publication date**

2020

**Document Version**

Final published version

**Citation (APA)**

Hong, Z. (2020). *Optimal Design of Structures and Variable Stiffness Laminates with Strength and Manufacturing Constraints*. [Dissertation (TU Delft), Delft University of Technology].  
<https://doi.org/10.4233/uuid:94c8973e-bf3d-4a12-86e2-24801ed008c9>

**Important note**

To cite this publication, please use the final published version (if applicable).  
Please check the document version above.

**Copyright**

Other than for strictly personal use, it is not permitted to download, forward or distribute the text or part of it, without the consent of the author(s) and/or copyright holder(s), unless the work is under an open content license such as Creative Commons.

**Takedown policy**

Please contact us and provide details if you believe this document breaches copyrights.  
We will remove access to the work immediately and investigate your claim.

**OPTIMAL DESIGN OF STRUCTURES AND VARIABLE  
STIFFNESS LAMINATES WITH STRENGTH AND  
MANUFACTURING CONSTRAINTS**



# **OPTIMAL DESIGN OF STRUCTURES AND VARIABLE STIFFNESS LAMINATES WITH STRENGTH AND MANUFACTURING CONSTRAINTS**

## **Proefschrift**

ter verkrijging van de graad van doctor  
aan de Technische Universiteit Delft,  
op gezag van de Rector Magnificus Prof. dr. ir. T.H.J.J. van der Hagen,  
voorzitter van het College voor Promoties,  
in het openbaar te verdedigen op donderdag 20 februari 2020 om 10.00 uur.

door

**Zhi HONG**

Master of Science in Aeronautical Engineering,  
Beihang University, Beijing, China,  
geboren te Chaoyang, Liaoning Province, China.



Dit proefschrift is goedgekeurd door de

promotor: Prof. dr. C. Bisagni

promotor: Dr. S. Turteltaub

Samenstelling promotiecommissie:

Rector Magnificus,  
Prof. dr. C. Bisagni,  
Dr. S. Turteltaub,

Voorzitter  
Delft University of Technology, promotor  
Delft University of Technology, promotor

*Onafhankelijke leden:*

Prof. P. Duysinx,  
Prof. R. Vescovini,  
Prof. dr. ir. A. Suiker,  
Prof. dr. C. Kassapoglou,  
Dr. ir. D. Peeters,  
Prof. C.A. Dransfeld

University of Liege  
Politecnico di Milano  
Eindhoven University of Technology  
Delft University of Technology  
Delft University of Technology  
Delft University of Technology, reservelid

This research work was supported by China Scholarship Council (CSC) and Delft University of Technology.



*Keywords:* efficient optimization, stress constraint, curvature constraint, variable stiffness laminate, strength optimization

*Printed by:* Ipskamp Printing

*Front & Back:* designed by Zhi Hong.

Copyright © 2020 by Zhi Hong. All rights reserved. No part of this publication may be reproduced, stored in a retrieval system, or transmitted, in any form or by any means, electronic, mechanical, photocopying, recording, or otherwise, without the prior permission in writing from the proprietor.

ISBN 978-94-028-1934-2

An electronic version of this dissertation is available at  
<http://repository.tudelft.nl/>.

*To my beloved parents*  
谨以此书献给我敬爱的父母



# CONTENTS

<b>Summary</b>	<b>xi</b>
<b>Samenvatting</b>	<b>xiii</b>
<b>1 Introduction</b>	<b>1</b>
1.1 Background and motivation . . . . .	1
1.2 Overview of the research topics . . . . .	6
1.2.1 Efficient stress constrained optimization . . . . .	6
1.2.2 Manufacturable optimal design of Variable Stiffness Laminate	7
1.2.3 Maximum strength design of Variable Stiffness Laminate . .	8
1.3 Thesis layout . . . . .	8
References . . . . .	9
<b>2 Efficient computational method for stress constraints</b>	<b>17</b>
2.1 Introduction . . . . .	17
2.2 Formulation of the optimization problem. . . . .	19
2.2.1 Prototypical optimization problem . . . . .	19
2.2.2 Associated finite element analysis of structure . . . . .	20
2.2.3 Optimization framework of the problem . . . . .	21
2.3 Formulation of modified fully stressed design. . . . .	22
2.3.1 Modified stress approximation. . . . .	22
2.3.2 Sensitivity analysis. . . . .	24
2.3.3 Conservative, convex and separable approximation . . . . .	25
2.3.4 Predictor-corrector Interior Point Method . . . . .	26
2.3.5 Computational complexity. . . . .	29
2.4 Numerical improvements. . . . .	31
2.4.1 Preconditioner for the Schur complement . . . . .	31
2.4.2 Implicit sensitivity analysis . . . . .	32
2.4.3 Summary of the optimization algorithm . . . . .	34
2.4.4 Computational complexity for the improved method . . . . .	35
2.5 Representative numerical examples. . . . .	36
2.5.1 Fully-clamped solid beam case . . . . .	36
2.5.2 Clamped/simply supported hollow beam case. . . . .	39
2.5.3 Multiple-span continuous beam . . . . .	42
2.6 Extension of the method to plate structures. . . . .	45
2.6.1 nodal stress constraints . . . . .	45
2.6.2 Sensitivity analysis of the stress constraints . . . . .	46
2.6.3 Numerical test of plate structures . . . . .	48
2.6.4 Investigation of the possible reasons for mission failure . . . .	54
2.7 Conclusions. . . . .	58

References . . . . .	59
<b>3 An enhanced curvature constrained design method for manufacturable variable stiffness composite laminate</b>	<b>63</b>
3.1 Introduction . . . . .	63
3.2 Formulation of the optimization problem. . . . .	66
3.2.1 Lamination Parameters . . . . .	66
3.2.2 Three-step optimization for variable stiffness composite . . . . .	66
3.2.3 Compliance approximation of 2D composite plates . . . . .	67
3.2.4 Two-level approximation for the VSL. . . . .	71
3.2.5 Optimization strategy . . . . .	72
3.3 Curvature constraint in terms of the lamination parameters . . . . .	73
3.3.1 Relationship between curvature constraints and gradient constraint on the lamination parameters . . . . .	73
3.3.2 Numerical implementation of gradient constraints on the lamination parameters . . . . .	75
3.4 Methods to apply curvature constraints. . . . .	76
3.4.1 General three-step framework with curvature constraints . . . . .	76
3.4.2 Direct control method . . . . .	77
3.4.3 Indirect control method . . . . .	77
3.4.4 Hybrid control method . . . . .	78
3.5 Test case 1: rectangular plate with point load . . . . .	78
3.5.1 Primary test on direct, indirect and hybrid control method . . . . .	79
3.5.2 Comparison of the optimal designs for one representative minimum turning radius . . . . .	82
3.6 Comparative analysis of test case 1 for distinct values of model parameters and minimum turning radius . . . . .	84
3.6.1 Comparison of the optimal compliance in Step 2 of the three methods. . . . .	84
3.6.2 Comparison of the computational cost for the curvature constraint methods . . . . .	86
3.6.3 Optimal upper bound factor $\delta$ in the hybrid control method. . . . .	87
3.7 Test case 2: square plate with a hole under distributed load. . . . .	88
3.7.1 Direct control method . . . . .	88
3.7.2 Indirect control method . . . . .	90
3.7.3 Hybrid control method . . . . .	91
3.7.4 Comparison of the optimal designs for one representative minimum turning radius . . . . .	92
3.8 Conclusion . . . . .	92
References . . . . .	93
<b>4 Efficient strength optimization of variable stiffness laminate</b>	<b>99</b>
4.1 Introduction . . . . .	99
4.2 Strength analysis for variable stiffness laminate and the global failure index . . . . .	101
4.2.1 Structural analysis for the VSL . . . . .	101

4.2.2	<i>p</i> -norm failure index . . . . .	102
4.2.3	Two level approximation for <i>p</i> -norm failure index . . . . .	103
4.3	Efficient strength optimization with <i>p</i> -norm failure index . . . . .	105
4.4	Strength optimization on a square plate with a cut-out . . . . .	108
4.4.1	Effect of <i>p</i> on the on the optimal result. . . . .	109
4.4.2	Numerical results on half of the reference model . . . . .	114
4.4.3	Optimal results with min-max bound formulation . . . . .	116
4.4.4	Comparative analysis for strength optimization . . . . .	118
4.5	Strength optimization on a L-shaped plate . . . . .	121
4.5.1	Mesh-convergence study on the L-shaped plate . . . . .	122
4.5.2	The optimal design from min-max bound formulation . . . . .	125
4.5.3	Comparative analysis of the optimal results from the <i>p</i> -norm failure index and min-max bound formulation . . . . .	126
4.6	Conclusion . . . . .	128
	References . . . . .	129
<b>5</b>	<b>Conclusion and future work</b>	<b>133</b>
5.1	Conclusion . . . . .	133
5.2	Future work. . . . .	136
	References . . . . .	138
	<b>Acknowledgements</b>	<b>139</b>
<b>A</b>	<b>Appendix</b>	<b>143</b>
A.1	Feasibility of the indirect control method . . . . .	143
A.1.1	Feasible/infeasible range for distinct upper bound factors $\delta$ in indirect control method . . . . .	143
A.1.2	Feasible/infeasible range for distinct minimum turning radius $r_{\min}$ in indirect control method . . . . .	144
	<b>Curriculum Vitae</b>	<b>147</b>



# SUMMARY

Reducing weight and improving strength of structures have always been major design goals in the aerospace industry since its inception. In particular, strength directly affects the safety and serviceability of an airplane and is therefore of great importance in structural design. Improving the strength of an airframe can effectively increase its damage tolerance in different failure modes, such as fracture, fatigue and impact damage. To pursue these goals, optimization techniques, which aim to seek for the “best solution” in mathematical models, can be applied in the structural design process. In addition, usage of lightweight carbon fiber reinforced composite laminates further serves this purpose.

Hence, in-depth studies are conducted in two aspects to achieve lightweight structures with superior strength in this research: efficient strength optimization and manufacturable design of variable stiffness laminate composites. For the existing strength optimization, the challenge in addressing large scale problems lies in the prohibitive computational demand. This is due to the fact that the strength of a structure is a local quantity measured with either stress or strain-based criteria. This results in the need to handle a large number of constraints for large scale structures, which leads to a super-quadratic growth in the computational cost. In the present work, computational efficiency is improved in two distinct areas: (i) for local strength sizing optimization, a new variant of an iterative method is developed, which streamlines the established algorithm to improve its efficiency and (ii) a global version of strength-oriented optimization is developed for variable stiffness laminates, which reduces the computational time compared to existing methods by reducing the number of constraints.

In combination with the aforementioned improvements in computational efficiency, a second aspect that is addressed in the present work is the design methodology for lightweight structures. In particular, the manufacturable design of variable stiffness laminates is further investigated to push forward the application of this novel composite material with excellent tailoring capacity.

For the efficient iterative method with local constraints developed in this work, the objective is to minimize the weight of structures made of steel or other homogeneous materials. Computational efficiency is improved by solving the Schur complement of the Karush-Kuhn-Tucker (KKT) condition with the preconditioned conjugate gradient method (PCG). Simultaneously, sensitivity analysis of the stress constraints is accomplished implicitly by implementing the adjoint method and the reanalysis method in the PCG to formulate a matrix-free solver for the Schur complement. A stress approximation based on a fully stressed design is developed to provide a diagonal preconditioner for the PCG. The numerical results show that the proposed method is able to achieve a linear relationship in the computational cost with respect to the problem size for beam struc-



tures.

The manufacturable design of variable stiffness laminate in this work is intended to enhance an existing method, called the direct control method, which imposes curvature constraints on the fiber paths in the angle retrieval step of a multi-step optimization method. In this work, an indirect control method to constrain the curvature of fiber paths implicitly through lamination parameters is developed for compliance minimization problem. This allows the curvature constraint to be imposed in the first step where the primary objective is optimized in the multi-step method. Thereafter, a hybrid control method, which combines the indirect control method and the existing direct control method, is applied to impose the curvature constraints in both steps. A comparative analysis of the indirect, direct and the hybrid control methods is conducted in terms of the matching of the optimal lamination parameters obtained from the two steps, optimal compliance achieved and the computational cost. The hybrid control method turns out to be the best approach to yield a design with the lowest compliance at the expense of a moderate increase in the computational cost.

The efficient strength optimization of variable stiffness laminate is explored with a global aggregation method ( $p$ -norm formulation) with failure indices based on the Tsai-Wu failure criterion in order to reduce the computational cost. The new variant of the method is able to work using lamination parameters as the primary design variables. To simplify the Tsai-Wu failure criterion with respect to the lamination parameters, an elliptical formulation of the conservative failure envelop is applied to represent the failure criterion. The  $p$ -norm formulation is then applied to aggregate the local failure indices into a global failure index, which condenses the size of the problem. The two level approximation is then employed for this global failure index to guarantee the conservativeness and convexity of the subproblem. The numerical results show that the computational cost is efficiently reduced, compared to addressing local constraints. Simultaneously, the method proposed in this part generates a mesh-convergent result and behaves robust even in the presence of a stress singularity.

In conclusion, this research has undertaken an in-depth investigation into the efficient strength optimization and manufacturable design of variable stiffness laminate. Deep insight into stress constrained sizing optimization is achieved. The manufacturable design of variable stiffness laminate described in this work successfully improves the existing method of enforcing curvature constraints on the fiber paths. The efficient strength optimization of variable stiffness laminate with global failure index is shown to be promising for large scale structures. This may inspire further interesting, on-going research on high performance stress constrained sizing optimization and its wider application for variable stiffness laminate in the future.

# SAMENVATTING

Het verminderen van gewicht en verbeteren van de sterkte van constructies zijn altijd de hoofd ontwerpdoelen geweest van de lucht- en ruimtevaartindustrie. De sterkte heeft met name veel invloed op de veiligheid en onderhoudbaarheid van een vliegtuigconstructie, en is daarom erg belangrijk voor het ontwerp van de constructie. Het verbeteren van de sterkte van de structuren kan effectief de schade tolerantie verbeteren voor verschillende faalwijzen, zoals breuk, materiaalmoetheid en schade door impact. Om deze doelen na te streven worden optimalisatie technieken ingezet, welke gebruik maken van wiskundige modellen voor het vinden van de "beste oplossing", voor het constructie ontwerp proces. Tevens word er gebruik gemaakt van lichtgewicht met koolstofvezel versterkte composiet laminaten voor het verdere nastreven van deze doelen.

Derhalve, zijn er diepgaande studies uitgevoerd in twee aspecten voor het realiseren van lichtgewicht constructies met superieure sterkte in dit onderzoek: efficiënte sterkte optimalisatie en produceerbaar ontwerpen van variabele stijfheid laminaat composieten. Voor de bestaande sterkte optimalisatie, ligt de uitdaging van grootschalige problemen in de beperkende computationele vraag. Dit komt door het feit dat de sterkte van constructies in een lokale kwantiteit gemeten worden met een criterium gebaseerd op spanning of rek. Dit resulteert in de behoefte om een groot aantal voorwaarden te verwerken voor grootschalige constructies, wat leid tot een super-kwadratische groei van computationele kosten. In het huidige werk is de computationele efficiëntie verbeterd in twee te onderscheiden gebieden: (i) voor lokale sterkte dimensionering optimalisatie, is een nieuwe variant van een iteratieve methode ontwikkeld, welke het vastgestelde algoritme stroomlijnt voor verbeterde efficiëntie en (ii) een globale versie van een sterkte-oriënterende optimalisatie is ontwikkeld voor variabele stijfheid laminaten, welke voor een vermindering zorgt van computationele tijd in vergelijking tot bestaande methodes door het reduceren van het aantal voorwaarden.

In combinatie met de voorheen genoemde verbeteringen in computationele efficiëntie, een tweede aspect dat is geadresseerd in het huidige werk is de ontwerp methodologie voor lichtgewicht constructies. Met name het produceerbaar ontwerpen van variabele stijfheid laminaten is verder onderzocht om vaart te zetten achter het toepassen van dit nieuwe composiet materiaal met uitstekende ontwerp mogelijkheden.

Voor de efficiënte iteratieve methode met lokale voorwaarden welke ontwikkeld is in dit werk, is het doel het gewicht te minimaliseren van constructies gemaakt van staal of andere homogene materialen. De computationele efficiëntie is verbeterd door het oplossen van de stelling van Schur van de Karush-Kuhn-Tucker (KKT) conditie met de gepreconditioneerde geconjugeerde gradiënten methode (PCG). Tegelijkertijd is er een gevoeligheidsanalyse van de spanning voorwaarden impliciet bereikt door het implementeren van de geadjungeerde methode en de her analyse methode in de PCG om een matrix vrije

oplosser van de stelling van Schur te formuleren. Een benadering van de spanning, gebaseerd op een ontwerp volledig onder spanning, is ontwikkeld om de PCG te voorzien van een diagonale preconditionering. De numerieke resultaten laten zien dat de voorgestelde methode een lineaire relatie kan bereiken in de computationele kosten in relatie tot de grootte van het probleem voor balk constructies.

Het produceerbaar ontwerpen van variabele stijfheid laminaten in dit werk is bedoeld om een bestaande methode te verbeteren, genaamd de directe controle methode, welke kromming voorwaardes oplegt aan de vezel paden in de hoek ophaalstap van een multi-criteria optimalisatie methode. In dit werk is er een indirecte controle methode ontwikkeld om de kromming van vezel paden impliciet vast te leggen met laminaat parameters voor een compliantie optimalisatie probleem. Dit laat toe dat de kromming voorwaarde opgelegd kan worden voor het eerste criterium waar het primaire doel is geoptimaliseerd in de multi-criteria methode. Daarna wordt er een hybride controle methode toegepast, welke een indirecte controle methode en de bestaande directe controle methode combineert, om de kromming voorwaarden op te leggen in beide criteria. Een vergelijkende analyse van de indirecte, de directe en de hybride controle methode is uitgevoerd in termen van overeenkomst van de optimale laminaat parameters verkregen van de twee criteria, het bereiken van optimale compliantie en de computationele kosten. De hybride controle methode blijkt de beste methode om een ontwerp op te leveren met de laagste compliantie ten kosten van een gematigde toename van computationele kosten.

De efficiënte sterkte optimalisatie van een variabele stijfheid laminaat is verkend met een globale aggregatie methode (p-norm formulatie) met faal indices gebaseerd op het Tsai-Wu faal criterium om de computationele kosten te reduceren. De nieuwe variant van de methode maakt het mogelijk om gebruik te maken van laminaat parameters als de primaire ontwerp variabelen. Ter vereenvoudiging van het Tsai-Wu faal criterium in relatie tot de laminaat parameters, een elliptische formulatie van de conservatie faal omhullende is toegepast om de faal criterium te representeren. De p-norm formulatie is vervolgens toegepast om de lokale faal indices te aggregeren in een globale faal index, welke de probleem grootte condenseert. De benadering op twee niveaus is dan gehanteerd voor de globale faal index om de conservativiteit en convexiteit van het sub probleem te garanderen. De numerieke resultaten laten zien dat de computationele kosten efficiënt gereduceerd zijn, vergeleken met het adresseren van lokale voorwaarden. Tegelijkertijd genereert de methode die in dit onderdeel is voorgesteld een mesh-convergerend resultaat en gedraagt het zich robuust, zelfs in de aanwezigheid van een spannings singulariteit.

Ter conclusie, dit onderzoek heeft een diepgaande studie ondernomen naar het efficiënt optimaliseren van de sterkte en produceerbare ontwerpen voor variabele stijfheid laminaten. Een diep inzicht is bereikt in dimensionering optimalisatie met spannings voorwaarden. Het produceerbaar ontwerpen van variabele stijfheid laminaten beschreven in dit werk verbeterd succesvol de bestaande methoden van het opleggen van kromming voorwaarden op vezel paden. Het is gepresenteerd dat het efficiënt optimaliseren voor sterkte van variabele stijfheid laminaten met globale faal index belovend is voor grootschalige constructies. Dit inspireert mogelijk verdere interesse van lopend onderzoek naar hoog presterende dimensionering optimalisatie met spannings voorwaarden

en wijdere toepassing van variabele stijfheid laminaten in de toekomst.



# 1

## INTRODUCTION

*A journey of a thousand miles begins with a single step.*  
千里之行始于足下。

Laozi

### 1.1. BACKGROUND AND MOTIVATION

The idea of structural optimization using gradient-based programming method was initially proposed in the 1960s through the integration of mathematical programming with finite element method (Vanderplaats [1]). Since then, a tremendous progress has been achieved in this field due to constant ongoing research. Nowadays, it plays an essential role in the product design of high-tech industries, driven by the continuous demand of efficient and robust structures, e.g., aerospace, automotive, offshore wind farms, microelectromechanical system and biomechanical industries etc. Its applications cover a wide range of cases, such as: reducing the weight of aircrafts (e.g., A350, A380), improving the aerodynamic performance of racing cars, enhancing aero-structural interaction for smart wind turbine blades, or designing bone-implants with functionally graded materials.

In particular for aircraft designers, weight reduction of airframe is a main focus, because the fuel efficiency and CO<sub>2</sub> emission of an aircraft are weight-based. An empirical estimation for airlines indicates that with 1% weight reduction, roughly 0.75% reduction in fuel consumption can be achieved (Capehart [2]). Moreover, the fuel required is further decreased recursively because of the less fuel carried. Such efficiency gain is larger for long-haul aircrafts (Peeters et al. [3]). As fuel cost accounts for 40% of airline's operational cost (Duval and Emmanuelle [4]), weight reduction in structural design can ultimately bring airlines a huge economic benefit given a constant increasing travel demand.

In addition, weight reduction of aircraft also effectively alleviates the overwhelming anthropogenic CO<sub>2</sub> emission issue, which causes global warming and ocean acidification. According to the International Air Transport Association (IATA), the flights worldwide generated 859 million tonnes of CO<sub>2</sub> in 2017 (International Air Transport Association [5]). In order to reduce this greenhouse gas emission, even a small reduction in weight can lead to great achievement due to the cumulative beneficial effects. For instance, a single Boeing 747, commuting from the UK to the US on a daily basis, can save 456.2t CO<sub>2</sub> a year by using lighter types of paint, taking fewer in-flight magazines and reducing the baggage allowance rates (Civil Aviation Authority [6]). In Flightpath 2050 (European Commission [7]), a road map for European aerospace industry, one goal regarding the sustainable air traffic is to “achieve a 75% reduction in CO<sub>2</sub> emissions per passenger kilometer and a 90% reduction in NO<sub>x</sub> emissions in 2050” comparing to the standard in 2000. In view of this ambition, the reduction of weight through optimization remains a critical research topic.

### WEIGHT MINIMIZATION WITH STRUCTURAL OPTIMIZATION

As a very powerful methodology, structural optimization has evolved into three sub-fields based on the design variables chosen in the process, namely, sizing optimization, shape optimization and topology optimization. Sizing and topology optimization are often used to exploit lightweight designs. In particular, sizing optimization has been extensively developed and applied in structural optimization (Kirsch [8], Rozvany and Zhou [9], Barthelemy and Haftka [10], Miura and Schmit [11], Grandhi and Venkayya [12], Vanderplaats and Salajegheh [13], Lagaros et al. [14], Rajan [15], Lingyun et al. [16]). Hereby, the process of “sizing” typically refers to changes in a selected number of parameters that describe the geometry of a structure. Two key advantages of this approach are the directness and robustness since it is intuitive and well regularized. Additionally, it is flexible to be applied in the design process (even in the detailed design phase) due to the fact that it only changes the size of a structure with the shape and topology intact.

As a result, sizing optimization is the most deployable tool for industrial weight minimization. One example in automotive industry can be found in Pedersen et al. [17], which successfully achieves a 15% to 19% mass reduction with stiffness constraints (including constraints on bending, torsional and axial stiffness). Another engineering example comes from Airbus, where sizing optimization packages have been developed for this purpose (Grihon [18]). They include trade-off studies in the preliminary design phase of A350 fuselage, where the intention is to select several optimum designs from a large number of backup configurations with limited computational cost. In the meanwhile, buckling, post-buckling and damage tolerance criteria can be taken into consideration. Such information can be coupled to the manufacturing and cost aspects in the design to streamline the process.

### WEIGHT MINIMIZATION WITH LIGHTWEIGHT MATERIAL

Apart from the optimization approaches, using lightweight material (i.e., carbon fiber reinforced composite material) to replace metal in weight sensitive structures also leads

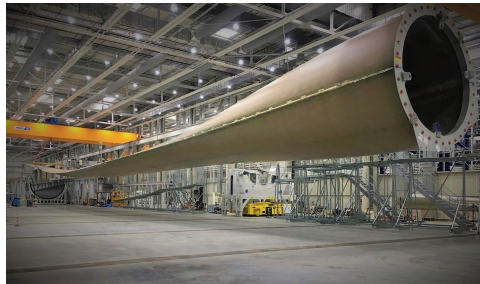
to significant weight reduction. This is due to the advantages of carbon fiber composite materials over metallic materials, including: high strength-to-weight ratio, damage tolerance, corrosion resistance, thermal insulating and rapidly moldable for complex shapes. In the early application stages, they were only limited to the secondary structures in airplanes (such as inspection panels, spoilers or air brakes) where failure does not immediately lead to a catastrophic consequence. Due to the advancement on the material and manufacture technologies, they are now applied in primary structures and have been adopted outside the aircraft industry. Now, the record-breaking case in air-



(a) A350



(b) McLaren MP4/1



(c) GE's Haliade-X wind turbine blade

Figure 1.1: Application of carbon fiber composite in industry (a)A350 (source: <https://www.aircraftcompare.com/aircraft/airbus-a350-xwb/>), (b)McLaren MP4/1 (source:<https://en.wikipedia.org/wiki/McLaren>), (c) GE's Haliade-X wind turbine blade (source: <https://www.ge.com/reports/extreme-measures-107-meters-worlds-largest-wind-turbine-blade-longer-football-field-heres-looks-like/>)

craft industry is the A350 (see Figure 1.1a), where nearly 53% of the structural weight is composed of composite materials. In high-speed Formula 1, McLaren MP4/1 (Figure 1.1b) first applied composite materials in the chassis and cockpit in 1981 in order to reinforce the mechanical properties and achieve weight saving. Thereafter, it is found that only a minor maintenance of the body is required in the race due to the high damage tolerance of composite materials. Carbon fiber composite is also being extensively used in the wind turbine blades, where the weight of the blade has a significant impact on the dynamic strength. Stronger and super lightweight composite structures are under investigation including the world's current most powerful offshore wind turbine (GE's Haliade-X 12MW in Figure 1.1c), which spans up to 107m long. Bigger and more powerful models are likely to be developed in the future.



According to different fabrication processes, the carbon fiber composite material has various architectures. The most commonly used ones are the composite laminates (Figure 1.2a), the braided composite material (Figure 1.2b) and the honeycomb composite material (Figure 1.2c). Each one has its own characteristics and advantages, which are described as follows. In particular, the composite laminate is outstanding for its lightweightness and tailorable stiffness. Therefore, it is generally used in thin-walled structures, such as the skin of the aircraft wing or chassis of the race-car. The braided composite performs well for impact and high temperature resistance, which ends up with energy absorber of helicopter structures, heat shield and throat nozzle of rocket motor etc. The honeycomb composite material has high impact resistance, and outstanding transverse and bending stiffness, thus, it is widely used in ailerons, fuselage, floors of aircraft, energy absorption protective structures of racing cars or roof of railway vehicle.

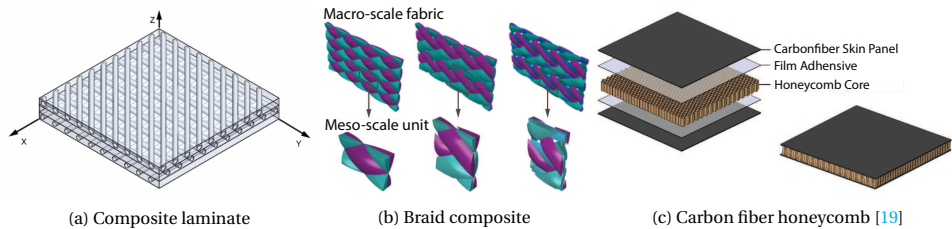


Figure 1.2: Carbon fiber composite material (a) Composite laminate (source: <https://blogs.solidworks.com/tech/2018/07/solidworks-simulation-an-intro-to-composite-analysis.html>), (b) Braid composite (source: <http://www.xcomposites.com>)

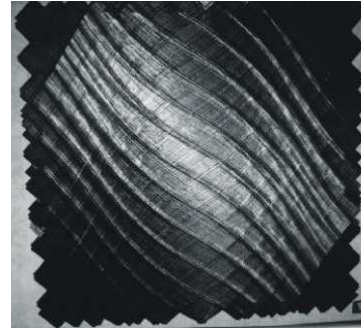
## NOVEL COMPOSITE LAMINATES

Composite laminates have traditionally been manufactured with straight fiber paths. With the advent of new manufacturing techniques, they are now viable to produce parts without homogeneous properties. In particular, for variable stiffness composite laminates (VSL), the stiffness in the laminate can be tailored locally by redirecting the fiber path orientation of each ply continuously. They have been demonstrated to be able to improve the mechanical performance enormously compared with conventional straight fiber composites (Tatting et al. [20]). Optimal design of VSLs has been studied for different properties such as buckling (Gürdal et al. [21], Setoodeh et al. [22], Wu et al. [23]), vibration (Abdalla et al. [24]), compliance (Setoodeh et al. [25]) and strength (Khani et al. [26]) etc. All these designs aim at producing efficient lightweight materials and structures.

To manufacture variable stiffness laminate structures, automated fiber placement (AFP) machine can be used to place the fibers layer by layer. An AFP machine and a sample of the VSL are shown in Figure 1.3. It is important to note that the capability of AFP is limited by the minimum allowable turning radius of the fiber paths. Specifically, the minimum allowable steering radius of an up-to-date AFP machine is 650mm for 6.35mm wide tows (Zympeloudis et al. [28]) in order to prevent the wrinkle of the fibers. Such



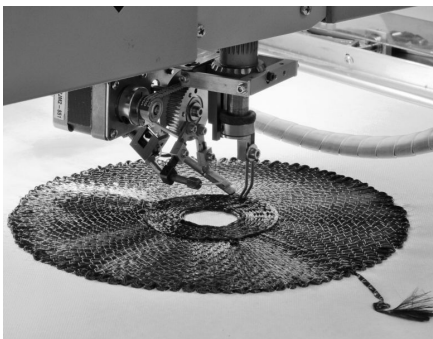
(a) Automated fiber placement machine



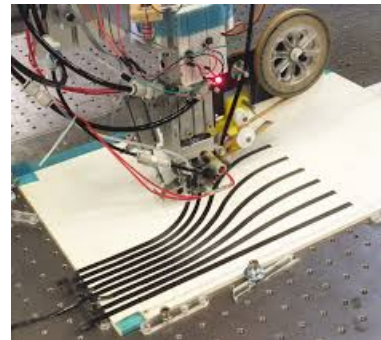
(b) Variable stiffness laminate [27]

Figure 1.3: Novel composite laminate and its manufacturing (a) Automated fiber placement machine (source:[https://www.dlr.de/zlp/en/desktopdefault.aspx/tabid-7842/13352\\_read-35924/](https://www.dlr.de/zlp/en/desktopdefault.aspx/tabid-7842/13352_read-35924/))

limitations need to be considered in the design to obtain manufacturable part (Lozano et al. [29]). Constraints on the minimum allowable turning radius have been considered in stacking sequence optimization of the VSL (Peeters et al. [30]) and for stress minimization problems (Brooks and Martins [31]).



(a) Tailored fiber placement



(b) Continuous tow shearing [32]

Figure 1.4: Two fiber placement methods (a) Tailored fiber placement machine (source: <https://www.tfp-tech.com/TFP-technology.html>)

In terms of the manufacturing technologies, two manufacturing methods (referred to as tailored fiber placement (TFP) (Uhlir et al. [33]) and continuous tow shearing (CTS) (Kim et al. [34]), respectively) are developed to break through the limitation of the AFP. The TFP (see Figure 1.4a) has no restriction on the turning radius of the fiber path. However, the main drawback of this method lies in its low production rate, which limits its application only to small scale components (Khaliulin et al. [35]). The minimum allowable turning radius for the CTS (see Figure 1.4b) is 50mm for 100mm wide taps (Zympeloudis et al. [28]), which is lower than that of the AFP machine by nearly one order of magnitude. Although, the design space of the VSL is effectively expanded with this new technology, imposing constraints on the minimum turning radius is still required in order to obtain

a manufacturable design. This is due to the fact that the turning radius can cause variations in the thickness in the composite laminate.

### AIM OF THIS RESEARCH

Strength, which is directly related to the safety of a structure, needs to be considered in structural optimization. Since it is a local measurement in a structure, be it the Von Mises stress or equivalent safety factors, it is computationally prohibitive to minimize or constrain with tens of thousands of strength constraints for large scale structures. As a result, it is a prerequisite to improve the computational efficiency of strength optimization for complex engineering design. Henceforth, one aim of this research is to provide efficient methods to solve large scale strength optimization problems for weight reduction purposes.

Furthermore, in order to guarantee that an optimal design of the variable stiffness laminate can be finally manufactured with AFP, the minimum allowable turning radius of fiber path needs to be considered in the optimization procedure. Existing methods to impose such constraints lead to significant deviations from the theoretical optimum for the actual design. To address this issue, a second aim of this research is to develop methods to minimize the loss in performance due to the manufacturing constraints for the AFP.

## 1.2. OVERVIEW OF THE RESEARCH TOPICS

This PhD research is composed of three parts correlated with the research objective of improving the existing optimization framework for lightweight materials both in terms of the computational efficiency of the design process as well as the performance of the optimal design. The first one is related to the computational efficiency of the optimization algorithm in the context of sizing with local stress constraints. The second part pertains to the performance of a design when manufacturing constraints are imposed in variable stiffness laminates and, finally, the third part addresses strength optimization for variable stiffness laminates. A brief overview of the state of the art in these three parts is given below.

### 1.2.1. EFFICIENT STRESS CONSTRAINED OPTIMIZATION

Stress constrained optimization is a topic that has been of interest in mechanical design for long. Several methods have been proposed to resolve stress constrained optimization (Schmit and Farshi [36], Fleury and Braibant [37], Svanberg [38], Fleury [39], Fadel et al. [40], M.Zhou and R.W.Xia [41], Vanderplaats and Kodiyalam [42], Vanderplaats and Thomas [43]). One practical limitation of these methods is that they are computationally costly due to two factors. First, the computational cost is dominated by the size of the Schur complement to be solved in the Karush-Kuhn-Tucker (KKT) condition. To deal with a problem with tens of thousands of stress constraints, the computational work associated to solve a matrix of this size repetitively is indeed heavy in the optimization.

Second, the sensitivity analysis for such a problem needs to be executed for every constraint individually due to the local nature of the constraints. Therefore, a significant computational effort is demanded.

Hence, the aim is to accelerate the optimization by building up an efficient numerical algorithm. The preconditioned conjugate gradient (PCG) method is applied as the solver to reduce the computational cost required by the Schur complement. A new stress approximation based on the fully stressed design is proposed to provide the PCG an efficient preconditioner in order to accelerate the convergence rate. Simultaneously, a creative approach to combine the adjoint, the reanalysis methods for sensitivity analysis within the PCG, which is termed as implicit sensitivity analysis, is proposed to enable the sensitivity analysis implemented in the meanwhile of the optimization is resolved. Therefore, the repetitive calculation with the adjoint method for the sensitivity can be removed for large scale problems. When the proposed stress approximation, implicit sensitivity analysis and the preconditioner are connected with each other in a convex optimization algorithm with quick convergence, the efficiency for the stress constrained sizing optimization can be effectively improved.

### 1.2.2. MANUFACTURABLE OPTIMAL DESIGN OF VARIABLE STIFFNESS LAMINATE

Since the advent of advanced fiber placement techniques, significant research work has been dedicated to improve the mechanical performance of the VSL by tailoring the fiber paths (Blom et al. [44], Akbarzadeh et al. [45], Cagdas [46], Abdalla et al. [47], Lopes et al. [48], Ijsselmuiden et al. [49], Setoodeh et al. [50], Rouhi et al. [51], Jibawy et al. [52], Kazemi and Verchery [53], Montemurro and Catapano [54]). One versatile methodology for the optimal design of the VSL is the three-step optimization method (Ijsselmuiden et al. [55]), where Step 1 optimizes the mechanical performance in the lamination parameter space, Step 2 retrieves the fiber angles based on the optimal lamination parameters and Step 3 constructs fiber paths. To constrain the minimum allowable turning radius, the existing method imposes a steering constraint to enforce the curvature in the Step 2 (Peeters et al. [30, 56]). However, since this is a purely geometrical restriction, the manufacturable design obtained after this step decreases the theoretical optimum obtained in Step 1.

In order to break through this drawback, an enhanced design method based on the three-step optimization method is developed. A partial manufacturing constraint in the parametric space is integrated in Step 1 of the method to tailor the optimal solution from the source based on the specific requirement on the minimum allowable turning radius of the AFP. However, the challenge lies in the fact that the mechanical optimization in Step 1 is implemented in the parametric space, where no detailed information about the fiber angles is available. To achieve this goal, a mapping between the curvature constraints with the fiber angles in Step 2 and a manufacturing constraints in the parametric space in Step 1 is proposed through the gradient constraints. Thereafter, an enhanced design method is achieved by incorporating the gradient constraints on the lamination parameters in Step 1 with the existing steering constraints in Step 2. Finally, the en-

hanced design method provides better design in terms of the manufacturability.

### 1.2.3. MAXIMUM STRENGTH DESIGN OF VARIABLE STIFFNESS LAMINATE

By tailoring the fiber paths of the variable stiffness laminate, the internal load can be efficiently reallocated to enhance the load bearing capacity of a structure. Similar to Section 1.2.1, the main issue of this part still lies in the computational cost for this problem. Therefore, the research in this topic aims to reduce the computational cost for the strength optimization of the VSL as well.

Existing methods on strength optimization addressing local failure measurements have been developed for composite laminates (Ijsselmuiden et al. [55], Groenwold and Haftka [57], Khani et al. [58], Guo et al. [59]). These methods, based on local constraints connected to the Tsai-Wu failure criterion, are generally computationally costly. To reduce the computational cost, the  $p$ -norm has been applied to aggregate the failure indices. In discrete material optimization (DMO) (Lund [60]), it has been utilized in maximum strain or maximum stress based criterion using fiber angles as the design variables. Mirzendehtel et al. [61] expand the  $p$ -norm aggregation for failure strength constraints for anisotropic material in additive manufacturing.

In this context, the present work explores a novel application of the  $p$ -norm approach, namely, its incorporation within the three-step optimization method. Since the Tsai-Wu failure criterion applied in the strength measurement is explicit to the fiber angles, a new version of the method needs to be developed in order to link the  $p$ -norm approach to a formulation that uses lamination parameters as primary variables. An elliptical formulation of a conservative failure envelope (Khani et al. [58]) is introduced to simplify the failure envelope of Tsai-Wu failure criterion for this purpose and a failure index is built thereafter. The advantage of this approach is that the method can be generalized to different types of failure criteria in the three-step optimization method. The computational efficiency of strength optimization is also improved significantly comparing with the local min-max formulation.

## 1.3. THESIS LAYOUT

The structure of this thesis is as follows: an efficient stress constrained sizing optimization method is described in Chapter 2. In this chapter, the details of the proposed numerical algorithm and numerical results for the beam and plate cases are demonstrated. The numerical results for the beam cases demonstrate that the efficiency anticipated theoretically is indeed obtained. In contrast, the results in the plate cases indicate that the method is approaching the efficiency expected even though not fully obtained. The optimal Lagrange multipliers and the sensitivity of stress constraints in the plate case is analyzed in this chapter regarding the efficiency to be obtained.

In Chapter 3, the compliance optimization of the VSL is implemented with an enhanced curvature constraint optimization method. In this chapter, an indirect constraint to control the curvature of fiber paths through the lamination parameters is proposed. There-

after, an enhanced curvature constraint is proposed and compared with the indirect constraints and the existing direct curvature constraints on the fiber angles. The results show that the enhanced curvature constraint cost less CPU time than the average of the three methods and also provides the best design in terms of the compliance.

In Chapter 4, the global aggregation method ( $p$ -norm formulation) is introduced to the strength optimization of the VSL to accelerate the optimization procedure. An elliptical formulation of the conservative failure envelope is employed to ensure the Tsai-Wu failure criterion is valid in terms of the lamination parameters. A two layer approximation is built for the global failure index to preserve the conservativeness, which provides a robust convergence. Numerical results confirm that the global aggregation effectively reduce the computational cost comparing with the local min-max formulation. In addition, it demonstrates that the strength can be reduced efficiently with a proper  $p$  value. Also, the numerical results are demonstrated to be mesh independent, even with stress singularity in L-shaped plate.

Finally, concluding remarks are given in Chapter 5, where the research for each chapter is summarized. Moreover, some ideas for the future work to proceed are also outlined.

## REFERENCES

- [1] G.N. Vanderplaats. Structural optimization-past, present, and future. *AIAA journal*, 20(7):992–1000, 1982.
- [2] B. L. Capehart. *Encyclopedia of energy engineering and technology*. Boca Raton, FL: CRC Press, 2007.
- [3] P.M. Peeters, J. Middel, and A. Hoolhorst. Fuel efficiency of commercial aircraft. Technical report, National Aerospace Laboratory NLR, 2005.
- [4] Nicolas Duval and Aygat Emmanuelle. *Focus on fuel*. Airbus technical magazine, October 2018.
- [5] International Air Transport Association. Fact sheet Climate change & corsia. [https://www.iata.org/pressroom/facts\\_figures/fact\\_sheets/Documents/fact-sheet-climate-change.pdf](https://www.iata.org/pressroom/facts_figures/fact_sheets/Documents/fact-sheet-climate-change.pdf), 2018. Online; accessed May 2018.
- [6] Civil Aviation Authority. Information on aviation's environment impact. Technical report, Civil Aviation Authority, 2017.
- [7] European Commission. *Flightpath 2050: Europe's vision for aviation*. Directorate-General for Research and Innovation, Directorate-General for Mobility and Transport, 2011.
- [8] Uri Kirsch. Reduced basis approximations of structural displacements for optimal design. *AIAA journal*, 29(10):1751–1758, 1991.



- [9] G.I.N. Rozvany and M Zhou. A note on truss design for stress and displacement constraints by optimality criteria methods. *Structural optimization*, 3(1):45–50, 1991.
- [10] J. F. M. Barthelemy and R. T. Haftka. Approximation concepts for optimum structural design — a review. *Structural optimization*, 5(3):129–144, Sep 1993. ISSN 1615-1488. doi: 10.1007/BF01743349. URL <https://doi.org/10.1007/BF01743349>.
- [11] Hirokazu Miura and Lucien A. Schmit. Second order approximation of natural frequency constraints in structural synthesis. *International Journal for Numerical Methods in Engineering*, 13(2):337–351. doi: 10.1002/nme.1620130209. URL <https://onlinelibrary.wiley.com/doi/abs/10.1002/nme.1620130209>.
- [12] R.V. Grandhi and V.B. Venkayya. Structural optimization with frequency constraints. *AIAA journal*, 26(7):858–866, 1988.
- [13] Garret N. Vanderplaats and Eysa Salajegheh. An efficient approximation technique for frequency constraints in frame optimization. *International Journal for Numerical Methods in Engineering*, 26(5):1057–1069. doi: 10.1002/nme.1620260505. URL <https://onlinelibrary.wiley.com/doi/abs/10.1002/nme.1620260505>.
- [14] Nikolaos D. Lagaros, Manolis Papadrakakis, and George Kokossalakis. Structural optimization using evolutionary algorithms. *Computers & Structures*, 80(7):571 – 589, 2002. ISSN 0045-7949. doi: [https://doi.org/10.1016/S0045-7949\(02\)00027-5](https://doi.org/10.1016/S0045-7949(02)00027-5). URL <http://www.sciencedirect.com/science/article/pii/S0045794902000275>.
- [15] S. D. Rajan. Sizing, shape, and topology design optimization of trusses using genetic algorithm. *Journal of Structural Engineering*, 121(10):1480–1487, 1995.
- [16] Wei Lingyun, Zhao Mei, Wu Guangming, and Meng Guang. Truss optimization on shape and sizing with frequency constraints based on genetic algorithm. *Computational Mechanics*, 35(5):361–368, Apr 2005. ISSN 1432-0924. doi: 10.1007/s00466-004-0623-8. URL <https://doi.org/10.1007/s00466-004-0623-8>.
- [17] Claus Pedersen, Miguel Matos, and Peter Clausen. Sizing optimization for industrial applications. 06 2015. doi: 10.1007/s00158-014-1172-1.
- [18] Stéphane Grihon. Structure sizing optimization capabilities at airbus. In Axel Schumacher, Thomas Vietor, Sierk Fiebig, Kai-Uwe Bletzinger, and Kurt Maute, editors, *Advances in Structural and Multidisciplinary Optimization*, pages 719–737, Cham, 2018. Springer International Publishing. ISBN 978-3-319-67988-4.
- [19] Garam Kim, Ronald Sterkenburg, and Waterloo Tsutsui. Investigating the effects of fluid intrusion on nomex honeycomb sandwich structures with carbon fiber facesheets. *Composite Structures*, 206:535 – 549, 2018. ISSN 0263-8223. doi: <https://doi.org/10.1016/j.compstruct.2018.08.054>. URL <http://www.sciencedirect.com/science/article/pii/S0263822318316039>.
- [20] Brain F. Tatting, Zafer Gürdal, and Dawn Jegley. Design and manufacture of elastically tailored tow placed plates. 2002.

- [21] Zafer Gürdal, Brian F Tatting, and CK Wu. Variable stiffness composite panels: effects of stiffness variation on the in-plane and buckling response. *Composites Part A: Applied Science and Manufacturing*, 39(5):911–922, 2008.
- [22] Shahriar Setoodeh, Mostafa M. Abdalla, Samuel T. IJsselmuiden, and Zafer Gürdal. Design of variable-stiffness composite panels for maximum buckling load. *Composite structures*, 87(1):109–117, 2009.
- [23] Zhangming Wu, Paul M. Weaver, Gangadharan Raju, and Byung Chul Kim. Buckling analysis and optimisation of variable angle tow composite plates. *Thin-Walled Structures*, 60:163 – 172, 2012. ISSN 0263-8231. doi: <https://doi.org/10.1016/j.tws.2012.07.008>. URL <http://www.sciencedirect.com/science/article/pii/S0263823112001930>.
- [24] Mostafa M. Abdalla, Shahriar Setoodeh, and Zafer Gürdal. Design of variable stiffness composite panels for maximum fundamental frequency using lamination parameters. *Composite structures*, 81(2):283–291, 2007.
- [25] Shahriar Setoodeh, Mostafa M. Abdalla, and Zafer Gürdal. Design of variable-stiffness laminates using lamination parameters. *Composites Part B: Engineering*, 37(4-5):301–309, 2006.
- [26] Ali Khani, Samuel T. IJsselmuiden, Mostafa M. Abdalla, and Zafer Gürdal. Design of variable stiffness panels for maximum strength using lamination parameters. *Composites Part B: Engineering*, 42(3):546–552, 2011.
- [27] Cláudio S. Lopes, Pedro Ponces Camanho, Zafer Gürdal, and Brian F Tatting. Progressive failure analysis of tow-placed, variable-stiffness composite panels. *International Journal of Solids and Structures*, 44(25-26):8493–8516, 2007.
- [28] Evangelos Zypeloudis, Kevin Potter, Paul M. Weaver, and Byung Chul Kim. Advanced automated tape laying with fibre steering capability using continuous tow shearing mechanism. In *21st International Conference on Composites Materials*, 2017.
- [29] Gustavo Gonzalez Lozano, Ashutosh Tiwari, Christopher Turner, and Simon Astwood. A review on design for manufacture of variable stiffness composite laminates. *Proceedings of the Institution of Mechanical Engineers, Part B: Journal of Engineering Manufacture*, 230(6):981–992, 2016.
- [30] Daniël M.J. Peeters, Simon Hesse, and Mostafa M. Abdalla. Stacking sequence optimisation of variable stiffness laminates with manufacturing constraints. *Composite Structures*, 125:596–604, 2015.
- [31] Timothy R. Brooks and Joaquim R.R.A. Martins. On manufacturing constraints for tow-steered composite design optimization. *Composite Structures*, 204: 548 – 559, 2018. ISSN 0263-8223. doi: <https://doi.org/10.1016/j.compstruct.2018.07.100>. URL <http://www.sciencedirect.com/science/article/pii/S0263822318308158>.



- [32] Evangelos Zypeloudis Byung Chul Kim. Improvement of fiber placement accuracy in continuous tow shearing process. In *20th International Conference on Composite Materials*, 2015.
- [33] K. Uhlig, M. Tosch, L. Bittrich, A. Leipprand, S. Dey, A. Spickenheuer, and G. Heinrich. Meso-scaled finite element analysis of fiber reinforced plastics made by tailored fiber placement. *Composite Structures*, 143:53 – 62, 2016. ISSN 0263-8223. doi: <https://doi.org/10.1016/j.compstruct.2016.01.049>. URL <http://www.sciencedirect.com/science/article/pii/S0263822316000623>.
- [34] Byung Chul Kim, Kevin Potter, and Paul M. Weaver. Continuous tow shearing for manufacturing variable angle tow composites. *Composites Part A: Applied Science and Manufacturing*, 43(8):1347 – 1356, 2012. ISSN 1359-835X. doi: <https://doi.org/10.1016/j.compositesa.2012.02.024>. URL <http://www.sciencedirect.com/science/article/pii/S1359835X12000929>.
- [35] V. I. Khaliulin, P. A. Khilov, and D. M. Toroptsova. Prospects of applying the tailored fiber placement (tfp) technology for manufacture of composite aircraft parts. *Russian Aeronautics (Iz VUZ)*, 58(4):495–500, Oct 2015. ISSN 1934-7901. doi: 10.3103/S1068799815040236. URL <https://doi.org/10.3103/S1068799815040236>.
- [36] Lucien A. Schmit and B. Farshi. Some approximation concepts for structural synthesis. *AIAA journal*, 12(5):692–699, 1974.
- [37] Claude Fleury and Vincent Braibant. Structural optimisation: a new dual method using mixed variables. *International journal for numerical methods in Engineering*, 23(3):409–428, 1986.
- [38] Krister Svanberg. The method of moving asymptotes—a new method for structural optimisation. *International journal for numerical methods in Engineering*, 24(2): 359–373, 1987.
- [39] C. Fleury. First and second order convex approximation strategies in structural optimization. *Structural optimization*, 1(1):3–10, 1989. ISSN 1615-1488. doi: 10.1007/BF01743804. URL <http://dx.doi.org/10.1007/BF01743804>.
- [40] G.M. Fadel, M.F. Riley, and J.M. Barthelemy. Two point exponential approximation method for structural optimization. *Structural and Multidisciplinary Optimization*, 2(2):117–124, 1990.
- [41] M.Zhou and R.W.Xia. Two-level approximation concept in structural synthesis. *International journal for numerical methods in Engineering*, 29(8):1681–1699, 1990.
- [42] Garret N. Vanderplaats and Srinivas Kodiyalam. Two-level approximation method for stress constraints in structural optimization. *AIAA journal*, 28(5):948–951, 1990.
- [43] G. N. Vanderplaats and H. L. Thomas. An improved approximation for stress constraints in plate structures. *Structural optimization*, 6(1):1–6, 1993. ISSN 1615-1488.

- [44] Adriana W. Blom, Patrick B. Stickler, and Zafer Gürdal. Optimization of a composite cylinder under bending by tailoring stiffness properties in circumferential direction. *Composites Part B: Engineering*, 41(2):157 – 165, 2010. ISSN 1359-8368. doi: <https://doi.org/10.1016/j.compositesb.2009.10.004>. URL <http://www.sciencedirect.com/science/article/pii/S1359836809001887>.
- [45] A.H. Akbarzadeh, M. Arian Nik, and D. Pasini. Vibration responses and suppression of variable stiffness laminates with optimally steered fibers and magnetostrictive layers. *Composites Part B: Engineering*, 91:315 – 326, 2016. ISSN 1359-8368. doi: <https://doi.org/10.1016/j.compositesb.2016.02.003>. URL <http://www.sciencedirect.com/science/article/pii/S1359836816001037>.
- [46] Izzet U. Cagdas. Optimal design of variable stiffness laminated composite truncated cones under lateral external pressure. *Ocean Engineering*, 145:268 – 276, 2017. ISSN 0029-8018. doi: <https://doi.org/10.1016/j.oceaneng.2017.09.011>. URL <http://www.sciencedirect.com/science/article/pii/S0029801817305309>.
- [47] Mostafa M. Abdalla, Shahriar Setoodeh, and Zafer Gürdal. Design of variable stiffness composite panels for maximum fundamental frequency using lamination parameters. *Composite Structures*, 81(2):283 – 291, 2007. ISSN 0263-8223. doi: <https://doi.org/10.1016/j.compstruct.2006.08.018>. URL <http://www.sciencedirect.com/science/article/pii/S0263822306003278>.
- [48] C.S. Lopes, Z. Gürdal, and P.P. Camanho. Variable-stiffness composite panels: Buckling and first-ply failure improvements over straight-fibre laminates. *Computers & Structures*, 86(9):897 – 907, 2008. ISSN 0045-7949. doi: <https://doi.org/10.1016/j.compstruc.2007.04.016>. URL <http://www.sciencedirect.com/science/article/pii/S0045794907001654>. Composites.
- [49] Samuel T. IJsselmuiden, Mostafa M. Abdalla, and Zafer Gürdal. Optimization of variable-stiffness panels for maximum buckling load using lamination parameters. *AIAA journal*, 48(1):134–143, 2010.
- [50] Shahriar Setoodeh, Mostafa M. Abdalla, Samuel T. IJsselmuiden, and Zafer Gürdal. Design of variable-stiffness composite panels for maximum buckling load. *Composite Structures*, 87(1):109 – 117, 2009. ISSN 0263-8223. doi: <https://doi.org/10.1016/j.compstruct.2008.01.008>. URL <http://www.sciencedirect.com/science/article/pii/S0263822308000135>.
- [51] Mohammad Rouhi, Hossein Ghayoor, Suong V. Hoa, and Mehdi Hojjati. Computational efficiency and accuracy of multi-step design optimization method for variable stiffness composite structures. *Thin-Walled Structures*, 113:136 – 143, 2017. ISSN 0263-8231. doi: <https://doi.org/10.1016/j.tws.2017.01.019>. URL <http://www.sciencedirect.com/science/article/pii/S0263823116303494>.
- [52] A. Jibawy, C. Julien, B. Desmorat, A. Vincenti, and F. Léné. Hierarchical structural optimization of laminated plates using polar representation. *International Journal of Solids and Structures*, 48(18):2576 – 2584, 2011. ISSN 0020-7683. doi:

- <https://doi.org/10.1016/j.jisolstr.2011.05.015>. URL <http://www.sciencedirect.com/science/article/pii/S0020768311001879>.
- [53] Masoud Kazemi and Georges Verchery. Design of composite laminated plates for maximum buckling load with stiffness and elastic modulus constraints. *Composite Structures*, 148:27 – 38, 2016. ISSN 0263-8223. doi: <https://doi.org/10.1016/j.compstruct.2016.03.051>. URL <http://www.sciencedirect.com/science/article/pii/S0263822316302136>.
- [54] Marco Montemurro and Anita Catapano. A general b-spline surfaces theoretical framework for optimisation of variable angle-tow laminates. *Composite Structures*, 209:561 – 578, 2019. ISSN 0263-8223. doi: <https://doi.org/10.1016/j.compstruct.2018.10.094>. URL <http://www.sciencedirect.com/science/article/pii/S0263822318324334>.
- [55] Samuel T. Ijsselmuiden, Mostafa M. Abdalla, and Zafer Gürdal. Implementation of strength-based failure criteria in the lamination parameter design space. *AIAA journal*, 46(7):1826–1834, 2008.
- [56] Daniël M.J. Peeters, Gustavo Gonzalez Lozano, and Mostafa M. Abdalla. Effect of steering limit constraints on the performance of variable stiffness laminates. *Computers & Structures*, 196:94 – 111, 2018. ISSN 0045-7949. doi: <https://doi.org/10.1016/j.compstruc.2017.11.002>. URL <http://www.sciencedirect.com/science/article/pii/S004579491730411X>.
- [57] Albert A. Groenwold and Raphael T. Haftka. Optimization with non-homogeneous failure criteria like tsai–wu for composite laminates. *Structural and Multidisciplinary Optimization*, 32(3):183–190, Sep 2006. ISSN 1615-1488. doi: 10.1007/s00158-006-0020-3. URL <https://doi.org/10.1007/s00158-006-0020-3>.
- [58] A. Khani, S.T. Ijsselmuiden, M.M. Abdalla, and Z. Gürdal. Design of variable stiffness panels for maximum strength using lamination parameters. *Composites Part B: Engineering*, 42(3):546 – 552, 2011. ISSN 1359-8368. doi: <https://doi.org/10.1016/j.compositesb.2010.11.005>. URL <http://www.sciencedirect.com/science/article/pii/S1359836810002131>.
- [59] S. Guo, D. Li, and Y. Liu. Multi-objective optimization of a composite wing subject to strength and aeroelastic constraints. *Proceedings of the Institution of Mechanical Engineers, Part G: Journal of Aerospace Engineering*, 226(9):1095–1106, 2012. doi: 10.1177/0954410011417789. URL <https://doi.org/10.1177/0954410011417789>.
- [60] Erik Lund. Discrete material and thickness optimization of laminated composite structures including failure criteria. *Structural and Multidisciplinary Optimization*, pages 1–19, 2017.
- [61] Amir M. Mirzendehtdel, Behzad Rankouhi, and Krishnan Suresh. Strength-based topology optimization for anisotropic parts. *Additive Manufacturing*, 19:104 – 113, 2018. ISSN 2214-8604. doi: <https://doi.org/10.1016/j.addma.>

2017.11.007. URL <http://www.sciencedirect.com/science/article/pii/S2214860416303475>.



# 2

## EFFICIENT COMPUTATIONAL METHOD FOR STRESS CONSTRAINTS

*I succeeded because I willed it, I never hesitated.*  
我成功是因为我有决心，从不踌躇。

Napoleon Bonaparte

### 2.1. INTRODUCTION

The choice of a solution method for a structural optimization problem is usually based on the overall computational cost and the ability of the method to converge to a useful solution. Zeroth-order methods, such as evolutionary algorithms, are often used for non-convex problems as they are most suitable for finding global solutions. However, these methods require a large number of functional evaluations to scan the design space and, consequently, they often become unmanageable for problems with a large number of variables and/or constraints. Gradient-based methods are attractive alternatives for large problems where the time and resources for computation are limited (Setoodeh et al. [1], Holmberg et al. [2], Nesterov [3]). In general, the efficiency of a method depends directly on how it scales with the size of problem, i.e., its computational complexity. Interior Point Methods (IPM), which are gradient-based algorithms, are specifically designed for large scale inequality constrained problems (Megiddo [4]). They have been actively adapted to solve a wide range of problems in material and structural design optimization (see. e.g., Maar and Schulz [5], Weldeyesus and Stolpe [6]). One of the most successful versions is Mehrotra's IPM (Mehrotra [7]), which from its inception was identified as be-

---

Part of this chapter is based on the conference paper Zhi Hong, Mostafa Abdalla, *An efficient optimization method for stress constrained sizing design*, European Community on Computational Methods in Applied Sciences (ECCOMAS), Crete, Greece, 2016, pp. 3436-3460.

ing more efficient and stable compared with other gradient-based methods (Lustig et al. [8]).

Regarding optimization problems with local stress constraints, numerous stress approximations have been proposed in order to reduce the computational cost since the pioneering work of Schmit and Farshi [9]. Fleury and Braibant [10] combined linear and reciprocal terms in the approximation, which leads the optimization steadily to the optimal solution. Svanberg [11] achieved more stable and faster convergence for weight minimization of a bar truss with stress constraint by the Method of the Moving Asymptotes (MMA). Fleury [12] added a diagonal second order term in stress approximation with ConLin, MMA and Sequential Quadratic Programming (SQP). Fadel et al. [13] proposed a two-point exponential approximation method for stress constraint which reduced CPU time and total number of iterations for convergence. M.Zhou and R.W.Xia [14], Vanderplaats and Kodiyalam [15], Vanderplaats and Thomas [16] introduced a two-level approximation that improved the accuracy of the approximation in the optimization. Since their development, these types of stress constraint approximations have been extensively used in structural optimization.

To further accelerate the stress-constrained optimization procedure, different strategies have been proposed. Nagy et al. [17] employed a variational formulation for stress constraints in isogeometric design. Paris et al. [18] proposed three ways to deal with stress constraints such as a global and block constraints aggregation and parallel computing. Duysinx and Bendsøe [19] and Holmberg et al. [20] combined local stress constraints with a  $p$ -norm to reduce the number of constraints, while Kiyono et al. [21] introduced a multi- $p$ -norm for stress constraint. The main driver in all these improvements has been to be able to solve increasingly larger scale problems.

In the spirit of the aforementioned methods, the main purpose of the present work is to develop an improved algorithm that reduces the computational complexity of stress-constrained optimal design problems. The proposed method is obtained by improvements in existing methods within the framework of the conservative convex separable approximations (CCSA, Svanberg [22]). There are three computational processes in the optimization framework, namely (1) the Finite Element Method (FEM) analysis of the structure, (2) the formulation of a sub-problem with convex approximation and the computation of the gradient of the stress constraints using the adjoint method and (3) the application of Mehrotra's predictor-corrector IPM (Mehrotra [7]) to solve the optimization problem where the direct method is employed to solve the Schur complement. In a large scale optimization problem, the Schur complement in the IPM is the most computationally expensive part, followed by the adjoint method for the local stress constraints, with the computational effort increasing exponentially with the problem size.

To alleviate the overall computational cost, three improvements are proposed in this work. First, a new approximation for the stress constraint is developed based on the fully-stressed design (Haftka and Gürdal [23]). The approximation is convex, conservative and separable, therefore efficiently reduces the cost to calculate the Hessian and accelerates the convergence. Second, an implicit sensitivity analysis is proposed, which reduces the computational complexity with the adjoint method and the reanalysis method.

Third, a preconditioner, which employs the fully stressed design, is introduced for the Schur complement of the Karush-Kuhn-Tucker (KKT) conditions, implemented as a preconditioned conjugate gradient method (PCG). When the three aforementioned modifications are embedded in Mehrotra's IPM, the computational cost can be reduced if the number of iterations in the PCG is sufficiently small, in which case it can be applied to solve large scale problems efficiently.

The content of this chapter is structured as follows: In Section 2.2, the prototype problem, its associated Finite Element formulation and the framework of the optimization are described first. Section 2.3 introduces the modified stress approximation for the proposed method and all the formulations for the prototype method. In Section 2.4, a preconditioner for the PCG is introduced together with an implicit sensitivity analysis to reduce the computational cost. Three numerical cases with the proposed optimization method are shown in Section 2.5. Concluding remarks are given in Section 2.7.

## 2.2. FORMULATION OF THE OPTIMIZATION PROBLEM

### 2.2.1. PROTOTYPICAL OPTIMIZATION PROBLEM

The objective of the sizing optimization is to minimize the volume of structures, which corresponds to minimizing their weight assuming a homogeneous material. For beam-based structures, a beam is discretized using the finite element method and the design variables  $x_i$ , with  $i = 1, 2, \dots, n$ , correspond to local values of the width or height of a beam. For convenience, these design variables are collected in a vector,

$$\mathbf{x} := [x_1, x_2, \dots, x_n] \quad (2.1)$$

where  $n$  is the total number of design variables. These design variables are subjected to side constraints (i.e., minimum and maximum allowable values denoted as  $\underline{x}_i$ , and  $\bar{x}_i$ , respectively). In addition, the magnitude of the local stress  $f_i(\mathbf{x})$ ,  $i = 1, \dots, m$ , is constrained such that it should not exceed a maximum allowable stress  $\bar{\sigma}$ , with  $m$  representing the total number of stress constraints.

Denoting the normalized volume of the structure as  $f_0$ , the optimization problem is formulated as finding a vector  $\mathbf{x}$  which minimizes  $f_0(\mathbf{x})$  subject to equilibrium, local stress constraints and local upper and lower bounds, i.e.,

$$\min_{\mathbf{x}} f_0(\mathbf{x}) = \sum_{i=1}^n x_i c_i / V_0 \quad (2.2)$$

subject to:

$$f_i(\mathbf{x}) / \bar{\sigma} \leq 1 \quad i = 1 \dots m \quad (2.3)$$

$$\underline{x}_j \leq x_j \leq \bar{x}_j \quad j = 1 \dots n \quad (2.4)$$

where the coefficients  $c_i$  are geometrical parameters at each node  $i = 1, \dots, n$  used to calculate the volume of the structure and  $V_0$  is the initial volume. In the present work,



the stress constraints are applied at the same locations where the design variables are defined, hence  $m = n$ . The condition of equilibrium is not stated explicitly in the problem formulation but, rather, implicitly through the stress constraint which must be computed from a finite element analysis of the structure as described in the next subsection.

### 2.2.2. ASSOCIATED FINITE ELEMENT ANALYSIS OF STRUCTURE

In the static case, the finite element formulation of the equation of equilibrium is

$$\mathbf{K}\mathbf{u} = \mathbf{b} \quad (2.5)$$

where  $\mathbf{K}$  is the global stiffness matrix obtained by assembling the stiffness matrices from each element,  $\mathbf{u}$  is the global displacement vector, and  $\mathbf{b}$  represents the loading applied on the structure.

Upon obtaining the solution  $\mathbf{u}$  from Eq.(2.5) in global coordinates, the displacement vector  $\tilde{\mathbf{u}}_e$  in the  $e^{\text{th}}$  element in local coordinates can be obtained as

$$\tilde{\mathbf{u}}_e = \mathbf{T}_e \mathbf{u}_e \quad (2.6)$$

where  $\mathbf{T}_e$  is the transformation matrix from the global coordinates to the local element coordinates and  $\mathbf{u}_e$  is the nodal displacement corresponding to the degrees of freedom in the  $e^{\text{th}}$  element. In an Euler-Bernoulli beam, the normal stress  $\sigma_g$  on the  $g^{\text{th}}$  Gauss point in the  $e^{\text{th}}$  element can be computed as

$$\sigma_g = \mathbf{C}\mathbf{B}_g \tilde{\mathbf{u}}_e \quad (2.7)$$

where,  $\mathbf{C}$  is the material stiffness, which depends on Young's modulus  $E$ , and  $\mathbf{B}_g$  is the strain-displacement matrix. Since the width or height of the cross section in a beam is variable, the stiffness matrix in each element is a function of position. For definiteness, an Euler-Bernoulli beam with two Gauss point in each element is employed in the present analysis. Further, a reciprocal interpolation is used to compute the structural stiffness  $D = EI$  at Gauss points, where  $I$  is the moment of inertia. To demonstrate this idea, consider the beam element shown in Figure 2.1. The structural stiffness  $D_g$  at the  $g^{\text{th}}$  Gauss point in the element is

$$D_g^{-1} = \sum_{i=i'}^{i'+1} N_{(i,g)} D_i^{-1} \quad (2.8)$$

where  $D_i$  is the structural stiffness evaluated at node  $i$  in an element (black nodes in Figure 2.1), and  $N_{(i,g)}$  is the linear shape function of the  $i^{\text{th}}$  node evaluated at the  $g^{\text{th}}$  Gauss point. The range  $i = i', i' + 1$  is meant to represent two generic adjacent nodes in a global numbering system. This type of interpolation enhances the continuity of the stress distribution across elements (Khani et al. [24]).

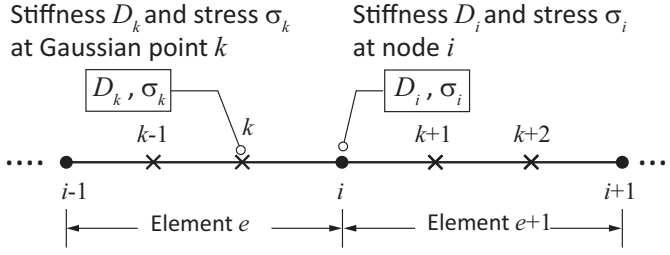


Figure 2.1: Illustration of two adjacent beam elements, each with two integration points, used for interpolation.

### 2.2.3. OPTIMIZATION FRAMEWORK OF THE PROBLEM

The Lagrangian function for the problem is

$$L(\mathbf{x}, \mathbf{y}^s, \mathbf{y}^u, \mathbf{y}^l) = f_0(\mathbf{x}) + (\mathbf{y}^s)^T \left( \frac{\mathbf{f}(\mathbf{x})}{\bar{\sigma}} - \mathbf{e} \right) + (\mathbf{y}^u)^T (\mathbf{x} - \bar{\mathbf{x}}) + (\mathbf{y}^l)^T (\underline{\mathbf{x}} - \mathbf{x}) \quad (2.9)$$

where  $\mathbf{y}^s$  is the vector of Lagrange multipliers associated to the corresponding stress constraints. The Lagrange multipliers for the upper and lower bound of the design variables are denoted by  $\mathbf{y}^u$  and  $\mathbf{y}^l$ , respectively. The superscript  $T$  denotes the transpose and  $\mathbf{e} = [1, 1, \dots, 1]^T$  with  $n$  components.

To project the stress from each Gauss point into a node, the variational stress constraint formulation (Nagy et al. [17]) is used here. To this end, observe that the second term on the right hand side in Eq.(2.9) represents the discrete formulation of the continuous stress constraint  $\mathcal{L}^\sigma$ , which is defined as

$$\mathcal{L}^\sigma := \int \tilde{y}^s \left( \frac{\sigma}{\bar{\sigma}} - 1 \right) d\Omega \quad (2.10)$$

where  $\tilde{y}^s$  is the Lagrange multiplier for the stress constraint at each point in the domain. Upon discretization the Lagrange multiplier field  $\tilde{y}^s$  using linear shape functions  $N_{(i,g)}$ , the term  $\mathcal{L}^\sigma$  can be approximated as

$$\begin{aligned} \mathcal{L}^\sigma &\approx \sum_{g=1}^{n_g} \left[ \left( \sum_{i=1}^n \tilde{y}_i^s N_{(i,g)} \right) \left( \frac{\sigma_g}{\bar{\sigma}} - 1 \right) \Omega_g \right] \\ &= \sum_{i=1}^n \tilde{y}_i^s \left( \sum_{g=1}^{n_g} N_{(i,g)} \left( \frac{\sigma_g}{\bar{\sigma}} \Omega_g - \Omega_g \right) \right). \end{aligned} \quad (2.11)$$

where  $n_g$  is total number of Gauss points in the design domain  $\Omega$ ,  $\Omega_g$  is the domain measured at Gauss point  $g$  related to the numerical integration rule and  $\sigma_g$  is the normal stress at the  $g^{\text{th}}$  Gauss point. Dividing and multiplying Eq.(2.11) by  $\sum_{g=1}^{n_g} N_{(i,g)} \Omega_g$  provides the equivalent formula

$$\mathcal{L}^\sigma = \sum_{i=1}^n \tilde{y}_i^s \left( \sum_{g=1}^{n_g} N_{(i,g)} \Omega_g \right) \left( \frac{\sum_{g=1}^{n_g} N_{(i,g)} \sigma_g \Omega_g}{\bar{\sigma} \sum_{g=1}^{n_g} N_{(i,g)} \Omega_g} - 1 \right). \quad (2.12)$$

From Eq.(2.12), it follows that the stress at node  $i$  can be approximated by

$$\sigma_i = \frac{\sum_{g=1}^{n_g} N_{(i,g)} \sigma_g \Omega_g}{\sum_{g=1}^{n_g} N_{(i,g)} \Omega_g}. \quad (2.13)$$

For a regular mesh, using the partition of unity property, expression (2.13) can be simplified as

$$\sigma_i = \frac{\sum_{g=1}^{n_g} N_{(i,g)} \sigma_g \Omega_g}{\sum_{p=1}^{n'_g} \Omega_p} \quad (2.14)$$

where  $n'_g$  is the number of Gauss points directly connected with the  $i^{\text{th}}$  node. In this way, both the stress and the Lagrange multiplier are continuous across elements.

## 2.3. FORMULATION OF MODIFIED FULLY STRESSED DESIGN

### 2.3.1. MODIFIED STRESS APPROXIMATION

In this section, an improved convex approximation for the stress constraints is introduced in order to accelerate the computational process. As noted in Vanderplaats and Thomas [16], Vanderplaats and Salajegheh [25], approximating the internal forces is more accurate than approximating the stress constraints directly with local constraints. One potential drawback, however, is that separability and convexity are not guaranteed by force approximations. To overcome this issue, a convex and separable stress approximation is developed here. The starting point is to use the fully-stressed design (Haftka and Gürdal [23]), which is a zeroth order force approximation, and add linear terms to formulate a computationally-efficient improved approximation. The underlying idea is to use only computationally inexpensive terms in the derivative that, nonetheless, improve the quality of the first-order approximation.

To develop the modified stress approximation, consider first the normalized stress constraint, which takes the form

$$r - 1 \leq 0, \quad r = \frac{|\sigma|}{\bar{\sigma}} \quad (2.15)$$

where  $\bar{\sigma}$  is the allowable stress and, in a fully-stressed design, the stress  $\sigma$  is related to an internal force-like term  $\mathcal{F}$  and an area-like function  $\mathcal{A}$  such that

$$|\sigma| = \frac{|\mathcal{F}|}{\mathcal{A}(x)}, \quad (2.16)$$

where  $x$  is the design variable. In the beam case,  $\mathcal{F}$  denotes the bending moment while  $\mathcal{A}(x) = y/I_z(x)$  is the geometrical term used to calculate the normal stress,  $y$  is the distance from top edge to the neutral axis and  $I_z(x)$  is the area moment of inertia.

The numerical treatment of the problem starts by discretizing the structure using finite elements. In the CCSA, the approximations are updated at the beginning of each outer loop and the design variables are updated inside the IPM step by step. The pair of indices

$\{\alpha, \lambda\}$  will be used to indicate the outer loop in CCSA (index  $\alpha$ ) and the steps in the IPM (index  $\lambda$ ). The fully-stressed approximation for the  $i^{\text{th}}$  node at the  $\lambda^{\text{th}}$  inner loop may be written as a function of the internal force  $\mathcal{F}_i^{(\alpha)}$  at the  $\alpha^{\text{th}}$  outer loop and the design variables at the  $\lambda^{\text{th}}$  iteration as

$$r_i^{(\alpha, \lambda)} := r_i(\mathcal{F}_i^{(\alpha)}, x_i^{(\lambda)}) = \frac{|\mathcal{F}_i^{(\alpha)}|}{\mathcal{A}(x_i^{(\lambda)})\bar{\sigma}} \leq 1, \quad i = 1, 2, \dots, n. \quad (2.17)$$

Note that the internal force  $\mathcal{F}_i^{(\alpha)}$  at any given node  $i$  is assumed to be *constant* (obtained at  $\mathbf{x}^{(\alpha)}$ ) in the inner loop  $\lambda$ . The vector  $\mathbf{x}^{(\alpha)}$  is referred to as the approximation point. The approximation Eq.(2.17) would be exact only for statically determinate structures where the internal force  $\mathcal{F}_i^{(\alpha)}$  is independent of the design variables.

To improve the representation of the stress constraint Eq.(2.17), a modified approximation  $\hat{r}_i$  at the  $\{\alpha, \lambda\}$  iteration is proposed which corresponds to a combination of two optimization methods, namely the optimality criterion method and a gradient-based optimization algorithm. To this end, the fully stressed optimality condition Eq.(2.17) is modified as follows:

$$\hat{r}_i^{(\alpha, \lambda)} = \frac{|\mathcal{F}_i^{(\alpha)}|}{\mathcal{A}_i(x_i^{(\lambda)})\bar{\sigma}} + \sum_{j=1}^n A_{ji}^{(\alpha)} (x_j^{(\lambda)} - x_j^{(\alpha)}). \quad (2.18)$$

The second term provides a linear correction and represents the effect of *load redistribution* present in statically indeterminate structures. The approximation  $\hat{r}_i^{(\alpha, \lambda)}$  in Eq.(2.18) evaluated at  $x_i^{(\lambda)} = x_i^{(\alpha)}$  should match both the value and the gradient of the term  $r$  in Eq.(2.15) at each node  $i$  of the FEM model evaluated at  $\mathbf{x}^{(\alpha)}$ , i.e.,

$$\hat{r}_i^{(\alpha, \alpha)} = r_i \Big|_{x^{(\alpha)}} = \frac{|\sigma|}{\bar{\sigma}} \Big|_{x^{(\alpha)}} \quad (2.19)$$

$$\frac{\partial \hat{r}_i}{\partial x_j^{(\lambda)}} \Big|_{x^{(\alpha)}} = \frac{\partial r_i}{\partial x_j} \Big|_{x^{(\alpha)}} = \frac{\text{sgn}(\sigma_i)}{\bar{\sigma}} \cdot \frac{\partial \sigma_i}{\partial x_j} \Big|_{x^{(\alpha)}} \quad (2.20)$$

The condition Eq.(2.19) is automatically satisfied from Eq.(2.18). The coefficients  $A_{ji}^{(\alpha)}$  can be obtained from Eq.(2.18) and Eq.(2.20)

$$-\frac{|\mathcal{F}_i^{(\alpha)}|}{\mathcal{A}_i(x_i^{(\lambda)})^2 \bar{\sigma}} \cdot \frac{\partial \mathcal{A}_i(x_i^{(\lambda)})}{\partial x_j^{(\lambda)}} \Big|_{x^{(\alpha)}} + A_{ji}^{(\alpha)} = \frac{\text{sgn}(\sigma_i)}{\bar{\sigma}} \cdot \frac{\partial \sigma_i}{\partial x_j} \Big|_{x^{(\alpha)}}, \quad (2.21)$$

therefore

$$A_{ji}^{(\alpha)} = \frac{\text{sgn}(\sigma_i)}{\bar{\sigma}} \cdot \frac{\partial \sigma_i}{\partial x_j} \Big|_{x^{(\alpha)}} + \frac{|\mathcal{F}_i^{(\alpha)}|}{\mathcal{A}_i(x_i^{(\lambda)})^2 \bar{\sigma}} \cdot \frac{\partial \mathcal{A}_i(x_i^{(\lambda)})}{\partial x_j^{(\lambda)}} \Big|_{x^{(\alpha)}}. \quad (2.22)$$

The approximation proposed here for the stress constraints provides the foundation for the implementation of the implicit sensitivity analysis and the preconditioner for the Schur complement in the PCG, which will be introduced in Section 2.4.

In contrast, the ConLin and MMA require the explicit gradient matrix and the formula is different for each design variable. Hence it prohibits the application of an implicit sensitivity analysis. The reciprocal approximation also requires the adjoint method to calculate the components in the preconditioner if embedded in the proposed method. Therefore, the ConLin, MMA and reciprocal approximations are not compatible with the method proposed in this chapter.

In order to compute the first term on the right-hand side of Eq.(2.22), it is useful to introduce the design sensitivity analysis.

### 2.3.2. SENSITIVITY ANALYSIS

Sensitivity analysis for the objective and constraints starts before each outer loop of the CCSA. The gradient information then guides the optimizer towards the optimal solution step by step in each inner iteration. The adjoint method is employed to estimate the sensitivity in the proposed method.

From Eq.(2.7) and (2.13), the sensitivity of the node-based stress  $\sigma_i$  with respect to the design variable  $x_j$  is given by

$$\frac{\partial \sigma_i}{\partial x_j} = \mathbf{z}_i^T \frac{\partial \mathbf{u}_i}{\partial x_j} \quad (2.23)$$

where

$$\mathbf{z}_i = \frac{\sum_{g=1}^{n_g} N_{(i,g)} \Omega_g \mathbf{z}_g}{\sum_{g=1}^{n_g} N_{(i,g)} \Omega_g},$$

and  $\mathbf{z}_g$  is obtained by

$$\mathbf{z}_g = \mathbf{T}_{(e,g)}^T \mathbf{B}_g^T \mathbf{C}^T \quad (2.24)$$

where  $\mathbf{T}_{(e,g)}$  is the transformation matrix from the global to local coordinates in the  $e^{\text{th}}$  element for the  $g^{\text{th}}$  Gauss point.

In accordance with the adjoint method, and assuming that the external load  $\mathbf{b}$  does not depend on the design variables, the sensitivity of the stress is

$$\frac{\partial \sigma_i}{\partial x_j} = -\mathbf{t}_i^T \frac{\partial \mathbf{K}}{\partial x_j} \mathbf{u} \quad (2.25)$$

where  $\mathbf{t}_i$  is obtained through

$$\mathbf{K} \mathbf{t}_i = \mathbf{z}_i. \quad (2.26)$$

In the adjoint method, Eq.(2.26) needs to be solved at each node  $i$  where there is a stress constraint. These expressions will be subsequently used in the implicit sensitivity analysis.

### 2.3.3. CONSERVATIVE, CONVEX AND SEPARABLE APPROXIMATION

In CCSA, the approximation should be conservative, convex and separable. From Eq.(2.18), it can be observed that the stress approximation is separable. Consequently, the corresponding Hessian matrix is diagonal and can be efficiently computed as

$$\frac{\partial^2 \hat{r}_i^{(\alpha, \beta)}}{\partial (x_j^{(\beta)})^2} \Big|_{\mathbf{x}^{(\alpha)}} = \begin{cases} \frac{2|\mathcal{F}_i^{(\alpha)}|}{\mathcal{A}_i^3(x_i)\bar{\sigma}} \left( \frac{\partial \mathcal{A}_i(x_i)}{\partial x_i} \right)^2 - \frac{|\mathcal{F}_i^{(\alpha)}|}{\mathcal{A}_i^2(x_i)\bar{\sigma}} \cdot \frac{\partial^2 \mathcal{A}_i(x_i)}{\partial x_i^2} > 0 \text{ if } j = i \\ 0 \text{ if } j \neq i \end{cases} \quad (2.27)$$

Since the second derivative of the stress approximation with respect to the design variable is non-negative, the proposed stress approximation is convex as required for CCSA. Moreover, the fully stressed part in Eq.(2.18) makes the approximation easily scalable compared with linear constraints to find the feasible design.

To enforce the property of being conservative, the following *damping function* is added to the stress approximation:

$$d = \sum_{i=1}^n q_i \left( \frac{x_i}{x_i^{(\alpha)}} + \frac{x_i^{(\alpha)}}{x_i} - 2 \right) \quad (2.28)$$

where  $q_i = \sum_{g=1}^{n_g} N_{(i,g)} \Omega_g / \left( \sum_{g=1}^{n_g} \Omega_g \right)$  is the weight factor for  $x_i$ .

This damping function has two important features namely, (i) the damping function is separable and (ii) both the damping function and its gradient are 0 at  $\mathbf{x}^{(\alpha)}$ . These features guarantees that the stress approximation and its gradient match the values from the FEM calculation. With the addition of the damping term, the complete stress approximation  $\check{r}$  in the optimization becomes

$$\check{r}_i = \hat{r}_i + \rho_i d \quad (2.29)$$

where  $\hat{r}_i$  is the stress approximation Eq.(2.18), and  $\rho_i$  is a damping factor for the  $i^{th}$  stress constraint, which can be updated iteratively.

In order to initialize the damping factor  $\rho_i$ , the following value is used as an initial guess for all nodes:

$$\rho_{i,0}^2 = \frac{1}{2} (\mathbf{A}^{(\alpha)} \mathbf{y}^s)^T \mathbf{H}_d(\mathbf{x}_0)^{-1} (\mathbf{A}^{(\alpha)} \mathbf{y}^s) \quad (2.30)$$

where  $\mathbf{x}_0$  are the initial design variables,  $\mathbf{A}^{(\alpha)}$  is the matrix with components  $A_{ji}^{(\alpha)}$  as defined in Eq.(2.18),  $\mathbf{H}_d(\mathbf{x}_0)$  is a diagonal matrix consisting of the second derivative of the damping function with respect to the design variables,  $\mathbf{y}^s$  are the Lagrange multipliers as introduced in Eq.(2.9) and  $n$  is the total number of nodes in the FE model. Although Eq.(2.30) is somewhat arbitrarily chosen, numerical experiments show that it provides a reasonable initial guess.

The update of  $\rho_i$  in the CCSA will be explained in Section 2.4.3. As a preliminary step, the interior point method (IPM) in the CCSA is introduced next.

### 2.3.4. PREDICTOR-CORRECTOR INTERIOR POINT METHOD

In this work, Mehrotra's predictor-corrector IPM is employed due to its efficient convergence (Lustig et al. [8], Zillober [26]). By introducing the slacks for the inequality constraints and adding logarithmic barrier functions, the Lagrangian function of Eq.(2.2) becomes

$$\begin{aligned} \mathcal{L}_\mu(\mathbf{x}, \mathbf{s}, \mathbf{y}^s, \mathbf{s}^u, \mathbf{y}^l, \mathbf{s}^l, \mathbf{y}^l) &= f_0 + (\mathbf{y}^s)^T (\mathbf{f}(\mathbf{x}) + \mathbf{s}) \\ &+ (\mathbf{y}^u)^T (\mathbf{x} - \bar{\mathbf{x}} + \mathbf{s}^u) + (\mathbf{y}^l)^T (\underline{\mathbf{x}} - \mathbf{x} + \mathbf{s}^l) \\ &- \mu \sum_{i=1}^n \ln s_i - \mu \sum_{i=1}^n \ln s_i^u - \mu \sum_{i=1}^n \ln s_i^l \end{aligned} \quad (2.31)$$

where  $\mathbf{s}$  are the slacks for stress constraints,  $\mathbf{s}^u$  and  $\mathbf{s}^l$  are upper and lower bounds of the design variables, respectively,  $\mathbf{f}(\mathbf{x})$  is the stress approximation  $\check{\mathbf{r}} - \mathbf{1}$  according to Eq.(2.29), and  $\mu$  is the penalty parameter. As  $\mu \rightarrow 0$ , the value of  $\mathcal{L}_\mu$  in Eq.(2.31) converges to the value of  $\mathcal{L}$  in Eq.(2.9) evaluated at the optimal solution.

According to the Karush-Kuhn-Tucker formulation, the necessary conditions for optimality are:

$$\frac{\partial \mathcal{L}}{\partial \mathbf{x}} = \nabla f_0(\mathbf{x}) + \mathbf{G}(\mathbf{x})\mathbf{y}^s + \mathbf{y}^u - \mathbf{y}^l = \mathbf{0} \quad (2.32)$$

$$\frac{\partial \mathcal{L}}{\partial \mathbf{y}^s} = \mathbf{f}(\mathbf{x}) + \mathbf{s} = \mathbf{0} \quad (2.33)$$

$$\frac{\partial \mathcal{L}}{\partial \mathbf{y}^u} = \mathbf{x} - \bar{\mathbf{x}} + \mathbf{s}^u = \mathbf{0} \quad (2.34)$$

$$\frac{\partial \mathcal{L}}{\partial \mathbf{y}^l} = \underline{\mathbf{x}} - \mathbf{x} + \mathbf{s}^l = \mathbf{0} \quad (2.35)$$

$$\frac{\partial \mathcal{L}}{\partial \mathbf{s}} = \mathbf{Y}^s \mathbf{s} - \mu \mathbf{e} = \mathbf{0} \quad (2.36)$$

$$\frac{\partial \mathcal{L}}{\partial \mathbf{s}^u} = \mathbf{Y}^u \mathbf{s}^u - \mu \mathbf{e} = \mathbf{0} \quad (2.37)$$

$$\frac{\partial \mathcal{L}}{\partial \mathbf{s}^l} = \mathbf{Y}^l \mathbf{s}^l - \mu \mathbf{e} = \mathbf{0} \quad (2.38)$$

where  $\mathbf{G}(\mathbf{x})$  is the gradient of the stress approximation (Eq.(2.29)), the diagonal matrix  $\mathbf{Y}^s$  is constructed with the Lagrange multipliers associated to the stress constraints  $y_i^s$  as  $\mathbf{Y}^s = \text{diag}(y_1^s, \dots, y_n^s)$ , and a similar definition is used for the diagonal matrices  $\mathbf{Y}^u$  and  $\mathbf{Y}^l$  with the corresponding Lagrange multipliers of the upper and lower bounds.

Expanding the above equations with Newton's method, the following linear subproblem

can be obtained:

$$\begin{aligned} G(\mathbf{x})\Delta\mathbf{y}^s + (\mathbf{y}^s)^T H(\mathbf{x}) \Delta\mathbf{x} + \Delta\mathbf{y}^u - \Delta\mathbf{y}^l = \\ -\nabla f_0 - G(\mathbf{x})\mathbf{y}^s - \mathbf{y}^u + \mathbf{y}^l \end{aligned} \quad (2.39)$$

$$G^T(\mathbf{x})\Delta\mathbf{x} + \Delta\mathbf{s} = -\mathbf{f}(\mathbf{x}) - \mathbf{s} \quad (2.40)$$

$$\Delta\mathbf{x} + \Delta\mathbf{s}^u = \bar{\mathbf{x}} - \mathbf{x} - \mathbf{s}^u \quad (2.41)$$

$$-\Delta\mathbf{x} + \Delta\mathbf{s}^l = \mathbf{x} - \underline{\mathbf{x}} - \mathbf{s}^l \quad (2.42)$$

$$S\Delta\mathbf{y}^s + Y^s\Delta\mathbf{s} = \mu\bar{\mathbf{e}} - Y^s\mathbf{s} - \Delta Y^s\Delta\mathbf{s} \quad (2.43)$$

$$S^u\Delta\mathbf{y}^u + Y^u\Delta\mathbf{s}^u = \mu\bar{\mathbf{e}} - Y^u\mathbf{s}^u - \Delta Y^u\Delta\mathbf{s}^u \quad (2.44)$$

$$S^l\Delta\mathbf{y}^l + Y^l\Delta\mathbf{s}^l = \mu\bar{\mathbf{e}} - Y^l\mathbf{s}^l - \Delta Y^l\Delta\mathbf{s}^l \quad (2.45)$$

where  $S$  is the diagonal matrix of the form  $S = \text{diag}(s_1, \dots, s_n)$ . The same notation applies to  $S^u$ ,  $S^l$ ,  $\Delta Y^s$ ,  $\Delta Y^u$ ,  $\Delta Y^l$ . The  $n \times n \times n$  matrix  $H(\mathbf{x})$  is a collection of  $n$  Hessian matrices for each stress constraint with respect to the design variables. The notation  $(\mathbf{y}^s)^T H(\mathbf{x})$  indicated in Eq.(2.39) refers to the diagonal matrix of components  $i, j$  obtained as  $\sum_{k=1}^n H_{kij} y_k^s = \sum_{k=1}^n \frac{\partial^2 f_k}{\partial x_i \partial x_j} y_k^s$ .

For convenience, all variables are collected in a single vector  $\chi$  as

$$\chi = (\mathbf{x}, \mathbf{y}^s, \mathbf{y}^u, \mathbf{y}^l, \mathbf{s}, \mathbf{s}^u, \mathbf{s}^l).$$

The purpose of the above subproblem is to calculate  $\Delta\chi$ , which will be used to update the variable  $\chi$  in each inner iteration in IPM by  $\chi^{(\lambda+1)} = \chi^{(\lambda)} + \Delta\chi$  from

$$C_\mu \Delta\chi = \mathbf{F}_\mu \quad (2.46)$$

where

$$\mathbf{F}_\mu(\chi) = \begin{bmatrix} \mathbf{F}_x \\ \mathbf{F}_{y^s} \\ \mathbf{F}_{y^u} \\ \mathbf{F}_{y^l} \\ \mathbf{F}_s \\ \mathbf{F}_{s^u} \\ \mathbf{F}_{s^l} \end{bmatrix} = \begin{bmatrix} -\nabla f_0 - G(\mathbf{x})\mathbf{y}^s - \mathbf{y}^u + \mathbf{y}^l \\ -\mathbf{f}(\mathbf{x}) - \mathbf{s} \\ \bar{\mathbf{x}} - \mathbf{x} - \mathbf{s}^u \\ \mathbf{x} - \underline{\mathbf{x}} - \mathbf{s}^l \\ \mu\mathbf{e} - Y^s\mathbf{s} - \gamma\Delta Y^s\Delta\mathbf{s} \\ \mu\mathbf{e} - Y^u\mathbf{s}^u - \gamma\Delta Y^u\Delta\mathbf{s}^u \\ \mu\mathbf{e} - Y^l\mathbf{s}^l - \gamma\Delta Y^l\Delta\mathbf{s}^l \end{bmatrix} \quad (2.47)$$

and  $\gamma$  is a scalar which will be changed between the predictor ( $\gamma = 0$ ) and corrector ( $\gamma = 1$ ) steps. In Eq.(2.46), the matrix  $C_\mu$  is given as

$$C_\mu = \begin{bmatrix} (\mathbf{y}^s)^T H(\mathbf{x}) & G(\mathbf{x}) & \mathbf{I} & -\mathbf{I} & 0 & 0 & 0 \\ G^T(\mathbf{x}) & 0 & 0 & 0 & \mathbf{I} & 0 & 0 \\ \mathbf{I} & 0 & 0 & 0 & 0 & \mathbf{I} & 0 \\ -\mathbf{I} & 0 & 0 & 0 & 0 & 0 & \mathbf{I} \\ 0 & S & 0 & 0 & Y^s & 0 & 0 \\ 0 & 0 & S^u & 0 & 0 & Y^u & 0 \\ 0 & 0 & 0 & S^l & 0 & 0 & Y^l \end{bmatrix}. \quad (2.48)$$



The matrix  $C_\mu$  depends implicitly on  $\mu$  through its components that are updated iteratively. To simplify Eq.(2.46), some variables can be eliminated by substitution. From Eq.(2.41) and Eq.(2.44), and since the matrix  $S^u$  is diagonal,  $\Delta \mathbf{s}^u$  and  $\Delta \mathbf{y}^u$  can be expressed in terms of  $\Delta \mathbf{x}$ . Similarly, from Eq.(2.42) and Eq.(2.45),  $\Delta \mathbf{s}^l$  and  $\Delta \mathbf{y}^l$  can be expressed in terms of  $\Delta \mathbf{x}$ . From Eq.(2.43),  $\Delta \mathbf{s}$  can be expressed in terms of  $\Delta \mathbf{y}^s$ . Finally expressing  $\Delta \mathbf{x}$  in terms of  $\Delta \mathbf{y}^s$ , the Schur complement of the subproblem, which is also called the normal equation, can be obtained as

$$D_\mu \Delta \mathbf{y}^s = \mathbf{F}_{\text{schur}} \quad (2.49)$$

where

$$D_\mu = [(\mathbf{Y}^s)^{-1} \mathbf{S} + \mathbf{G}^T(x) \mathbf{Q}^{-1} \mathbf{G}(x)], \quad (2.50)$$

$$\mathbf{Q} = (\mathbf{y}^s)^T \mathbf{H}(\mathbf{x}) + \mathbf{Y}^u (\mathbf{S}^u)^{-1} + \mathbf{Y}^l (\mathbf{S}^l)^{-1}, \quad (2.51)$$

$$\mathbf{F}_{\text{schur}} = -\mathbf{F}_{\mathbf{y}^s} + (\mathbf{Y}^s)^{-1} \mathbf{F}_s + \mathbf{G}^T(x) \mathbf{Q}^{-1} \mathbf{F}_{\text{sys}_x}, \quad (2.52)$$

$$\mathbf{F}_{\text{sys}_x} = \mathbf{F}_x - (\mathbf{S}^u)^{(-1)} \mathbf{F}_{s^u} + \mathbf{Y}^u (\mathbf{S}^u)^{(-1)} \mathbf{F}_{\mathbf{y}^u} + (\mathbf{S}^l)^{(-1)} \mathbf{F}_{s^l} - \mathbf{Y}^l (\mathbf{S}^l)^{(-1)} \mathbf{F}_{\mathbf{y}^l}. \quad (2.53)$$

The term  $\Delta \mathbf{y}^s$  can be obtained from Eq.(2.49), which can be substituted in Eq.(2.39) - (2.45) and update the following terms:  $\Delta \mathbf{x}$ ,  $\Delta \mathbf{y}^u$ ,  $\Delta \mathbf{y}^l$ ,  $\Delta \mathbf{s}$ ,  $\Delta \mathbf{s}^u$  and  $\Delta \mathbf{s}^l$ .

The initialization of the penalty parameter  $\mu$ , slack ( $\mathbf{s}$ ,  $\mathbf{s}^u$ ,  $\mathbf{s}^l$ ) and dual ( $\mathbf{y}^s$ ,  $\mathbf{y}^u$ ,  $\mathbf{y}^l$ ) is

$$\begin{aligned} \mu^{(1)} &= \frac{1}{3n} & s_i^{(1)} &= 1 \\ s_i^{u(1)} &= \bar{x}_i & s_i^{l(1)} &= x_i \\ y_i^{s(1)} &= \frac{\mu}{s_i} & y_i^{u(1)} &= \frac{\mu}{s_i^u} \\ y_i^{l(1)} &= \frac{\mu}{s_i^l}, & i &= 1 \cdots n \end{aligned} \quad (2.54)$$

where the term  $3n$  corresponds to the sum of the number of the stress constraints, the upper and lower bounds of the design variables. The idea for  $\mu^{(1)}$  is to choose a sufficiently small number so that it monotonically decreases and converges towards the optimal value more quickly. The initialization of the slack and dual parameters is to scale the Lagrangian terms for the stress constraints, the upper and lower bounds in Eq.(2.31) close to  $f_0$ .

The procedure of the algorithm is as follows: In the predictor step of the  $(\lambda+1)^{\text{th}}$  iteration in the predictor-corrector IPM,  $\mu = 0$ ,  $\gamma = 0$  in Eq.(2.47). The penalty parameter  $\mu^{(\lambda+1)}$  will be updated adaptively by

$$\mu^{(\lambda+1)} = \min \left\{ \max \left( \left( \frac{d_{\text{gap}}^{(\lambda+1)}}{d_{\text{gap}}^{(\lambda)}} \right)^2, \underline{\varepsilon} \right), \bar{\varepsilon} \right\} \cdot \mu^{(\lambda)}, \quad (2.55)$$

where  $\underline{\varepsilon}$  and  $\bar{\varepsilon}$  are the lower and upper bound of the ratio for  $\mu^{(\lambda)}$ . Typical values, as the ones used in the present work, are  $\underline{\varepsilon} = 0.1$  and  $\bar{\varepsilon} = 1$ . Therefore the ratio is within the region  $[0.1, 1]$ , which prevents the penalty parameter  $\mu$  from either increasing or decreasing drastically. The duality gap  $d_{\text{gap}}$  is calculated by

$$d_{\text{gap}}^{(\lambda)} = \mathbf{s}^T \mathbf{y}^s + (\mathbf{s}^u)^T \mathbf{y}^u + (\mathbf{s}^l)^T \mathbf{y}^l, \quad (2.56)$$

$$\begin{aligned} d_{\text{gap}}^{(\lambda+1)} &= (\mathbf{s} + \delta_p \Delta \mathbf{s})^T (\mathbf{y}^s + \delta_d \Delta \mathbf{y}^s) + \\ &\quad (\mathbf{s}^u + \delta_p \Delta \mathbf{s}^u)^T (\mathbf{y}^u + \delta_d \Delta \mathbf{y}^u) + \\ &\quad (\mathbf{s}^l + \delta_p \Delta \mathbf{s}^l)^T (\mathbf{y}^l + \delta_d \Delta \mathbf{y}^l) \end{aligned} \quad (2.57)$$

where  $\delta_p, \delta_d$  are the step size for the primal and dual variables respectively. They are calculated based on the following rule, which is modified from Zillober [26] for convenient implementation:

$$\begin{aligned} \delta_p &= (1 - \delta_{\text{step}}) / \max \left\{ \max_{i=1 \dots n} \left\{ -\frac{\Delta s_i}{s_i} \right\}, \max_{i=1 \dots n} \left\{ -\frac{\Delta s_i^l}{s_i^l} \right\}, \right. \\ &\quad \left. \max_{i=1 \dots n} \left\{ -\frac{\Delta s_i^u}{s_i^u} \right\}, (1 - \delta_{\text{step}}) \right\} \end{aligned} \quad (2.58)$$

$$\begin{aligned} \delta_d &= (1 - \delta_{\text{step}}) / \max \left\{ \max_{i=1 \dots n} \left\{ -\frac{\Delta y_i^s}{y_i^s} \right\}, \max_{i=1 \dots n} \left\{ -\frac{\Delta y_i^l}{y_i^l} \right\}, \right. \\ &\quad \left. \max_{i=1 \dots n} \left\{ -\frac{\Delta y_i^u}{y_i^u} \right\}, (1 - \delta_{\text{step}}) \right\}. \end{aligned} \quad (2.59)$$

where  $\delta_{\text{step}}$  is the control step size to provide the slacks ( $\mathbf{s}, \mathbf{s}^l, \mathbf{s}^u$ ) and duals ( $\mathbf{y}^s, \mathbf{y}^l, \mathbf{y}^u$ ) some margin when they approach 0 in the updating procedure. The region for both  $\delta_p$  and  $\delta_d$  is  $(0, 1]$ . Further, the value of  $\delta_{\text{step}}$  is chosen as  $\delta_{\text{step}} = 0.05$ .

In the corrector step,  $\gamma = 1$ , and  $\mu$  takes the value  $\mu^{(\lambda+1)}$  from the predictor step (Eq.(2.55)). The vector  $\Delta \chi$  from Eq.(2.46) in the corrector step is used to update the variable  $\chi$  by

$$\begin{aligned} \mathbf{x}^{(\lambda+1)} &= \mathbf{x}^{(\lambda)} + \delta_p \Delta \mathbf{x} & \mathbf{s}^{(\lambda+1)} &= \mathbf{s}^{(\lambda)} + \delta_p \Delta \mathbf{s} \\ \mathbf{s}^{u(\lambda+1)} &= \mathbf{s}^{u(\lambda)} + \delta_p \Delta \mathbf{s}^u & \mathbf{s}^{l(\lambda+1)} &= \mathbf{s}^{l(\lambda)} + \delta_p \Delta \mathbf{s}^l \\ \mathbf{y}^{s(\lambda+1)} &= \mathbf{y}^{s(\lambda)} + \delta_d \Delta \mathbf{y}^s & \mathbf{y}^{u(\lambda+1)} &= \mathbf{y}^{u(\lambda)} + \delta_d \Delta \mathbf{y}^u \\ \mathbf{y}^{l(\lambda+1)} &= \mathbf{y}^{l(\lambda)} + \delta_d \Delta \mathbf{y}^l. \end{aligned} \quad (2.60)$$

The algorithm of the predictor-corrector IPM is summarized below.

### 2.3.5. COMPUTATIONAL COMPLEXITY

The target of the work in this paper is to accelerate the computational speed of sizing optimization with stress constraints. Therefore, the computational cost of the expensive parts needs to be detected first before predicting how much efficiency can be achieved.

**Algorithm 1 Algorithm of Predictor-Corrector Interior Point Method**

- 
- 1: Set  $\lambda = 1$ , initialize the parameters  $\mu^{(1)}, \chi^{(1)}$  (Eq.(2.54)), and  $\rho$  (Eq.(2.30)), set tolerance  $\eta_{\text{gap}}$ .
  - 2: **while**  $d_{\text{gap}}^{(\lambda)} \geq \eta_{\text{gap}}$  **do** ▷ stop if duality gap  $< \eta_{\text{gap}}$
  - 3:   Using  $\chi^{(\lambda)}$  to compute  $G$  and  $(\mathbf{y}^s)^T H(\mathbf{x})$ , and assemble the matrices  $\mathbf{Y}^s, \mathbf{Y}^u, \mathbf{Y}^l, \mathbf{S}, \mathbf{S}^u, \mathbf{S}^l$ . Set  $\mu^{(\lambda)} = 0, \gamma = 0$  and assemble the matrices  $\mathbf{C}_\mu$  and the vector  $\mathbf{F}_\mu$  from Eq.(2.47),(2.48)
  - 4:   Solve for  $\Delta \mathbf{y}^s$  from Eq.(2.49) and use it to get the complete vector  $\Delta \chi$  in the predictor step
  - 5:   Compute the gaps  $d_{\text{gap}}^{(\lambda)}$  and  $d_{\text{gap}}^{(\lambda+1)}$  from Eq.(2.56) and (2.57)
  - 6:    $\mu^{(\lambda+1)} \leftarrow$  use Eq.(2.55) to update  $\mu$  in the predictor step
  - 7:   Update  $\mathbf{F}_\mu$  in Eq.(2.47) and  $\mathbf{F}_{\text{schur}}$  in Eq.(2.52) by setting  $\mu = \mu^{(\lambda+1)}, \gamma = 1$
  - 8:   Solve for  $\Delta \mathbf{y}^s$  from Eq.(2.49) in the corrector step with the updated vector  $\mathbf{F}_\mu$ , and substitute to get  $\Delta \chi^{(\lambda+1)}$
  - 9:    $\chi^{(\lambda+1)} \leftarrow$  compute  $\delta_p, \delta_d$  from Eq.(2.58),(2.59) using  $\Delta \chi^{(\lambda+1)}$  and compute  $\chi$  from Eq.(2.60) in the corrector step
  - 10:   Update  $d_{\text{gap}}^{(\lambda+1)}$  with  $\chi^{(\lambda+1)}$  in Eq.(2.56) and check for convergence
  - 11: **end while**
- 

In sizing optimization, the costly operations are the FEM analysis, the sensitivity analysis of the stress constraints, and the iterative optimization with the IPM. In this section, the number of nodes in a FEM model is denoted by  $n$ . Since all the design variables and stress constraints are defined node-wise, the complexity of these operations is a function of  $n$ .

Assuming that the linear finite element problem is formulated with a symmetric positive definite stiffness matrix and the corresponding equilibrium equation solved using a Cholesky decomposition, the computational cost of one FEM analysis is

$$C_{\text{fem}} = O(nb^2), \quad (2.61)$$

where  $b$  is the bandwidth of the system of equations. For a beam structure,  $b \ll n$ , hence the cost is close to a linear function of  $n$ .

For the sensitivity analysis of the stress constraints, the most expensive part is to solve the adjoint system Eq.(2.26) since the cost for solving each adjoint system is the same as that of one FEM analysis. Given that there is one stress constraint per node, the number of stress constraints is  $n$  and the overall computational cost for the stress sensitivity analysis is

$$C_{\text{sensitivity}} = O(n^2 b^2). \quad (2.62)$$

One advantage of Mehrotra's IPM is that the number of iterations is not sensitive to the size of the optimization problem. The most expensive cost of each iteration inside the IPM is the construction and resolution of the Schur complement Eq.(2.49). The cost to build the coefficient matrix by matrix multiplication is  $O(n^3)$ . Furthermore, assuming

that Eq.(2.49) is solved using a Cholesky decomposition, the computational complexity of the Schur complement is

$$C_{\text{schur}} = O(n^3). \quad (2.63)$$

Observe that for the Schur complement problem the system matrix is full hence the computational cost is significantly more expensive than the cost of one FEM analysis for a beam problem.

From the above analysis, it is clear that the overall cost of the optimization is dominated by the Schur complement and, to a lesser extent, the sensitivity analysis. Therefore the algorithm could be accelerated by reducing the complexity of the Schur complement first, followed by the sensitivity analysis. The acceleration scheme is introduced in the next section.

## 2.4. NUMERICAL IMPROVEMENTS

### 2.4.1. PRECONDITIONER FOR THE SCHUR COMPLEMENT

Conjugate gradient method is known to be a fast solver for large scale linear equations compared with direct methods. However, an effective preconditioner is generally required to guarantee the efficient convergence for the Schur complement problem (Oliveira and Sorensen [27], Benzi et al. [28]). Simultaneously, another requisite is to make sure that the preconditioner may be easily inverted. In this section, a heuristic preconditioner for the Schur complement Eq.(2.49) is introduced. The main guiding principle to develop the preconditioner is to generate an easily invertible diagonal matrix that preserves the main ingredients of the Schur complement.

Recall that the coefficient matrix of the Schur complement of the sub-problem Eq.(2.49) is given by Eq.(2.50), which is repeated here for convenience, i.e.,

$$D_{\mu} = [(Y^s)^{-1}S + G^T(\mathbf{x})Q^{-1}G(\mathbf{x})].$$

The first term in the right-hand side and  $Q$  in the second term are diagonal matrices. However, the gradient matrix  $G(\mathbf{x})$  is generally a full matrix for statically indeterminate structures. Since the approximation (Eq.(2.18)) is a modification of the fully stressed design, only this part is assumed to dominate the gradient matrix  $G(\mathbf{x})$ . In more detail, the matrix  $G(\mathbf{x})$  takes the form

$$G(\mathbf{x}) = G_f(\mathbf{x}) + A^{(a)} + G_d(\mathbf{x})R, \quad (2.64)$$

where  $G_f(\mathbf{x})$  is a diagonal matrix for the gradient of the fully stressed part in Eq.(2.18),  $A^{(a)}$  is the gradient matrix of the linear part representing load redistribution,  $G_d(\mathbf{x})$  is the gradient matrix for the damping function in Eq.(2.29), and  $R = \text{diag}(\rho_1, \dots, \rho_n)$ .

To achieve the goal of working with an easily invertible preconditioner, the load redistribution part  $A^{(a)}$  and the damping part  $G_d(\mathbf{x})R$  are *neglected*. By taking only the fully stressed part in the gradient matrix  $G(\mathbf{x})$ , the diagonal preconditioner  $M$  takes the form

$$M = (Y^s)^{-1}S + G_f^T(\mathbf{x})Q^{-1}G_f(\mathbf{x}). \quad (2.65)$$

The preconditioner is verified to work well in the numerical experiments in Section 2.5.

### 2.4.2. IMPLICIT SENSITIVITY ANALYSIS

One advantage of solving the Schur complement (Eq.(2.49)) with the preconditioned conjugate gradient method (PCG) in the IPM is that the explicit form of coefficient matrix is not required. Iterations in the PCG can be completed by matrix vector calculation, i.e.,

$$D_{\mu}\Delta\mathbf{y}^s = (\mathbf{Y}^s)^{-1}\mathbf{S}\Delta\mathbf{y}^s + \mathbf{G}^T(\mathbf{x})\mathbf{Q}^{-1}\mathbf{G}(\mathbf{x})\Delta\mathbf{y}^s. \quad (2.66)$$

Since  $(\mathbf{Y}^s)^{-1}\mathbf{S}$ , and  $\mathbf{Q}$  are diagonal matrices, the related calculation is inexpensive. However,  $\mathbf{G}(\mathbf{x})\Delta\mathbf{y}^s$  and  $\mathbf{G}^T(\mathbf{x})\mathbf{v}$  ( with  $\mathbf{v} = \mathbf{Q}^{-1}\mathbf{G}(\mathbf{x})\Delta\mathbf{y}^s$ ) in the second term are expensive for large problems because significant computational work is required to obtain  $\mathbf{G}(\mathbf{x})$  first. Recall that the gradient matrix  $\mathbf{G}(\mathbf{x})$  of  $\check{\mathbf{r}}$ , as given in Eq.(2.64), is

$$\mathbf{G}(\mathbf{x}) = \mathbf{G}_f(\mathbf{x}) + \mathbf{A}^{(\alpha)} + \mathbf{G}_d(\mathbf{x})\mathbf{R}.$$

The first term  $\mathbf{G}_f(\mathbf{x})$  is diagonal, and  $\mathbf{G}_d(\mathbf{x})\mathbf{R}$  is inexpensive to compute because the damping function Eq.(2.28) is the same for each stress constraint. The load redistribution part  $\mathbf{A}^{(\alpha)}$  is calculated at the approximation point  $\mathbf{x}^{(\alpha)}$  by Eq.(2.20)

$$\mathbf{G}_{\text{fem}}(\mathbf{x}^{(\alpha)}) = \mathbf{G}_f(\mathbf{x}^{(\alpha)}) + \mathbf{A}^{(\alpha)}, \quad (2.67)$$

where  $\mathbf{G}_{\text{fem}}(\mathbf{x}^{(\alpha)})$  is the gradient matrix assembled from the terms  $\frac{\text{sgn}(\sigma_i)}{\bar{\sigma}} \cdot \frac{\partial \sigma_i}{\partial x_j} \Big|_{\mathbf{x}^{(\alpha)}}$  at  $\mathbf{x}^{(\alpha)}$  in Eq.(2.20) for all nodes  $i$  and computed using the adjoint method. Using Eq.(2.67) to solve for  $\mathbf{A}^{(\alpha)}$ , the gradient matrix  $\mathbf{G}(\mathbf{x})$  can be written as

$$\mathbf{G}(\mathbf{x}) = \mathbf{G}_f(\mathbf{x}) + \mathbf{G}_{\text{fem}}(\mathbf{x}^{(\alpha)}) - \mathbf{G}_f(\mathbf{x}^{(\alpha)}) + \mathbf{G}_d(\mathbf{x})\mathbf{R}. \quad (2.68)$$

As shown in Eq.(2.62), the cost to calculate  $\mathbf{G}_{\text{fem}}(\mathbf{x})$  with the adjoint method increases quadratically when the number of nodes  $n$  increases. Therefore, among the terms in Eq.(2.66),  $\mathbf{G}_{\text{fem}}(\mathbf{x}^{(\alpha)})\mathbf{v}$  and  $\mathbf{G}_{\text{fem}}^T(\mathbf{x}^{(\alpha)})\mathbf{v}$  are the most expensive parts, where  $\mathbf{v}$  represents any vector in the iteration of PCG.

In this part an *implicit sensitivity analysis* will be developed, which reduces the computational work for the calculation. The advantage of the implicit sensitivity analysis is to calculate  $\mathbf{G}_{\text{fem}}(\mathbf{x}^{(\alpha)})\mathbf{v}$  and  $\mathbf{G}_{\text{fem}}^T(\mathbf{x}^{(\alpha)})\mathbf{v}$  in the PCG without calculating the gradient matrix explicitly. This not only saves the computational cost for the iterations in the PCG, it also saves the costly computational work to calculate  $\mathbf{G}_{\text{fem}}$ .

The first step is to express the term  $\mathbf{G}_{\text{fem}}(\mathbf{x}^{(\alpha)})\mathbf{v}$  symbolically from Eq.(2.25),(2.26) as

$$\mathbf{G}_{\text{fem}}(\mathbf{x}^{(\alpha)})\mathbf{v} = \begin{bmatrix} -\sum_{i=1}^n v_i \mathbf{z}_i^T (\mathbf{K}^{-1}) \frac{\partial \mathbf{K}}{\partial x_1} \mathbf{u} \\ -\sum_{i=1}^n v_i \mathbf{z}_i^T (\mathbf{K}^{-1}) \frac{\partial \mathbf{K}}{\partial x_2} \mathbf{u} \\ \vdots \\ -\sum_{i=1}^n v_i \mathbf{z}_i^T (\mathbf{K}^{-1}) \frac{\partial \mathbf{K}}{\partial x_n} \mathbf{u} \end{bmatrix} \Big|_{\mathbf{x}^{(\alpha)}}. \quad (2.69)$$

Note that the first part  $\sum_{i=1}^n v_i \mathbf{z}_i^T (\mathbf{K}^{-1})$  is the same in each term of the above equation. Since the global stiffness matrix  $\mathbf{K}$  is symmetric, this term can be obtained by the adjoint method, i.e.,

$$\mathbf{K} \bar{\mathbf{t}} = \bar{\mathbf{z}}, \quad (2.70)$$

where  $\bar{\mathbf{z}} = \sum_i v_i \mathbf{z}_i$  is the dummy load.

The resultant vector becomes

$$\mathbf{G}_{\text{fem}}(\mathbf{x}^{(\alpha)}) \mathbf{v} = \begin{bmatrix} -\bar{\mathbf{t}}^T \frac{\partial \mathbf{K}}{\partial x_1} \mathbf{u} \\ -\bar{\mathbf{t}}^T \frac{\partial \mathbf{K}}{\partial x_2} \mathbf{u} \\ \vdots \\ -\bar{\mathbf{t}}^T \frac{\partial \mathbf{K}}{\partial x_n} \mathbf{u} \end{bmatrix} \Big|_{\mathbf{x}^{(\alpha)}}. \quad (2.71)$$

The size of  $\frac{\partial \mathbf{K}}{\partial x_i}$  is small compared with the entire stiffness matrix. Hence,  $\frac{\partial \mathbf{K}}{\partial x_i} \mathbf{u}$  is inexpensive to compute. Consequently, the dominant cost for the above calculation is to solve the adjoint Eq.(2.70). The computational cost is  $O(nb^2)$  (Eq.(2.61)) to evaluate  $\mathbf{G}_{\text{fem}}(\mathbf{x}^{(\alpha)}) \mathbf{v}$  once.

Next, calculating  $\mathbf{G}_{\text{fem}}^T(\mathbf{x}^{(\alpha)}) \mathbf{v}$  can be completed by

$$\mathbf{G}_{\text{fem}}^T(\mathbf{x}^{(\alpha)}) \mathbf{v} = \begin{bmatrix} -\mathbf{z}_1^T (\mathbf{K}^{-1}) \sum_{i=1}^n v_i \frac{\partial \mathbf{K}}{\partial x_i} \mathbf{u} \\ -\mathbf{z}_2^T (\mathbf{K}^{-1}) \sum_{i=1}^n v_i \frac{\partial \mathbf{K}}{\partial x_i} \mathbf{u} \\ \vdots \\ -\mathbf{z}_n^T (\mathbf{K}^{-1}) \sum_{i=1}^n v_i \frac{\partial \mathbf{K}}{\partial x_i} \mathbf{u} \end{bmatrix} \Big|_{\mathbf{x}^{(\alpha)}}. \quad (2.72)$$

The term  $(\mathbf{K}^{-1}) \sum_{i=1}^n v_i \frac{\partial \mathbf{K}}{\partial x_i} \mathbf{u}$  is the same in each component of the above vector. For the term  $\sum_{i=1}^n v_i \frac{\partial \mathbf{K}}{\partial x_i}$ , it can be assembled into a single matrix  $\overline{\Delta \mathbf{K}}$ . Since  $\mathbf{K}$  is symmetric,  $(\mathbf{K}^{-1}) \sum_{i=1}^n v_i \frac{\partial \mathbf{K}}{\partial x_i} \mathbf{u}$  becomes  $(\mathbf{K}^{-1}) \overline{\Delta \mathbf{K}} \mathbf{u}$ , which can be solved with Gauss elimination, similar to the reanalysis method (Haftka and Gürdal [23])

$$\overline{\Delta \mathbf{K}} \mathbf{u} + \mathbf{K} \Delta \mathbf{u} = \mathbf{0}. \quad (2.73)$$

Consequently, Eq.(2.72) becomes

$$\mathbf{G}_{\text{fem}}^T(\mathbf{x}^{(\alpha)}) \mathbf{v} = \begin{bmatrix} \mathbf{z}_1^T \Delta \mathbf{u} \\ \mathbf{z}_2^T \Delta \mathbf{u} \\ \vdots \\ \mathbf{z}_n^T \Delta \mathbf{u} \end{bmatrix} \Big|_{\mathbf{x}^{(\alpha)}}. \quad (2.74)$$

The system Eq.(2.73) is solved only once to calculate  $\mathbf{G}_{\text{fem}}^T(\mathbf{x}^{(\alpha)}) \mathbf{v}$ , where the computational cost is  $O(nb^2)$ . The load redistribution part in the stress approximation (Eq.(2.18)) can also be completed with this equation. An additional advantage of this approach is that the matrix  $\mathbf{G}(\mathbf{x})$  does not need to be stored separately.

With the implicit approach mentioned above, it is no longer required to perform an explicit sensitivity analysis. Furthermore, the FEM and the iterative optimization are not independent of each other, but rather linked by the reanalysis and adjoint method in the implicit sensitivity analysis. This framework is similar to the simultaneous analysis and design (SAND) method (Haftka [29]). The optimizer updates the Lagrange multipliers and design variables with the adjoint (Eq.(2.70)) and the reanalysis method (Eq.(2.73)) using the global stiffness matrix of the FEM. In turn, the stress approximation can update the mechanical response  $\sigma$  by using the reanalysis method (Eq.(2.73)) with the updated design. In the next section, the new algorithm will be summarized.

### 2.4.3. SUMMARY OF THE OPTIMIZATION ALGORITHM

In the sequel, Svanberg's CCSA is employed as the optimization framework for the proposed algorithm. The outer loop leads the feasible solution of the sub-problem towards the optimal solution step by step. Meanwhile, inside each outer loop, a sub-loop solves the sub-problem iteratively to get the feasible solution. The superscript  $(\alpha, \beta)$  is used to denote the index of the outer loop and sub-loop respectively.

The damping factor is updated at the end of each outer loop of the CCSA and sub-loop in IPM. The pattern is the same as described in Svanberg [22]. At the end of each sub-loop, where the optimal results are not accepted, the damping factors either remain the same for those stress approximations that are conservative, or increase for those that are not conservative according to

$$\rho_i^{\text{new}} = 1 + \frac{(r_i^* - \check{r}^{\text{old}})}{\rho_i^{\text{old}} d^{\text{old}}}, \quad (2.75)$$

where  $d^{\text{old}}$  is estimated with Eq.(2.28) at the optimal point. In the outer loop, where the feasible solution is obtained, the damping factors are increased by Eq.(2.75) for those stress approximations that are not conservative. In contrast, for the approximations that are conservative, the damping factor is decreased by

$$\rho_i^{\text{new}} = 1 + (1 - \underline{\delta}_\rho) \arctan \left( \frac{(r_i^* - \check{r}^{\text{old}})}{\rho_i^{\text{old}} d^{\text{old}}} / (1 - \underline{\delta}_\rho) \right) \quad (2.76)$$

where  $r_i^* = |\sigma_i|/\bar{\sigma}$  is obtained from step 9 in Algorithm 3, and  $\underline{\delta}_\rho$  is the lower bound for the decrement ratio between  $\rho_i^{\text{new}}$  and  $\rho_i^{\text{old}}$ . The parameter  $\underline{\delta}_\rho$  is chosen here equal to 0.5.

The proposed optimization framework is described in the Algorithm 3.

In step 8 of Algorithm 3, the PCG is applied to solve the Schur complement Eq.(2.49) with the preconditioner in Section 2.4.1 in the predictor and corrector steps. The explicit sensitivity analysis module is removed from the optimization procedure by deploying the implicit sensitivity analysis (Eqs.(2.71) and (2.74)) in stress approximation and solving the Schur complement in the IPM. In the next section, the computational complexity of the proposed method will be demonstrated.

**Algorithm 2 Algorithm for the proposed optimization method**

- 
- 1: Set  $\alpha = 1$ , initialize  $\chi^{(1,1)}$  and set the tolerances  $\eta_\nu, \eta_\sigma$
  - 2: Start FE analysis to calculate  $\sigma$  (Eq.(2.5) and (2.13))
  - 3: Initialize the damping factor  $\rho^{(1,1)}$  with Eq.(2.30)
  - 4: Build up the sub-problem of the optimization with Eq.(2.2), Eq.(2.29)
  - 5: **while**  $\left| (f_0^{(\alpha,1)} - f_0^{(\alpha-1,1)}) / f_0^{(1,1)} \right| \geq \eta_\nu$  ( $\alpha \geq 2$ ) **do**  $\triangleright$  stop if the relative volume variation is smaller than  $\eta_\nu$
  - 6:     Set  $\beta = 1$
  - 7:     **while**  $\max(\tilde{\mathbf{r}}^{(\alpha,\beta)}) \geq \eta_\sigma$  or  $(f_0^{(\alpha,\beta)} - f_0^{(\alpha,\beta-1)}) \geq \eta_\nu$  ( $\beta \geq 2$ ) **do**  $\triangleright$  stop if both stress constraints are satisfied and volume is decreasing
  - 8:     Update  $\mathbf{x}^{(\alpha,\beta+1)} \leftarrow$  solve the sub-problem with predictor-corrector IPM with Algorithm 1  $\triangleright$  see Section 2.3.4
  - 9:     FE analysis (Eq.(2.5) and (2.13)) to calculate  $\sigma^{(\alpha,\beta+1)}$
  - 10:     Update damping factor  $\rho^{(\alpha,\beta+1)}$  with Eq.(2.75)
  - 11:     **end while**
  - 12:     Update damping factor  $\rho^{(\alpha+1,1)}$  with Eq.(2.75) (2.76)
  - 13:      $\mathbf{x}^{(\alpha+1,1)} \leftarrow \mathbf{x}^{(\alpha,\beta+1)}$  Update design variables  $\mathbf{x}^{(\alpha+1,1)}$
  - 14:     Update the sub-problem of the optimization with Eq.(2.2), Eq.(2.29)
  - 15: **end while**
- 

**2.4.4. COMPUTATIONAL COMPLEXITY FOR THE IMPROVED METHOD**

In this section, the computational complexity of the proposed optimization method will be analyzed to estimate the potential efficiency that can be obtained. The most expensive parts in the optimization are now the implicit sensitivity analysis and the PCG iterations. In the PCG, since the full coefficient matrix for the Schur complement is not required, the computational work ( $O(n^3)$ ) to build the coefficient matrix by matrix-matrix multiplication is saved. Since the preconditioner for the system is diagonal, it is also inexpensive to be inverted. For the implicit sensitivity analysis, the most expensive cost is for the reanalysis and the adjoint method. As indicated in Section 2.4.2, the cost of implicit sensitivity analysis once is

$$C'_{\text{sensitivity}} = O(nb^2). \quad (2.77)$$

The proposed method could successfully reduce the cost for the Schur complement from  $O(n^3)$  to  $O(nb^2)$ , if the number of iterations of the PCG for the Schur complement in the IPM is small, and is independent on the size of optimization problem. If the total number implicit analyses  $n_{\text{iter}}$  required in the IPM is  $n_{\text{iter}} \ll n$  when  $n$  is large enough, the computational cost for the complete IPM is

$$C'_{\text{total}} = O(nb^2). \quad (2.78)$$

Here it is important to note that the proposed method can help to save the computational cost for large scale problems only if

$$n_{\text{iter}} \ll n \quad (2.79)$$



is satisfied. In the next section, the efficiency of the method will be demonstrated in the context of sizing optimization of a beam structure.

## 2

## 2.5. REPRESENTATIVE NUMERICAL EXAMPLES

To demonstrate the efficiency of the proposed improvements, three representative numerical examples are shown in this section for the optimization of beam structures, namely (i) a clamped solid beam subjected to a concentrated load, (ii) a clamped/simply-supported hollow beam subjected to a distributed load and (iii) multiple-span continuous beam loaded with a distributed force. In the three examples, the objective is to minimize the total weight subjected to local stress constraints, which corresponds to minimize the total volume since the beams are assumed to be made out of a homogeneous material. In each case, the optimization procedure is repeated with increasing number of elements in the FEM model.

The performance is compared to that of a benchmark method, referred to as the “original method”. The original method uses only one of the three proposed improvements, namely the proposed stress approximation. However, instead of the implicit sensitivity analysis and the preconditioned conjugate gradient, the original method uses the *explicit* version of the adjoint sensitivity analysis and a *direct* solver for the original Schur complement of the KKT conditions. Other than these changes, the two methods are implemented in the same computational environment and hardware in order to have a meaningful comparison. Performance is measured in terms of number of iterations and CPU time.

In addition, for the second numerical example (hollow beam), the CPU time from the proposed method is compared with that from the method of moving asymptotes (MMA) [22] and a representative implementation of the sequential quadratic programming approach (SQP). This alternative comparison is done mostly as an order-of-magnitude verification since a meaningful pragmatic comparison requires optimized implementations of all methods.

### 2.5.1. FULLY-CLAMPED SOLID BEAM CASE

The first example is a stress-constrained, minimum weight optimization problem of a beam structure clamped at both ends and subjected to a concentrated vertical force as shown in Figure 2.2. This is a benchmark problem with a known analytical solution as presented in Rozvany [30]. Hence, in addition to serve as a test case for performance, one goal in this case is to verify that the numerical solution obtained from the proposed method matches with the analytical solution. The beam has a solid rectangular cross section with variable design width  $w$  and a fixed height.

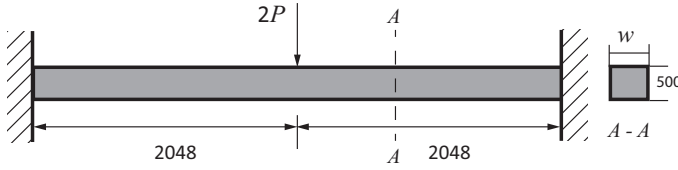


Figure 2.2: Clamped beam structure with variable width. Lengths are given in mm

The optimization problem is,

$$\min_{\mathbf{w}} f_0(\mathbf{w}) = h \sum_{i=1}^n l_i w_i / V_0$$

subject to:

$$\begin{aligned} f_i(\mathbf{w}) / \bar{\sigma} &\leq 1 \\ w_l &\leq w_i \leq w_u \quad i = 1 \dots n \end{aligned}$$

where  $n$  is the number of nodes,  $V_0$  is the initial volume,  $h = 500$  mm is the height of the cross-section,  $l_i$  is the length of beam connected with the  $i^{\text{th}}$  node,  $w_i$  is the width at the  $i^{\text{th}}$  node,  $f_i(\mathbf{w})$  is the stress approximation at the  $i^{\text{th}}$  node, and  $w_l$  and  $w_u$  are the lower and upper bound of the design variable, respectively. In this case the moment of inertia is given by  $I_z(w_i) = \frac{1}{12} w_i h^3$ . The optimization starts with a uniform width distribution  $w_0$  as indicated in Table 2.1 together with other parameters of the optimization problem. In this case, the error tolerance of PCG is  $e_{\text{PCG}} = 10^{-7}$ . The stopping criteria of the IPM is that the duality gap has to be smaller than  $\eta_{\text{gap}} = 10^{-10}$  (see also Zillober [26]). The tolerance for the stress constraints is  $\eta_{\sigma} = 10^{-3}$ , which controls the inner loops in the algorithm. The overall optimization stops when the variation in the volume is smaller than  $\eta_v = 10^{-3}$ .

Table 2.1: Parameters of clamped beam structure

Young's Modulus	$E = 20$ GPa
Allowable stress	$\bar{\sigma} = 172$ MPa
Initial design width	$w_0 = 1000$ mm
Minimum width	$w_l = 100$ mm
Maximum width	$w_u = 1000$ mm
Concentrated load	$P = 4000$ kN

As a preliminary step, not shown here for the sake of conciseness, it was verified that the analytical and numerical solutions of the optimization problem coincide to within FEM tolerance (see Rozvany [30]). To test the performance of the method, the optimal width for the stress-constrained minimum weight problem was computed for various meshes. A typical result for a mesh with  $n = 1280$  nodes is depicted in Figure 2.3a in terms of the optimal width along the beam. As shown in the figure, the optimal beam is

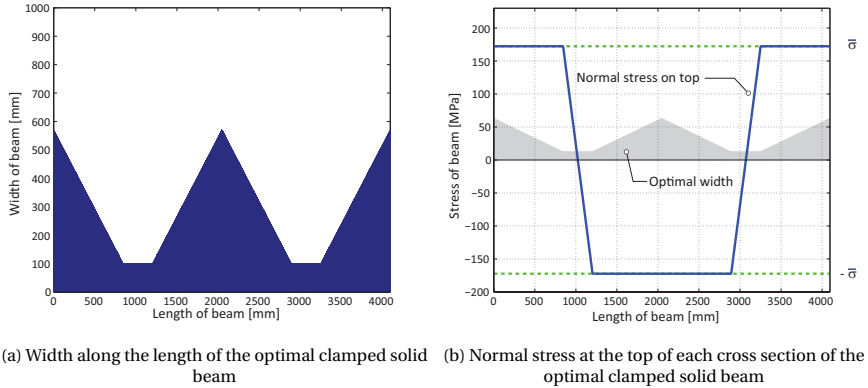


Figure 2.3: Optimal width distribution in the beam and the corresponding stress on the top edge

wider closer to the supports and close to the middle point where the load is applied. The corresponding normal stress at the top of each cross-section is shown in 2.3b.

As may be observed from Figure 2.3b, the normal stress at the top of each cross section is equal to the maximum allowable value 172MPa (in absolute value) at all locations along the length where the width exceeds its minimum allowable value. This result is in accordance with the fact that the optimum solution should use the minimum amount of material while keeping the absolute value of the stress below or at most equal to the critical value to prevent failure (i.e., fully-stressed design).

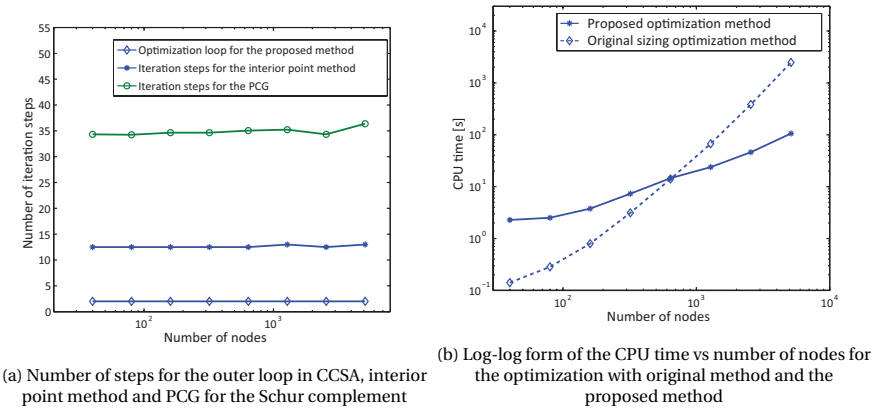


Figure 2.4: Computational performance of the proposed method

As shown in Figure 2.4a, the performance of the method is monitored based on the number of outer loops in the CCSA, the averaged number of iterations in the IPM and the total averaged PCG iterations, plotted as a function of the number of nodes when the structure is discretized with different number of elements. The procedure starts from

$n = 40$  nodes and the number of elements (and hence nodes) is doubled each time up to  $n = 5120$  nodes. As shown in the figure, the number of steps in the outer loop and the IPM remain relatively constant as a function of the number of nodes. The method also converges relatively fast as it only needs two outer iterations.

The CPU time for the optimization procedure with the original method and the proposed method is portrayed in a log–log form in Figure 2.4b. The dashed line for the original method increases more than quadratically when the number of nodes increases (average slope above 2). By contrast, the slope of the solid line, which is for the proposed optimization method, is almost linear (average slope close to 1). Consequently, the numerical results indicate that the computational complexity for the overall procedure has been decreased from at least  $O(n^2)$  to  $O(n)$ . It is relevant to observe that the actual gain is only achieved for sufficiently large  $n$  (in this case,  $n \approx 1000$  as shown in Figure 2.4b); the original method remains more efficient for small values of  $n$ .

### 2.5.2. CLAMPED/SIMPLY SUPPORTED HOLLOW BEAM CASE

The second example is a hollow beam structure as shown in Figure 2.5. The beam is

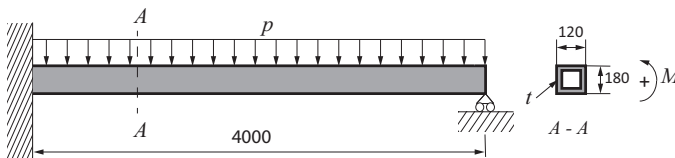


Figure 2.5: Clamped/simply supported hollow beam. Lengths are given in mm

clamped on the left side and the right edge it is simply supported while a uniformly distributed load is applied on the top edge. In this case, the beam structure is optimized with respect to its weight using the thickness  $t$  of a hollow rectangular cross-section as the design variable. The parameters used in the problem, including material properties and design constraints, are listed in Table 2.2. Observe that, although the total length and the elastic limit used in the this example are similar to the values used in the first example of a solid beam, the stiffness used here is larger and typical of metal-based hollow beams.

The formulation of the optimization is as follows:

$$\min_{\mathbf{t}} f_0(\mathbf{t}) = S \sum_{i=1}^n l_i t_i / V_0$$

subject to:

$$\begin{aligned} f_i(\mathbf{t}) / \bar{\sigma} &\leq 1 \\ t_l &\leq t_i \leq t_u \quad i = 1 \dots n \end{aligned}$$

where  $n$  is the number of nodes,  $V_0$  is the initial volume,  $S = 2(h + w)$  is the perimeter of the cross-section area,  $h = 180$  mm and  $w = 120$  mm are the height and width of the

cross-sectional area,  $l_i$  is the length of beam connected with  $i^{th}$  node,  $t_i$  is the thickness at  $i^{th}$  node,  $f_i(\mathbf{t})$  is the stress approximation at  $i^{th}$  node,  $t_l$  and  $t_u$  are the lower and upper bound of the design variable. Using an approximation for thin-walled sections, the moment of inertia is  $I_z(t_i) = 2 \left( \frac{t_i h^3}{12} + w t_i \left( \frac{h}{2} \right)^2 \right)$ .

Table 2.2: Parameters of hollow beam structure

Young's Modulus	$E = 200\text{GPa}$
Allowable stress	$\bar{\sigma} = 172\text{MPa}$
Initial design thickness	$t_0 = 20\text{mm}$
Minimum thickness	$t_l = 3\text{mm}$
Maximum thickness	$t_u = 20\text{mm}$
Distributed load	$p = 40\text{N mm}^{-1}$

The optimization starts with a uniform thickness distribution  $t_0$ , which is set equal to the maximum allowable value. The tolerances used are the same as in the previous example, i.e.,  $e_{\text{PCG}} = 10^{-7}$ ,  $\eta_{\text{gap}} = 10^{-10}$ ,  $\eta_{\sigma} = 10^{-3}$  and  $\eta_{\nu} = 10^{-3}$ .

The optimal thickness  $t_{\text{opt}}$  of the cross-sectional area along the length is shown in Figure 2.6a using a mesh with  $n = 1280$  nodes. As shown in Figure 2.6a, the largest thickness is reached at the clamped edge (with a maximum value of 16.7mm) while in the middle section, the thickness reaches a local maximum of 7.2mm. Consequently, the local constraint for the maximum allowable thickness is not active as  $t_{\text{opt}} < t_u$  at all points.

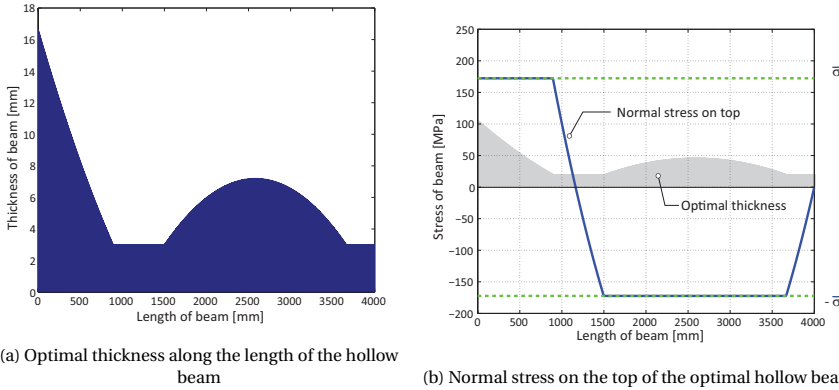


Figure 2.6: Optimal width distribution in the beam and the corresponding stress on the top edge

The normal stress on the top of each cross-section is shown in Figure 2.6b. Comparing this figure with 2.6a, it can be verified that the minimum bound  $t = t_l = 3\text{mm}$  is active at points where the fully-stressed optimality condition is not active, i.e., enforcing the minimum bound of the thickness precludes the stress from reaching its maximum allowable value.

As in the previous example, the performance of the proposed method is monitored record-

ing the number of iterations as follows: The total number of the outer loops in the CCSA, the averaged number of iterations in the IPM and the total averaged PCG iterations, which are plotted in Figure 2.7a with respect to the number of nodes (from  $n = 40$  to  $n = 2560$  nodes). As shown in the figure, the method converges relatively fast since it takes only 4 outer loops in total to reach an optimal solution with the given tolerance, a value that remains constant for all mesh sizes analyzed. Similarly, the averaged number of iterations in the IPM remains constant as a function of the problem size. However, the average number of iteration for the PCG increases from 24 to 42 for the range of number of nodes analyzed with the proposed diagonal preconditioner. This increment may be traced back to the change in the condition number of the equilibrium system, which increases from  $1.29 \times 10^9$  (for 40 nodes) to  $1.38 \times 10^{14}$  (for 2560 nodes). It is worth mentioning that the number of conjugate gradient iterations in the so-called original method (i.e., without preconditioner) scales linearly with the size of the problem, which also confirms the efficiency of the proposed preconditioner.

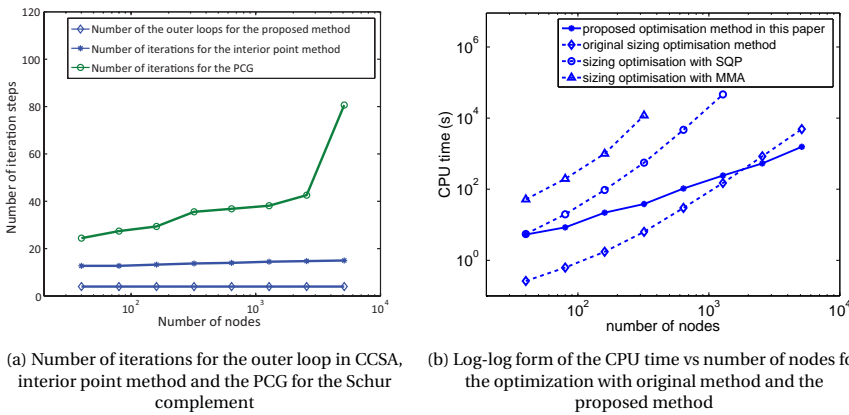


Figure 2.7: Computational performance of the proposed method

The actual performances of the proposed method and the benchmark original method (i.e., no preconditioner, direct solver method for the Schur complement, as outlined in 2.5.2) are shown in Figure 2.7b in terms of a log-log relation between the CPU time for the optimization procedure and the corresponding size of the problem. As an additional performance measure, the same problem was solved using the MMA and an SQP implementation, although it is noted that this comparison is only qualitative since the most optimized SQP variants may perform better than the off-the-shelf (Matlab) version.

From Figure 2.7b, it can be observed that the average slopes of the lines representing the original method, the MMA and the SQP are more than 2 while the slope for the proposed method is close to 1. Consequently, as in the previous example, the results indicate that the computational complexity for the whole procedure can be decreased from more than  $O(n^2)$  to  $O(n)$ . Again it is noticed that the proposed method only becomes

more efficient than the original method for sufficiently large problems. It is necessary to note that the CPU time for the MMA is higher than the original method, albeit both using IPM, mainly because there is no predictor-corrector step in the implementation of the MMA. In addition, the results indicate that the method performs better than the MMA and a "regular" SQP implementation, although a fair cross-method comparison would require a detailed analysis of the implementation details of both methods, which is beyond the scope of the present analysis.

### 2.5.3. MULTIPLE-SPAN CONTINUOUS BEAM

As a third test case, a multiple-span continuous beam with rectangular cross section is analyzed, as shown in Figure 2.8. In this case, the proposed method is tested in a more complex condition, namely a non-uniform distributed load along the span, together with an additional displacement constraint.

The width  $w$  in the rectangular cross-section  $A-A$  is the design variable while the height  $h = 500\text{mm}$  of the cross-section is fixed in the optimization problem. In this numerical case, apart from the stress constraints, and the lower and upper bound of the design variables, the displacement in the vertical direction at a location  $x_0 = 7000\text{mm}$  measured from the left is also constrained such that the vertical displacement  $u$  should not exceed a prescribed maximum value  $u_{\max} = l_{\text{span}} r_{\text{span}}$ , where  $l_{\text{span}} = 6000\text{mm}$  is the free span between two adjacent supports and  $r_{\text{span}}$  is a prescribed allowable displacement to span ratio. The displacement at this point is approximated using the ConLin approach without a damping function.

The optimization problem to be solved is as follows: find  $\mathbf{w}$  such that

$$\min_{\mathbf{w}} f_0(\mathbf{w}) = h \sum_{i=1}^n l_i w_i / V_0$$

subject to:

$$\begin{aligned} f_i(\mathbf{w}) / \bar{\sigma} &\leq 1 \\ u(x_0, \mathbf{w}) &\leq u_{\max} \\ w_l &\leq w_i \leq w_u \quad i = 1 \dots n \end{aligned}$$

where  $n$  is the number of nodes,  $V_0$  is the initial volume,  $h = 500\text{mm}$  is the height of the cross-section,  $l_i$  is the length of beam connected with  $i^{\text{th}}$  node,  $w_i$  is the width at the  $i^{\text{th}}$  node,  $f_i(\mathbf{w})$  is the stress approximation at the  $i^{\text{th}}$  node,  $w_l$  and  $w_u$  are the lower and upper bound of the design variable. In this case the moment of inertia is given by  $I_z(w_i) = \frac{1}{12} w_i h^3$ .

The parameters of the optimization problem are listed in Table 2.3. The tolerances used in this problem are the same as in the previous examples, i.e.,  $e_{\text{PCG}} = 10^{-7}$ ,  $\eta_{\text{gap}} = 10^{-10}$ ,  $\eta_{\sigma} = 10^{-3}$  and  $\eta_{\nu} = 10^{-3}$ . In addition, the tolerance used for displacement constraint for the sub-loop is  $\eta_u = 10^{-3}$ .

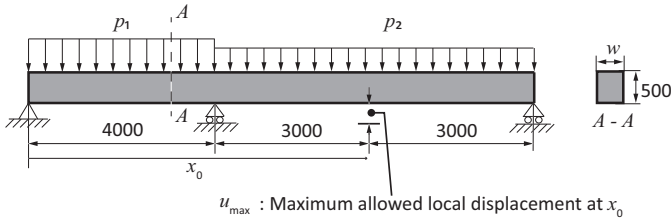


Figure 2.8: Multiple-span continuous beam

Table 2.3: Parameters of the two-span continuous beam

Young's Modulus	$E = 20 \text{ GPa}$
Allowable stress	$\bar{\sigma} = 5 \text{ MPa}$
Initial design width	$w_0 = 1000 \text{ mm}$
Minimum width	$w_l = 100 \text{ mm}$
Maximum width	$w_u = 1000 \text{ mm}$
Distributed load	$p_1 = 35 \text{ kN mm}^{-1}$
Distributed load	$p_2 = 25 \text{ kN mm}^{-1}$
Allowable span/displacement ratio	$r_{\text{span}} = 1/3500$

The optimal width for the model with  $n = 640$  nodes is shown in Figure 2.9a. The corresponding normal (axial) stress on the top of the of the beam is reported in Figure 2.9b. In contrast with the previous two examples, in the present case the normal stress, which is derived from the optimal width and the bending moment, has a more complex distribution along the beam. Furthermore, for this example, it is also relevant to analyze the vertical displacement of the beam, which is included in Figure 2.10.

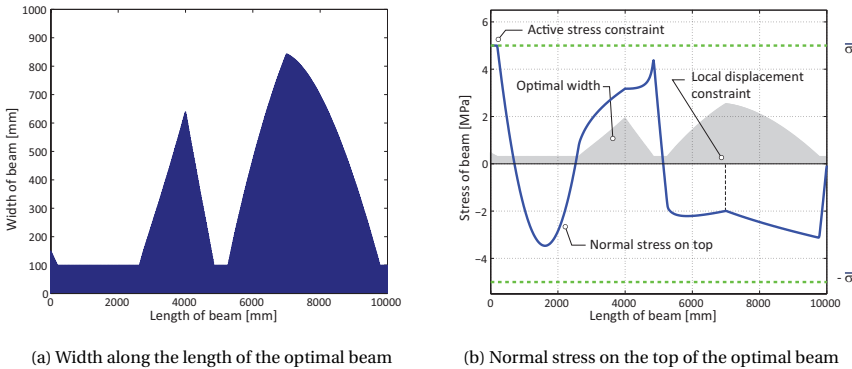


Figure 2.9: Optimal width distribution in the beam and the corresponding stress on the top edge

As may be observed from the results, the local displacement constraint at  $x = x_0 = 7000$  mm is active (i.e.,  $u(x_0) = u_{\max}$ , see Figure 2.10). Some adjacent points have larger dis-



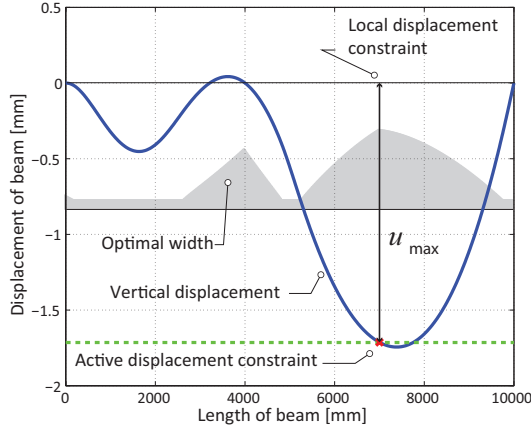


Figure 2.10: Displacement of the beam along the length

placements since these are not constrained in terms of displacements but rather in terms of stress. However, the displacement constraint has a significant effect on the optimal design since the region where the stress constraint is active is relatively small (only close to the leftmost support as shown in Figure 2.9b). Consequently, the width of the optimal beam is larger than a fully-stressed design, but necessary to meet the displacement constraint.

In terms of the optimization procedure using the proposed improved scheme, the number of iterations from the PCG, the iterations in the IPM and the number of the outer loops in the CCSA are shown in Figure 2.11a for mesh sizes from  $n = 40$  to  $n = 5120$  nodes. In general, it was observed that the volume of the beam decreases rapidly in the first two outer loops before it converges on the fourth loop. The number of iterations for the IPM and the outer loops in the CCSA are relatively constant with respect to the problem size. The average number of iterations for the PCG for the Schur complement increases slightly from 18 to about 50 for the range of problem sizes analyzed.

To assess the performance of the method in this example, which is dominated by the displacement constraint instead of the stress constraint, the CPU time of the proposed method and the original sizing optimization method are compared in a log-log form in Figure 2.11b. From the figure it may be observed that the slope of the CPU time for the proposed method is close to 1. In contrast, the slope of the curve for the original method keeps increasing to more than 2. This trends provides additional evidence of the estimated computational speed-up as observed in the previous examples, i.e., from more than  $O(n^2)$  to  $O(n)$ . Similarly, it is noted that the proposed method only becomes more efficient for sufficiently large problems, in this case for meshes with more than  $n = 10^3$  nodes.

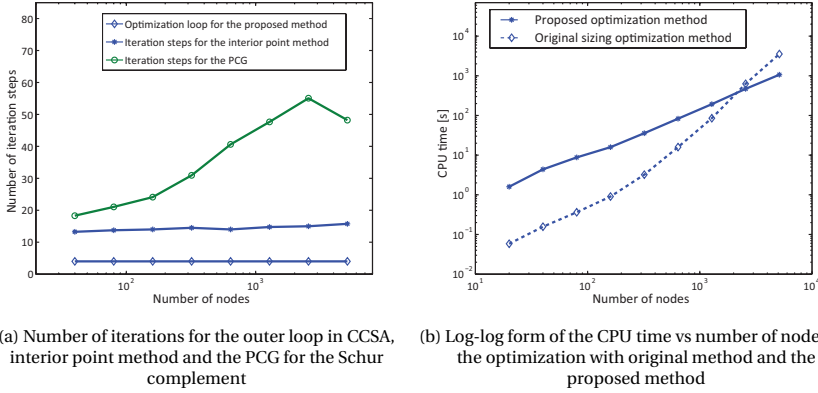


Figure 2.11: Computational performance of the proposed method

## 2.6. EXTENSION OF THE METHOD TO PLATE STRUCTURES

In this section, the proposed method is extended to plate structures for more general applications. Similar to the beam case, the design variable is the local thickness of the plate. The stress constraint is expressed as

$$\sigma_v \leq \bar{\sigma}, \quad (2.80)$$

where  $\sigma_v$  is the Von Mises stress and  $\bar{\sigma}$  is the maximum allowable value.

### 2.6.1. NODAL STRESS CONSTRAINTS

For the plate structures, the finite element discretization is carried out using a 8-node serendipity element (Kikuchi et al. [31]) with reduced integration (i.e., 4 Gauss points). Both the stress constraints and the design variables are defined at the vertices of each element, which are henceforth named as design nodes. The node-wised design variables ensure a smooth thickness distribution. To enforce the stress constraints, the Von Mises stress are evaluated at the design nodes.

As opposed to the beam case, the discretizations used for analysis and for design are different. In particular, the 8-node serendipity element is used for the FEM analysis to improve the continuity of the stress field. The linear quadrilateral element is used to interpolate the Lagrange multiplier in the variational stress constraint form (Eq.(2.10)), which results in a continuous field across elements. The structure of the mesh is shown in Figure 2.12. Correspondingly, the Von Mises stress at the  $i^{\text{th}}$  design node obtained through Eq.(2.10) is given by

$$\sigma_{v,i} = \frac{\sum_{g=1}^{n_g} N_{i,g} \sigma_{v,g} \Omega_g}{\sum_{g=1}^{n_g} N_{i,g} \Omega_g}, \quad (2.81)$$

where  $n_g$  is the total number of Gauss points in the model,  $N_{i,g}$  is the shape function of the  $i^{\text{th}}$  design node in the design and interpolation element at the  $g^{\text{th}}$  Gauss point,  $\Omega_g$  is the domain measured at the  $g^{\text{th}}$  Gauss point,  $\sigma_{v,g}$  is the Von Mises stress obtained at Gauss point  $g$ . Observe that, since the serendipity element uses reduced integration, then it shares the same Gauss points with the linear design element (see Figure 2.12)

The  $\sigma_{v,g}$  for the plane stress state is calculated by

$$\sigma_{v,g} = \sqrt{\sigma_{11,g}^2 - \sigma_{11,g}\sigma_{22,g} + \sigma_{22,g}^2 + 3\sigma_{12,g}^2}, \quad (2.82)$$

where  $\sigma_{11,g}$ ,  $\sigma_{22,g}$  are the normal stresses in the 1 and 2 direction respectively, and  $\sigma_{12,g}$  is the corresponding shear stress.

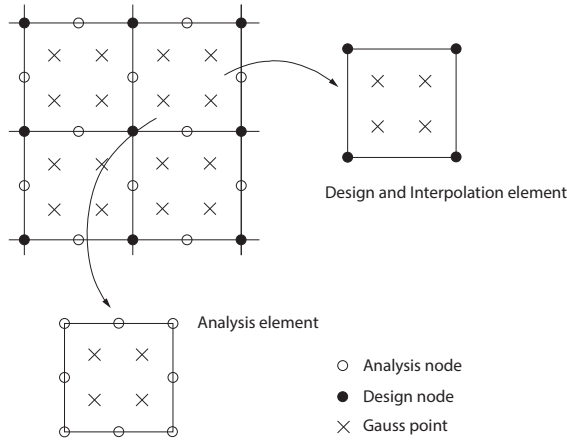


Figure 2.12: Element for interpolation and analysis

The theoretical part of the optimization framework (CCSA), the interior point method to solve the subproblem and the iterative solver for the Schur complement are identical to the beam case.

### 2.6.2. SENSITIVITY ANALYSIS OF THE STRESS CONSTRAINTS

The calculation of the sensitivity for the stress constraints at design node  $i$  with respect to the design variable  $x_j$  in the plate is obtained from Eq.(2.81) using the chain rule as follows:

$$\frac{\partial \sigma_{v,i}}{\partial x_j} = \frac{1}{\sum_{g=1}^{n_g} N_{i,g} \Omega_g} \left( \sum_{g=1}^{n_g} N_{i,g} \frac{\partial \sigma_{v,g}}{\partial x_j} \Omega_g \right), \quad (2.83)$$

where  $x_j$  is the thickness of the plate at the  $j^{\text{th}}$  design node.

The sensitivity of the Von Mises stress at Gauss point  $g$  is also obtained from Eq.(2.82)

with the chain rule as follows:

$$\frac{\partial \sigma_{v,g}}{\partial x_j} = \left( \frac{\sigma_{11,g}}{\sigma_{v,g}} + \frac{\sigma_{22,g}}{2\sigma_{v,g}} \right) \cdot \frac{\partial \sigma_{11,g}}{\partial x_j} + \left( \frac{\sigma_{11,g}}{2\sigma_{v,g}} + \frac{\sigma_{22,g}}{\sigma_{v,g}} \right) \cdot \frac{\partial \sigma_{22,g}}{\partial x_j} + \frac{3\sigma_{12,g}}{\sigma_{v,g}} \cdot \frac{\partial \sigma_{12,g}}{\partial x_j}. \quad (2.84)$$

The calculation of  $\frac{\partial \sigma_{11,g}}{\partial x_j}$ ,  $\frac{\partial \sigma_{22,g}}{\partial x_j}$  and  $\frac{\partial \sigma_{12,g}}{\partial x_j}$  is completed by using the adjoint method, which leads to

$$\frac{\partial \sigma_{v,g}}{\partial x_j} = -\mathbf{z}_{v,g}^T \mathbf{K}^{-1} \frac{\partial \mathbf{K}}{\partial x_j} \mathbf{u}, \quad (2.85)$$

where  $\mathbf{z}_{v,g}$  is the dummy load for the Von Mises stress at the Gauss node  $g$ ,  $\mathbf{K}$  is the stiffness matrix of the FEM model and  $\mathbf{u}$  is the displacement vector. The dummy load vector  $\mathbf{z}_{v,g}^T$  is obtained by

$$\mathbf{z}_{v,g}^T = \left( \frac{\sigma_{11,g}}{\sigma_{v,g}} + \frac{\sigma_{22,g}}{2\sigma_{v,g}} \right) \mathbf{z}_{1,g}^T + \left( \frac{\sigma_{11,g}}{2\sigma_{v,g}} + \frac{\sigma_{22,g}}{\sigma_{v,g}} \right) \mathbf{z}_{2,g}^T + \frac{3\sigma_{12,g}}{\sigma_{v,g}} \mathbf{z}_{3,g}^T, \quad (2.86)$$

where  $\mathbf{z}_{1,g}^T$ ,  $\mathbf{z}_{2,g}^T$ ,  $\mathbf{z}_{3,g}^T$  are the dummy load vectors for  $\sigma_{11,g}$ ,  $\sigma_{22,g}$  and  $\sigma_{12,g}$ , respectively. They are obtained from the row components of a matrix as follows:

$$\begin{bmatrix} \mathbf{z}_{1,g}^T \\ \mathbf{z}_{2,g}^T \\ \mathbf{z}_{3,g}^T \end{bmatrix} = \mathbf{D} \mathbf{B}_g, \quad (2.87)$$

where  $\mathbf{D}$  is the material stiffness matrix for the plane stress state and  $\mathbf{B}_g$  is the strain displacement matrix at Gauss point  $g$ .

The sensitivity of the nodal stress constraint  $i$  with respect to design variable  $x_j$  can be obtained through the adjoint method by

$$\frac{\partial \sigma_{v,i}}{\partial x_j} = -\mathbf{z}_{v,i}^T \mathbf{K}^{-1} \frac{\partial \mathbf{K}}{\partial x_j} \mathbf{u}, \quad (2.88)$$

where  $\mathbf{z}_{v,i}^T$  is the dummy load vector for the stress constraint at the  $i^{\text{th}}$  design node. To obtain  $\mathbf{z}_{v,i}^T$ , substituting Eq.(2.85) into Eq.(2.83) and use Eq.(2.88) provides

$$\mathbf{z}_{v,i} = \frac{1}{\sum_{g=1}^{n_g} N_{i,g} \Omega_g} \left( \sum_{g=1}^{n_g} N_{i,g} \mathbf{z}_{v,g} \Omega_g \right). \quad (2.89)$$

Since both the nodal Von Mises stress and the corresponding sensitivity can be obtained through Eq.(2.81),(2.88), the stress approximation with modified fully stressed design (in the form of Eq.(2.18)) for the plate structure can be obtained thereafter. Therefore, the proposed method can be applied directly to optimize the plate structures considering stress constraints. In the next section, results from the numerical tests will be demonstrated and discussed.

### 2.6.3. NUMERICAL TEST OF PLATE STRUCTURES

#### SIMPLY SUPPORTED PLATE CASE

In this test case, the model of the square plate is shown in Figure 2.13. The length  $L = 2400\text{mm}$ .

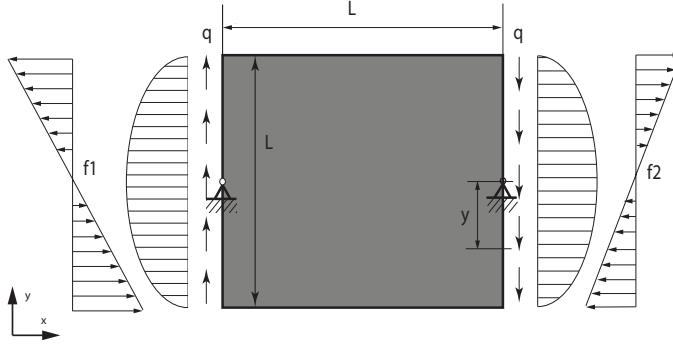


Figure 2.13: plate structure to be optimised

The central points of both the left and right edge of the plate are fixed. A quadratically distributed shear load is applied on both the left and right edge as shown in Figure 2.13 with

$$q = \frac{0.15}{1000} \left( \frac{L^2}{4} - y^2 \right).$$

There is also a bending moment applied on both edges of the plate. Specifically, the bending moment on the right edge of the structure is applied with

$$f_2 = \frac{0.45L}{1000} y,$$

that on the left edge of the structure is applied to balance the overall moment on the right with

$$f_1 = -\frac{0.75L}{1000} y.$$

Constraints of the optimization include the box constraints of the design variables and the stress constraint (Eq.(2.83)) at each design node.

The material properties of the plate and the upper bound  $t_u$ , lower bound  $t_l$  of the thickness is listed in Table 2.4.

In this optimization procedure (with Algorithm 3), the relative tolerance of PCG is  $e_{PCG} = 10^{-9}$ , the tolerance of the IPM is the duality gap to be smaller than  $\eta_{gap} = 10^{-10}$ , the tolerance of the inner loops of the CCSA is stress constraints violation to be smaller than  $\eta_\sigma = 10^{-3}$ , the tolerance of the outer loops is the volume variation to be smaller than  $\eta_v = 10^{-3}$ .

Table 2.4: Parameters of the plate case

Young's Modulus	Poisson's ratio	Allowable stress
$E = 200\text{GPa}$	$\nu = 0.3$	$\bar{\sigma} = 172\text{MPa}$
Initial design thickness	Minimum thickness	Maximum thickness
$t_i = 20\text{mm}$	$t_l = 7\text{mm}$	$t_u = 40\text{mm}$

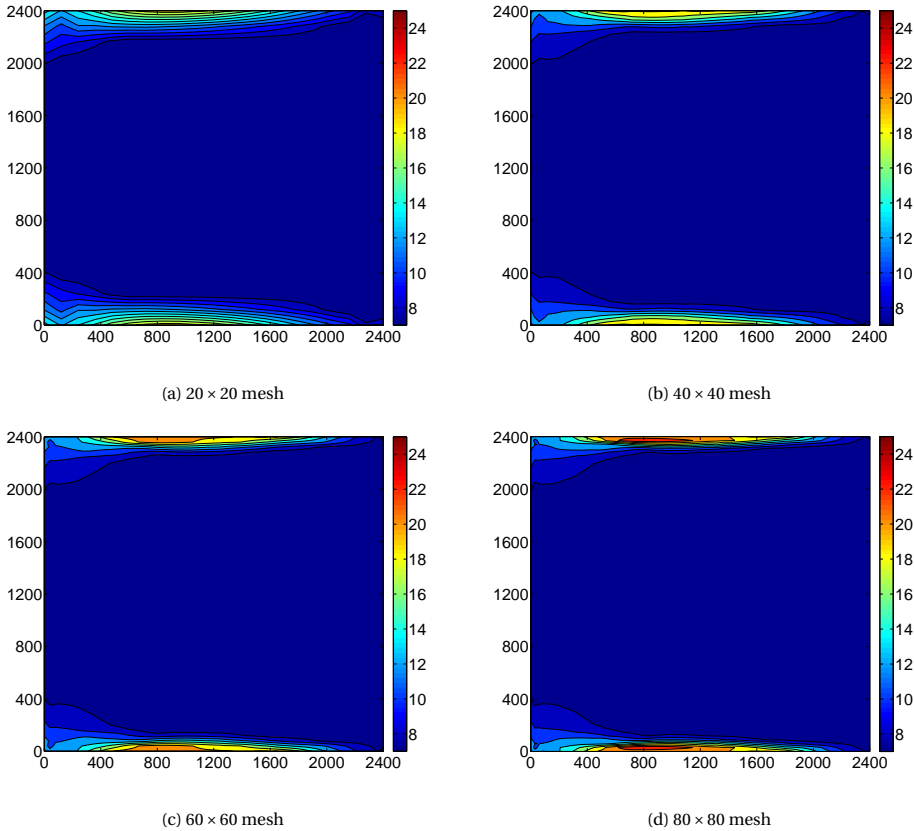


Figure 2.14: Optimal thickness distribution

The optimal thickness distribution is shown in Figure 2.14 for four different meshes, namely  $20 \times 20$ ,  $40 \times 40$ ,  $60 \times 60$  and  $80 \times 80$  elements in  $x$  and  $y$  direction, respectively. As shown in the figure, the optimal design can be interpreted similar to the I-beam, where the thickness on the top and bottom edge is high to resist the bending moment. Meanwhile, the design also shows features of a typical cantilever plate structure since the lower and upper corners on the left side become thicker, which is a characteristic of clamped structures.

The convergence history of the normalized volume (with respect to the initial volume

$V_0$ ) for these four meshes are shown in Figure 2.15. According to this figure, the curves of history of the normalized volume overlap for the four meshes, which reduce from initial 1 to 0.386. This indicates that the optimal volume obtained at each outer loop of the CCSA is the same regardless of the mesh size. In addition, the CCSA converges in 3 steps, which demonstrates the fast convergence of the framework in the proposed method.

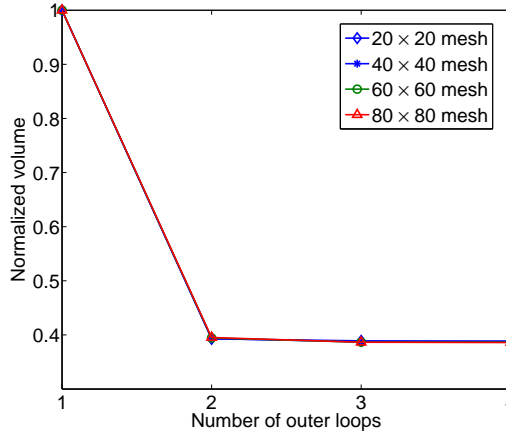


Figure 2.15: Convergence history for  $20 \times 20$ ,  $40 \times 40$ ,  $60 \times 60$ ,  $80 \times 80$  mesh

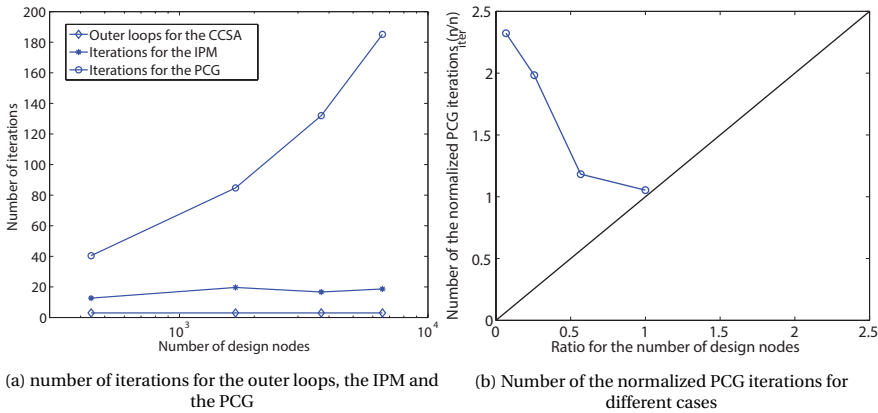


Figure 2.16: Number of iterations records for different meshes

To estimate the computational work of the proposed method in plate case, the number of the outer loops of the CCSA, the number of iterations of the IPM and the PCG for the Schur complement required through the mesh refinement is demonstrated in Figure 2.16a. From the result, it can be observed that the number of iterations for the outer loops of the CCSA and the IPM is stable. They remain at 3 and around 18, respectively, as the mesh of the model is refined. However, regarding the number of iterations for

the PCG, the average value of the iterations increases from 40 to 185 to solve the Schur complement as the number of design nodes increases from 441 to 6561. Therefore, the overall number of iterations of the PCG in the IPM  $n_{iter}$  is larger than the total number of design nodes  $n$ . This breaks the condition for the method to be effective (Eq.(2.79)). Consequently, the computational cost for the stress constrained sizing optimization of the plate structures can not be reduced with the proposed method. To further explore this issue, a second test is carried out.

### PLATE CASE WITH TRUSS REINFORCED

In the second test case, a reinforced plate is analyzed as shown in Figure 2.17. A distinguished constant normal load  $P$  is applied to the flange. The right edge is subjected to a mixed boundary condition: the displacement in  $x$  is zero and a distributed shear load  $q$  is applied to balance the load  $P$  on the top flange in  $y$  direction. The right bottom node is fixed to prevent rigid body motion.

In this case, the design variables are the cross-sectional area of the truss on the top edge as well as the thickness of the plate at each design node. The material properties and the upper and lower bounds of the design variables are listed in Table 2.5.

Table 2.5: Parameters of the reinforced plate structure

Young's Modulus $E = 69\text{GPa}$	Poisson's ratio $\nu = 0.3$	Allowable stress $\bar{\sigma} = 200\text{MPa}$	Initial plate thickness $t_i = 12\text{mm}$
Initial cross-sectional area truss $A_i = 398\text{m}^2$	Minimum plate thickness $t_l = 2\text{mm}$	Maximum plate thickness $t_u = 100\text{mm}$	Minimum cross sectional area truss $A_l = 100\text{m}^2$
Maximum cross sectional area truss $A_u = 10000\text{m}^2$	distributed load $P = 90\text{Nmm}^{-1}$		

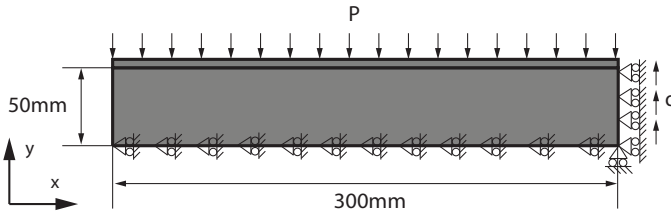


Figure 2.17: Plate Structure Reinforced by Truss

The tolerance for the optimization procedure (Algorithm 3) is identical to the simply supported plate case. The mesh of the FEM model is refined in four distinct meshes, namely,  $20 \times 5$ ,  $40 \times 10$ ,  $60 \times 16$  and  $80 \times 20$  in  $x$  and  $y$  direction, respectively. The optimal solutions for the cross sectional areas of the truss and thickness of the plate with different meshes are shown in Figures 2.18 and 2.19, respectively.

From Figure 2.18, it is obvious to find that the optimal cross sectional area of the truss on the top edge converges to the same solution as the mesh is refined in the model. For the results of  $60 \times 16$  and  $80 \times 20$  mesh, there are some slight trend disruptions on the optimal cross sectional area at around 270mm in  $x$  direction. These are due to the effect of the



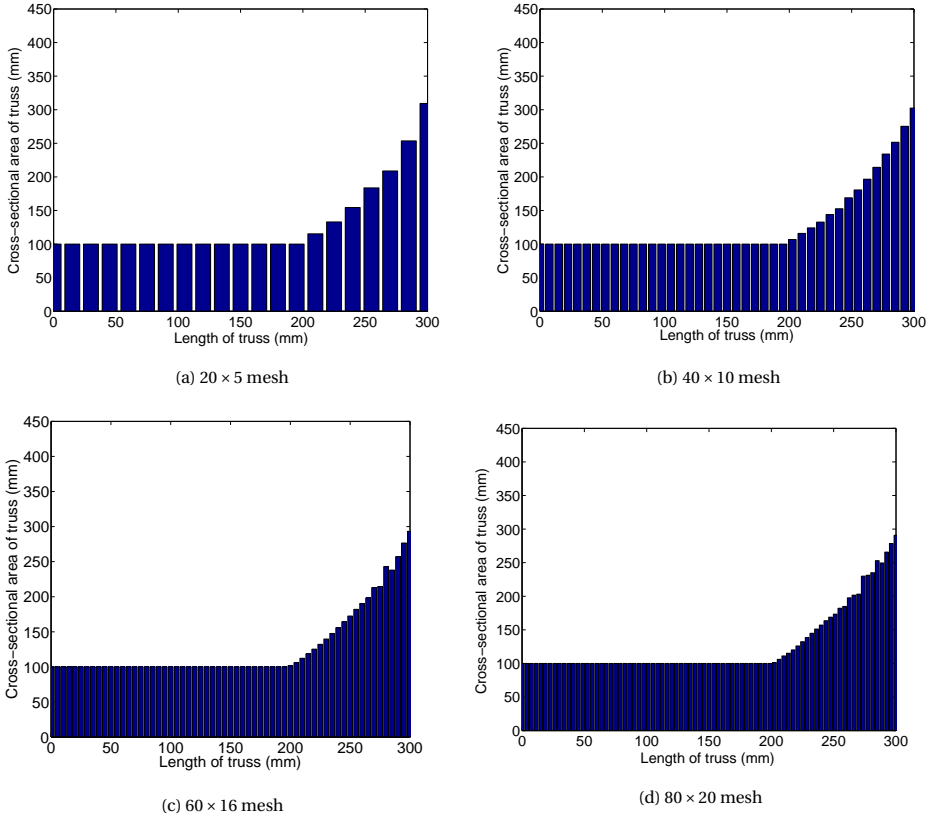


Figure 2.18: Optimal cross sectional area of truss

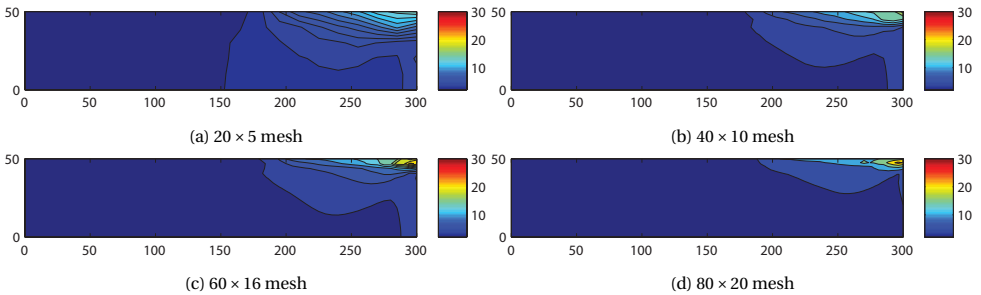


Figure 2.19: Optimal thickness distribution of plate

damping in the stress approximation (Eq.(2.29)). Specifically, the damping factors of each stress constraint are updated by the end of every inner loop of the CCSA by Eq.(2.75) and Eq.(2.76). However, the update for each stress constraint along  $x$  direction is not guaranteed to be uniform. The corresponding difference results in the distributions in

the optimal cross sectional areas.

In Figure 2.19, the optimal thickness in the plate for different meshes are shown. From the results, the maximum thickness of the plate on the top right corner keeps increasing as the mesh is refined. Consequently, the optimal thickness converges to different results with different meshes. This also happens to the previous test case. Therefore, the sizing optimization for plate structures has a mesh dependency issue according to both plate cases.

The convergence history of the normalized volume is shown in Figure 2.20. This figure shows that the normalized volume eventually converges to the same solution with different meshes. Similar to the previous case, the number of the outer loops in the CCSA is small in the optimization. For  $20 \times 5$ ,  $40 \times 10$ ,  $60 \times 16$  mesh, it takes 6 outer loops to converge. The number of outer loops increases slightly to 7 for  $80 \times 20$  mesh. Therefore, the framework of the proposed method is demonstrated to preserve a fast convergence rate.

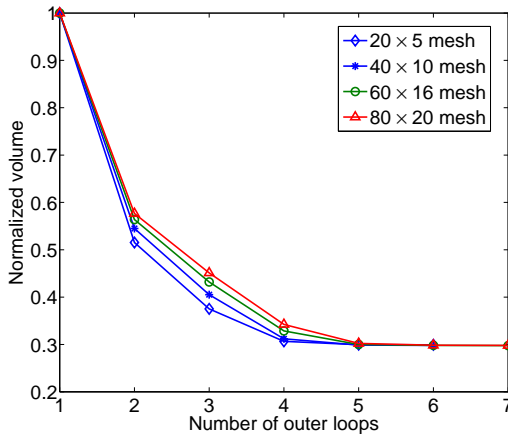


Figure 2.20: Convergence history for  $20 \times 5$ ,  $40 \times 10$ ,  $60 \times 16$ ,  $80 \times 20$  mesh

The number of the outer loops of the CCSA, the number of iterations of the IPM and the PCG are demonstrated in Figure 2.21a. The number of iterations for the outer loops and the IPM is stable at 6 and 15 respectively, when the number of design nodes increases. However, as also observed in the first test case, the number of iterations for the PCG to solve the Schur complement increases as the number of design nodes increases sharply from 53 to 191 with the mesh refinement. Although the trend decreases slightly for the  $80 \times 20$  mesh, the condition  $n_{iter} < n$ , for the proposed method to be efficient is still violated. Therefore, the proposed method does not reduce the computational cost for the plate case.

In the next section, some investigation is implemented to study the possible reasons in the equation of the Schur complement. Details in the optimal results and the sensitivity

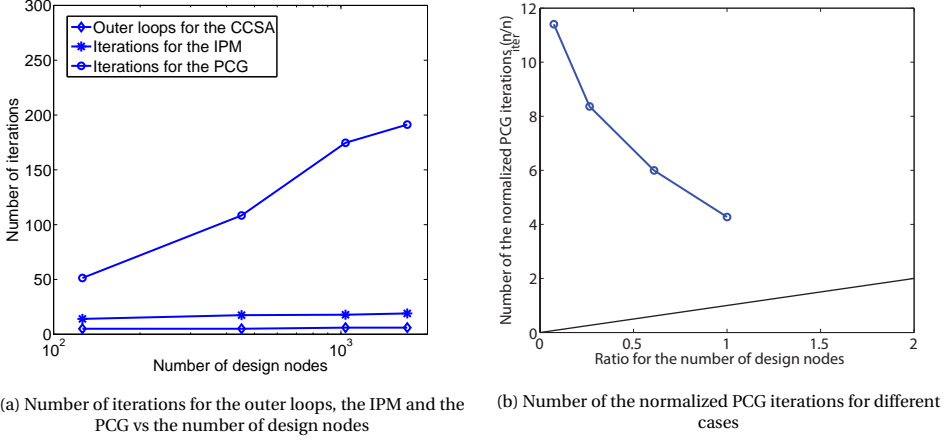


Figure 2.21: Number of iterations records for different meshes

analysis are checked. The numerical model in the simply supported plate case is used in the investigation.

## 2.6.4. INVESTIGATION OF THE POSSIBLE REASONS FOR MISSION FAILURE

### STUDY ON NORMALIZED LAGRANGE MULTIPLIER

In the first study, the distribution of the normalized Lagrange multipliers  $\tilde{y}^s$  correlated with the stress constraints (as in Eq.(2.10)) obtained in the optimization is investigated. The simply supported plate case is employed in this study. Specifically, the normalized Lagrange multiplier refers to the value of the Lagrange multiplier  $y_i^s$  obtained for the  $i^{\text{th}}$  stress constraint in the optimization over the domain measured at the  $i^{\text{th}}$  design node.

The relation between the three variables originates from the continuous form to the discrete form of the stress constraint  $\mathcal{L}^\sigma$  in the Lagrangian function as follows:

$$\begin{aligned}
 \mathcal{L}^\sigma &:= \int \tilde{y}^s \left( \frac{\sigma}{\bar{\sigma}} - 1 \right) d\Omega \\
 &\approx \sum_{i=1}^n \tilde{y}_i^s \left( \frac{\sigma_i}{\bar{\sigma}} - 1 \right) |\Omega_i| \\
 &= \sum_{i=1}^n y_i^s \left( \frac{\sigma_i}{\bar{\sigma}} - 1 \right).
 \end{aligned} \tag{2.90}$$

Therefore,  $y_i$  in the discrete form represents

$$y_i^s = \tilde{y}_i^s |\Omega_i| \tag{2.91}$$

in the continuous form. If the continuous optimization converges to an analytical solution, the discrete solution over the unit area of the domain should be identical regardless

of the mesh.

The results of  $\bar{\gamma}^s$  over the different meshes are shown in Figure 2.22,2.23.

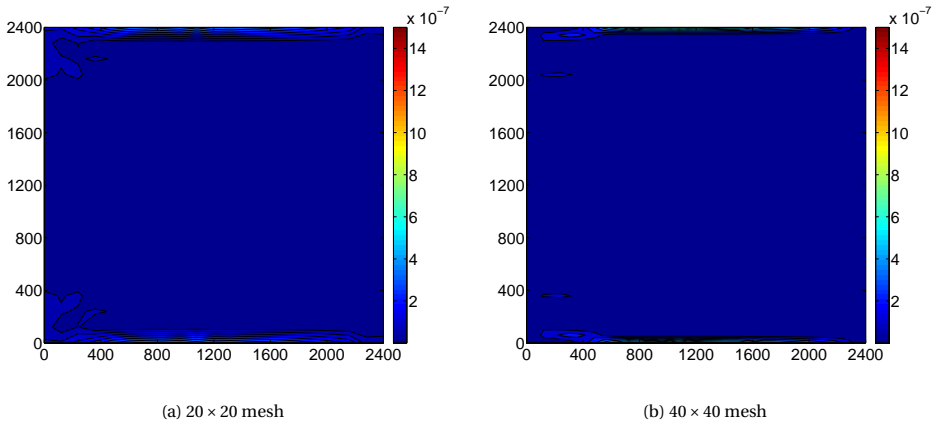


Figure 2.22: Distribution of normalized Lagrangian multiplier (1)

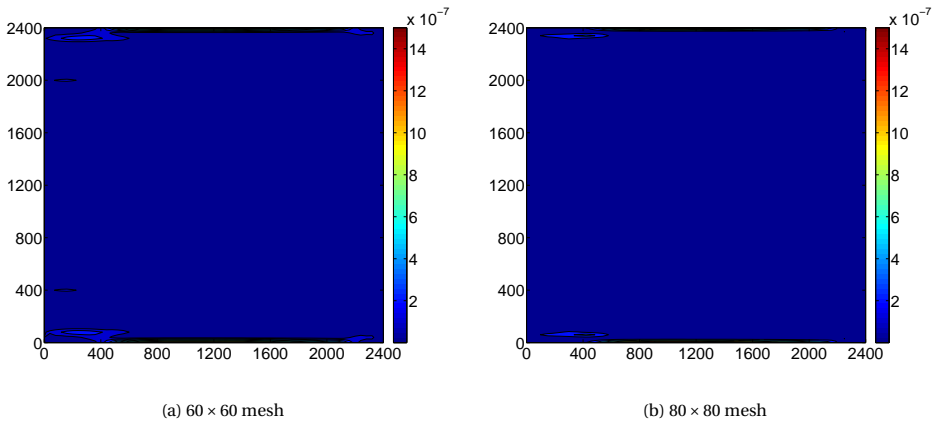


Figure 2.23: Distribution of normalized Lagrangian multiplier (2)

From the results, it can be observed that the normalized Lagrange multiplier does not have the same distribution in different meshes. Simultaneously, it is not well distributed in the left top and left bottom part of the plate, where the stress constraints are active. Theoretically, the Lagrange multiplier for an active stress constraint should be a relatively large positive value. However, the results in Figure 2.22a,2.22b,2.23a,2.23b demonstrate that some of the normalized Lagrange multipliers drop close to zero in this region. One possible reason is that the continuity of the constraints in the design domain should be higher than that of the Lagrange multipliers. Since the continuity of the Lagrange

multiplier is linear due to the linear shape function in the design and interpolation element, the continuity of the stress constraints should be at least linear in the design domain.

## 2

## STUDY ON THE SENSITIVITY OF STRESS CONSTRAINTS

Since the optimal thickness of the plate are found to be mesh dependent in the previous test cases, the sensitivity of the stress constraint is worthy to be studied as well. The numerical model in this case is the same as the previous study. The stress constraint for the central design node in the plate model is taken to check the convergence of the sensitivity of the stress approximation.

With the same ideology in the previous study, the stress approximation can be written as

$$\begin{aligned}\hat{r}_i^{(\alpha,\lambda)} &:= \frac{|\mathcal{F}_i^{(\alpha)}|}{x_i^{(\lambda)}\bar{\sigma}} + \int \tilde{a}^{(\alpha)}(x^{(\lambda)} - x^{(\alpha)})d\Omega \\ &\approx \frac{|\mathcal{F}_i^{(\alpha)}|}{x_i^{(\lambda)}\bar{\sigma}} + \sum_{j=1}^n \tilde{a}_j^{(\alpha)}(x_j^{(\lambda)} - x_j^{(\alpha)})|\Omega_j| \\ &= \frac{|\mathcal{F}_i^{(\alpha)}|}{x_i^{(\lambda)}\bar{\sigma}} + \sum_{j=1}^n a_j^{(\alpha)}(x_j^{(\lambda)} - x_j^{(\alpha)}),\end{aligned}\quad (2.92)$$

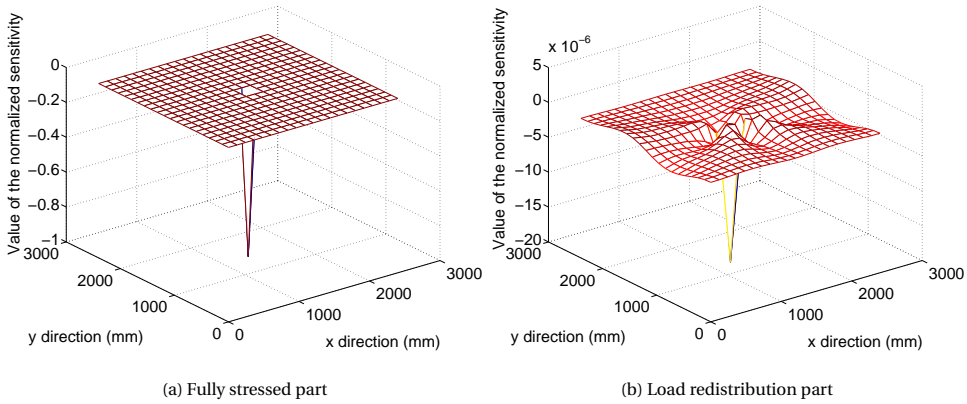
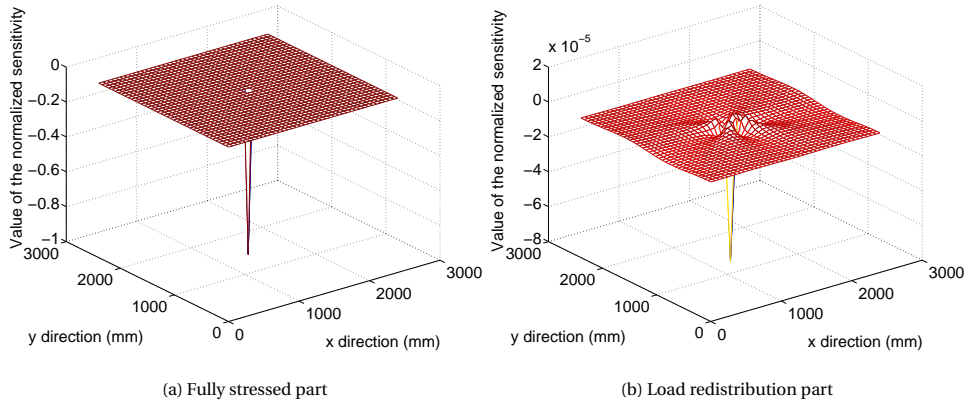
where  $\mathcal{F}_i$  is the internal force at design node  $i$ ,  $\bar{\sigma}$  is the maximum allowable value,  $x$  is the design variable (thickness of the plate),  $\tilde{a}$  is the sensitivity of the stress approximation for the load redistribution part in the continuous form, namely the normalized sensitivity,  $\alpha$  is the index for the outer loop,  $\lambda$  is the index for the inner loop.

Hence, the coefficient  $a_j^{(\alpha)}$  in the discrete form equals to

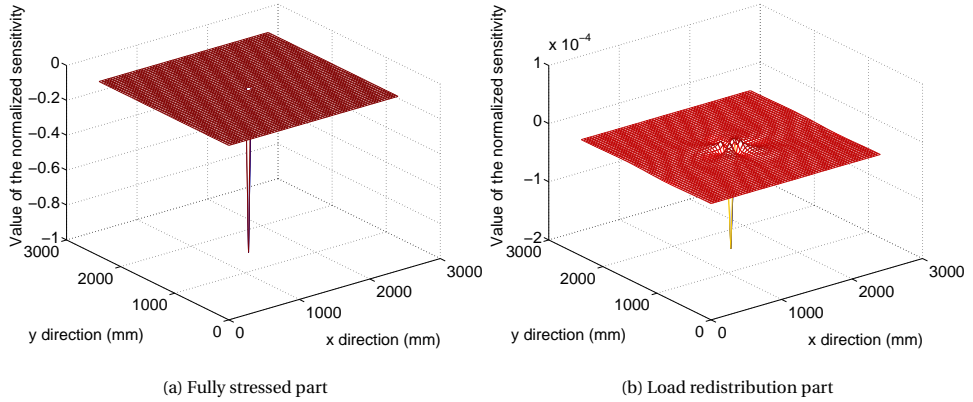
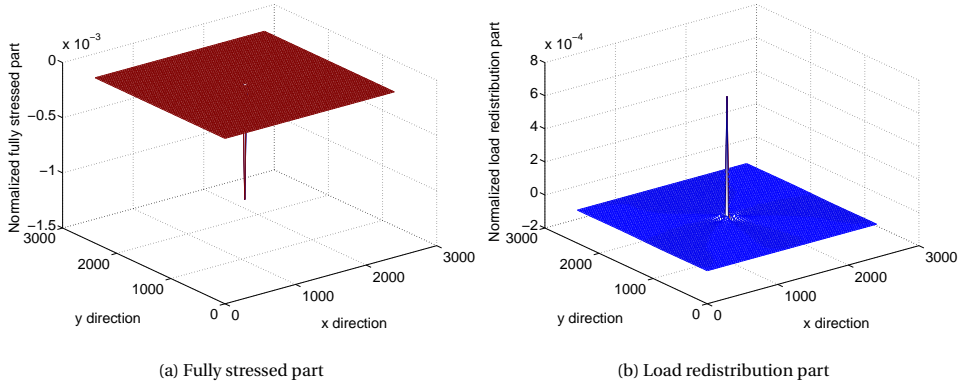
$$a_j^{(\alpha)} = \tilde{a}_j^{(\alpha)}|\Omega_j|. \quad (2.93)$$

Since the discrete approximation (Eq.(2.18)) would be mesh independent only if the normalized sensitivity is mesh independent, the convergence of the fully stressed part and the normalized sensitivity of the load redistribution part of the proposed approximation is calculated with different mesh size. The sensitivity of the fully stressed part and the normalized load redistribution part for the stress constraint at the central design node for different meshes are demonstrated in Figure 2.24, 2.25, 2.26, 2.27.

From the results, it can be found that the peak of the fully stressed part converges to around  $-0.9$  as the mesh is refined. This is due to the fact that the internal force  $\mathcal{F}_i^{(\alpha)}$  from the FEM converges. However, the peak of the normalized load redistribution part keeps increasing as the mesh is refined. Therefore, the sensitivity of the load redistribution part in the stress approximation is mesh dependent. Correspondingly, this results in the mesh dependency of the Schur complement in the IPM, which relates to the gradient matrix of the stress constraint. Therefore, the optimal solution can be mesh dependent as well.

Figure 2.24: Normalized sensitivity distribution ( $20 \times 20$  mesh)Figure 2.25: Normalized sensitivity distribution ( $40 \times 40$  mesh)

From the above two studies, it can be found that the normalized Lagrange multiplier obtained in the optimization and the normalized sensitivity of stress constraints need to be improved in the plate case. Both are the output and the input of the Schur complement, respectively. Therefore, one way of improvement is to elevate the continuity of the stress field in the numerical model. To this end, the Lagrange multiplier obtained from the Schur complement can be well distributed in the domain. Simultaneously, the mesh dependent issue on the sensitivity of stress approximation can be removed hopefully because of the continuous stress field. Otherwise, the sensitivity of stress field should be calculated in the continuous form first before discretization. Further tests are required to make the improvement. If the above approaches still do not help to reduce the computational work, then another preconditioner needs to be employed in the PCG for the Schur complement.

Figure 2.26: Normalized sensitivity distribution ( $60 \times 60$  mesh)Figure 2.27: Normalized sensitivity distribution ( $80 \times 80$  mesh)

## 2.7. CONCLUSIONS

An improved algorithm for size optimization for structural problems with local stress constraints is proposed in order to reduce the overall computational cost. The new method is based on combining three ingredients. First, a new stress approximation is proposed, which is separable, convex, scalable and conservative. It leads to a diagonal Hessian matrix that reduces the computational work when calculating the Schur complement. Second, the implicit sensitivity analysis provides an efficient way for the matrix vector calculation with gradient matrix in the optimization. Finally, an effective preconditioner for the PCG to cut the number of iterations for solving the Schur complement.

Numerical cases show that when these improvements are implemented in the Mehrotra's IPM, the computational cost of the optimization decreases by one order for the

beam case. However, the proposed method is relatively expensive to apply to problems where the number of stress constraints and design variables is small. This is because the computational work of the direct method for the Schur complement, such as Gauss elimination, is comparable to the PCG for small problems. Furthermore, the total number of iterations for the PCG in the IPM  $n_{\text{iter}}$  is larger than the total number of design variables  $n$  for small problems. This violates the condition to obtain the efficiency of the method Eq.(2.79). Consequently, this method should only be used for sufficiently large scale problems, which in the case of a beam is the order of  $n \approx 10^3$  nodes.

By contrast, the proposed method does not yet successfully accelerate the stress constrained sizing optimization with plate structures. The computational cost for the PCG in solving the Schur complement keeps increasing as the mesh of the model is refined. The correlated phenomenon discovered till now is that the optimal Lagrange multiplier is not well distributed in the optimization. Besides, there is a mesh dependency issue on the sensitivity of the stress constraints. One possible way to improve the proposed method in plate case is to increase the continuity of the stress field in the model or to calculate the sensitivity in the continuous form first before discretization. If these still do not achieve the efficiency, then another preconditioner needs to be considered for the PCG to solve the Schur complement. Otherwise, another strategy needs to be taken, such as the p-norm stress constraint.

## REFERENCES

- [1] Shahriar Setoodeh, Mostafa M. Abdalla, and Zafer Gürdal. Design of variable-stiffness laminates using lamination parameters. *Composites Part B: Engineering*, 37(4-5):301–309, 2006.
- [2] Erik Holmberg, Bo Torstenfelt, and Anders Klarbring. Fatigue constrained topology optimization. *Structural and Multidisciplinary Optimization*, 50(2):207–219, Aug 2014. ISSN 1615-1488. doi: 10.1007/s00158-014-1054-6. URL <https://doi.org/10.1007/s00158-014-1054-6>.
- [3] Yu Nesterov. Universal gradient methods for convex optimization problems. *Mathematical Programming*, 152(1):381–404, Aug 2015. ISSN 1436-4646. doi: 10.1007/s10107-014-0790-0. URL <https://doi.org/10.1007/s10107-014-0790-0>.
- [4] Nimrod Megiddo. *Progress in mathematical programming*. Springer, 1989.
- [5] B. Maar and V. Schulz. Interior point multigrid methods for topology optimization. *Structural and Multidisciplinary Optimization*, 19(3):214–224, May 2000. ISSN 1615-1488. doi: 10.1007/s001580050104. URL <https://doi.org/10.1007/s001580050104>.
- [6] Alemseged Gebrehiwot Weldeyesus and Mathias Stolpe. A primal-dual interior point method for large-scale free material optimization. *Computational Optimization and Applications*, 61(2):409–435, Jun 2015. ISSN 1573-2894. doi: 10.1007/s10589-014-9720-6. URL <https://doi.org/10.1007/s10589-014-9720-6>.



- [7] Sanjay Mehrotra. On the implementation of a primal-dual interior point method. *SIAM Journal on Optimization*, 2(4):575–601, 1992.
- [8] Irvin J. Lustig, Roy E. Marsten, and David F. Shanno. On implementing mehrotra's predictor–corrector interior-point method for linear programming. *SIAM Journal on Optimization*, 2(3):435–449, 1992.
- [9] Lucien A. Schmit and B. Farshi. Some approximation concepts for structural synthesis. *AIAA journal*, 12(5):692–699, 1974.
- [10] Claude Fleury and Vincent Braibant. Structural optimisation: a new dual method using mixed variables. *International journal for numerical methods in Engineering*, 23(3):409–428, 1986.
- [11] Krister Svanberg. The method of moving asymptotes—a new method for structural optimisation. *International journal for numerical methods in Engineering*, 24(2):359–373, 1987.
- [12] C. Fleury. First and second order convex approximation strategies in structural optimization. *Structural optimization*, 1(1):3–10, 1989. ISSN 1615-1488. doi: 10.1007/BF01743804. URL <http://dx.doi.org/10.1007/BF01743804>.
- [13] G.M. Fadel, M.F. Riley, and J.M. Barthelemy. Two point exponential approximation method for structural optimization. *Structural and Multidisciplinary Optimization*, 2(2):117–124, 1990.
- [14] M.Zhou and R.W.Xia. Two-level approximation concept in structural synthesis. *International journal for numerical methods in Engineering*, 29(8):1681–1699, 1990.
- [15] Garret N. Vanderplaats and Srinivas Kodiyalam. Two-level approximation method for stress constraints in structural optimization. *AIAA journal*, 28(5):948–951, 1990.
- [16] G. N. Vanderplaats and H. L. Thomas. An improved approximation for stress constraints in plate structures. *Structural optimization*, 6(1):1–6, 1993. ISSN 1615-1488.
- [17] Attila P. Nagy, Mostafa M. Abdalla, and Zafer Gürdal. On the variational formulation of stress constraints in isogeometric design. *Computer Methods in Applied Mechanics and Engineering*, 199(41):2687–2696, 2010.
- [18] J. París, F. Navarrina, I. Colominas, and M. Casteleiro. Improvements in the treatment of stress constraints in structural topology optimization problems. *Journal of Computational and Applied Mathematics*, 234(7):2231 – 2238, 2010. ISSN 0377-0427. doi: <http://dx.doi.org/10.1016/j.cam.2009.08.080>. URL <http://www.sciencedirect.com/science/article/pii/S0377042709005597>. Fourth International Conference on Advanced COmputational Methods in ENgineering (ACOMEN 2008).
- [19] P. Duysinx and M. P. Bendsøe. Topology optimization of continuum structures with local stress constraints. *International Journal for Numerical Methods in Engineering*, 43(8):1453–1478, 1998. ISSN 1097-0207. doi:

- 10.1002/(SICI)1097-0207(19981230)43:8<1453::AID-NME480>3.0.CO;2-2. URL [http://dx.doi.org/10.1002/\(SICI\)1097-0207\(19981230\)43:8<1453::AID-NME480>3.0.CO;2-2](http://dx.doi.org/10.1002/(SICI)1097-0207(19981230)43:8<1453::AID-NME480>3.0.CO;2-2).
- [20] Erik Holmberg, Bo Torstenfelt, and Anders Klarbring. Stress constrained topology optimization. *Structural and Multidisciplinary Optimization*, 48(1):33–47, 2013.
- [21] C.Y. Kiyono, S.L. Vatanabe, E.C.N. Silva, and J.N. Reddy. A new multi-p-norm formulation approach for stress-based topology optimization design. *Composite Structures*, 156:10–19, 2016. ISSN 0263-8223. doi: <https://doi.org/10.1016/j.compstruct.2016.05.058>. URL <http://www.sciencedirect.com/science/article/pii/S0263822316306419>. 70th Anniversary of Professor J. N. Reddy.
- [22] Krister Svanberg. A class of globally convergent optimization methods based on conservative convex separable approximations. *SIAM Journal on Optimization*, 12(2):555–573, 2002. doi: [10.1137/S1052623499362822](https://doi.org/10.1137/S1052623499362822). URL <http://dx.doi.org/10.1137/S1052623499362822>.
- [23] Raphael T. Haftka and Zafer Gürdal. *Elements of structural optimization*, volume 11. Springer Science & Business Media, 2012.
- [24] Ali Khani, Samuel T. IJsselmuiden, Mostafa M. Abdalla, and Zafer Gürdal. Design of variable stiffness panels for maximum strength using lamination parameters. *Composites Part B: Engineering*, 42(3):546–552, 2011.
- [25] Garret N. Vanderplaats and Eysa Salajegheh. New approximation method for stress constraints in structural synthesis. *AIAA journal*, 27(3):352–358, 1989.
- [26] Christian Zillober. A combined convex approximation—interior point approach for large scale nonlinear programming. *Optimization and Engineering*, 2(1):51–73, 2001.
- [27] A.R.L. Oliveira and D.C. Sorensen. A new class of preconditioners for large-scale linear systems from interior point methods for linear programming. *Linear Algebra and its Applications*, 394:1–24, 2005. ISSN 0024-3795. doi: <http://dx.doi.org/10.1016/j.laa.2004.08.019>. URL <http://www.sciencedirect.com/science/article/pii/S0024379504003799>.
- [28] Michele Benzi, Gene H. Golub, and Jörg Liesen. Numerical solution of saddle point problems. *Acta numerica*, 14:1–137, 2005.
- [29] Raphael T. Haftka. Simultaneous analysis and design. *AIAA journal*, 23(7):1099–1103, 1985.
- [30] George I.N. Rozvany. *Structural design via optimality criteria: the Prager approach to structural optimization*, volume 8. Springer Science & Business Media, 1989.
- [31] Fumio Kikuchi, Masayuki Okabe, and Hidehiro Fujio. Modification of the 8-node serendipity element. *Computer methods in applied mechanics and engineering*, 179(1):91–109, 1999.



# 3

## AN ENHANCED CURVATURE CONSTRAINED DESIGN METHOD FOR MANUFACTURABLE VARIABLE STIFFNESS COMPOSITE LAMINATE

*I did not think; I experimented.*  
我不过度思考，我只专注试验。

Wilhelm Röntgen

### 3.1. INTRODUCTION

Robotic-driven manufacturing techniques for composite materials, such as Automated Fiber Placement (AFP), allow to tailor layer-wise the path of fiber-reinforced laminates to manufacture complex structural components that do not conform to simple geometries and/or stacking sequences of layers with straight fibers. Due to their spatially-varying fiber orientation, these laminates have non-homogeneous stiffness and are commonly known as variable stiffness laminates (VSLs, Gürdal and Olmedo [1]). With the advent of these advanced manufacturing techniques, VSL composites were soon recognized as a feasible way to improve the structural response (see, e.g., Hyer and Lee [2], Setoodeh

---

This chapter is based on the following papers:

Zhi Hong, Daniël Peeters, Sergio Turteltaub, *An enhanced curvature constrained design method for manufacturable variable stiffness laminate*, Computers & Structures, under review.

Daniël Peeters, Zhi Hong, Mostafa Abdalla, *A compliance approximation method applied to variable stiffness composite optimization*, Structural and Multidisciplinary Optimization, Vol. 58, No. 5, 2018, pp. 1981-2001. doi:10.1007/s00158-018-2007-2.

et al. [3]). Hence, in parallel with new improvements of the manufacturing technique, companion design methods are also being actively developed to exploit the material design freedom enabled by VSLs. Some examples are methods based on Genetic Algorithms that have been used to optimize for buckling (Blom et al. [4]), for vibration response (Akbarzadeh et al. [5]) and for strength (Cagdas [6]). For gradient-based methods, Stegmann and Lund [7] developed the Discrete Material Optimization Method to maximize the buckling load of a wind turbine. Later, this method has been applied in topology optimization with, among others, buckling, eigenfrequency or displacement constraints (Sørensen et al. [8]). The aforementioned methods use a parametrization of the design space based directly on the fiber paths (using either continuously varying fiber angles or a limited set of angles).

Alternatively, other design methods start from a broader design space without specifying or constraining a priori the number of layers in the laminate, but require post-processing to translate the optimal designs into a specific number of layers and actual fiber paths within the layers. Correspondingly, these design strategies can be classified as multi-step methods. In a first step, an optimal design is identified within a broad design space typically parametrized by homogenized properties such as lamination parameters (Abdalla et al. [9], Lopes et al. [10], Setoodeh et al. [11], IJsselmuiden et al. [12], Rouhi et al. [13]) or polar formalism (Jibawy et al. [14], Kazemi and Verchery [15], Stanford and Jutte [16], Montemurro and Catapano [17]). Homogenization refers here to the through-the-thickness effective properties in a relatively thin laminate as commonly encountered in aerospace structures. Subsequently, in a second step, the optimal homogenized parameters are used to retrieve physical and/or geometrical information about the optimal laminate. These multistep methods are usually efficient in terms of exploring a large design space at a minimal computational cost.

Experimental tests confirm that VSLs can indeed improve the performance of components. For example, a rectangular specimen with a cut-out made of a VSL was found to have an increase in 13% of its buckling capacity over a conventional straight fiber laminate (Hyer et al. [18], Jegley et al. [19]). More recently, Khani et al. [20] implemented an experimental test to validate that the ultimate tensile failure load of a VSL wing lower-skin with a large access hole is 35% higher than that of the composite with homogeneous (constant) stiffness.

Despite recent progress in manufacturing techniques, AFP still has limitations in terms of the variable path designs that can actually be produced. In particular, fiber paths that have sharp turns result in defects such as wrinkles, which can decrease the load carrying capacity of the composite or may become a location where delamination nucleates. Similarly, depending on the width of the tow in the AFP machine, unacceptable gaps and/or overlaps between adjacent tows may occur if the fiber path curvature exceeds a critical value. Correspondingly, manufacturing constraints need to be considered in the design process to exclude designs with inherent flaws or may otherwise be deemed unacceptable (Blom et al. [21], Lozano et al. [22]). In order to guarantee that the minimum turning radius of the design (reciprocal of curvature) remains above a critical value (manufacturing limit), a constraint can be imposed on the fiber path curvature. However, it has been challenging to impose this type of constraint in multistep meth-

ods without a significant performance loss. This is particularly problematic in methods where the retrieval step is carried out by matching the physical and geometrical properties of the laminate to the optimal homogenized parameters without considering the mechanical performance. Since the net gain in the optimization process can be jeopardized by these type of losses, it is important to address these issues within the overall design process.

Two basic types of methods are considered here to impose the curvature constraint, namely direct and indirect control methods. In the direct control methods, the curvature constraint is imposed directly on the fiber angles (van Campen et al. [23], Peeters et al. [24, 25]). In contrast, methods where a constraint is imposed on the homogenized parameters can be called “indirect control methods” since the constraint only restricts the curvature of the fiber angles indirectly through an implicit relation between them and the homogenized properties (see de Quadros and Hernandez [26] for a recent example). The drawback of the indirect method is that in general it cannot guarantee a priori the satisfaction of the local fiber path curvature constraint.

In the present work, an indirect control method based on lamination parameters is developed and implemented in the context of the first step of a multi-step method. The approach consists on imposing an upper bound on the spatial gradient of the lamination parameters, which indirectly imposes a constraint on the fiber path curvature that is retrieved in subsequent steps of the multistep method (Ijsselmuiden [27]). Separately, the direct control method of Peeters et al. [24] is implemented in the retrieval step of the multi-step approach as a reference. The direct method guarantees that the local curvature constraint is satisfied in each layer of a laminate. Finally, an enhanced design strategy, termed the hybrid control method, is proposed as a combination of the two aforementioned control methods. The three methods (direct, indirect and hybrid) are tested with compliance minimization problems and a comparative analysis is carried out to assess their performance. For simplicity, the formulation in the present work is restricted to planar composite laminates (plates) but the general strategy can be extended to a three-dimensional context (thin shells).

The structure of this work is as follows: the formulation of the optimization problem is described in Section 3.2 and the curvature constraint on lamination parameters for manufacturable design is introduced in Section 3.3. The three aforementioned methods to control the steering of the fiber path are presented in Section 3.4. In Section 3.5, a basic verification problem, namely a rectangular plate with a point load, is used to assess the numerical performance of the methods. A comparative analysis of the three different methods to apply curvature constraints is shown in Section 3.6. A more complex numerical test, namely a square plate with a circular hole, is included in Section 3.7 in order to further assess the performance of the methods under more challenging conditions. Finally, concluding remarks are given in Section 3.8.

## 3.2. FORMULATION OF THE OPTIMIZATION PROBLEM

### 3.2.1. LAMINATION PARAMETERS

The current work focuses on the compliance optimization of planar structures (plate laminates), which are described by the in-plane stiffness. One commonly-used way to homogenize the through-the-thickness stiffness properties of a composite laminate is by using Lamination Parameters (LPs, [28]). The in-plane stiffness  $A$  is parameterized using four lamination parameters ( $V_1, V_2, V_3, V_4$ ) as follows

$$A = h(\Gamma_0 + V_1\Gamma_1 + V_2\Gamma_2 + V_3\Gamma_3 + V_4\Gamma_4), \quad (3.1)$$

where  $h$  is the thickness of the laminate, and the lamination parameters are obtained by

$$(V_1, V_2, V_3, V_4) = \int_{-\frac{1}{2}}^{\frac{1}{2}} (\cos 2\theta(\bar{z}), \sin 2\theta(\bar{z}), \cos 4\theta(\bar{z}), \sin 4\theta(\bar{z})) d\bar{z}. \quad (3.2)$$

In Eq.(3.2),  $\bar{z} = z/h$  is the normalized position in the thickness direction and  $\theta(\bar{z})$  is the in-plane fiber angle at  $\bar{z}$ . The detailed expressions for the five constant matrices ( $\Gamma_0, \Gamma_1, \Gamma_2, \Gamma_3, \Gamma_4$ ) appearing in Eq.(3.1) can be found in, for example, Abdalla et al. [9]. The stiffness matrix can be expressed as a function of the lamination parameters and the thickness of the layers. Assuming that the thickness is given (e.g., constant thickness throughout the plate), then the four lamination parameters at each point may be used as the design variables for a VSL. Consistent with Eq.(3.2), the lamination parameters are confined within a feasible convex domain, which is given by (Hammer et al. [29])

$$2V_1^2(1 - V_3) + 2V_2^2(1 + V_3) + V_3^2 + V_4^2 - 4V_1V_2V_4 \leq 1, \quad (3.3a)$$

$$V_1^2 + V_2^2 \leq 1, \quad (3.3b)$$

$$-1 \leq V_3 \leq 1. \quad (3.3c)$$

For a symmetric and balanced laminate,  $V_2$  and  $V_4$  are zero, which implies that the feasible domain simplifies to (Nagy [30])

$$2V_1^2 - V_3 - 1 \leq 0, \quad (3.4a)$$

$$V_3 - 1 \leq 0. \quad (3.4b)$$

For simplicity, the design space is henceforth limited to symmetric and balanced laminates, however the design strategy may be extended to a more general case.

### 3.2.2. THREE-STEP OPTIMIZATION FOR VARIABLE STIFFNESS COMPOSITE

A multistep approach to VSL optimization, which has proven to be very versatile, is the three-step optimization method presented in IJsselmuiden [27]. The steps, and their connection to the manufacturing constraints, are as follows:

- Step 1 Optimize a chosen objective functional, such as compliance or buckling, with the lamination parameters as design variables. Typically, the objective functional expressed in terms of the lamination parameters is convex (IJsselmuiden et al. [12],

Khani et al. [31], Peeters et al. [32]), which enables the use of efficient optimization algorithms to find a global optimum. This is the primary optimization step. However, since the actual fiber angles/paths are not immediately available from the optimal lamination parameters, manufacturability cannot be guaranteed in this step.

- Step 2 Determine the fiber angles of each ply (layer) in a specific number of plies that closely match the optimal lamination parameters obtained in Step 1. This step, referred to as the angle retrieval step in the present work, is formally an inverse problem with an objective functional meant to minimize the difference between the optimal homogenized properties from Step 1 and the actual homogenized properties corresponding to a finite number of plies. Alternatively, it can be implemented to optimize the objective functional in Step 1 with respect to the fiber angles to approach the optimal solution obtained in Step 1. This is referred to as angle optimization (see Peeters et al. [32]). Manufacturing constraints can be added in this step (see Peeters et al. [24]) with an additional loss in performance compared to unconstrained properties.
- Step 3 Construct the actual fiber paths using the optimal fiber angles obtained in Step 2. This is essentially a post processing step that uses methods similar to those employed to construct streamlines in computational fluid mechanics (Blom et al. [33]). The final design to be manufactured by AFP is obtained after this step. In this step it is typically not required to impose a curvature constraint since this has already been enforced in the previous steps. Correspondingly, emphasis is placed on the first two steps of the method.

### 3.2.3. COMPLIANCE APPROXIMATION OF 2D COMPOSITE PLATES

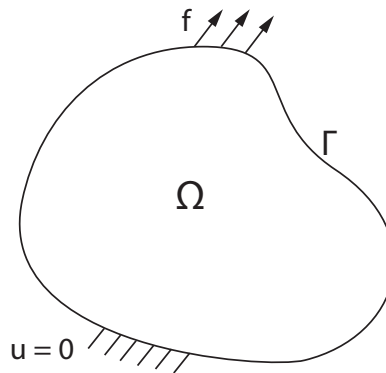


Figure 3.1: Example of a two-dimensional plate.

The compliance approximation applied in this work is presented in this section. For a general 2D plate with design domain  $\Omega$ , and boundary  $\Gamma$ , as shown in Figure 3.1, three equations need to be satisfied in a balanced state:



1. equilibrium:  $\sum_{i=1}^2 \frac{\partial \mathfrak{N}_{ij}}{\partial \mathfrak{x}_i} + f_j = 0$ , for  $j = 1, 2$
2. strain-displacement:  $\epsilon_{ij} = \frac{1}{2} \left( \frac{\partial u_i}{\partial \mathfrak{x}_j} + \frac{\partial u_j}{\partial \mathfrak{x}_i} \right)$ , for  $i, j = 1, 2$
3. material law:  $\mathfrak{N}_{ij} = A_{ij\ell l} \cdot \epsilon_{\ell l}$ , for  $i, j, \ell, l = 1, 2$ ,

where  $f_j$  is the external force in  $j$ -direction, the signal  $\mathfrak{N}_{i,j}$  is the internal force in the structure,  $u$  denotes the displacement,  $\epsilon$  refers to the associated strain,  $\mathfrak{x}$  is the in-plane coordinate in the design domain and  $A$  is the elastic in-plane stiffness matrix.

The compliance of a plate equals the minimum of complementary energy of the structure. Using the material law, the density of complementary energy  $u^*$  can be rewritten as

$$u^* = \frac{1}{2} \mathfrak{N}^T A^{-1} \mathfrak{N}, \quad (3.5)$$

where  $\mathfrak{N}$  is the vector for the internal force. The minimal compliance  $C^*(A)$  can be written as:

$$C^*(A) = \min_A \min_{\mathfrak{N}} \int_{\Omega} u^*(\mathfrak{N}, A) d\Omega. \quad (3.6)$$

Using the matrix contraction  $(:)$ , the approximation of the compliance  $f^{(l)}(A)$  is rewritten to

$$f^{(l)}(A) = \frac{1}{2} \int_{\Omega} (\mathfrak{N} \cdot \mathfrak{N}^T) : A^{-1} d\Omega = \int_{\Omega} \Phi : A^{-1} d\Omega, \quad (3.7)$$

where  $\Phi$  is the coefficient matrix with respect to  $A^{-1}$ . Observing the structure of this equation, the following approximation may be used in the finite element method (FEM):

$$f^{(l)}(A) \approx \sum_{e=1}^m \Phi_e : A_e^{-1}, \quad (3.8)$$

where  $e$  denotes the element number and  $m$  denotes the total number of elements. Using this equation, the expression for  $\Phi_e$  is found as

$$\Phi_e = \mathfrak{N}_e \cdot \mathfrak{N}_e^T \cdot \Omega_e, \quad (3.9)$$

where  $\Omega_e$  denotes the area of element  $e$ .

However, the design variables chosen in our case are not at the elements, but at the design nodes. Simply using

$$f^{(l)}(A) \approx \sum_{i=1}^n \Phi_i : A_i^{-1}, \quad (3.10)$$

where  $n$  denotes the total number of design nodes in the finite element model of the plate,  $A_i$  is the in-plane stiffness matrix at the  $i^{\text{th}}$  design node and defining  $\Phi_i$  as

$$\Phi_i = \mathfrak{N}_i \cdot \mathfrak{N}_i^T \cdot \Omega_i \quad (3.11)$$

does not work well: the forces at the nodes are a function of multiple elements. Hence, finding an appropriate expression for  $\Phi_i$  from the continuous model Eq. (3.7) is not straightforward. To implement the calculation with FEM easily, the derivation of an approximation will be done for a discretised plate below.

The strain energy of the plate  $U$  is defined as

$$U = \int_{\Omega} \frac{1}{2} \boldsymbol{\epsilon}^T \mathbf{A} \boldsymbol{\epsilon} d\Omega. \quad (3.12)$$

Discretising the plate to be used in the finite element method, the strain energy of the plate can be expressed as a summation at every Gauss point using the Gauss integration scheme.

Thus the strain energy can be obtained,

$$U = \frac{1}{2} \sum_{g=1}^{n_g} w_g \boldsymbol{\epsilon}_g^T \mathbf{A}_g \boldsymbol{\epsilon}_g, \quad (3.13)$$

where  $w_g$  is the weight coefficient times the determinate of Jacobian matrix of Gauss point  $g$ . The subscript  $g$  denotes the variables at the Gauss point,  $n_g$  is the total number of Gauss points in the structure. The total potential energy of the plate  $\Pi$  is

$$\Pi = U - \mathbf{f}^T \mathbf{u}. \quad (3.14)$$

The principle of total potential energy leads to

$$\begin{aligned} \min_{\boldsymbol{\epsilon}_g, \mathbf{u}} \quad & \Pi \\ \text{s.t.} \quad & \boldsymbol{\epsilon}_g - \mathbf{B}_g \mathbf{u} = \mathbf{0}, \end{aligned}$$

where  $\mathbf{B}_g$  is the strain-displacement matrix at the Gauss point. The Lagrangian is found to be

$$\mathcal{L} = \min_{\boldsymbol{\epsilon}_g, \mathbf{u}} \left( \frac{1}{2} \sum_{g=1}^{n_g} w_g \boldsymbol{\epsilon}_g^T \mathbf{A}_g \boldsymbol{\epsilon}_g - \mathbf{f}^T \mathbf{u} \right) + \max_{\lambda} \left( \sum_{g=1}^{n_g} \lambda_g^T (\boldsymbol{\epsilon}_g - \mathbf{B}_g \mathbf{u}) \right), \quad (3.15)$$

where  $\lambda$  is the Lagrangian multiplier. The optimality condition with respect to  $\boldsymbol{\epsilon}_g$  gives

$$\lambda_g = w_g \mathbf{A}_g \boldsymbol{\epsilon}_g.$$

Hence,

$$\lambda_g = w_g \mathfrak{N}_g, \quad (3.16)$$

where  $\mathfrak{N}_g$  is the stress resultant vector at Gauss point  $g$ . Substituting Eq. (3.16) into the Lagrangian Eq. (3.15), and replacing  $\boldsymbol{\epsilon}_g$  with  $\mathbf{A}_g^{-1} \mathfrak{N}_g$ , Eq. (3.15) is rewritten as

$$\mathcal{L} = \min_{\mathbf{u}} \max_{\mathfrak{N}_g} \left( \sum_{g=1}^{n_g} \left( \frac{1}{2} w_g \mathfrak{N}_g^T \mathbf{A}_g^{-1} \mathfrak{N}_g - w_g \mathfrak{N}_g^T \mathbf{A}_g^{-1} \mathfrak{N}_g \right) + \mathbf{u}^T \left( \sum_{g=1}^{n_g} w_g \mathbf{B}_g^T \mathfrak{N}_g - \mathbf{f} \right) \right). \quad (3.17)$$

Inverting the order of min and max leads to

$$\mathcal{L} = \max_{\mathfrak{N}_g} \min_{\mathbf{u}} \left( \sum_{g=1}^{n_g} \left( \frac{1}{2} w_g \mathfrak{N}_g^T \mathbf{A}_g^{-1} \mathfrak{N}_g - w_g \mathfrak{N}_g^T \mathbf{A}_g^{-1} \mathfrak{N}_g \right) + \mathbf{u}^T \left( \sum_{g=1}^{n_g} w_g \mathbf{B}_g^T \mathfrak{N}_g - \mathbf{f} \right) \right). \quad (3.18)$$

Rearranging terms leads to

$$\mathcal{L} = \max_{\mathfrak{N}_g} \left( \sum_{g=1}^{n_g} \left( -\frac{1}{2} w_g \mathfrak{N}_g^T A_g^{-1} \mathfrak{N}_g \right) + \min_{\mathbf{u}} \mathbf{u}^T \left( \sum_{g=1}^{n_g} w_g B_g^T \mathfrak{N}_g - \mathbf{f} \right) \right). \quad (3.19)$$

Thus the optimisation problem can be written as

$$\begin{aligned} \min_{\mathfrak{N}_g} \quad & \sum_{g=1}^{n_g} \frac{1}{2} w_g \mathfrak{N}_g^T A_g^{-1} \mathfrak{N}_g \\ \text{s.t.} \quad & \sum_{g=1}^{n_g} w_g B_g^T \mathfrak{N}_g - \mathbf{f} = 0. \end{aligned} \quad (3.20)$$

where the objective of this optimisation problem is the complementary energy of the structure  $U^*$ :

$$U^* = \sum_{g=1}^{n_g} \frac{1}{2} w_g \mathfrak{N}_g^T A_g^{-1} \mathfrak{N}_g. \quad (3.21)$$

By definition, the compliance of the plate  $C(A)$  can be written as

$$C(A) = \min_{\mathfrak{N}_g} U^*, \quad (3.22)$$

where  $A$  is the constitutive matrix of each Gauss point. The interpolation for  $A_g$  is defined to be reciprocal as

$$A_g^{-1} = \sum_{i=1}^n N_{i,g} A_i^{-1}, \quad (3.23)$$

where  $N_{i,g}$  is the shape function of design node  $i$  at the  $g^{\text{th}}$  Gauss point in the FEM. Using Eq. (3.23), the complementary energy of the plate is

$$U^* = \sum_{g=1}^{n_g} \frac{1}{2} w_g \mathfrak{N}_g^T \left( \sum_{i=1}^n N_{i,g} A_i^{-1} \right) \mathfrak{N}_g. \quad (3.24)$$

By changing the order of summation and employing the Frobenius product, this is rewritten to

$$U^* = \sum_{i=1}^n \left( \sum_{g=1}^{n_g} \frac{1}{2} w_g \mathfrak{N}_g^T \cdot N_{i,g} \cdot \mathfrak{N}_g \right) : A_i^{-1}. \quad (3.25)$$

The minimization of the compliance  $C_{\min}$  is formulated as

$$C_{\min}(A) = \min_A \left( \min_{\mathfrak{N}_g} U^* \right), \quad (3.26)$$

where  $A$  is the constitutive matrix of each design node.

Based on Eq. (3.25), the approximation of compliance of a plate in discrete form is

$$f^{(I)}(A) = \sum_{i=1}^n \left( \sum_{g=1}^{n_g} \frac{1}{2} w_g \mathfrak{N}_g^{(k)T} \cdot N_{i,g} \cdot \mathfrak{N}_g^{(k)} \right) : A_i^{-1}, \quad (3.27)$$

where  $\mathfrak{N}_g^{(k)}$  is the internal force that is both statically and kinematically admissible at the  $k^{\text{th}}$  approximation point, when this is iteration  $k + 1$ . Comparing this approximation to the one found starting from the continuous formula, Eq. (3.10), it can be seen that the form is exactly the same. Hence, the correct expression for  $\Phi_i$  is

$$\Phi_i = \sum_{g=1}^{n_g} \frac{1}{2} w_g \mathfrak{N}_g \cdot N_{i,g} \cdot \mathfrak{N}_g^T. \quad (3.28)$$

### 3.2.4. TWO-LEVEL APPROXIMATION FOR THE VSL

The objective functionals of the optimization problems in Step 1 (primary performance objective such as structural compliance) and Step 2 (objective functional for error minimization) can be both formally expressed using the same approach based on a two-level approximation. Correspondingly, a common general form of the two-level approximation for the VSL is introduced in this section in anticipation of the optimization strategy. Since the problem is solved numerically using a finite element discretization, it is also convenient to introduce a discretized version of the two-level approximation for VSLs. To this end, consider a finite element discretization of a laminate which is characterized by a collection of nodes associated to the finite elements.

The first level approximation  $f^{(I)}$  for an objective function  $f$  (for either Step 1 or 2) with respect to the in-plane global stiffness  $A$  is expressed as

$$f^{(I)}(A_1, A_2, \dots, A_n) = \sum_{i=1}^n \Phi_i : A_i^{-1} + \sum_{i=1}^n \Psi_i : A_i, \quad (3.29)$$

where  $\Phi_i$  and  $\Psi_i$  are  $3 \times 3$  coefficient matrices of the objective functional and  $:$  denotes the Frobenius product (inner product). The in-plane stiffness depends on the laminate layout (e.g. material elastic properties, number of layers, thicknesses, orientation), all or some of which can be viewed as design variables. In the present work, attention is focused on the fiber orientations as design variables for fixed thickness and elastic properties. Symbolically, all the necessary data required to specify a given design can be collected in a vector  $\mathbf{x}$ , the so-called design variable, and the in-plane stiffness at every node  $i$  can be expressed as a function of the design, i.e.,  $A_i = A_i(\mathbf{x})$ . Similarly, an objective functional  $f$  can also be viewed as a function of the design variable  $\mathbf{x}$ , i.e.,  $f = f(\mathbf{x})$ .

For the second level approximation  $f^{(II)}$ , the first level approximation  $f^{(I)}$ , viewed as a function of the design variable  $\mathbf{x}$ , is expanded about a design point  $\mathbf{x}_0$  using a Taylor series expansion with respect to  $\mathbf{x}$  up to the second-order, i.e.,

$$f^{(II)}(\mathbf{x}) = f^{(I)}(\mathbf{x}_0) + \mathbf{g}_{|\mathbf{x}_0}^T \cdot \Delta \mathbf{x} + \frac{1}{2} \Delta \mathbf{x}^T \cdot H_{|\mathbf{x}_0} \cdot \Delta \mathbf{x}, \quad (3.30)$$

where  $f^{(I)}(\mathbf{x}_0) = f^{(I)}(A_1(\mathbf{x}_0), \dots, A_n(\mathbf{x}_0))$  is the value of first level approximation  $f^{(I)}$  at  $\mathbf{x}_0$ . In the previous equation, the vector  $\mathbf{g}_{|\mathbf{x}_0}$  is the gradient of  $f^{(I)}$  with respect to  $\mathbf{x}$  evaluated at  $\mathbf{x}_0$ ,  $H_{|\mathbf{x}_0}$  is the Gauss-Newton part of the Hessian matrix at  $\mathbf{x}_0$  to ensure the positive semi-definiteness of the approximation,  $\Delta \mathbf{x} = \mathbf{x} - \mathbf{x}_0$ , the superscript  $T$  indicates the

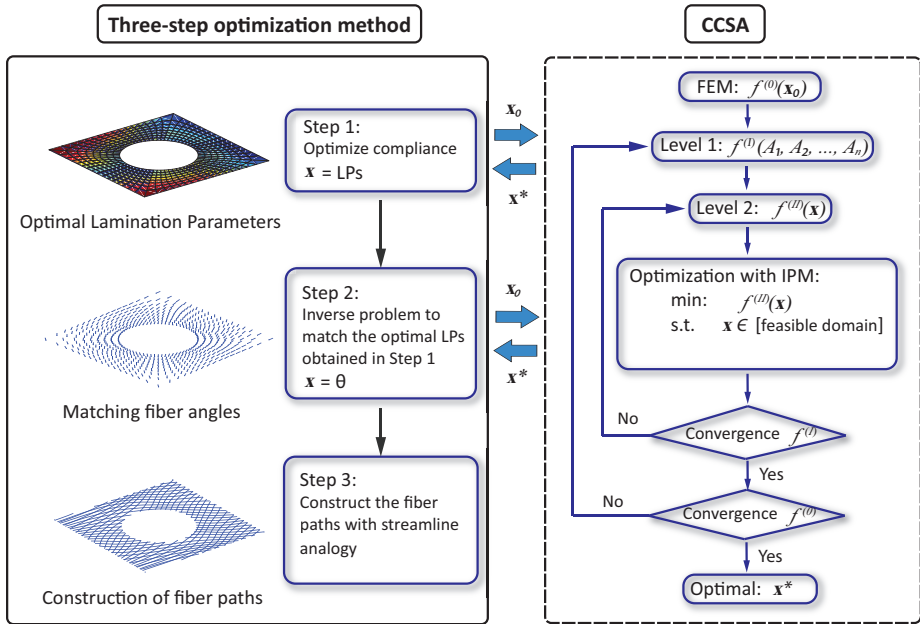


Figure 3.2: Three-step optimization framework: both Step 1 (e.g., minimization of structural compliance) and Step 2 (matching parameters) are solved using the same method, namely the conservative convex separable approximations (CCSA) with Mehrotra’s predictor-corrector interior point method (IPM). The third step (construction of fibers paths) is solved using a streamline analogy.

transpose and the single dot indicates composition. More details can be found in Peeters et al. [24].

### 3.2.5. OPTIMIZATION STRATEGY

The strategy regarding Step 1 and Step 2 of the three-step method is as follows: the overall framework employed to solve the optimization problem is Svanberg’s conservative convex separable approximations (CCSA, Svanberg [34]). The approach is illustrated in Figure 3.2, which shows the sub-problems used in the iterative method. Mehrotra’s interior point method (IPM) is used in combination with the Karush-Kuhn-Tucker (KKT) conditions of the sub-problems (Mehrotra [35]). Details of these methods can be found in the above mentioned references. The element used in the FEM model in Step 1 of the optimization is an 8-noded serendipity element (Kikuchi et al. [36]), where the lamination parameters are defined on the vertices. In the remainder of the text, the nodal value correlated to the design variables refers to the value at the vertices. Since Step 2 does not require FEM for analysis, the discretization is carried out using triangular elements (see e.g., Felippa [37]). Formally, the sub-problem to be solved in both Step 1 and Step 2 is as

follows:

$$\min_{\mathbf{x}} f^{(II)}(\mathbf{x}) \quad (3.31a)$$

$$\text{subject to } \mathbf{x} \in \text{Feasible domain.} \quad (3.31b)$$

For Step 1, for the minimum compliance problem using symmetric and balanced laminates, the design variables are collected in a vector  $\mathbf{x} = [\mathbf{V}_1; \mathbf{V}_3]$ , where the local values of the lamination parameters  $V_1$  and  $V_3$  at a node  $i$  are collected in the vectors  $\mathbf{V}_1$  and  $\mathbf{V}_3$ , i.e.,  $\mathbf{V}_1 = [V_{1,1}, V_{1,2}, \dots, V_{1,n}]$  and  $\mathbf{V}_3 = [V_{3,1}, V_{3,2}, \dots, V_{3,n}]$ . The global feasible domain for  $\mathbf{x}$  is defined upon applying Eq.(3.4) at each node  $i$ . The objective  $f^{(II)}(\mathbf{x})$  in Step 1 is the second level approximation of the compliance. Further details can also be found in Peeters et al. [32].

For Step 2, the objective functional is formulated in accordance with an inverse problem to retrieve the fiber angles. The corresponding first level approximation is computed from Eq.(3.29) using  $\Phi_i = A_i^*$  and  $\Psi_i = (A_i^*)^{-1}$ , and  $A_i^*$  is the optimal in-plane stiffness at node  $i$  obtained during Step 1. In this step, the design variable  $\mathbf{x}$  represents the fiber angles at layer  $l$  associated to node  $i$ , i.e.,  $\mathbf{x} = [\theta_l^{(i)}]_{(i=1, \dots, n)(l=1, \dots, n_d)}$ , where  $n_d$  is the number of design layers. Since the final laminate is to be symmetric and balanced, each design layer represents four layers in the actual laminate: a negative of the design layer is right next to the layer, and the complete stack is symmetric. For example, if two design layers are expressed as  $[\theta_1/\theta_2]$ , the actual physical laminate is  $[\theta_1 / -\theta_1 / \theta_2 / -\theta_2]_s$ , with the subscript  $s$  indicating symmetry. Therefore, the number of design layers  $n_d$  is a quarter of the total layers  $n_l$ . The feasible domain for each fiber angle at each location is  $[-\pi, \pi]$ . The objective function  $f^{(II)}(\mathbf{x})$  for the sub-problem in Step 2 is the second level approximation of the error between the optimized properties from Step 1 and the actual properties of a finite number of layers. For implementation purposes, the vector  $\mathbf{x}$  in Step 2 (and also in Step 1) can be vectorized with a single index.

Additional manufacturing constraints, which affect the actual feasible domain, will be specified in more detail in Section 3.4.2. Details about the streamline analogy in Step 3, which pertains to the continuous fiber paths, can be found in Blom et al. [33] and will not be discussed here. In the next section, gradient constraints on the lamination parameters, which aim to indirectly impose a curvature constraint, will be described.

### 3.3. CURVATURE CONSTRAINT IN TERMS OF THE LAMINATION PARAMETERS

#### 3.3.1. RELATIONSHIP BETWEEN CURVATURE CONSTRAINTS AND GRADIENT CONSTRAINT ON THE LAMINATION PARAMETERS

The curvature of a fiber path in the  $l^{\text{th}}$  layer of a VSL can be expressed in terms of the norm of the gradient of the corresponding fiber angle, i.e.,  $\|\nabla\theta_l(x, y)\|$ , where  $\nabla$  is the gradient with respect to the in-plane coordinates  $x$  and  $y$  on the surface of the model. In

order to control the minimum turning radius in the  $l^{\text{th}}$  layer of a VSL, the direct implementation of the curvature constraints on the fiber angles is as follows:

$$\|\nabla\theta_l(x, y)\| \leq \frac{1}{r_{\min}}, \quad l = 1, \dots, n_d, \quad \forall x, y \quad (3.32)$$

where  $r_{\min}$  is the minimum allowable turning radius. However, this constraint requires a layer-by-layer approach, which is computationally expensive for complex structures with a relatively large number of layers. Alternatively, one can implement the gradient constraints on the lamination parameters to implicitly constrain the gradient of the fiber angle. One way to achieve this is to link the constraints on the lamination parameters with that on the fiber angles through the chain rule. Consider for example the lamination parameter  $V_1$ , which in view of Eq.(3.2) can be expressed as

$$V_1(x, y) = \sum_{l=1}^{n_l} \cos(2\theta_l(x, y)) \bar{h}_l, \quad (3.33)$$

where  $\bar{h}_l = \bar{z}_{(l+1)} - \bar{z}_l$  is the normalized thickness of the  $l^{\text{th}}$  layer. From this relation, the gradient of  $V_1(x, y)$  can be obtained as

$$\nabla V_1(x, y) = -2 \sum_{l=1}^{n_l} \sin(2\theta_l(x, y)) \nabla\theta_l(x, y) \bar{h}_l. \quad (3.34)$$

Taking the norm of the vectors in Eq.(3.34) and using the Cauchy-Schwarz inequality, it follows that

$$\|\nabla V_1(x, y)\| \leq 2 \sum_{l=1}^{n_l} |\sin(2\theta_l(x, y))| \|\nabla\theta_l(x, y)\| \bar{h}_l. \quad (3.35)$$

Inequality (3.35) indicates that  $\|\nabla V_1(x, y)\|$  can act as a lower bound for the sum of  $\|\nabla\theta_l(x, y)\|$ . To directly control the curvature in each layer, an upper bound needs to be imposed on  $\|\nabla\theta_l(x, y)\|$  as indicated in Eq.(3.32). However, a method to indirectly control the minimum turning radius is to impose a sufficiently stringent constraint on the sum of  $\|\nabla\theta_l(x, y)\|$  in order to limit the layer-wise contributions to the sum. To avoid using explicitly a parametrization that requires the fiber angles during this step, an upper bound constraint is imposed on  $\|\nabla V_1(x, y)\|$ . To this end, the condition Eq.(3.32) can be used in Eq.(3.35), i.e.,

$$\|\nabla V_1(x, y)\| \leq 2 \sum_{l=1}^{n_l} |\sin(2\theta_l(x, y))| \frac{\bar{h}_l}{r_{\min}}. \quad (3.36)$$

Since

$$|\sin(2\theta_l(x, y))| \leq 1, \quad (3.37)$$

an artificially stringent upper bound on  $\|\nabla V_1(x, y)\|$  can be imposed with the purpose of constraining  $\|\nabla\theta_l(x, y)\|$  as follows:

$$\|\nabla V_1(x, y)\| \leq 2\sqrt{\delta} \frac{\bar{h}}{r_{\min}}, \quad (3.38)$$

where  $\bar{h} = \sum_{l=1}^{n_l} \bar{h}_l = 1$  and  $\delta > 0$  being an adjustable parameter, called the upper bound factor. The upper bound factor  $\delta$  is a scalar to smear the effect of  $|\sin(2\theta_l(x, y))|$  in each layer in Eq.(3.36) into one parameter. The parameter  $\delta$  is chosen such that it allows to indirectly impose an upper bound on  $\|\nabla\theta_l(x, y)\|$  at all points and all layers through a bound on the gradient of the lamination parameters.

The same upper bound factor  $\delta$  is used for  $\|\nabla V_3(x, y)\|$  to simulate the effect of  $|\sin(4\theta_l(x, y))|$  in each layer. Correspondingly, the following constraint is imposed on the gradient of  $V_3(x, y)$  (with  $\bar{h} = 1$ )

$$\|\nabla V_3(x, y)\| \leq 4\sqrt{\delta} \frac{\bar{h}}{r_{\min}}. \quad (3.39)$$

In general, it is not possible to choose a priori a value of  $\delta$  such that Eq.(3.32) is automatically satisfied during Step 1. However, a suitable value of  $\delta$  can be identified a posteriori as shown in A.1. A discussion on the choice of  $\delta$  will be provided in the sequel but for the foregoing analysis it is sufficient to remark that it is feasible to find a suitable value.

### 3.3.2. NUMERICAL IMPLEMENTATION OF GRADIENT CONSTRAINTS ON THE LAMINATION PARAMETERS

As indicated in the previous section, the indirect control of the steering of the fiber path in Step 1 of the three-step optimization method requires the gradients of the lamination parameters (i.e.,  $\nabla V_1(x, y)$  and  $\nabla V_3(x, y)$ ). In the present implementation, a four-noded quadrilateral element with four Gauss points is used. For subsequent use, the basic notation and interpolations are recorded here. In particular, the value of the lamination parameters  $V_\alpha$ ,  $\alpha = 1, 3$ , at a Gauss point  $g$  is calculated by

$$V_{\alpha,g} = \sum_{i=1}^4 N_{i,g} V_{\alpha,i}, \quad (3.40)$$

where  $N_{i,g}$  is the shape function of the  $i^{\text{th}}$  node evaluated at Gauss point  $g$ , and  $V_{\alpha,i}$  is the value of  $V_\alpha$  at the  $i^{\text{th}}$  node. Consequently, the gradient of  $V_\alpha$  at Gauss point  $g$  is calculated by

$$\nabla V_{\alpha,g} = \sum_{i=1}^4 \nabla N_{i,g} V_{\alpha,i}, \quad (3.41)$$

where  $\nabla N_{i,g} = [\frac{\partial N_{i,g}}{\partial x}, \frac{\partial N_{i,g}}{\partial y}]^T$ . Finally, the calculation of the norm of the gradient at each Gauss point in an element is given by

$$\|\nabla V_\alpha\|^2 = \frac{\sum_{g=1}^4 w_g \|\nabla V_{\alpha,g}\|^2}{\sum_{g=1}^4 w_g}, \quad (3.42)$$

where  $w_g = \det J$  is the determinant of the Jacobian matrix  $J$  of the mapping between the physical domain and the master element at the  $g^{\text{th}}$  Gauss point. The constraints



Eqs.(3.38) and (3.39) are imposed element-wise using Eq.(3.42) with the corresponding bound. Three different methods to apply curvature constraints will be described in the next section.

### 3.4. METHODS TO APPLY CURVATURE CONSTRAINTS

The curvature constraint has been implemented in previous works directly in Step 2 in an element-wise fashion in the form of steering constraints (see e.g., van Campen et al. [23], Peeters et al. [24, 25]). This approach will be henceforth called the *direct control method*. The method has the advantage to guarantee that the curvature constraint is satisfied locally at each point of each layer in a VSL composite plate. However, since the constraint is imposed during the angle retrieval step (Step 2 of the three-step method), it is uncoupled from the primary objective functional of the first step. Consequently, one drawback of this approach is that it may lead to a significant loss in performance between Step 1 and Step 2 in terms of the primary objective functional.

To address this loss in performance using the direct control method, two new strategies to apply the curvature constraints are proposed in this section. The first strategy is called the *indirect control method*, where the gradient constraints are imposed on the lamination parameters in Step 1 only. The second strategy, referred to as the *hybrid control method*, combines the use of the gradient constraints on the lamination parameters in Step 1 and the steering constraints on the fiber angles in Step 2.

#### 3.4.1. GENERAL THREE-STEP FRAMEWORK WITH CURVATURE CONSTRAINTS

Formally, the three methods (direct, indirect and hybrid) may be expressed in a general three-step framework with curvature constraints. Each method corresponds to a distinct and characteristic set of parameters. In this framework, the Step 1 corresponds to the primary objective functional, with or without gradient constraints on the lamination parameters depending on the method. For definiteness, the primary objective in Step 1 is chosen as the compliance  $C$  of a VSL, normalized by a referential compliance  $C_0$  that may correspond to an initial or a benchmark design. In principle the methods used here may be applied to other types of objective functionals as long as they are parametrized with lamination parameters as design variables. In Step 2 (angle retrieval step) the objective function  $D$  represents the sum over all nodes  $i$  of the difference between the optimal stiffness matrix  $A_i^*$  obtained in Step 1 and the stiffness matrix  $A_i$  for a VSL with a finite number of layers and a given set of fiber angles at the same node  $i$ , i.e.,

$$D = \sum_{i=1}^n A_i^* : A_i^{-1} + \sum_{i=1}^n (A_i^*)^{-1} : A_i . \quad (3.43)$$

The optimization problem in Step 2 is to minimize  $D$  with respect to the fiber angles on each layer and for all nodes with or without steering constraints. If the steering constraints are taken into account, these may be imposed locally in each element and each design layer as  $\zeta_{e,l}^2 \leq \zeta_{\max}^2$ , where the value of  $\zeta_{e,l}$  is the fiber path curvature in the  $e^{\text{th}}$  element and the  $l^{\text{th}}$  design layer, and  $\zeta_{\max} = 1/r_{\min}$  being the upper bound based on the

minimum turning radius  $r_{\min}$  of the AFP (more details can be found in Peeters et al. [24]). Hence, for all methods, Step 1 and 2 are formally expressed as follows:

1. The minimum compliance problem (primary optimization problem) is expressed as

$$\min_{\mathbf{V}_1, \mathbf{V}_3} C(\mathbf{V}_1, \mathbf{V}_3)/C_0 \quad (3.44)$$

$$\text{subject to } 2V_{1,i}^2 - V_{3,i} - 1 \leq 0 \quad (3.45)$$

$$V_{3,i} - 1 \leq 0 \quad i = 1 \dots n \quad (3.46)$$

$$\|(\nabla \mathbf{V}_1)^e\|^2 \leq \delta (2/r_{\min})^2 \quad (3.47)$$

$$\|(\nabla \mathbf{V}_3)^e\|^2 \leq \delta (4/r_{\min})^2 \quad e = 1 \dots m \quad (3.48)$$

2. The angle retrieval step

$$\min_{\theta_l^{(i)}} D(\theta_l^{(i)}) \quad (3.49)$$

$$\text{subject to } \theta_l^{(i)} \in [-\pi, \pi] \quad i = 1 \dots n \quad (3.50)$$

$$\zeta_{e,l}^2 \leq \zeta_{\max}^2 \quad e = 1 \dots m, \quad l = 1 \dots n_d \quad (3.51)$$

The distinction between the methods is through the choice of the key parameters  $\delta$  and  $\zeta_{\max}$  as indicated below. In order to distinguish the different types of constraints, the term “gradient constraint” is primarily used for a gradient constraint on the lamination parameters in Step 1, the term “steering constraint” refers to a constraint on the gradient of the fiber angles per layer in Step 2 and the expression “curvature constraint” is used interchangeably for both types of constraints.

### 3.4.2. DIRECT CONTROL METHOD

In Step 1 of the direct control method, the normalized compliance  $C/C_0$  is minimized with respect to the lamination parameters without constraints on their local gradients. However, rather than suppressing the constraints, it is formally equivalent to relax the gradient constraints on the lamination parameters by setting  $\delta \rightarrow \infty$  so that they will not be active, hence the direct control method is characterized by a sufficiently large value of  $\delta$ . This approach has the advantage of employing the same code as other strategies at an acceptable computational cost since the constraints do not become active. In Step 2 (angle retrieval step) the objective function  $D$  as given in Eq.(3.43) is minimized with the parameter  $\zeta_{\max} = 1/r_{\min}$  chosen as an upper bound on the steering constraints, i.e., based on the actual minimum turning radius  $r_{\min}$ .

### 3.4.3. INDIRECT CONTROL METHOD

In the proposed indirect control method, the normalized compliance  $C/C_0$  is minimized in Step 1 with respect to the lamination parameters with constraints on their local gra-

Table 3.1: Parameters for three different manufacturing constraint schemes

Method	Gradient constraints in Step 1	Steering constraints in Step 2
Direct control	$\delta \rightarrow \infty$	$\zeta_{\max} = 1/r_{\min}$
Indirect control	$\delta \in [0, \delta^*]$	$\zeta_{\max} \rightarrow \infty$
Hybrid control	$\delta \in (\delta^*, \infty)$	$\zeta_{\max} = 1/r_{\min}$

dients. In this case, it is not possible to guarantee a priori that the actual fiber path curvature  $\zeta$  remains below a critical value  $\zeta_{\max}$  (or, equivalently, that the radius of curvature  $r$  remains above a critical value  $r_{\min}$ ). Hence, it is necessary to choose a stringent upper bound factor  $\delta \in [0, \delta^*]$  where the limit value  $\delta^*$  is the largest upper bound that indirectly restricts the curvatures for a manufacturable design in Step 1 without steering constraints in Step 2. This value  $\delta^*$  is not known a priori hence the actual upper bound factor  $\delta$  used requires calibration. In Step 2, the angle retrieval step, the difference  $D$  is minimized without a steering constraint, which formally can be seen as taking a sufficiently large upper bound  $\zeta_{\max} \rightarrow \infty$ . In this case, the steering constraints in Step 2 are not active.

### 3.4.4. HYBRID CONTROL METHOD

The proposed hybrid control method consists of minimizing the normalized compliance  $C/C_0$  of the VSL using the gradient constraints on the lamination parameters in Step 1 but with a relaxed upper bound factor  $\delta \in [\delta^*, \infty)$  and, subsequently, minimizing the difference  $D$  with local steering constraints on the fiber angles in Step 2 using  $\zeta_{\max} = 1/r_{\min}$ . Observe that the upper bound factor  $\delta$  in the hybrid control method is chosen in a different range than for the indirect control method, hence in general the intermediate design obtained after Step 1 (primary optimization) will in general be different for the indirect and hybrid methods. Furthermore, because of this relaxed value for the upper bound factor, the hybrid control method requires that the steering constraints in Step 2 should be based on the actual minimum turning radius (just like the direct control method) in order to guarantee that the manufacturing requirements are satisfied.

For clarity, the formulations of the three different curvature constraint methods are summarized in Table 3.1. The three methods are applied to a benchmark case with the purpose of assessing the relative loss in performance associated to each method.

## 3.5. TEST CASE 1: RECTANGULAR PLATE WITH POINT LOAD

To study the distinct methodologies to impose curvature constraints, a simple test case of a cantilever rectangular plate is considered. The dimensions of the plate are  $a = 1.2$  m,  $b = 0.4$  m. The left edge is clamped and a unit point load  $F$  is applied at the right bottom corner. The linear elastic properties of each ply are taken as  $E_1 = 148$  GPa,  $E_2 = 9.65$  GPa,  $G_{12} = 4.55$  GPa,  $\nu_{12} = 0.3$  with 1 denoting the local fiber direction. The quasi-isotropic layout is used as a reference to compare the performance of the non-homogeneous op-

timal design, hence the objective is to minimize  $C/C_{QI}$  with  $C$  being the compliance of a non-homogeneous design and  $C_{QI}$  being the compliance of the quasi-isotropic layout.

It is worth pointing out that, due to a lack of an analytical solution for the optimization problem, a verification of the finite element implementation and the (unconstrained) optimization algorithm was done by comparing the results of the current work with those presented in Nagy [30], which were obtained from an independently-developed code and algorithm. It was found that the results obtained from the current code for the unconstrained minimum compliance problem had a relative difference of less than 3% compared to the results found in Nagy [30]) using the same geometrical, material and design data. Both solutions provided similar distributions of  $\mathbf{V}_1$  and  $\mathbf{V}_3$  and small differences may be attributed to the fact that the work of Nagy [30] uses isogeometric analysis whereas the present code uses a more traditional finite element implementation. This comparison provides (indirect) evidence for verification of the finite element and optimization code used in the present analysis.

### 3.5.1. PRIMARY TEST ON DIRECT, INDIRECT AND HYBRID CONTROL METHOD

To illustrate in detail the effect of the curvature constraints with the direct, indirect and hybrid control methods, one specific case for each method is presented in this section (i.e., for a fixed pair of values  $\delta$  and  $\zeta_{\max}$  and a fixed number of design layers  $n_d$ ). In particular, for the purposes of the angle retrieval step (Step 2), all cases presented in this section are solved with  $n_d = 6$  design layers using a symmetric and balanced laminate, hence with  $n_l = 24$  layers. The thickness of each layer is 0.6 mm and hence the total thickness is 14.4 mm. The initial lamination parameters at each node in Step 1 are obtained with design layers oriented as  $[40^\circ, 70^\circ, 40^\circ, 10^\circ, 70^\circ, 70^\circ]$ , the initial fiber angles in Step 2 are  $10^\circ$  for each layer at each node. The actual minimum allowable turning radius of an AFP machine is chosen in this test case as  $r_{\min} = 0.8$  m.

#### DIRECT CONTROL METHOD WITH REPRESENTATIVE MINIMUM TURNING RADIUS

In the direct control method, the value of  $\delta$  is chosen sufficiently large so that the gradient constraints are not active during Step 1 (i.e.,  $\delta \rightarrow \infty$ ). As indicated above, the steering constraints are enforced in this case with  $\zeta_{\max} = 1/r_{\min} = 1/0.8\text{m}^{-1}$ . The distributions of  $\mathbf{V}_1$  and  $\mathbf{V}_3$  of the optimal solution from Step 1 and Step 2 are shown in Figure 3.3. From the figure, it can be observed that the distributions of both  $\mathbf{V}_1$  and  $\mathbf{V}_3$  after Step 1 have relatively steep gradients with values changing from  $-1$  to  $1$  throughout a small region, which reflect the fact that no gradient constraints are active in Step 1. After retrieving the fiber angles (i.e., Step 2 of the method) for a given number of design layers ( $n_d = 6$  in this case), the corresponding lamination parameters vary more gradually as may be observed in the figure. Furthermore, comparing the optimal lamination parameters from Steps 1 and 2, it can be seen that there is a significant difference, which implies that there is a loss in performance of the primary objective functional since the design space in Step 1 is larger (unconstrained) than the design space in Step 2 (constrained). Indeed, in this example the optimal normalized compliance from Step 1 is 0.482 whereas

**Direct control method**

$$\delta \rightarrow \infty$$

$$\zeta_{\max} = 1/r_{\min} \quad r_{\min} = 0.8 \text{ m}$$

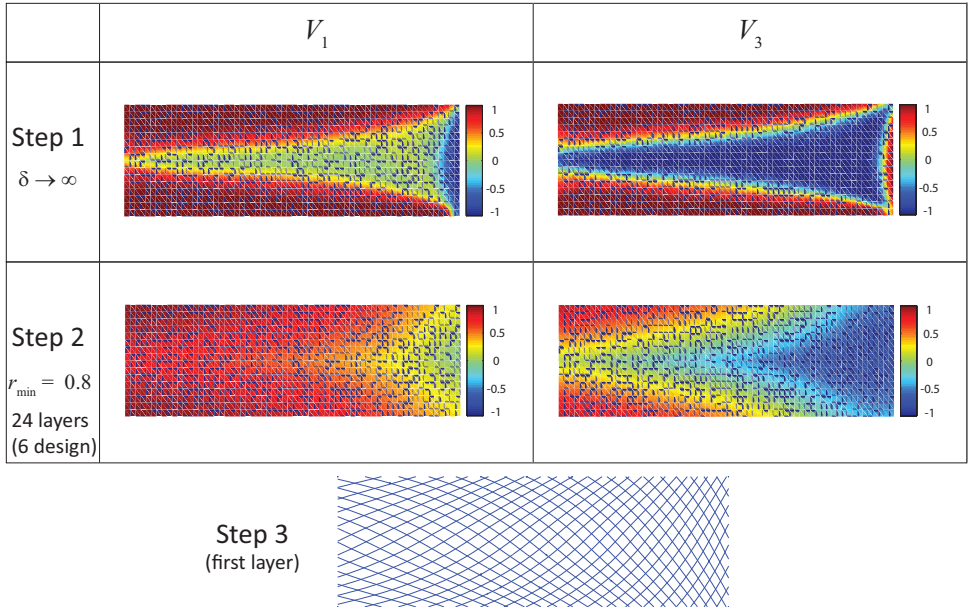
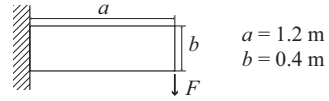


Figure 3.3: Optimal lamination parameters  $V_1$  and  $V_3$  for minimum compliance after Steps 1 and 2 obtained using the direct control method with  $\delta \rightarrow \infty$ ,  $r_{\min} = 0.8 \text{ m}$  and 6 design layers. For illustration purposes, the fiber paths in the first layer and its balanced counterpart are also shown (Step 3)

the compliance for the “manufacturable” design obtained after Step 2 is 0.593, which implies a relative loss of performance of 23% (i.e., increase of compliance to achieve a manufacturable design).

The fiber paths of the first design layer (i.e., the outer layer) are also shown in Figure 3.3 (Step 3). In general, the resulting design follows the general pattern that is expected for a minimum compliance laminate whereby the fibers optimally oppose the deformation by transmitting the applied load on the right to the clamped edge on the left following a classical arch-like layout. The key aspect in the present case pertains to the curvature. The resulting design complies with the manufacturing constraint of a minimum turning radius, which is in fact attained locally in this design after Step 2.

**INDIRECT CONTROL METHOD WITH IMPLICIT REPRESENTATIVE MINIMUM TURNING RADIUS**

In the indirect control method, the gradient constraints on the lamination parameters in Step 1 need to be sufficiently stringent to control the actual minimum turning radius locally in each layer. It was found through numerical experimentation, as shown in A.1.1,

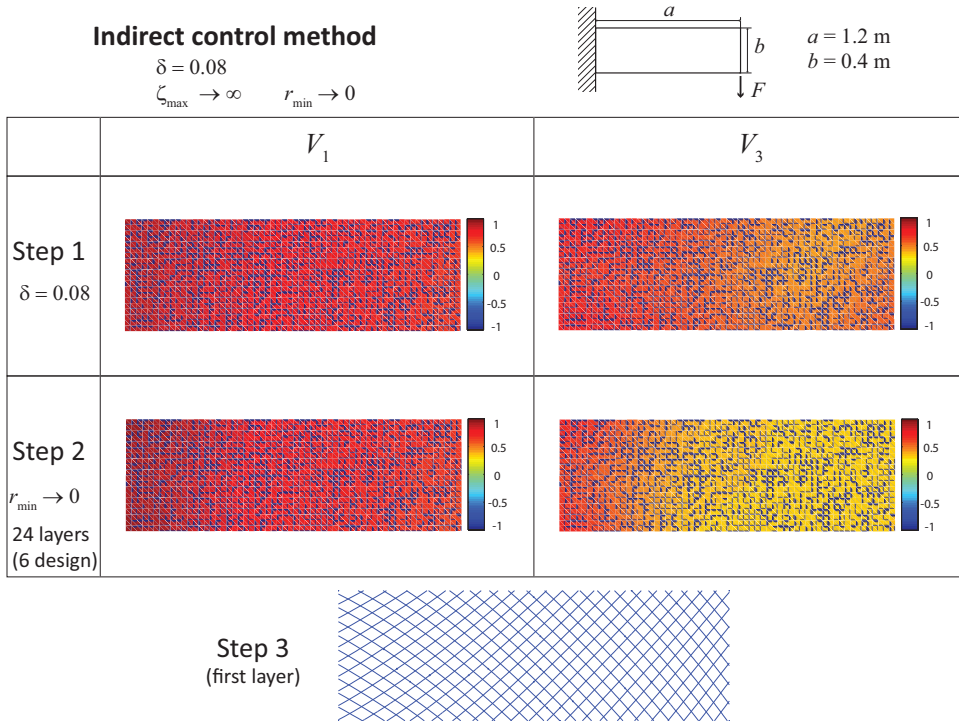


Figure 3.4: Optimal lamination parameters  $V_1$  and  $V_3$  for minimum compliance after Steps 1 and 2 obtained using the indirect control method with  $\delta = 0.08$ ,  $r_{\min} \rightarrow 0$  and 6 design layers. For illustration purposes, the fiber paths in the first layer and its balanced counterpart are also shown (Step 3)

that the value of  $\delta = 0.08$  allows to satisfy the curvature constraints at every layer without explicitly imposing a steering constraint (i.e., using formally zero as minimum radius of curvature or, equivalently, infinity as a maximum curvature, i.e.,  $\zeta_{\max} \rightarrow \infty$ ).

The distributions of the optimal  $V_1$  and  $V_3$  from Steps 1 and 2 are shown in Figure 3.3. Clearly, the effect of a small value  $\delta$  can be seen in the figures since the lamination parameters after Step 1 change slowly from point to point. Correspondingly, the design itself is nearly homogeneous and, as anticipated, the design after Step 2 is rather similar to the design of Step 1 since the (constrained) design space of Step 1 can be relatively well approximated with the (unconstrained) design space of Step 2 with six design layers. Indeed, the normalized optimal compliance in Step 1 is 0.636 whereas the normalized compliance of the “manufacturable” design after Step 2 is 0.647, which implies a small increase of 1.7%. This small difference, which may be also observed in the contour plots of  $V_3$  between Step 1 and 2, can be ascribed to the fact that not all lamination parameters can be matched exactly with only 6 design layers (see Setoodeh et al. [38]).

This example illustrates that the indirect control method can achieve a manufacturable design (e.g., if one would have used  $r_{\min} = 0.8 \text{ m}$  as a minimum turning radius for AFP), but it is in general inefficient in terms of exploiting the local curvature. Indeed, the fiber

paths of the first layer (and also in other layers) are relatively straight and the smallest turning radius in the design is 1.34 m, which implies that the steering capability is not being used to its fullest extent.

#### HYBRID CONTROL METHOD WITH REPRESENTATIVE MINIMUM TURNING RADIUS

The third method used is the hybrid control method, which combines the direct control method with the indirect control method but using a distinct set of parameters. As mentioned above, the gradient constraints in Step 1 are relaxed since, as opposed to the indirect control method, it is not the intention to fully enforce the curvature constraint in Step 1. The rationale of this method is to partially enforce the curvature constraint in Step 1 and use the steering constraints in Step 2 to guarantee that the manufacturing constraints are satisfied. Partially enforcing the curvature constraints has the advantage of coupling geometrical requirements to the primary objective functional but leaving sufficient flexibility in the design space to prevent the negative effects of the indirect control method. This pre-conditioning in the design mollifies the negative effect of the direct control method, which imposes a geometrical curvature constraint in an uncoupled fashion in Step 2.

The optimal  $\mathbf{V}_1$  and  $\mathbf{V}_3$  in Step 1 of the hybrid control method, with relaxed gradient constraints on the lamination parameters by  $\delta = 0.8$  and local steering constraints with maximum curvature  $\zeta_{\max} = 1/r_{\min} = 1/0.8\text{m}^{-1}$  is shown in Figure 3.5.

In this case, the local steering constraints in Step 2 only induce relatively small changes during the angle retrieval step as can be observed comparing the lamination parameters from Steps 1 and 2. Indeed, the normalized optimal compliance from Step 1 is 0.523 whereas the normalized compliance from Step 2 is 0.549, indicating a relatively small increase of about 5%. From the fiber paths of the first layer (outer layer) shown in Figure 3.5 (Step 3), it can be seen that the design obtained from the hybrid method also follows a classical arch-like approach for minimum compliance. In this case the design complies with the local curvature constraint with a combination of active gradient constraints in Step 1 and active steering constraints in Step 2.

#### 3.5.2. COMPARISON OF THE OPTIMAL DESIGNS FOR ONE REPRESENTATIVE MINIMUM TURNING RADIUS

The numerical results of the primary test in Section 3.5.1 using the representative value of the minimum turning radius  $r_{\min} = 0.8$  m are summarized in Table 3.2. From the table, it can be observed that at the end of Step 1 the best design (smallest compliance) is obtained from the direct control method, followed by the hybrid control method and finally the worst design is the one obtained from the indirect control method. This outcome was anticipated since it follows the size of the corresponding design spaces (i.e., unconstrained for the direct control method, partially constrained for the hybrid control method and fully-constrained for the indirect control method). However, the order of performance changes for the final design obtained after Step 2, where the hybrid control method provides the best design, followed by the design obtained from the direct con-



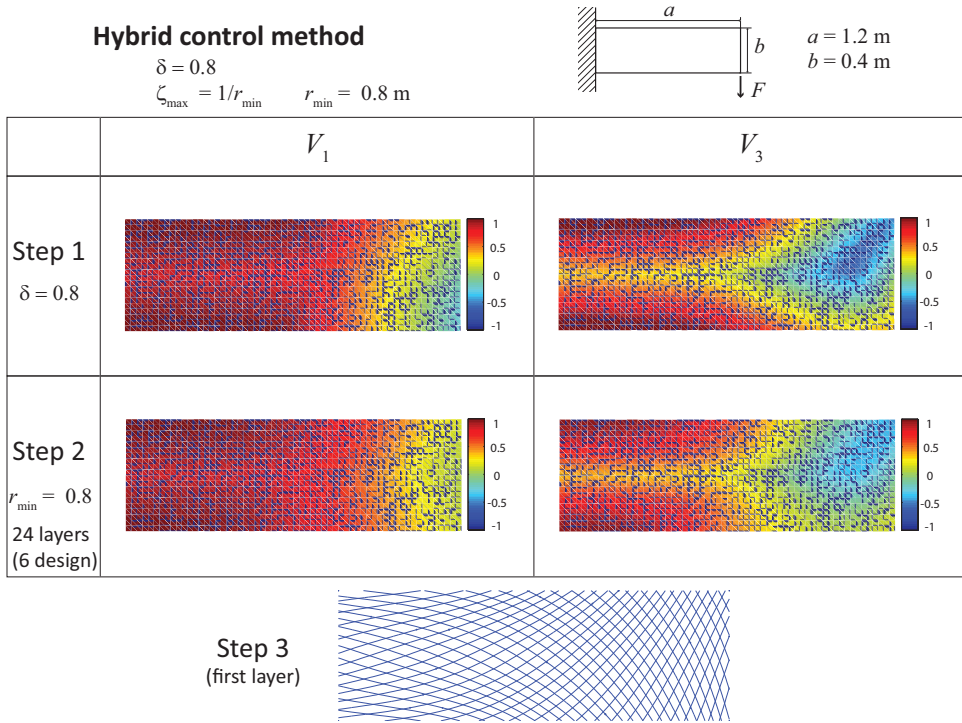


Figure 3.5: Optimal lamination parameters  $V_1$  and  $V_3$  for minimum compliance after Steps 1 and 2 obtained using the hybrid control method with  $\delta = 0.08$ ,  $\zeta_{\max} = 1/0.8\text{m}^{-1}$  and 6 design layers. For illustration purposes, the fiber paths in the first layer and its balanced counterpart are also shown (Step 3)

trol and finally the worst design corresponds to the one associated to the indirect control method.

The fact that the hybrid control method delivers the best design among the three methods can be ascribed to the coupling between the curvature constraints (via the gradient of the lamination parameters) and the primary objective functional. Indeed, the partial loss in performance in the intermediate design obtained from the hybrid method after Step 1 is compensated by a less significant loss in performance in Step 2 compared to the direct control method, which enforces the geometrical curvature constraint in an uncoupled fashion, thus locally increasing the radius of curvature without accounting for changes in the structural stiffness. Observe that the indirect control method also couples the curvature constraint to the primary objective, however the constraints are too strict in the sense that, as shown in the table, the smallest turning radius in the design remains significantly above the allowed minimum turning radius. From this perspective, the hybrid control method may be interpreted as a “pre-conditioner” of the design in Step 1 that mollifies the loss of performance in Step 2 while it still takes full advantage of the steering of the fiber path since it pushes the local steering radius towards its minimum value locally.



Table 3.2: Numerical results of test case 1 (rectangular plate) for  $r_{\min} = 0.8$  m.

	Direct $\delta \rightarrow \infty$	Indirect $\delta = 0.08$	Hybrid $\delta = 0.8$
Normalized optimal compliance after Step 1	0.482	0.636	0.523
Normalized compliance after Step 2	0.593	0.647	0.549
Smallest turning radius after Step 2 (m)	0.8003	1.34	0.8002

### 3.6. COMPARATIVE ANALYSIS OF TEST CASE 1 FOR DISTINCT VALUES OF MODEL PARAMETERS AND MINIMUM TURNING RADIUS

In the previous section, it is shown that the hybrid control method provides the best design considering a curvature constraint for a selected value of the minimum turning radius, namely  $r_{\min} = 0.8$  m. In this section, the comparative analysis is extended to a wide range of values with  $r_{\min} = \{0.4, 0.8, 1.2, 1.6, 2.0\}$  m and  $\delta = \{0.05, 0.08, 0.8\}$  to have an overall assessment of the performance of the direct, indirect and hybrid control methods. The comparative analysis is done both in terms of the compliance and computational efficiency. The number of design layers used for all calculations in this section is taken as  $n_d = 6$  design layers.

#### 3.6.1. COMPARISON OF THE OPTIMAL COMPLIANCE IN STEP 2 OF THE THREE METHODS

The optimal normalized compliance for different values of the minimum turning radius  $r_{\min}$  obtained from the direct, indirect and hybrid control methods which satisfies the curvature constraint at the end of Step 2 is shown in Figure 3.6. As a reference, the optimum unconstrained compliance obtained from the lamination parameters is indicated in the figure as a dashed line. This reference value corresponds formally to a zero minimum turning radius and an unspecified (infinite) number of design layers of arbitrarily small thickness. As expected, the normalized optimal compliance increases for all methods as the minimum allowable turning radius  $r_{\min}$  increases. This is due to the reduced capacity to steer the fibers as the minimum allowable turning radius  $r_{\min}$  increases, which prevents the fibers to optimally transmit the loads throughout the structure to increase its structural stiffness and hence reduce its structural compliance.

Since the reference dashed line without curvature constraint also coincides with the performance of the intermediate design obtained after Step 1 of the direct control method ( $\delta \rightarrow \infty$ ), it can be seen from Figure 3.6 that there is a significant loss in performance between Step 1 and Step 2 for the direct control method. Indeed, imposing the curvature constraint only via steering constraints results in increases of compliance ranging from about 14% for  $r_{\min} = 0.4$  m to about 35% for  $r_{\min} = 2$  m. This indicates that the optimal stiffness distribution obtained in Step 1 of the direct control method can not be closely matched when the curvature of the fiber angles is constrained in Step 2.

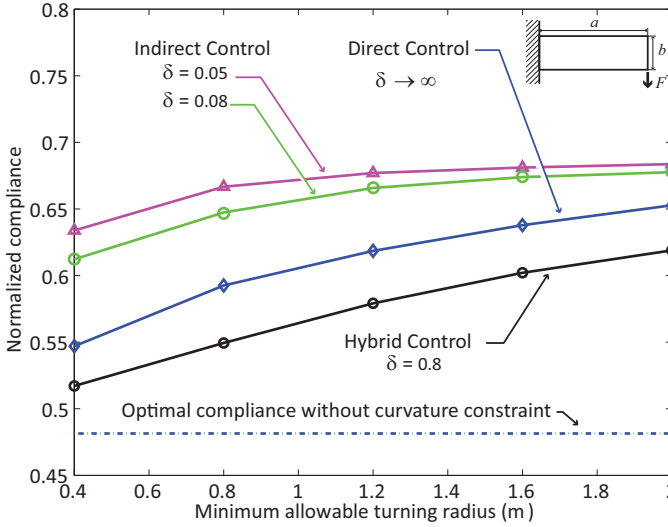


Figure 3.6: Comparison of optimal normalized compliance under different values of the minimum turning radius  $r_{\min}$  for the direct, indirect and hybrid control methods using 6 design layers. The optimum normalized compliance for the unconstrained case (formally zero minimum turning radius and 6 design layers) is indicated as a dashed line

Moreover, as may be inferred from Figure 3.6, the indirect control method provides the worst design of the three methods (highest optimal compliance) for the whole range of minimum allowable turning radius  $r_{\min}$ . This is due to the fact that the gradient constraints on the lamination parameters with  $\delta = 0.05$  and  $\delta = 0.08$  are so stringent that the design domain is reduced severely (i.e., limited steering). Higher values of  $\delta$  are not acceptable in the indirect control method because the curvature constraints will be violated as shown in A.1.

The hybrid control method generates the best design of the three methods provided that the value of the upper bound factor  $\delta$  is appropriately chosen. Indeed, as shown in Figure 3.6, the compliance of the designs obtained from the hybrid control method are the lowest for all values considered for the minimum allowable turning radius  $r_{\min}$  with  $\delta = 0.8$ . However, if the value of  $\delta$  is taken too low, namely  $\delta < \delta^*$ , then the hybrid method actually becomes the indirect method and the steering constraints in Step 2 become inactive. Consequently, the improvements from the hybrid control method require a value of  $\delta$  that is neither too low (where it coincides with the indirect control method) nor too high (where it coincides with the direct control method). A proper choice of  $\delta$  is therefore critical for the implementation of the hybrid control method which typically requires some calibration, namely a test to check that both the gradient constraints in Step 1 and the steering constraints in Step 2 are active. More details on the choice of  $\delta$  are provided in A.1.

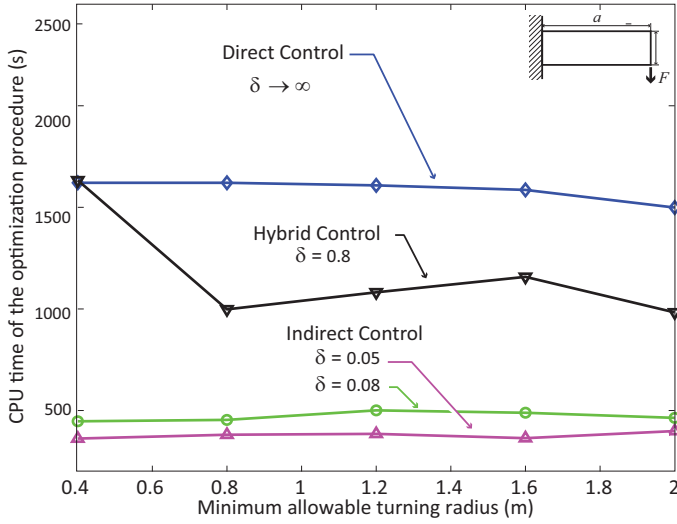


Figure 3.7: Comparison of the required CPU time for different values of the minimum turning radius  $r_{\min}$  for the direct, indirect and hybrid control methods using 6 design layers.

### 3.6.2. COMPARISON OF THE COMPUTATIONAL COST FOR THE CURVATURE CONSTRAINED METHODS

In general, multistep methods that use homogenized parameters such as lamination parameters tend to outperform design formulations that explicitly use layer-by-layer angles as design variables in a primary optimization problem (single step formulation). A comparison between single step and multistep methods is beyond the scope of the present work, partly because the results of the comparative analysis may strongly depend on the numerical implementation and the hardware used. However, imposing curvature constraints in a multistep method increases the computational cost, hence it is relevant to quantify this effect within the same computational framework. The performance indicators reported here are only meant to provide values for a comparative analysis and should not be taken as representative of a highly optimized code and/or hardware.

The CPU time of each design sample analyzed in Section 3.6.1 is shown in Figure 3.7. From the figure it can be observed that the indirect control method with  $\delta = 0.05$  requires the least amount of time to converge, followed by the case of  $\delta = 0.08$  with the same method. The reason is that the number of active constraints is relatively small, i.e., only the gradient constraints on the lamination parameters are active. It is also worth pointing out that in practice the sensitivities of the local steering constraints, which can be computationally costly, are not computed in the implementation of the indirect control method.

Indeed, the CPU time for the hybrid control method with  $\delta = 0.8$  increases further compared to the indirect control method due to the sensitivity analysis for the local steering constraints in Step 2. Similarly, The CPU time required for the direct control method is the highest among the three methods in general because more steering constraints become active in Step 2. In addition, although not reported here in detail for reasons of conciseness, it was found that the number of iterations in Step 1 for the direct control method is actually larger than for the other methods, which implies that the imposing gradient constraints in Step 1 actually helps to reduce the computational time.

From the results shown in Figure 3.5 and Figure 3.6, it can be seen that the hybrid control method not only provides the best optimal compliance and but it is also more efficient in terms of computational cost compared to the direct control method.

### 3.6.3. OPTIMAL UPPER BOUND FACTOR $\delta$ IN THE HYBRID CONTROL METHOD

As indicated above, the enhanced performance of the hybrid control method depends on the choice of the upper bound factor  $\delta$  which should be large enough to avoid the excessive constraints in Step 1 (as in the indirect control method) but it should be small enough to provide a useful coupling between the primary objective and the curvature constraints and avoid an uncoupled formulation (as in the direct control method). This compromise implies that there should be an optimum value for the upper bound factor  $\delta$ . In view of this, five sets of numerical tests are implemented to detect the optimal range of the upper bound factor  $\delta$  for the hybrid control method. The minimum allowable turning radius  $r_{\min}$  is chosen among  $\{0.4, 0.8, 1.2, 1.6, 2.0\}$  m and the value of  $\delta$  is uniformly varied from 0.4 to 1.6 for each set.

The normalized compliance obtained in Step 2 of the hybrid control method is shown in Figure 3.8. From the figure, it can be observed that for the larger values of the minimum allowable turning radius considered (namely  $r_{\min} = 1.6\text{m}, 2.0\text{m}$ ), the compliance obtained from the hybrid control method only changes slightly, indicating a weak dependency on the exact value of the upper bound factor  $\delta$  for the range of values considered in the parametric analysis. The compliance decreases slightly for increasing values of  $\delta$ , suggesting that the optimal value may be larger than the largest value analyzed. Nonetheless, the conclusion is also that for large values of the minimum allowable turning radius, there is only a limited amount of optimization that can be performed with fiber steering and most of the optimization comes simply from choosing a stacking sequence with nearly straight fibers, in which case the influence of the factor  $\delta$  becomes less important. However, if there is more freedom for the steering of fiber path, which corresponds to smaller values of  $r_{\min}$  such as 0.4 m and 0.8 m, the results shown in Figure 3.8 indicate an increased sensitivity with respect to the upper bound factor  $\delta$ , with an optimum value around  $\delta = 0.8$  for  $r_{\min} = 0.4$  m and around  $\delta = 1$  for  $r_{\min} = 0.8$  m. In general, the results suggest that the optimal value of  $\delta$  increases with increasing values of  $r_{\min}$ , which would mean that the increase in  $\delta$  has to compensate the increase in  $r_{\min}$  to limit the changes in the upper bounds in Eqs. (3.38) and (3.39). However, an analytical expression cannot be easily determined and the optimal value of  $\delta$  currently requires numerical calibration.

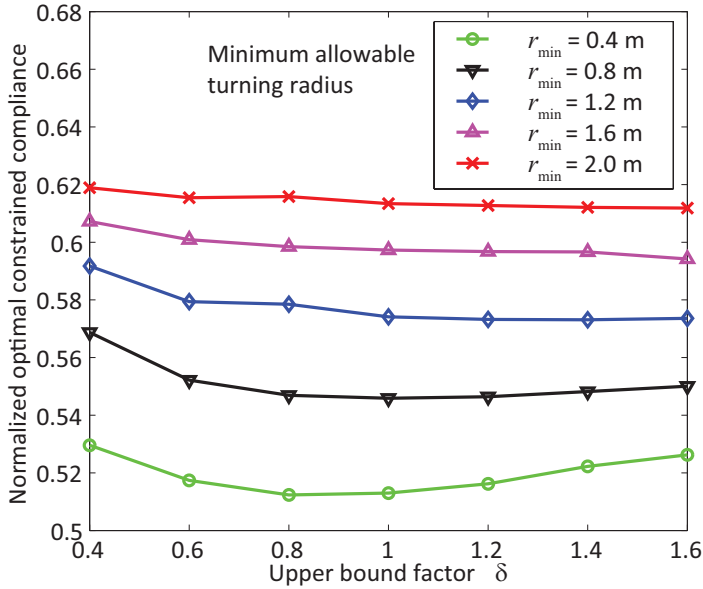


Figure 3.8: Normalized compliance obtained after Step 2 from the hybrid control method using different upper bound factors  $\delta$  for various values of the minimum allowable turning radius

### 3.7. TEST CASE 2: SQUARE PLATE WITH A HOLE UNDER DISTRIBUTED LOAD

To further explore the performance of the three optimization strategies, a second design case is analyzed, namely a minimum compliance problem for a square plate with a circular hole clamped on one edge and subjected to a uniformly distributed tangential load  $t = 20 \text{ kN m}^{-1}$  on the opposite edge. The intention is to study a more complex geometry that is also prototypical of a cut-as commonly encountered in aerospace structures. The side length of the square plate is  $a = 0.4 \text{ m}$  and the radius of the cut-out is  $R = 0.1 \text{ m}$ . As in the previous example, The quasi-isotropic layout is used as a reference to compare the performance of the non-homogeneous optimal design. For the angle retrieval step,  $n_d = 6$  design layers are used and, where applicable, the minimum allowable turning radius in this case is  $r_{\min} = 0.2 \text{ m}$ . The chosen value of  $r_{\min}$  is relatively low in terms of current AFP technology but it is chosen in accordance with the panel's dimension to allow for a more complex design with more fiber steering. The material properties of the laminate are the same as in test case 1.

#### 3.7.1. DIRECT CONTROL METHOD

With the direct control method, the optimal values for the lamination parameters  $\mathbf{V}_1$  and  $\mathbf{V}_3$  from the unconstrained Step 1 and the constrained Step 2 are shown in Figure 3.9.

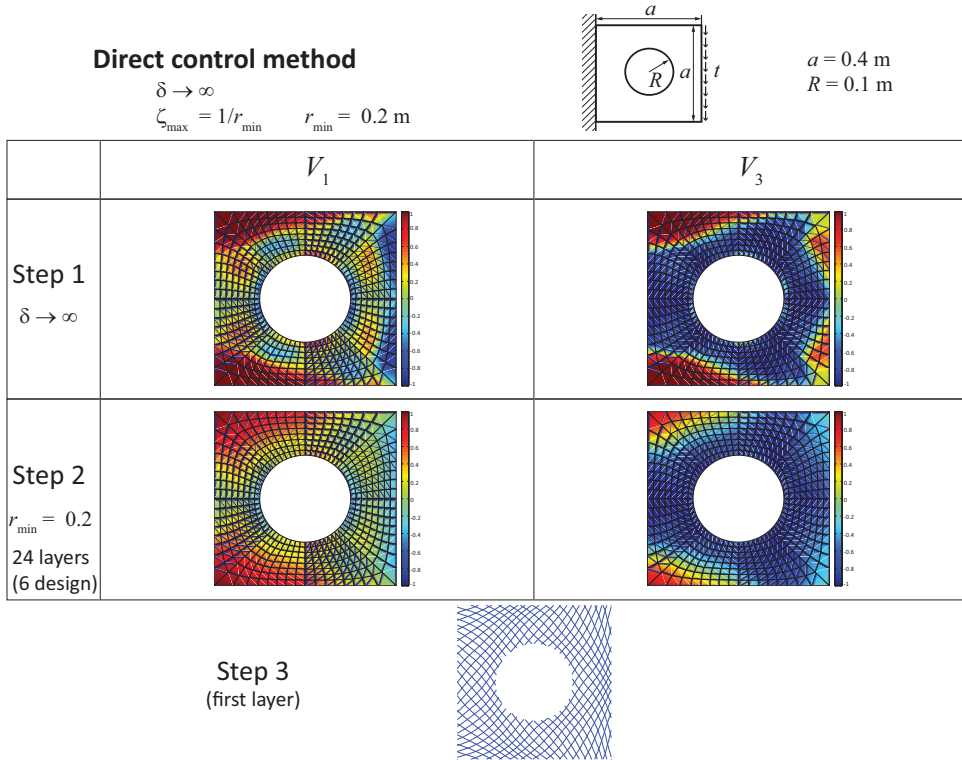


Figure 3.9: Optimal lamination parameters  $V_1$  and  $V_3$  for minimum compliance after Steps 1 and 2 obtained using the direct control method with  $\delta \rightarrow \infty$ ,  $r_{\min} = 0.2 \text{ m}$  and 6 design layers. For illustration purposes, the fiber paths in the first layer and its balanced counterpart are also shown (Step 3)

Similar to the previous test case, the values of the lamination parameters after Step 1 have relatively steep gradients as they vary from 1 to -1 throughout a small region; the values are then forced to have a more gradual change after imposing the steering constraints in Step 2.

For illustration purposes, the fiber path orientations of the first layer are also shown in Figure 3.9 as part of Step 3 of the three-step method. In this design, the local steering constraint was found to be active in all design layers, i.e., the smallest turning radius in each layer coincided with the minimum allowable turning radius  $r_{\min} = 0.2 \text{ m}$ . From the fiber paths, it is possible to recognize that the fiber steering design recovered from Step 2 contains classical aspects of maximum stiffness layouts, namely that the load is optimally transmitted from the edge where it is applied to the rigid support on the opposite side, adapting the path to the traction-free surfaces on the cut-out and the corresponding areas of stress concentrations along the cut-out. The effect of the steering constraints in Step 2 is that the performance of the design is reduced since the normalized compliance increases from 0.613 in Step 1 to 0.698 in Step 2, which represents a change of nearly 14 %. This is a relatively important loss in performance in optimization problems

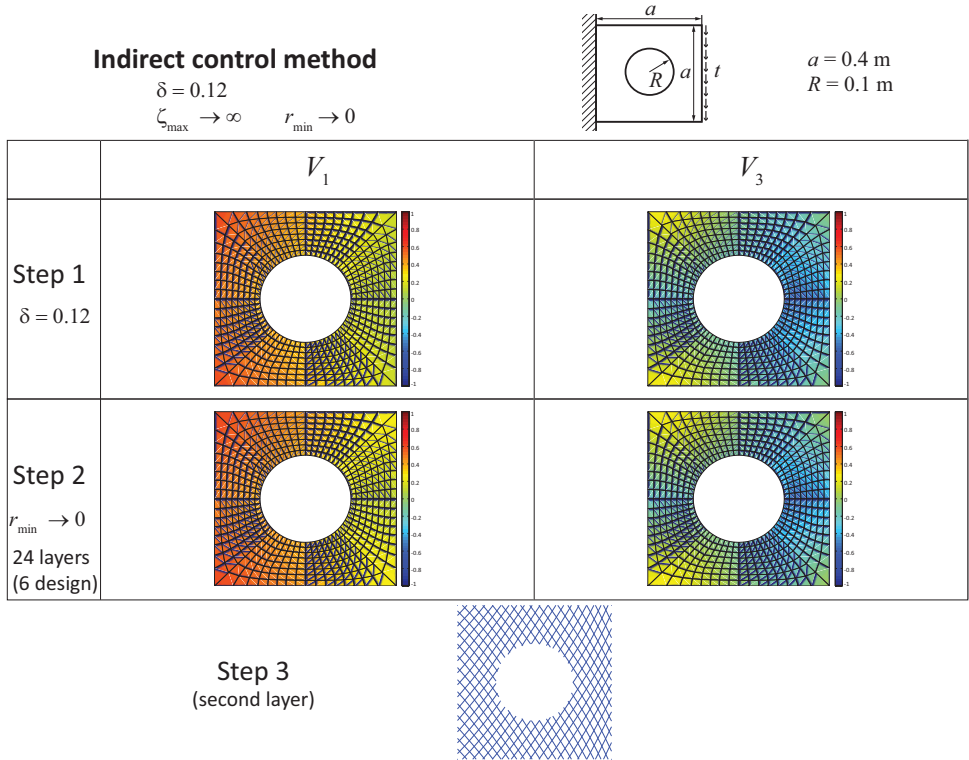


Figure 3.10: Optimal lamination parameters  $V_1$  and  $V_3$  for minimum compliance after Steps 1 and 2 obtained using the indirect control method with  $\delta = 0.08$ ,  $r_{\min} \rightarrow 0$  and 6 design layers. For illustration purposes, the fiber paths in the second layer and its balanced counterpart are also shown (Step 3), see text for details.

in which the margin of improvement is often in the same order of magnitude. Indeed, compared to the quasi-isotropic design, a significant part of the improvement is lost due to the curvature constraint imposed by manufacturing limitations.

### 3.7.2. INDIRECT CONTROL METHOD

Through numerical tests (not shown here for conciseness), it was determined that choosing an upper bound factor  $\delta = 0.12$  in test case 2 guarantees that the design obtained from the indirect control method satisfies the curvature constraints with  $r_{\min} = 0.2 \text{ m}$ . The corresponding optimal  $V_1$  and  $V_3$  after Steps 1 and 2 are shown in Figure 3.10, together with the fibers paths of the second layer of the design (Step 3).

In this case, the second layer is selected for illustration purposes since it contains the smallest turning radius of all layers. From Figure 3.10, it can be observed that the design consists of nearly straight paths due to the stringent constraints in Step 1. Since the lamination parameters are nearly homogeneous, they can be easily matched with straight paths and  $n_d = 6$  design layers is sufficient for a good approximation where the steer-

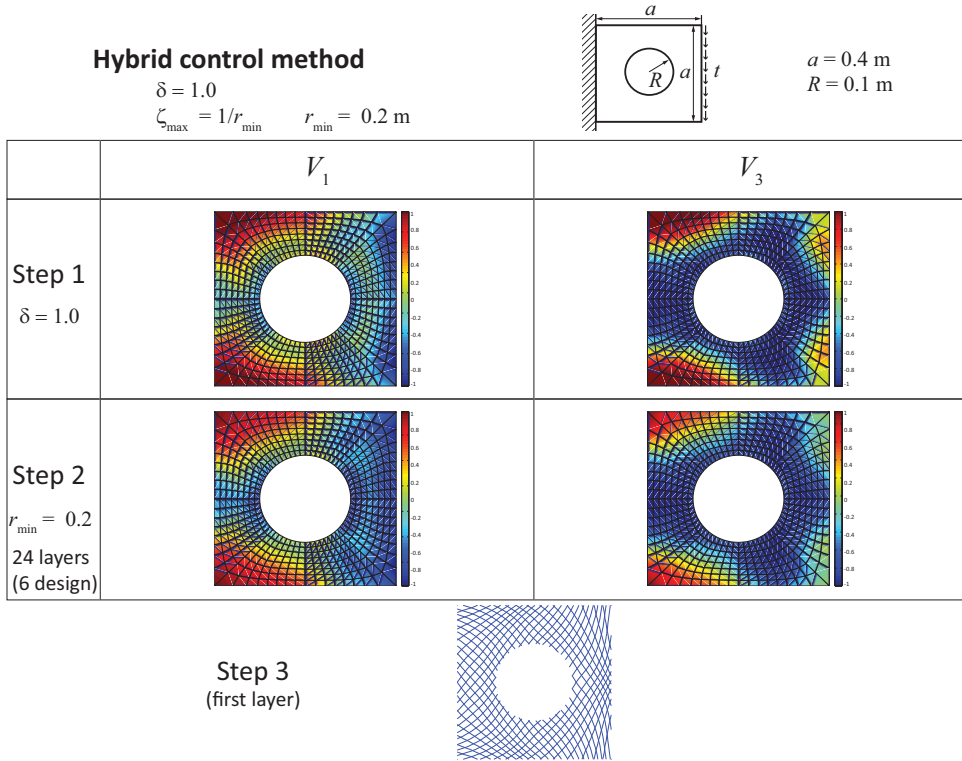


Figure 3.11: Optimal lamination parameters  $V_1$  and  $V_3$  for minimum compliance after Steps 1 and 2 obtained using the hybrid control method with  $\delta = 0.08$ ,  $\zeta_{\max} = 1/r_{\min} = 1/0.8\text{m}^{-1}$  and 6 design layers. For illustration purposes, the fiber paths in the first layer and its balanced counterpart are also shown (Step 3)

ing constraints are not active. Indeed, the values of the lamination parameters in Step 2 are nearly identical as those in Step 1. Consistent with the strong limitations in steering imposed by the indirect control method, the optimal compliance between Step 1 (equal to 0.796) and Step 2 (equal to 0.802) does not change significantly. The smallest turning radius in the second design layer is 0.3509 m (located around the left bottom part of the hole) which is significantly larger than the minimum allowable turning radius  $r_{\min} = 0.2$  m.

**3.7.3. HYBRID CONTROL METHOD**

In the hybrid control method, the upper bound factor is chosen in this test case as  $\delta = 1.0$  in Step 1. This value was found based on a simple scan of various values of  $\delta$  using a similar approach as the one discussed for test case 1. The corresponding optimal values of  $V_1$  and  $V_3$  in Steps 1 and 2 are shown in Figure 3.11 with the first design layer as a visual reference of the optimal design.

In this case, the normalized optimal compliance from Step 1 is 0.632, and the compli-



Table 3.3: Numerical results of test case 2 (square plate with a central hole) for  $r_{\min} = 0.2$  m.

	Direct $\delta \rightarrow \infty$	Indirect $\delta = 0.12$	Hybrid $\delta = 1.0$
Normalized optimal compliance Step 1	0.613	0.796	0.632
Normalized optimal compliance Step 2	0.698	0.802	0.679
Smallest turning radius [m]	0.20003	0.3509	0.2002

3

ance corresponding to the retrieved angles in Step 2 is 0.679, hence the performance loss between the two steps is relatively moderate (increase of 7.4% in compliance). The smallest turning radius found in all layers coincides with the allowable minimum value 0.2 m.

### 3.7.4. COMPARISON OF THE OPTIMAL DESIGNS FOR ONE REPRESENTATIVE MINIMUM TURNING RADIUS

In this section, a comparison is made between the designs for the square plate with a central hole using the direct, indirect and hybrid control methods. The results are summarized in Table 3.3 for the specific case of  $r_{\min} = 0.2$  m.

For the manufacturable designs obtained at the end of Step 2 for test case 2, the hybrid control method generates the design with the best performance, which is similar to the results for the rectangular plate analyzed in Section 3.5.2. As previously indicated, the improved performance of the design obtained from the hybrid control method can be ascribed to the suitable combination of a partial enforcement of the curvature constraint during Step 1, which couples manufacturing constraint to the mechanical performance. Although in this case the differences between the direct and hybrid control method are smaller, the design obtained from the hybrid control method is superior in terms of performance, which again indicates that the hybrid control method is the best option for imposing curvature constraints in the three-step optimization method. For the sake of conciseness, no parametric analysis is reported here for test case 2 (i.e., only the results for the minimum turning radius  $r_{\min} = 0.2$  m are shown), but the results for other values of  $r_{\min}$  indicate a similar ranking in terms of the performance of the designs obtained from the three methods.

## 3.8. CONCLUSION

In this chapter, the three-step optimization design method is modified to reduce the performance loss between Step 1 (optimization with respect to lamination parameters) and Step 2 (angle retrieval step) when curvature constraints are considered. A simple indirect control method is proposed to constrain the fiber path curvature through the use of gradient constraints on the lamination parameters in the first step while carrying out an angle retrieval step without steering constraints on the fiber curvature. A second method, which combines a relaxed version of the indirect method with an existing

method (the direct control method), is also proposed to satisfy curvature constraints in designs of composite structures for AFP technology.

Through numerical experimentation in two representative examples, it is shown that the indirect control method can indeed produce feasible designs but it severely limits the design space and prevents taking full advantage of the fiber steering capacity of AFP machines. Due to its detrimental effect on the optimization capacity, the indirect control method is not recommended as a stand-alone strategy. However, and more importantly, numerical results demonstrate that designs obtained from the new hybrid control method outperform individual designs obtained from the direct and indirect control methods and, in addition, tend to converge faster to a solution compared to the existing direct control method.

The improved performance of the designs obtained from the hybrid control method can be ascribed to a couple of factors, namely (1) the global coupling between curvature constraints and primary objective in the first step allows to partially increase the curvature throughout the structure while accounting for the transmission of loads (global redistribution of loads) and (2) the relaxation of the constraints in Step 1 provides sufficient flexibility to locally adjust the fiber path in Step 2 up to the minimum allowable turning radius, hence fully employing the fiber steering capacity.

The partial enforcement of the curvature constraints in the hybrid control method via the gradient constraints in Step 1 also proves to be beneficial in terms of computational time compared to the direct control method. In view of these findings, the hybrid control method becomes the recommended strategy to enforce curvature constraints, at least in the context of the minimum compliance problem. Applications of this method to other commonly-used objectives, such as buckling or strength, are to be implemented in the future work.

## REFERENCES

- [1] Zafer Gürdal and Reynaldo Olmedo. In-plane response of laminates with spatially varying fiber orientations-variable stiffness concept. *AIAA journal*, 31(4):751–758, 1993.
- [2] M.W. Hyer and H.H. Lee. The use of curvilinear fiber format to improve buckling resistance of composite plates with central circular holes. *Composite Structures*, 18(3):239 – 261, 1991. ISSN 0263-8223. doi: [https://doi.org/10.1016/0263-8223\(91\)90035-W](https://doi.org/10.1016/0263-8223(91)90035-W). URL <http://www.sciencedirect.com/science/article/pii/026382239190035W>.
- [3] Shahriar Setoodeh, Mostafa M. Abdalla, and Zafer Gürdal. Design of variable-stiffness laminates using lamination parameters. *Composites Part B: Engineering*, 37(4-5):301–309, 2006.
- [4] Adriana W. Blom, Patrick B. Stickler, and Zafer Gürdal. Optimization of a composite cylinder under bending by tailoring stiffness properties in circumferential

- direction. *Composites Part B: Engineering*, 41(2):157 – 165, 2010. ISSN 1359-8368. doi: <https://doi.org/10.1016/j.compositesb.2009.10.004>. URL <http://www.sciencedirect.com/science/article/pii/S1359836809001887>.
- [5] A.H. Akbarzadeh, M. Arian Nik, and D. Pasini. Vibration responses and suppression of variable stiffness laminates with optimally steered fibers and magnetostrictive layers. *Composites Part B: Engineering*, 91:315 – 326, 2016. ISSN 1359-8368. doi: <https://doi.org/10.1016/j.compositesb.2016.02.003>. URL <http://www.sciencedirect.com/science/article/pii/S1359836816001037>.
- [6] Izzet U. Cagdas. Optimal design of variable stiffness laminated composite truncated cones under lateral external pressure. *Ocean Engineering*, 145:268 – 276, 2017. ISSN 0029-8018. doi: <https://doi.org/10.1016/j.oceaneng.2017.09.011>. URL <http://www.sciencedirect.com/science/article/pii/S0029801817305309>.
- [7] Jan Stegmann and Erik Lund. Discrete material optimization of general composite shell structures. *International Journal for Numerical Methods in Engineering*, 62(14):2009–2027, 2005.
- [8] Søren N. Sørensen, René Sørensen, and Erik Lund. Dmto—a method for discrete material and thickness optimization of laminated composite structures. *Structural and Multidisciplinary Optimization*, 50(1):25–47, 2014.
- [9] Mostafa M. Abdalla, Shahriar Setoodeh, and Zafer Gürdal. Design of variable stiffness composite panels for maximum fundamental frequency using lamination parameters. *Composite Structures*, 81(2):283 – 291, 2007. ISSN 0263-8223. doi: <https://doi.org/10.1016/j.compstruct.2006.08.018>. URL <http://www.sciencedirect.com/science/article/pii/S0263822306003278>.
- [10] C.S. Lopes, Z. Gürdal, and P.P. Camanho. Variable-stiffness composite panels: Buckling and first-ply failure improvements over straight-fibre laminates. *Computers & Structures*, 86(9):897 – 907, 2008. ISSN 0045-7949. doi: <https://doi.org/10.1016/j.compstruc.2007.04.016>. URL <http://www.sciencedirect.com/science/article/pii/S0045794907001654>. Composites.
- [11] Shahriar Setoodeh, Mostafa M. Abdalla, Samuel T. IJsselmuiden, and Zafer Gürdal. Design of variable-stiffness composite panels for maximum buckling load. *Composite Structures*, 87(1):109 – 117, 2009. ISSN 0263-8223. doi: <https://doi.org/10.1016/j.compstruct.2008.01.008>. URL <http://www.sciencedirect.com/science/article/pii/S0263822308000135>.
- [12] Samuel T. IJsselmuiden, Mostafa M. Abdalla, and Zafer Gürdal. Optimization of variable-stiffness panels for maximum buckling load using lamination parameters. *AIAA Journal*, 48(1):134–143, 2010.
- [13] Mohammad Rouhi, Hossein Ghayoor, Suong V. Hoa, and Mehdi Hojjati. Computational efficiency and accuracy of multi-step design optimization method for variable stiffness composite structures. *Thin-Walled Structures*, 113:136 – 143,

2017. ISSN 0263-8231. doi: <https://doi.org/10.1016/j.tws.2017.01.019>. URL <http://www.sciencedirect.com/science/article/pii/S0263823116303494>.
- [14] A. Jibawy, C. Julien, B. Desmorat, A. Vincenti, and F. L  n  . Hierarchical structural optimization of laminated plates using polar representation. *International Journal of Solids and Structures*, 48(18):2576 – 2584, 2011. ISSN 0020-7683. doi: <https://doi.org/10.1016/j.ijsolstr.2011.05.015>. URL <http://www.sciencedirect.com/science/article/pii/S0020768311001879>.
- [15] Masoud Kazemi and Georges Verchery. Design of composite laminated plates for maximum buckling load with stiffness and elastic modulus constraints. *Composite Structures*, 148:27 – 38, 2016. ISSN 0263-8223. doi: <https://doi.org/10.1016/j.compstruct.2016.03.051>. URL <http://www.sciencedirect.com/science/article/pii/S0263822316302136>.
- [16] Bret K. Stanford and Christine V. Jutte. Comparison of curvilinear stiffeners and tow steered composites for aeroelastic tailoring of aircraft wings. *Computers & Structures*, 183:48 – 60, 2017. ISSN 0045-7949. doi: <https://doi.org/10.1016/j.compstruc.2017.01.010>. URL <http://www.sciencedirect.com/science/article/pii/S0045794916305569>.
- [17] Marco Montemurro and Anita Catapano. A general b-spline surfaces theoretical framework for optimisation of variable angle-tow laminates. *Composite Structures*, 209:561 – 578, 2019. ISSN 0263-8223. doi: <https://doi.org/10.1016/j.compstruct.2018.10.094>. URL <http://www.sciencedirect.com/science/article/pii/S0263822318324334>.
- [18] M.W. Hyer, R.J. Rust, and W.A. Waters Jr. Innovative design of composite structures: design, manufacturing, and testing of plates utilizing curvilinear fiber trajectories. 1994.
- [19] Dawn Jegley, Brian Tatting, and Zafer G  rdal. Optimization of elastically tailored tow-placed plates with holes. In *44th AIAA/ASME/ASCE/AHS/ASC Structures, Structural Dynamics, and Materials Conference*, page 1420, 2003.
- [20] A. Khani, M.M. Abdalla, Z. G  rdal, J. Sinke, A. Buitenhuis, and M.J.L. Van Tooren. Design, manufacturing and testing of a fibre steered panel with a large cut-out. *Composite Structures*, 180:821 – 830, 2017. ISSN 0263-8223. doi: <https://doi.org/10.1016/j.compstruct.2017.07.086>. URL <http://www.sciencedirect.com/science/article/pii/S0263822317305998>.
- [21] Adriana W. Blom, Shahriar Setoodeh, Jan M.A.M. Hol, and Zafer G  rdal. Design of variable-stiffness conical shells for maximum fundamental eigenfrequency. *Computers & Structures*, 86(9):870 – 878, 2008. ISSN 0045-7949. doi: <https://doi.org/10.1016/j.compstruc.2007.04.020>. URL <http://www.sciencedirect.com/science/article/pii/S0045794907001630>. Composites.

- [22] Gustavo Gonzalez Lozano, Ashutosh Tiwari, Christopher Turner, and Simon Astwood. A review on design for manufacture of variable stiffness composite laminates. *Proceedings of the Institution of Mechanical Engineers, Part B: Journal of Engineering Manufacture*, 230(6):981–992, 2016.
- [23] Julien M.J.F. van Campen, Christos Kassapoglou, and Zafer Gürdal. Generating realistic laminate fiber angle distributions for optimal variable stiffness laminates. *Composites Part B: Engineering*, 43(2):354–360, 2012. ISSN 1359-8368. doi: <https://doi.org/10.1016/j.compositesb.2011.10.014>. URL <http://www.sciencedirect.com/science/article/pii/S1359836811004616>.
- [24] Daniël M.J. Peeters, Simon Hesse, and Mostafa M. Abdalla. Stacking sequence optimisation of variable stiffness laminates with manufacturing constraints. *Composite Structures*, 125:596–604, 2015.
- [25] Daniël M.J. Peeters, Gustavo Gonzalez Lozano, and Mostafa M. Abdalla. Effect of steering limit constraints on the performance of variable stiffness laminates. *Computers & Structures*, 196:94 – 111, 2018. ISSN 0045-7949. doi: <https://doi.org/10.1016/j.compstruc.2017.11.002>. URL <http://www.sciencedirect.com/science/article/pii/S004579491730411X>.
- [26] Hugo Borges de Quadros and José Antonio Hernandez. A lagrange parametrization for the design of variable stiffness laminates. *Structural and Multidisciplinary Optimization*, Feb 2018. ISSN 1615-1488. doi: 10.1007/s00158-017-1882-2. URL <https://doi.org/10.1007/s00158-017-1882-2>.
- [27] Samuel Tsunduka IJsselmuiden. *Optimal design of variable stiffness composite structures using lamination parameters*. PhD thesis, Delft University of Technology, 2011.
- [28] Stephen W. Tsai and Nicholas J. Pagano. Invariant properties of composite materials. Technical report, AIR FORCE MATERIALS LAB WRIGHT-PATTERSON AFB OHIO, 1968.
- [29] V.B. Hammer, M.P. Bendsøe, R. Lipton, and P. Pedersen. Parametrization in laminate design for optimal compliance. *International Journal of Solids and Structures*, 34(4):415 – 434, 1997. ISSN 0020-7683. doi: [https://doi.org/10.1016/S0020-7683\(96\)00023-6](https://doi.org/10.1016/S0020-7683(96)00023-6). URL <http://www.sciencedirect.com/science/article/pii/S0020768396000236>.
- [30] Atilla Peter Nagy. *Isogeometric design optimisation*. PhD thesis, Delft University of Technology, 2011.
- [31] Ali Khani, Samuel T. IJsselmuiden, Mostafa M. Abdalla, and Zafer Gürdal. Design of variable stiffness panels for maximum strength using lamination parameters. *Composites Part B: Engineering*, 42(3):546–552, 2011.
- [32] Daniël Peeters, Zhi Hong, and Mostafa Abdalla. A compliance approximation method applied to variable stiffness composite optimisation. *Structural and Multidisciplinary Optimization*, 58(5):1981–2001, 2018.

- [33] Adriana W. Blom, Mostafa M. Abdalla, and Zafer Gürdal. Optimization of course locations in fiber-placed panels for general fiber angle distributions. *Composites Science and Technology*, 70(4):564–570, 2010.
- [34] Krister Svanberg. A class of globally convergent optimization methods based on conservative convex separable approximations. *SIAM Journal on Optimization*, 12(2):555–573, 2002. doi: 10.1137/S1052623499362822. URL <http://dx.doi.org/10.1137/S1052623499362822>.
- [35] Sanjay Mehrotra. On the implementation of a primal-dual interior point method. *SIAM Journal on Optimization*, 2(4):575–601, 1992.
- [36] Fumio Kikuchi, Masayuki Okabe, and Hidehiro Fujio. Modification of the 8-node serendipity element. *Computer methods in applied mechanics and engineering*, 179(1):91–109, 1999.
- [37] Carlos A. Felippa. A study of optimal membrane triangles with drilling freedoms. *Computer Methods in Applied Mechanics and Engineering*, 192(16):2125–2168, 2003.
- [38] Shahriar Setoodeh, Mostafa Abdallah, Zafer Gürdal, and Brian Tatting. Design of variable-stiffness composite laminates for maximum in-plane stiffness using lamination parameters. In *46th AIAA/ASME/ASCE/AHS/ASC Structures, Structural Dynamics and Materials Conference*, page 2083, 2005.



# 4

## EFFICIENT STRENGTH OPTIMIZATION OF VARIABLE STIFFNESS LAMINATE

*When we see men of virtue, we should think of equaling them*  
见贤思齐

Confucius

### 4.1. INTRODUCTION

In structural design, it is necessary to verify that the internal loads during operation do not exceed an allowable limit, also named as failure strength, in order to guarantee the integrity of a structure. This process typically requires the computation of a stress or strain-based scalar measured at every point in the structure under design loads and, subsequently, a verification that it does not exceed the critical value. Correspondingly, the formulation of a strength-oriented optimal design problem requires this local measurement (i.e., either element or point wise) to be constrained. One way to formulate such a problem is using the min-max format in which the maximum local failure stress is minimized with respect to the design (Khani et al. [1]). However, a significant drawback of this format is that an extreme computational cost is demanded in order to deal with a large scale problem. Two principal sources of the computational cost are the sensitivity analysis executed for every individual failure index and the massive size of the sub-problem to be solved in the optimization.

In order to reduce the computational cost of structural optimization with local constraints,  $p$ -norm formulation can be applied to aggregate the local constraints into a



single global constraint in the design domain. In contrast to the min-max formulation, the computational work of the sensitivity analysis using the  $p$ -norm failure index can be reduced dramatically with the adjoint method, since the local failure indices are condensed into a global one. Simultaneously, the size of the subproblem is reduced effectively, which makes the optimization efficient to be solved. This approach was used by Duysinx and Sigmund [2] to reduce the computational cost of stress constrained topology optimization for an isotropic material. Le et al. [3] proposed an adaptive normalization scheme as well as an interlacing regional stress measure for the  $p$ -norm stress constraint, which together provide direct control on the local stresses. Holmberg et al. [4] proposed two different ways of clustering the stress constraints in the  $p$ -norm formulation, which effectively reduced the stress concentration in topology optimization. The  $p$ -norm aggregation has also been applied in a multi-constrained and multi-load topology optimization by Deng and Suresh [5]. In order to successfully constrain the maximum stress, a correction for the upper bound  $p$ -norm stress constraint was proposed by Lee et al. [6] in topology optimization with the phase-field method. It was achieved by scaling the upper bound  $p$ -norm formulation with a scalar computed from the ratio between the lower bound  $p$ -norm formulation and its upper bound counter-part. Kiyono et al. [7] used a multi- $p$ -norm to maximize the safety factor in topology optimization. Moreover, Verbart et al. [8] demonstrated that the lower bound  $p$ -norm function also has a relaxation effect on the stress constraint in topology optimization.

The aforementioned research has focused on isotropic materials. Whereas, relevant research on efficient strength-oriented optimization of novel composite laminate is relatively rare due to the increasing complexity in addressing the failure criteria. Based on the discrete material optimization (DMO) method developed by Lund and Stegmann [9], the  $p$ -norm was applied to aggregate the failure indices based on maximum strain or maximum stress criterion (Lund [10]). It was utilized as both objective and constraints in the numerical tests which were solved by sequential linear programming (SLP). In a follow-up research (Sjølund and Lund [11]), the  $p$ -norm for strength constraints considering fiber failure and inter-fiber failure separately were applied in the design of wind turbine blades made of composite material. Another relevant work recently available was from Mirzendehtdel et al. [12], who employed the  $p$ -norm aggregation on failure constraints based on the Tsai-Wu failure criterion in topology optimization for additive manufacturing using an anisotropic material.

One commonly-used method for optimal design of variable stiffness laminate (VSL) is the three-step optimization method (Khani et al. [1], IJsselmuiden [13], Setoodeh et al. [14], IJsselmuiden et al. [15], Dillinger et al. [16], Abdalla et al. [17], Hao et al. [18]), which relies on the lamination parameters as a primary set of design variables. In the first step of the method, the optimal lamination parameters are identified. Subsequently, in the second step, the fiber angles in each ply of a composite laminate are retrieved from the optimal lamination parameters. Finally, in the third step, the fiber paths of the VSL are constructed based on the fiber angles obtained.

The aim of this chapter is two-fold: (*i*) to develop and implement a  $p$ -norm approach for strength optimization of the VSL using the lamination parameters as primary design variables, and (*ii*) to compare the performance of the  $p$ -norm approach with an

existing min-max bound formulation (Khani et al. [1]) within the same three-step optimization framework. Till now, the  $p$ -norm approach has not been investigated with the lamination parameters as design variables in the three-step optimization framework for strength optimization. Moreover, the advantage of the current work is that it can be generalized to the DMO or to address different failure criteria in strength optimization.

In order to validate and simplify the Tsai-Wu failure criterion in terms of the lamination parameters in this work, an elliptical formulation of the conservative failure envelope (Khani et al. [1]) is employed. The  $p$ -norm failure index is then obtained with the upper bound  $p$ -norm function. To set up the sub-problem, a two level approximation for the  $p$ -norm failure index is employed. Finally, the strength optimization is resolved with Mehrotra's predictor-corrector interior point method (Mehrotra [19]) within the framework of conservative convex separable approximation (CCSA) by Svanberg [20]. In the numerical results, the effect of the  $p$  value on the optimal result, the mesh convergence of the numerical results and the CPU time are checked in detail.

The structure of this chapter is as follows: Section 4.2 describes the structural analysis of the VSL, the  $p$ -norm failure index and its two level approximation. The formulation of the strength optimization and the corresponding methods to solve the problem are discussed in Section 4.3. In Section 4.4, numerical results on the effect of  $p$  and the mesh convergence of the optimal solutions and comparison with min-max bound formulation are demonstrated for a square plate with a cut-out. Another numerical case of the L-shaped plate is tested in Section 4.5 to examine the performance of the proposed strength optimization under an extreme condition. Finally, concluding remarks are provided in Section 4.6.

## 4.2. STRENGTH ANALYSIS FOR VARIABLE STIFFNESS LAMINATE AND THE GLOBAL FAILURE INDEX

The structural analysis of the VSL is undertaken using the well-established finite element method, which aims to compute the stress or strain in a model for strength estimation. The strength of the VSL is represented locally by a failure index based on the Tsai-Wu failure criterion in this work. In order to reduce the computational cost of the strength optimization, a global aggregation is introduced with the upper bound  $p$ -norm formulation to aggregate the local failure indices into a global one, also referred to as " $p$ -norm failure index". Subsequently, a two level approximation is employed for the global failure index to ensure both the convexity and conservativeness of the sub-problem required by the convex optimization framework. Details about the structural analysis of the VSL,  $p$ -norm failure index, its two level approximation are described in this section.

### 4.2.1. STRUCTURAL ANALYSIS FOR THE VSL

The structural analysis for the VSL in Step 1 of the three-step optimization method is implemented with the finite element method (FEM) in this work, where the standard

procedure remains but the material stiffness is defined node-wise in the model. In particular, the 8-node serendipity element (Kikuchi et al. [21]) is applied in this work, which aims to enhance the continuity of the stress field. This is necessary based on the previous experience of sizing optimization with stress constraints (discussed in Chapter 2). The material stiffness is defined on the vertices of the element, which are also named as design nodes in the following text. The calculation of the material stiffness of the VSL is based on the classical lamination theory.

To evaluate the stiffness matrix in one element, the material stiffness at a Gauss point is obtained using a reciprocal interpolation. Taking the in-plane stiffness matrix  $A_g$  at Gauss point  $g$  as an example

$$A_g^{-1} = \sum_{i=1}^n R_{i,g} A_i^{-1}, \quad (4.1)$$

where  $A_i$  is the stiffness matrix at the  $i^{\text{th}}$  design node in the element,  $R_{i,g}$  is the shape function of the  $i^{\text{th}}$  design node estimated at the  $g^{\text{th}}$  Gauss point, and  $n$  is the total number of design nodes. In the remainder of the text, the subscript  $g$  refers to the value at the  $g^{\text{th}}$  Gauss point, and the subscript  $i$  indicates the value at the  $i^{\text{th}}$  design node consistently.

Once the stiffness matrix is obtained for each element, the global stiffness matrix  $K$  can be obtained following the standard assembling procedure. The displacement  $\mathbf{u}$  for each degree of freedom can be obtained through

$$K\mathbf{u} = \mathbf{f}, \quad (4.2)$$

where  $\mathbf{f}$  is the external force applied on the model. Thereafter, the strain or stress of the VSL can be obtained for strength calculation.

#### 4.2.2. $p$ -NORM FAILURE INDEX

First of all, an elliptical formulation of the conservative failure envelope (Khani et al. [1]) is applied in this study to approximate the safe region given by the Tsai-Wu failure criterion. The motivation is to simplify the conservative failure envelope and to ensure its effectiveness with respect to the lamination parameters. Since the explicit fiber angles are unknown a priori from the lamination parameters in the optimization, the elliptical formulation aims to approximate the Tsai-Wu failure criterion in the strain space using a quadratic function for the most critical fiber angles. Thereafter, the failure index  $r$  can be calculated as the strength measurement of the VSL from

$$a_0 r^2 + a_1 r + a_2 = 0, \quad (4.3)$$

where the coefficients  $a_0$ ,  $a_1$  and  $a_2$  are given as follows:

$$a_0 = C_0, \quad (4.4)$$

$$a_1 = C_I e_I + C_{II} e_{II}, \quad (4.5)$$

$$a_2 = C_{I,I} e_I^2 + C_{II,II} e_{II}^2 + 2C_{I,II} e_I e_{II}. \quad (4.6)$$

The values of  $e_I$  and  $e_{II}$  are the principal strains, with the subscripts refer to the maximum and minimum strain directions, respectively. The coefficients  $C_0$ ,  $C_I$ ,  $C_{II}$ ,  $C_{I,I}$ ,  $C_{II,II}$  and  $C_{I,II}$  are obtained from material strength and material stiffness matrix. Details associated with the calculation are discussed in Khani [22]. To estimate the local failure index, Eq.(4.3) is first solved at each Gauss point in the FEM model. The critical envelope is defined by  $r = 1$ . The safe region, where no strength failure occurs, is bounded by  $r \leq 1$ .

The nodal failure indices at the design nodes are then interpolated from the values at each Gauss point. This is for the convenience to have both the failure indices and the design variables (the lamination parameters) defined at the design nodes in the two level approximation (see Section 3.2.4). The failure index at the  $i^{\text{th}}$  design node is recovered using the variational formulation described in Nagy et al. [23], which results in

$$r_i = \frac{\int r R_i d\Omega}{\int R_i d\Omega}, \tag{4.7}$$

where  $R_i$  is the linear shape function of quadrilateral element for the interpolation of the Lagrange multiplier in the variational stress constraint formulation Eq.(2.10),  $\Omega$  is the entire design domain.

Once the nodal failure index is obtained, the upper bound  $p$ -norm failure index  $r^{pN}$  can be estimated by

$$r^{pN} = \left( \frac{\int_{\Omega} r^p d\Omega}{\int_{\Omega} d\Omega} \right)^{\frac{1}{p}} = \left( \frac{1}{|\Omega|} \sum_{i=1}^n |\Omega_i| r_i^p \right)^{\frac{1}{p}}, \tag{4.8}$$

where  $\Omega_i$  is the domain measured at the  $i^{\text{th}}$  design node and  $p$  is the coefficient of the  $p$ -norm formulation.

### 4.2.3. TWO LEVEL APPROXIMATION FOR $p$ -NORM FAILURE INDEX

The calculation of a convex two level approximation for the  $p$ -norm failure index  $r^{pN}$  is discussed in this section. Through a linear expansion of local failure index based on the conservative failure envelope (Eq.(4.3)) with respect to the local strain  $\mathbf{e}_g$ ,  $r_g$  can be locally approximated at Gauss point  $g$  by

$$r_g \approx \Phi_g : \mathbf{A}_g^{-1}. \tag{4.9}$$

The coefficient matrix  $\Phi_g$  is a symmetric matrix calculated by

$$\Phi_g = \frac{1}{2} \left( \mathbf{N}_g \mathbf{q}_g^T + \mathbf{q}_g \mathbf{N}_g^T \right), \tag{4.10}$$

with  $\mathbf{q}_g = \frac{\partial r_g}{\partial \mathbf{e}_g}$  being the sensitivity of  $r_g$  with respect to  $\mathbf{e}_g$ , and  $\mathbf{N}_g$  is the resultant internal force. Note that the approximation in Eq.(4.9) is called ‘‘locally approximated’’ as it only considers the variation of the stiffness matrix  $\mathbf{A}_g$ . Whereas, the load redistribution

associated with  $\mathbf{N}_g$  in  $\Phi_g$  (Eq.(4.10)) due to the variation of  $\mathbf{A}_g$  still needs to be calculated through the adjoint method. More details about Eq.(4.9) can be found in Khani et al. [1].

The nodal failure index can be obtained by substituting Eq.(4.9) into Eq.(4.7) and using the Gauss quadrature, resulting in

$$r_i = \frac{\sum_{g=1}^{n_g} (\Phi_g : \mathbf{A}_g^{-1}) R_{i,g} w_g \|\mathbf{J}_g\|}{\sum_{g=1}^{n_g} R_{i,g} w_g \|\mathbf{J}_g\|}, \quad (4.11)$$

where  $n_g$  is the total number of Gauss points in the model,  $\|\mathbf{J}_g\|$  is the determinant of the Jacobian matrix in the element, and  $w_g$  is the weight of the Gauss points. After substituting the interpolation of  $\mathbf{A}_g$  (Eq.(4.1)) into Eq.(4.11), the following expression is obtained

$$r_i = \frac{\sum_{g=1}^{n_g} (R_{i,g} w_g \|\mathbf{J}_g\| \Phi_g : (\sum_{j=1}^n R_{j,g} \mathbf{A}_j^{-1}))}{\sum_{g=1}^{n_g} R_{i,g} w_g \|\mathbf{J}_g\|}. \quad (4.12)$$

By rearranging the terms, the formulation for the nodal failure index is given by

$$r_i = \sum_{j=1}^n \Phi_{i,j} : \mathbf{A}_j^{-1}, \quad (4.13)$$

where the coefficient matrix  $\Phi_{i,j}$  of  $r_i$  with respect to  $\mathbf{A}_j^{-1}$  is

$$\Phi_{i,j} = \frac{\sum_{g=1}^{n_g} R_{i,g} w_g \|\mathbf{J}_g\| R_{j,g} \Phi_g}{\sum_{g=1}^{n_g} R_{i,g} w_g \|\mathbf{J}_g\|}. \quad (4.14)$$

Thereafter, the expression for the global failure index can be obtained by substituting Eq.(4.13) into the global failure index Eq.(4.8), which leads to

$$r^{PN}(\mathbf{A}^{-1}) = \sum_{j=1}^n \Phi_j^{PN} : \mathbf{A}_j^{-1}, \quad (4.15)$$

where  $\Phi_j^{PN}$  is obtained through the chain rule as follows:

$$\Phi_j^{PN} = \frac{\partial r^{PN}}{\partial \mathbf{A}_j^{-1}} = \sum_{i=1}^n \frac{\partial r^{PN}}{\partial r_i} \frac{\partial r_i}{\partial \mathbf{A}_j^{-1}}. \quad (4.16)$$

Hence, combining Eq.(4.8) and Eq.(4.13), the complete formulation of  $\Phi_j^{PN}$  is given by

$$\Phi_j^{PN} = \sum_{i=1}^n \left( \frac{1}{|\Omega|} \sum_{i=1}^n |\Omega_i| r_i^p \right)^{\left(\frac{1}{p}-1\right)} \left( \frac{|\Omega_i|}{|\Omega|} r_i^{(p-1)} \right) \Phi_{i,j}. \quad (4.17)$$

Since  $\Phi_j^{PN}$  is not guaranteed to be a positive semi-definite matrix, spectral decomposition is applied to convexify Eq.(4.15), which leads to

$$r^{PN}(\mathbf{A}, \mathbf{A}^{-1}) \approx \sum_{j=1}^n (\Psi_j^{PN})^- : \mathbf{A}_j + \sum_{j=1}^n (\Phi_j^{PN})^+ : \mathbf{A}_j^{-1}, \quad (4.18)$$

where  $(\Phi_j^{pN})^+$  is the positive definite part of  $\Phi_j^{pN}$  obtained from the spectral decomposition, and  $\sum_{j=1}^n (\Psi_j^{pN})^- : A_j$  is the linear expansion of the corresponding non-definite part. Details on the implementation of this spectral decomposition can be found in Khani et al. [1].

Finally, the complete first level approximation of the  $p$ -norm failure index, taking the linear expansion and load redistribution part obtained through adjoint method into consideration, is

$$r^{pN(I)}(A, A^{-1}) = \sum_{j=1}^n \Psi_j^{pN} : A_j + \sum_{j=1}^n (\Phi_j^{pN})^+ : A_j^{-1}, \quad (4.19)$$

where  $\Psi_j^{pN}$  includes  $(\Psi_j^{pN})^-$ , the linear expansion of  $r^{pN(I)}(A, A^{-1})$  and the load redistribution part calculated by solving the adjoint method (Ijsselmuiden et al. [15]).

The second level approximation for the  $p$ -norm failure index  $r^{pN(II)}(\mathbf{x})$  is

$$r^{pN(II)}(\mathbf{x}) \approx r_0^{pN(I)}(\mathbf{x}_0) + (\mathbf{g}^{pN}|_{\mathbf{x}_0})^T \cdot \Delta \mathbf{x} + \frac{1}{2} \Delta \mathbf{x}^T \cdot H^{pN}|_{\mathbf{x}_0} \cdot \Delta \mathbf{x}, \quad (4.20)$$

where  $r_0^{pN(I)}(\mathbf{x}_0)$  is the value of  $r^{pN(I)}$  at the approximation point  $\mathbf{x}_0$ ,  $\mathbf{x}$  refers to the lamination parameters in this case,  $\mathbf{g}^{pN}|_{\mathbf{x}_0}$  is the gradient of  $r^{pN(I)}$  with respect to the lamination parameters at  $\mathbf{x}_0$ , and  $H^{pN}|_{\mathbf{x}_0}$  is the Gauss-Newton part of Hessian matrix. The calculation of the  $i^{\text{th}}$  component of  $\mathbf{g}^{pN}|_{\mathbf{x}_0}$  and the corresponding diagonal component of  $H^{pN}|_{\mathbf{x}_0}$  is as follows:

$$g_i^{pN} = \Psi_i^{pN} : \frac{\partial A_i}{\partial x_i} + (\Phi_i^{pN})^+ : \frac{\partial A_i^{-1}}{\partial x_i}, \quad (4.21)$$

and

$$H_{i,i}^{pN} = (\Phi_i^{pN})^+ : \frac{\partial^2 A_i^{-1}}{\partial x_i^2}. \quad (4.22)$$

### 4.3. EFFICIENT STRENGTH OPTIMIZATION WITH $p$ -NORM FAILURE INDEX

The formulation and the algorithm to resolve the strength optimization with  $p$ -norm failure index are described in this section. The  $p$ -norm failure index is the objective and the feasible domain of the lamination parameters at each design node is the constraint. Since the current work focuses on the symmetric and balanced laminate,  $V_2 = V_4 = 0$  at each design node. Therefore, the formulation of the optimization is as follows:

$$\min_{V_1, V_3} r^{pN} \quad (4.23a)$$

$$\text{subject to } 2V_{1,i}^2 - V_{3,i} - 1 \leq 0, \quad (4.23b)$$

$$V_{3,i} - 1 \leq 0 \quad i = 1 \dots n. \quad (4.23c)$$

The aforementioned two level approximation for  $r^{PN}$  is employed to set up the sub-problem. The Karush-Kuhn-Tucker (KKT) condition of the sub-problem is addressed using Mehrotra's predictor-corrector interior point method (Mehrotra [19]) due to its fast convergence rate. The detailed process to deal with the sub-problem follows the procedure in Section 2.3.4, which is omitted here for conciseness. The conservative convex separable approximation (CCSA) (Svanberg [20]) is chosen as the optimization framework to control the convergence in different levels.

The conservativeness of the approximation ensures the value obtained from the approximation is higher than that from the physical analysis model in the convex optimization setup. To guarantee this character in the two level approximation for  $r^{PN}$  required in the CCSA, extra damping functions, featured to be convex and separable, are added to both the first and the second level in the framework. To this end, the first level approximation together with damping is denoted as

$$\check{r}^{PN(I)}(\mathbf{A}, \mathbf{A}^{-1}) = r^{PN(I)}(\mathbf{A}, \mathbf{A}^{-1}) + \rho^{(I)} d^{(I)}(\mathbf{A}, \mathbf{A}^{-1}), \quad (4.24)$$

where  $\rho^{(I)} \in \mathbb{R}^+$  is the damping factor in the first level to scale the effect of the damping function  $d^{(I)}$ . This ensures that the approximation Eq.(4.24) is conservative, but not over conservative. It is updated in the iterative procedure. The function  $d^{(I)}(\mathbf{A}, \mathbf{A}^{-1})$  is given by

$$d^{(I)}(\mathbf{A}, \mathbf{A}^{-1}) = \sum_{i=1}^n w_i \left( \mathbf{A}_i : \mathbf{A}_{0,i}^{-1} + \mathbf{A}_{0,i} : \mathbf{A}_i^{-1} - 2\mathbf{l} : \mathbf{l} \right), \quad (4.25)$$

where  $\mathbf{l}$  is the identity matrix,  $\mathbf{A}_{0,i}$  is the in-plane stiffness at the approximation point,  $w_i$  is the weight factor for the terms at each design node with  $w_i = \frac{|\Omega_i|}{|\Omega|}$ . The value of  $d^{(I)}(\mathbf{A}, \mathbf{A}^{-1})$  and its first derivative at the approximation point are zero, which ensures Eq.(4.24) is still valid at the approximation point.

The corresponding second level approximation with damping added is expressed as

$$\check{r}^{PN(II)}(\mathbf{V}_1, \mathbf{V}_3) = r^{PN(II)}(\mathbf{V}_1, \mathbf{V}_3) + \rho^{(II)} d^{(II)}(\mathbf{V}_1, \mathbf{V}_3), \quad (4.26)$$

where  $\rho^{(II)} \in \mathbb{R}^+$  is the damping factor in the second level to scale the effect of the damping function  $d^{(II)}$ . The function  $d^{(II)}(\mathbf{V}_1, \mathbf{V}_3)$  in this level is formulated as follows:

$$d^{(II)}(\mathbf{V}_1, \mathbf{V}_3) = \sum_{i=1}^n w_i \left( V_{1,i} - V_{1,i}^0 \right)^2 + \sum_{i=1}^n w_i \left( V_{3,i} - V_{3,i}^0 \right)^2, \quad (4.27)$$

where  $V_{1,i}^0$  and  $V_{3,i}^0$  are the lamination parameters at the approximation point.

The flowchart of the strength optimization in the CCSA is illustrated in Figure 4.1. The associated procedure is summarized in Algorithm 3. The optimization loop connected to the first level approximation is named as the "Level 1 optimization", which is in essence the outer loop of the CCSA. Similar rule applies to the "Level 2 optimization", which correlates with the inner loop of the CCSA. The sensitivity analysis and the convergence check using FEM analysis is called "Level FEM".

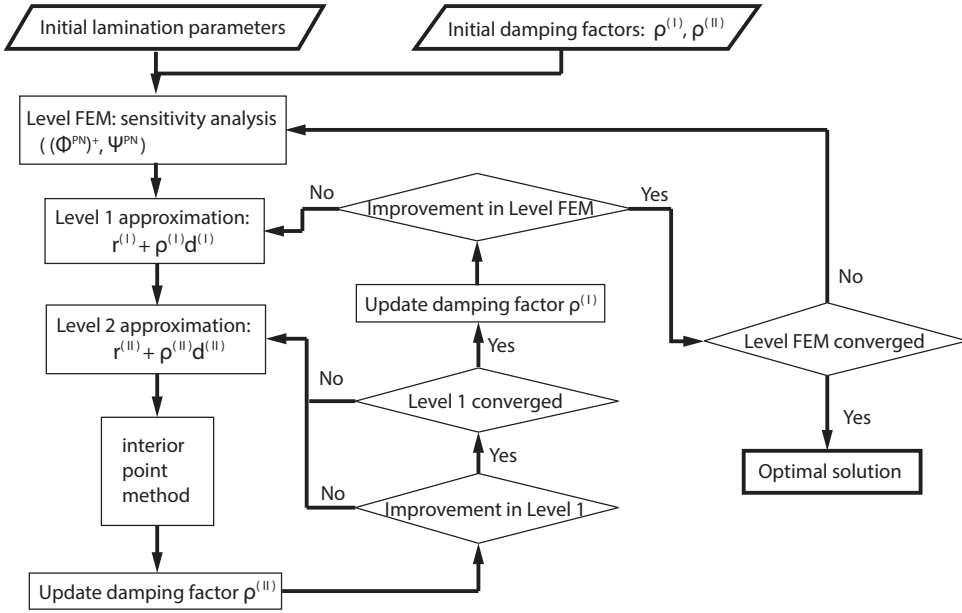


Figure 4.1: Flowchart of the strength optimization for the VSL

---

**Algorithm 3 Strength optimization with  $p$ -norm failure index**


---

- 1: Initialize  $\mathbf{x}_0$ ,  $\rho^{(I)}$ ,  $\rho^{(II)}$  and set the tolerance of stopping criterion in Level 1, Level 2 and Level FEM optimization  $\eta^{(I)}$ ,  $\eta^{(II)}$ ,  $\eta^{(0)}$ , respectively.
  - 2: Start FE analysis to calculate  $r^{PN}$  and its sensitivity  $(\Phi_j^{PN})^+$ ,  $\Psi_j^{PN}$ .
  - 3: Set up the Level 1 approximation  $\check{r}^{PN(I)}$ .
  - 4: Set up the Level 2 approximation  $\check{r}^{PN(II)}$ .
  - 5: Build up the subproblem with  $\check{r}^{PN(II)}$  and solve it with Mehrotra's predictor-corrector interior point method.
  - 6: Update damping factor  $\rho^{(II)}$ .
  - 7: Check if  $\check{r}^{PN(I)}$  improves. If  $|\Delta \check{r}^{PN(I)}| \leq \eta^{(I)}$ , solution accepted and update  $\check{r}^{PN(I)}$ . Otherwise go back to step 4.
  - 8: Check the convergence of  $\check{r}^{PN(I)}$ . If  $|\Delta \check{r}^{PN(I)}| \leq \eta^{(I)}$ , update  $\rho^{(I)}$ . Otherwise, go back to step 4.
  - 9: Check if  $r^{PN}$  from the Level FEM gets improved. If  $|\Delta r^{PN}| \leq \eta^{(0)}$ , solution accepted. Otherwise, go back to step 3.
  - 10: Check the convergence of  $r^{PN}$  from the Level FEM. If  $|\Delta r^{PN}| \leq \eta^{(0)}$ , optimal result  $\mathbf{x}^*$  is obtained, Otherwise, go back to step 2.
- 

In this work, the tolerance for the Level 2 optimization is  $\eta^{(II)} = 10^{-10}$ . The tolerance for the Level 1 optimization is  $\eta^{(I)} = 10^{-3}$  and the variation in the Level 1 approximation



$\Delta \check{r}^{PN(I)}$  is given by

$$\Delta \check{r}^{PN(I)} = r^{PN(I)} \left( (\mathbf{x}^{k+1})^* \right) - r^{PN(I)} \left( (\mathbf{x}^k)^* \right), \quad (4.28)$$

where  $(\mathbf{x}^k)^*$  is the optimal solution obtained in the  $k^{\text{th}}$  Level 1 iteration. Once the  $(k+1)^{\text{th}}$  Level 1 optimization converges, the in-plane stiffness  $A$  and its inverse  $A^{-1}$  in  $r^{PN(I)}$  (Eq.(4.19)) are updated.

The tolerance for the convergence of the Level FEM optimization is  $\eta^0 = 10^{-3}$  and the variation in this level  $\Delta \check{r}^{PN}$  is

$$\Delta \check{r}^{PN} = r^{PN} \left( (\mathbf{x}^{l+1})^* \right) - r^{PN} \left( (\mathbf{x}^l)^* \right), \quad (4.29)$$

where  $(\mathbf{x}^l)^*$  is the optimal solution obtained at the  $l^{\text{th}}$  Level FEM iteration.

The damping factor  $\rho^{(I)}$  and  $\rho^{(II)}$  are updated as follows:

$$\rho^{(\alpha),t+1} = \delta \rho^{(\alpha),t}, \quad (4.30)$$

where  $\alpha = I, II$  and  $t$  is the number of iterations in the  $\alpha^{\text{th}}$  level optimization. To calculate  $\delta$ , a parameter  $\underline{\delta}$  is computed first at an optimal solution  $\mathbf{x}^*$  in the  $\alpha^{\text{th}}$  level

$$\underline{\delta} = \frac{r^{PN(\alpha-1)}(\mathbf{x}^*) - \check{r}^{PN(\alpha)}(\mathbf{x}^*)}{\rho^{(\alpha),t} d^{(\alpha)}(\mathbf{x}^*)} + 1. \quad (4.31)$$

Then  $\delta$  in the  $\alpha^{\text{th}}$  level is obtained using:

$$\delta = \begin{cases} \check{\delta} & \underline{\delta} > \check{\delta} \\ \underline{\delta} & \check{\delta} < \underline{\delta} \leq \hat{\delta} \\ \hat{\delta} & 1 < \underline{\delta} \leq \hat{\delta} \\ 1 + 0.5 \tanh(2\underline{\delta} - 2) & \underline{\delta} \leq 1. \end{cases} \quad (4.32)$$

The function for the  $\underline{\delta} \leq 1$  case constrains the damping factor  $\rho^{(\alpha)}$  to decrease no further than to half of the current value when the accepted optimum  $\check{r}^{PN(\alpha)}(\mathbf{x}^*)$  is more than  $r^{PN(\alpha-1)}(\mathbf{x}^*)$ .

In this work, the value of  $\check{\delta}$  and  $\hat{\delta}$  are chosen to be 3 and 1.02, respectively. More details about the optimization procedure can also be found in Peeters et al. [24, 25].

#### 4.4. STRENGTH OPTIMIZATION ON A SQUARE PLATE WITH A CUT-OUT

To demonstrate the effectiveness and efficiency of the strength optimization with  $p$ -norm failure index, a typical numerical test is implemented. In this test case, a square plate with a circular cut-out is used to test the effect of  $p$  value on the optimal results. At the same time, the mesh convergence study of the optimal solution and the efficiency comparison with the min-max bound formulation are studied in this test.

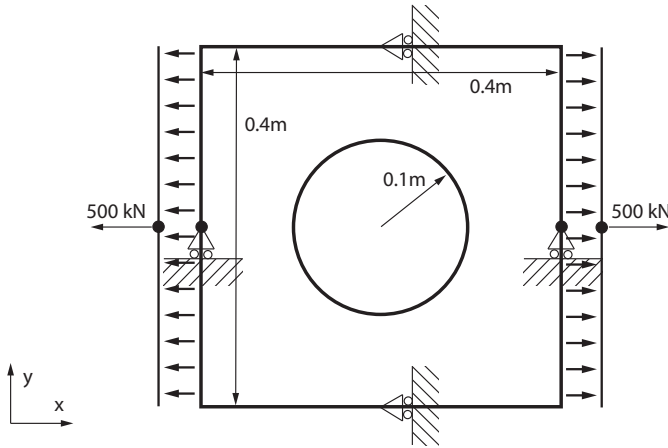


Figure 4.2: Square plate with a central hole

Figure 4.2 depicts the model in this numerical case. The central points of the top and bottom edges in the plate are fixed in the  $x$  direction. Meanwhile, the central points of the left and right edges are fixed in the  $y$  direction to prevent the rigid body motion. Multipoint constraints are applied on both the left and right edges to ensure an identical deformation in the  $x$  direction. A load of 500kN is applied on both the left and right edges. The material properties of the laminate are as follows:  $E_1 = 148\text{GPa}$ ,  $E_2 = 9.65\text{GPa}$ ,  $G_{12} = 4.55\text{GPa}$  and  $\nu_{12} = 0.3$ , with 1 indicating the fiber direction, 2 referring to the direction transverse to the fiber (see Nagy et al. [26]). The strength properties are chosen as those in Khani et al. [27]. The tensional and compressional strength along the fiber are  $X^t = 2.28\text{GPa}$  and  $X^c = 1.44\text{GPa}$ , respectively. The tensional and compressional strength transverse to the fiber are  $Y^t = 0.057\text{GPa}$  and  $Y^c = 0.228\text{GPa}$ , respectively. The pure shear strength is  $S = 0.071\text{GPa}$ .

The thickness of each ply is 0.6mm and the number of design layers is 6 in a symmetric and balanced stacking sequence (i.e., 24 layers in total). The initial design is a quasi-isotropic laminate, where both  $V_1, V_3 = 0$  at each design node. In order to have a broad view of the strength optimization with global failure index, the effect of  $p$  value is studied systematically on a reference FEM model, a refined model and half of the reference model with symmetric boundary condition. Finally, the numerical results from the local min-max bound formulation are illustrated for comparison.

#### 4.4.1. EFFECT OF $p$ ON THE ON THE OPTIMAL RESULT

In this test, the topology in Figure 4.2 is discretized using 512 elements and 576 design nodes, which also serves as a reference model in the subsequent sections. The maximum local failure index associated with the initial design is  $r_{max} = 1.033$ , slightly over the strength tolerance (which is  $r = 1$ ). This intends to demonstrate that the maximum

failure index in the model can be reduced below the critical value with the strength optimization. The strength optimization with global failure index is conducted with  $p = 1, 2, \dots, 11$ . To clarify the trend of the results, the distribution of the optimal  $V_1$ ,  $V_3$  and the corresponding local failure index (FI) are shown for four representative cases (i.e.,  $p = 1, 4, 6, 8$ ) in Figure 4.3.

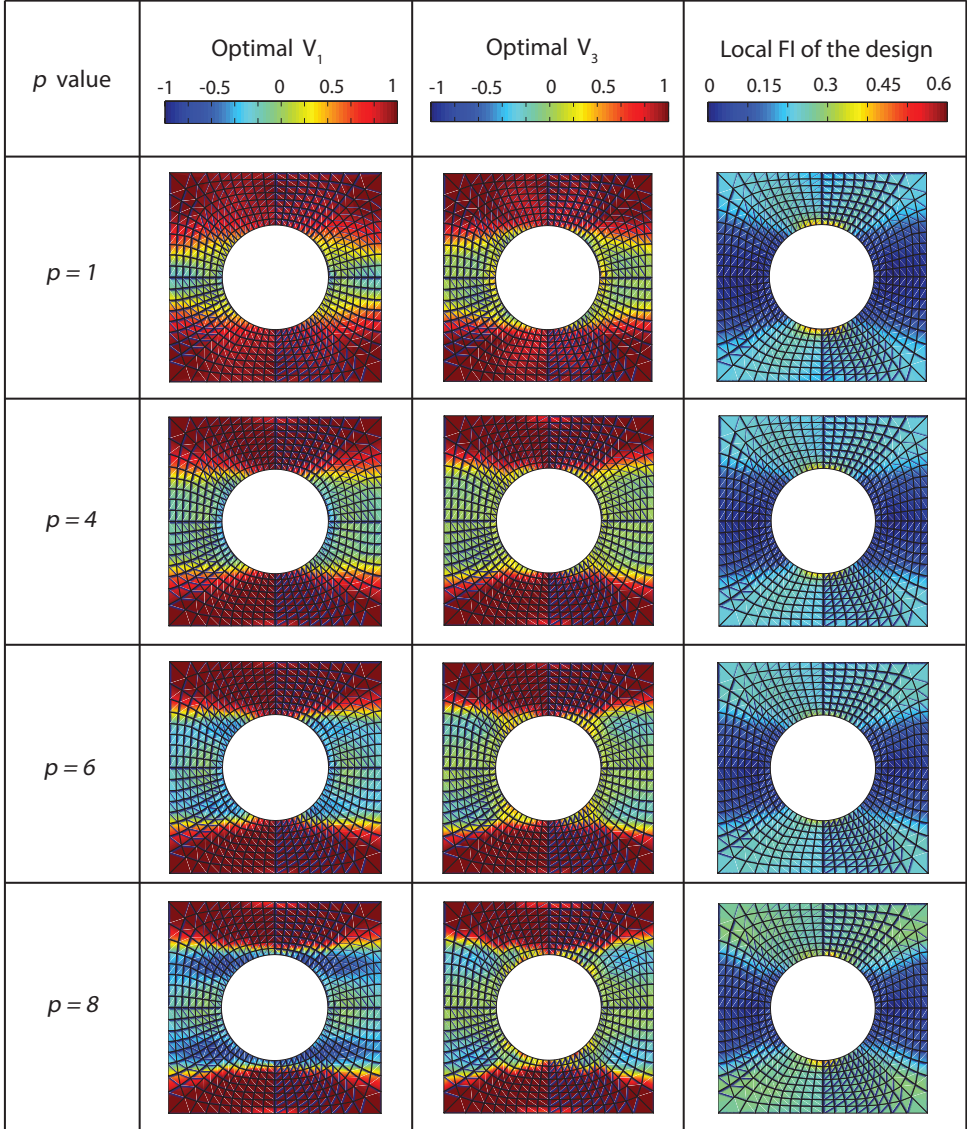


Figure 4.3: Effect of  $p$  on the optimal results in the reference model

From the contour plots of the optimal local failure index, all the figures feature a highly

stressed region located at the top and bottom half of the plate. Especially, a stress concentration can be observed around the edge of the cut-out with  $p = 1$ , which is to minimize the average of the local failure indices. When the  $p$  value increases to 4 and 6, the stress concentration region reduces in magnitude. This indicates that a higher  $p$  value, which elevates the effect of the highest local failure indices in the  $p$ -norm failure index, helps to reduce the maximum local failure index more effectively. In particular, for the results of  $p = 6$ , the maximum value is more uniform towards the highly stressed region of the plate (0.346 to 0.2 respectively). However, when the  $p$  value further increases to 8, the failure indices in the highly stressed region increase to roughly 0.3, which is undesirable. The stress concentration around the top and bottom edge of the central hole reappears. This indicates that a proper value of  $p$  in the  $p$ -norm failure index is required in order to effectively improve the load distribution in the plate.

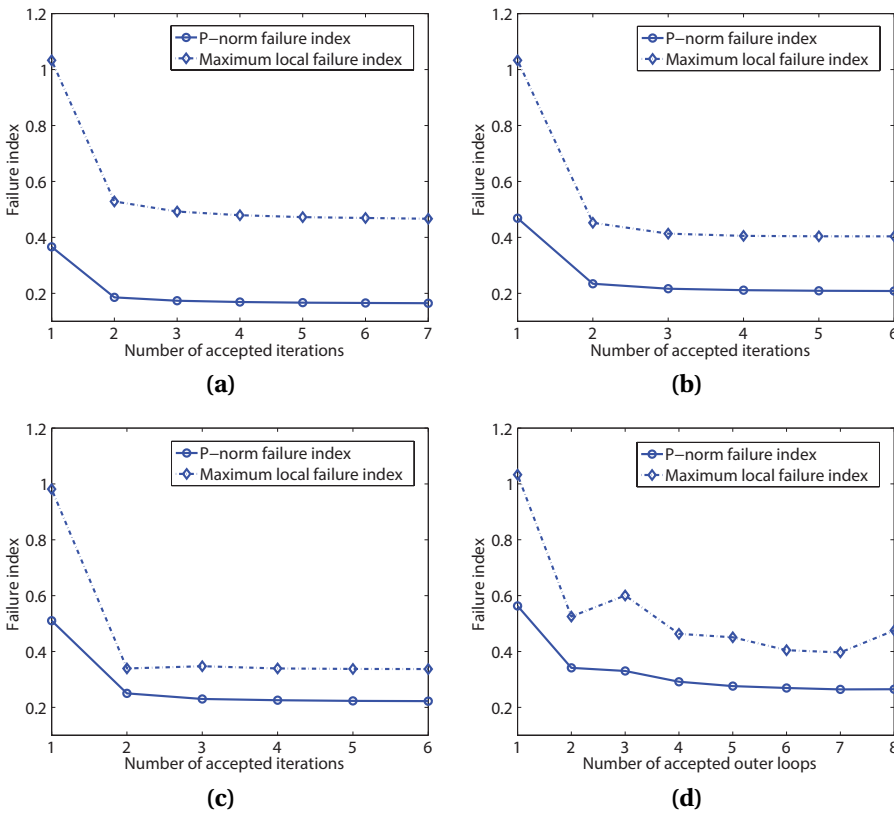


Figure 4.4: History of the failure index in the reference model (a)  $p = 1$  (b)  $p = 4$  (c)  $p = 6$  (d)  $p = 8$

The optimal  $\mathbf{V}_1$  and  $\mathbf{V}_3$  for the aforementioned  $p$  values are presented in the second and third column of Figure 4.3. For all of the cases, both  $\mathbf{V}_1$  and  $\mathbf{V}_3$  in the top and bottom of the plate are close to 1. The associated fiber paths are aligned with the x direction in order to carry the tension in the model. When  $p = 4, 6$ , this region is reshaped linking to the top

and bottom edge of the cut-out to reduce the stress concentration. The remaining parts of both  $\mathbf{V}_1$  and  $\mathbf{V}_3$  are close to 0 when  $p = 1, 4$ , indicating that the layup of fiber paths are still quasi-isotropic. Nevertheless for  $p = 6$ , on the edges next to the stress concentration region,  $\mathbf{V}_1$  appears to be around  $-0.5$  and  $\mathbf{V}_3$  is approximately  $0.5$ . This means that the fiber angles are oriented between  $60^\circ$  and  $90^\circ$  to transfer the internal force. The overall design results in an efficient reduction of the stress concentration. However, when  $p = 8$ , the contour plots of  $\mathbf{V}_1$  and  $\mathbf{V}_3$  exhibit obvious fluctuations, which reflects that numerical issues occur in this case. The lamination parameters around the top and bottom edges of the cut-out appear to be around  $-0.5$  for  $\mathbf{V}_1$  and  $0.6$  for  $\mathbf{V}_3$ . The orientation of the fiber paths become around  $70^\circ$ . Hence, the load carrying capacity for tension is reduced in this section.

## 4

The convergence history of both the  $p$ -norm failure index and the maximum local failure index for  $p = 1, 4, 6, 8$  is shown in Figure 4.4. Regarding the  $p$ -norm failure index, which is the objective of the strength optimization, it decreases consistently in each accepted iteration (outer loop in the CCSA) for all the  $p$  values. This demonstrates that the setup of the strength optimization with global failure index is stable. From the curves of the maximum local failure index, it can be observed that a reduction from 1.033 to below 0.6 is achieved for all cases. Therefore, at least a 42% improvement in strength has been achieved through the strength optimization with  $p$ -norm failure index. According to Figure 4.4 (a) and (b), the strength optimization converges steadily within 7 accepted outer loops when  $p = 1, 4$ . When  $p = 6$  as shown in Figure 4.4 (c), a slight increment appears for the maximum local failure index in the third accepted outer loops. In contrast, as  $p = 8$ , the convergence history fluctuates and the total number of iterations also increases to 8 (see Figure 4.4 (d)). Numerical test for  $p = 10$  indicates that the number of accepted iterations further increasing to 13, which is not shown here for brevity.

The fluctuation in the maximum local failure index is a drawback of the  $p$ -norm failure index. Since it does not control the maximum local failure index precisely, it may result in a slight increment of the maximum local value while the optimizer reduces the  $p$ -norm failure index. Together with the optimal  $\mathbf{V}_1$  and  $\mathbf{V}_3$  for  $p = 8$  in Figure 4.3, it demonstrates that numerical issues occur using a high value of  $p$ . This is due to the fact that the  $p$ -norm failure index amplifies the large local failure indices in the global aggregation with a high value of  $p$ . Correspondingly, the noises in the numerical computation of the  $p$ -norm failure index and its sensitivity are amplified as well. Also as discussed in the previous work (Le et al. [3], Lee et al. [6], Verbart et al. [8], Duysinx and Bendsøe [28]), numerical instability and high nonlinearity occur as  $p$  increases over a certain range (i.e., which is 6 in Lee et al. [6]). Therefore, a proper  $p$  value should be chosen for the  $p$ -norm aggregation formulation.

#### NUMERICAL RESULTS ON A REFINED MODEL

In the refined model, there are 2048 elements and 2176 design nodes (nearly fourfold as those in the reference model). The intention of the test is to check the effect of mesh size on the results. Particularly, the mesh dependency of the optimal solutions and effect of mesh size on the proper value of  $p$  value are investigated. As in the reference model, the



$p$  values also range from 1 to 11. Figure 4.5 illustrates the optimal  $V_1$ ,  $V_3$  as well as the optimal local failure indices (FI) for  $p = 1, 4, 6, 8$ .

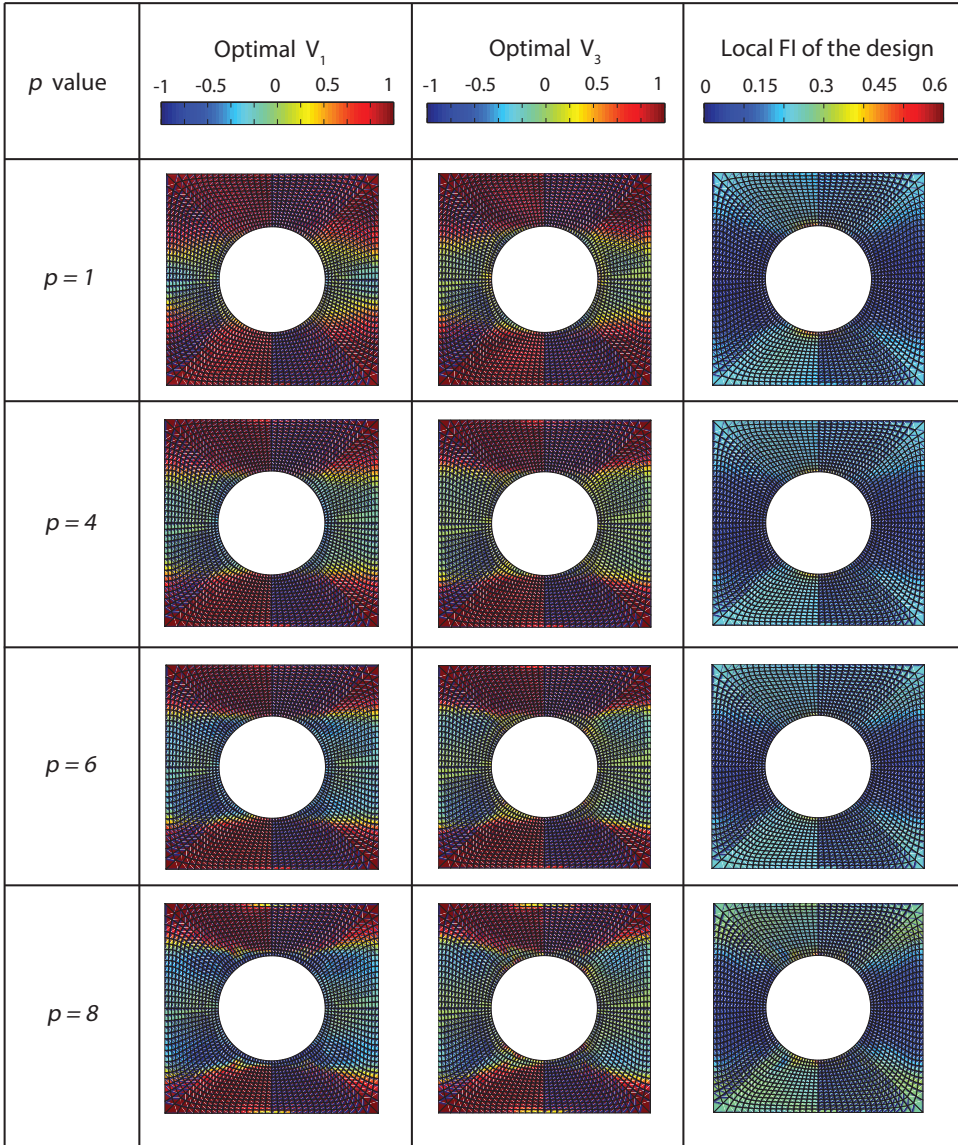


Figure 4.5: Effect of  $p$  on the optimal results with the refined mesh

First of all, the optimal solutions for each  $p$  value in the refined model (Figure 4.5) are compared with those in the reference model (Figure 4.3) to investigate the mesh convergence of the strength optimization. The contour plots of  $V_1$  and  $V_3$  between the two

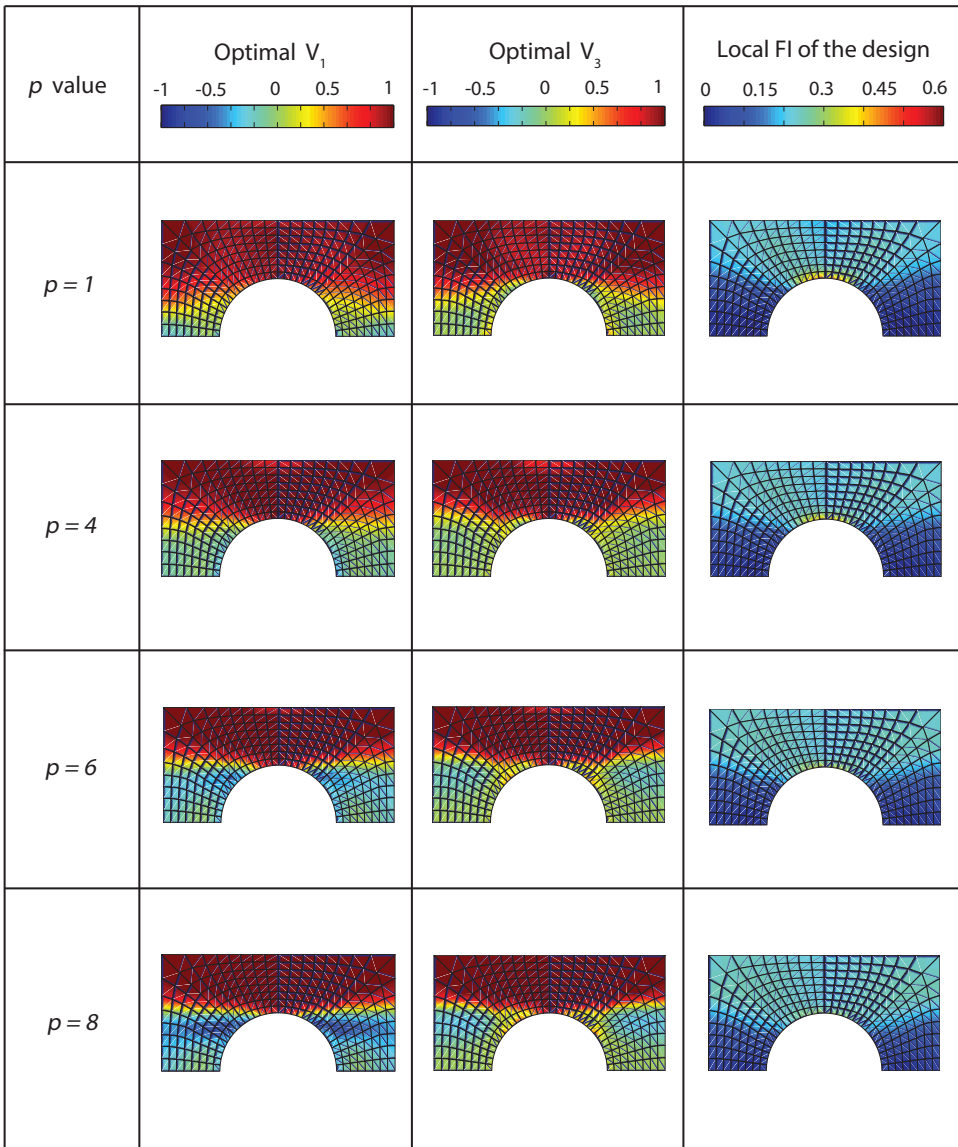
models are similar for each listed  $p$  value, which indicates mesh convergence for the optimal design. Specifically, the  $\mathbf{V}_1$  and  $\mathbf{V}_3$  are close to 1 on the top and bottom of the plate. As the  $p$  value increases to 4 and 6, the red regions of  $\mathbf{V}_1$  and  $\mathbf{V}_3$  become sharper towards the top and bottom edge of the central hole, which reduces the stress concentration in this part. Similar to the reference model for  $p = 6$ , the distributions of  $\mathbf{V}_1$  and  $\mathbf{V}_3$  next to the red regions around the cut-out appear to be approximately  $-0.5$  and  $0.5$ , respectively. When  $p = 8$ , the red regions in both  $\mathbf{V}_1$  and  $\mathbf{V}_3$  shift away from the top and bottom edge of the central hole. Hence, both quantitatively and qualitatively, the results confirm that the method developed in this work leads to mesh convergence in the optimal solutions.

The proper range of the  $p$  value can be recognized from the contour plots of the optimal failure indices in the fourth column of Figure 4.5. The optimal local failure indices are in the same trend to the reference model for each  $p$  value in Figure 4.3. The stress concentration still locates at the top and bottom edge of the central hole, when  $p = 1$ . For  $p = 4$ , the maximum local failure index is effectively reduced due to the power increasing in the  $p$ -norm failure index. Such effect becomes more obvious again when  $p = 6$ , which further reduces the failure indices in the stress concentration region. Whereas, as the value of  $p$  increases to 8, the local failure indices apparently increases in the top and bottom half of the plate as in the reference model. Thus, despite the increase in accuracy, the refinement of the mesh does not increase the maximum value of  $p$  that can be used for optimization.

#### 4.4.2. NUMERICAL RESULTS ON HALF OF THE REFERENCE MODEL

Both the reference model and the refined model are symmetric along the central line in  $x$  direction, which leads to a repetition of failure indices in the top and bottom sections. In addition, the mesh is not perfectly symmetric in the top and bottom of the plate. Therefore, there are two locations that simultaneously reach the maximum value. The presence of multiple local maximums could affect the proper range of  $p$  value in the  $p$ -norm failure index. In view of this hypothesis, numerical results on a half of the reference model is exploited with a corresponding symmetry boundary condition (with the movement in  $y$  direction fixed to zero for the nodes on the symmetric axis). The mesh for the half model is essentially the same as for the reference model.

The optimal lamination parameters  $\mathbf{V}_1$ ,  $\mathbf{V}_3$  as well as the distribution of the corresponding local failure indices are shown in Figure 4.6. Comparing Figure 4.3 and 4.6, it can be observed that the results for  $p = 1, 4, 6$  in the half model are similar to those in the reference model. The local failure indices decrease as  $p$  increases from 1 to 6 and the red regions in  $\mathbf{V}_1$ ,  $\mathbf{V}_3$  are linking to the top edge of the cut-out. However, the optimal lamination parameters for  $p = 8$  are different between the two models. In particular, the half model shows further improvement in terms of decreasing the maximum local failure index as  $p$  increases from 6 to 8 as shown in the contour plot (the fourth column in Figure 4.6). This result indicates that the maximum value of  $p$  that can be used in an actual numerical implementation is sensitive to details of the FEM solution (i.e., reference and half models)

Figure 4.6: Effect of  $p$  on the optimal results in the half model

The convergence history of the four test cases in Figure 4.6 is shown in Figure 4.7. Also similar to the tests with the reference model and the refined model, the curves for the  $p$ -norm failure index are decreasing monotonically. In terms of the maximum local failure index, the trend for the cases of  $p = 1, 4$  is stable (see Figure 4.7 (a), (b)). Simultaneously, the history of the maximum local failure index fluctuates slightly in the third accepted iteration for  $p = 6$ . All these features are in common with those in the reference model



and the refined model. Whereas, for  $p = 8$  in the half model, the optimal local failure index obtained (0.314) is lower than that for  $p = 6$  (0.345). The history of the maximum local failure index does not only fluctuate in this case, but the number of the accepted iterations (i.e., the outer loop of the CCSA) also increases to 18 (Figure 4.4 (d)). Thus, the results of the half model indicates that a higher value  $p$  in the  $p$ -norm failure index can help to reduce the maximum local failure index for the model with only one maximum failure index.

4

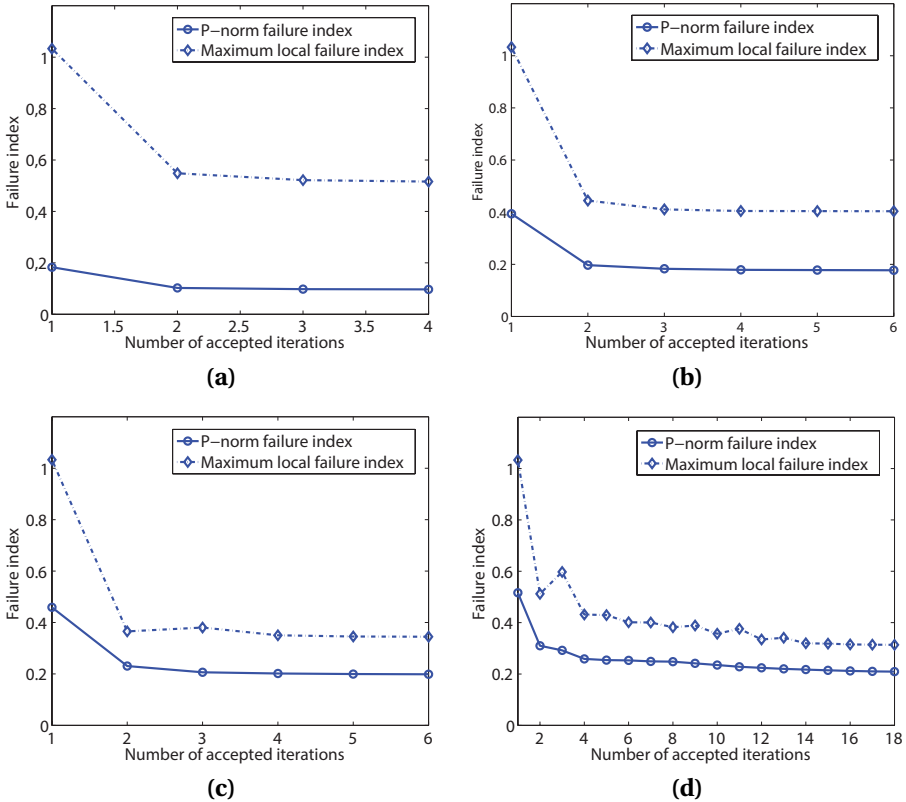


Figure 4.7: History of the failure index in the half model (a)  $p = 1$  (b)  $p = 4$  (c)  $p = 6$  (d)  $p = 8$

#### 4.4.3. OPTIMAL RESULTS WITH MIN-MAX BOUND FORMULATION

In order to execute the strength optimization using local failure indices, the bound formulation of multicriterion problem (Olhoff [29]) is applied in Khani et al. [1], which is

called *min-max bound formulation* in this section. The formulation is written as

$$\min_{\mathbf{V}_1, \mathbf{V}_3} \beta \quad (4.33a)$$

$$\text{subject to } r_i - \beta \leq 0, \quad (4.33b)$$

$$2V_{1,i}^2 - V_{3,i} - 1 \leq 0, \quad (4.33c)$$

$$V_{3,i} - 1 \leq 0 \quad i = 1 \dots n. \quad (4.33d)$$

The variable  $\beta = \max\{r_{i(i=1\dots n)}\}$  is the upper bound parameter for all of the failure indices in a structure. In essence, this formulation, which aims to minimize the maximum of the failure indices in a structure, is a local version alternative to minimize  $\|r_i\|_\infty$  (i.e.,  $r^{pN}$  with  $p \rightarrow \infty$ ) in Eq.(4.23). In order to have a global view of the strength optimization with both the global failure index and its local version alternative, the results from min-max bound formulation are provided in Figure 4.8.

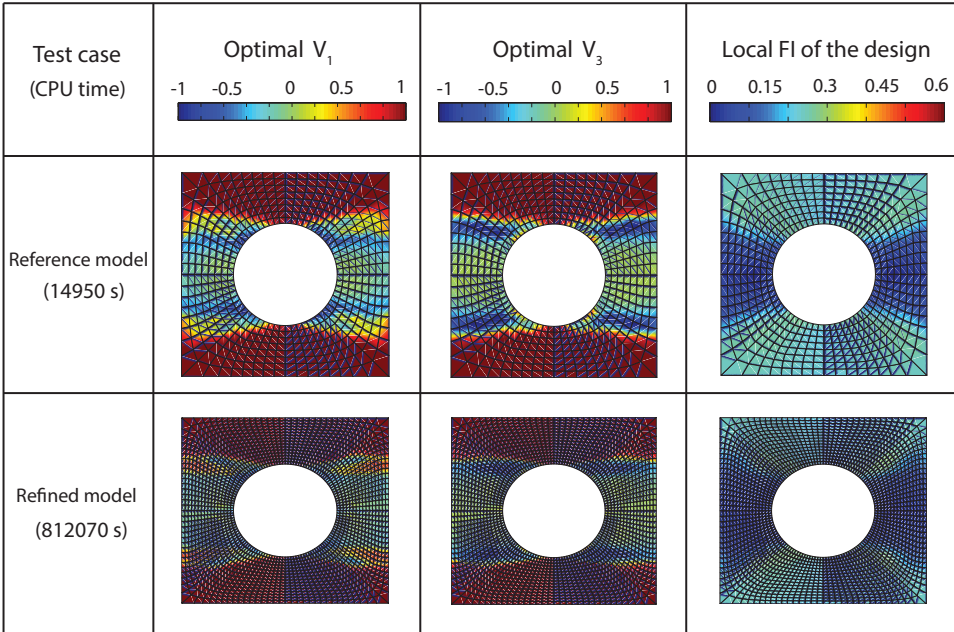


Figure 4.8: Numerical results with min-max bound formulation

From the local failure indices obtained in the optimal design, the highly stressed region is large and in the same level in both the reference model and the refined model, located next to the blue region. This is due to the fact that the failure indices reaching the upper bound in Eq.(4.33) are minimized simultaneously bounded by the parameter  $\beta$ . From the optimal  $V_1$  and  $V_3$ , it can be observed that the red regions, which are crucial to reduce the stress concentration region, converge to those with  $p = 6$  in the strength optimization using the  $p$ -norm failure index (See Figure 4.3 and 4.5). Thus, these are the optimum patterns to enhance the strength of this model effectively. Although some

discrepancy can be observed in the optimal  $\mathbf{V}_1$  and  $\mathbf{V}_3$  between the reference model and the refined model, the main features are similar. The CPU time for the two test cases is also depicted in the figure, which is 14950s for the reference model and 812070s for the refined model, respectively.

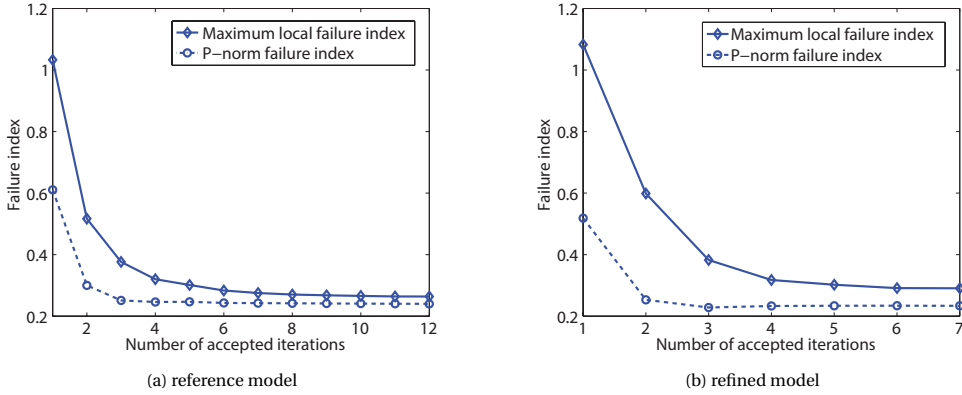


Figure 4.9: History of the failure index for the min-max bound formulation

The convergence of the history with the min-max bound formulation is shown in Figure 4.9. From both figures, the maximum local failure index is reducing consistently. The result for the reference model converges in 12 accepted iterations (outer loop in the CCSA). The maximum failure index drops from 1.033 to 0.264, with a 74.4% improvement in strength. In the refined model, maximum local failure index decrease from 1.083 to 0.291, achieving a 73.1% improvement. In both figures, the  $p$ -norm failure index with  $p = 6$  obtained in each iteration is also plotted with the dashed lines. It is found that with the min-max bound formulation, the  $p$ -norm failure index is not decreasing monotonically as the maximum local failure index. This is due to the fact that a large number of failure indices reach the upper bound during optimization in the min-max bound formulation. Therefore, the  $p$ -norm failure index increases slightly in the end of the iterations.

#### 4.4.4. COMPARATIVE ANALYSIS FOR STRENGTH OPTIMIZATION

In accordance with the  $p$ -norm approach, the goal is to take advantage of the simplicity of a global norm (i.e., integral over the whole domain) and increase the value of  $p$  as much as possible to approximate a local norm (i.e., maximum local value in the whole structure). To assess the suitability of the  $p$ -norm approach, the maximum local value of the failure index is shown in Figure 4.10a for each design obtained for a given value of  $p$  and the min-max bound formulation. The corresponding CPU time cost for various  $p$  values in the reference model, the refined model and the half models are shown in Figure 4.10b.

From Figure 4.10a, it is shown that, as expected, the maximum local failure index is decreasing as the  $p$  value increases from 1 to 6 in all the models (from 0.467 to 0.346 in the

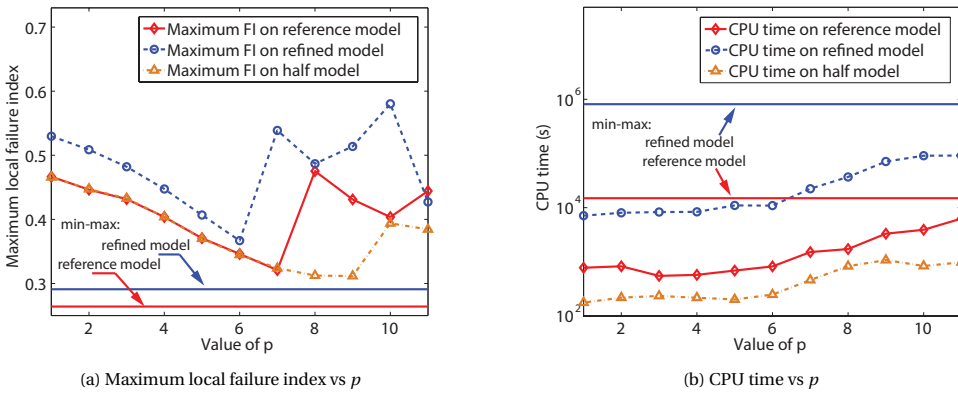


Figure 4.10: Comparison of the maximum local failure index and CPU time cost for various  $p$  values in the reference model, refined model and the half model for  $p$ -norm strength optimization

reference and the half model, and from 0.530 to 0.367 in the refined model). Observe that for the initial values of  $p$ , the reference and the half models have the same maximum local failure index since the meshes are essentially the same. The maximum local failure index for the refined mesh is higher, which reflects the increased capacity of the refined mesh to capture stress concentration in the FEM model. In the refined model, the maximum local failure index starts to increase directly to 0.539 when  $p = 7$ . Thereafter, it starts to fluctuate when  $p$  further increases. Whereas, in the reference model, the curve for the maximum local failure index drops to the lowest at 0.321 when  $p = 7$ . Later on, it starts to fluctuate from  $p = 8$ . In contrast, for the half model, the optimal failure index obtained overlaps with that in the reference model for  $p$  ranging from 1 to 7. When  $p$  is higher than 7, the maximum local failure index still decreases further until  $p = 9$  before the fluctuation starts.

In contrast, the maximum failure index obtained from the min-max bound formulation is much lower than those achieved with  $p$ -norm failure index. In particular, the value obtained in the reference model with min-max bound formulation is 0.264, which is 15.4% lower than 0.312 obtained in the half model with  $p$ -norm failure index of  $p = 9$ . Correspondingly, the value achieved in the refined model with the bound formulation is 0.291, which is 20.7% lower than 0.367 with  $p$ -norm failure index of  $p = 6$ . Therefore, the min-max bound formulation can enhance the strength of the VSL further than using the  $p$ -norm failure index.

As indicated in Section 4.4.1 and 4.4.2, the maximum value of  $p$  that can be used in practice depends on the model size as well as on qualitative aspects of the solution, such as preserving symmetry. The CPU time for the three test cases is shown in Figure 4.10b. The curves for all these cases show that the computational time is not sensitive to  $p$  as  $p$  changes from 1 to 6. In the reference model, the CPU time is constant at around 800s. Whereas, it is around 8500s in the refined model, the increment of the computational cost is close to quadratic with respect to the size of the problem (the number of design variables). In the half model, where the number of the design variables is reduced to

almost half of the reference problem, the computational cost is reduced to roughly 200s. It becomes almost a quarter of the original cost. This is due to the fact that the computational cost is dominated by the computational complexity to resolve the Schur Complement in the interior point method with direct solver. When the value of  $p$  is higher than 6, all the curves start to raise. The reason is that the number of inner loops taken within every outer loop increases evidently in the CCSA. This is another evidence to illustrate that the numerical nonlinearity becomes significant when  $p = 7$  or more, along with the contour plots of the optimal solutions (Figure 4.3, 4.5, 4.6) and the history of the maximum local failure index (Figure 4.4, 4.7).

However, the computational cost of the min-max bound formulation is indeed prohibitive comparing with that from the  $p$ -norm failure index. The CPU time for the reference model resolved with the min-max bound formulation is 14950s. Whereas, the CPU time for the best test case in the  $p$ -norm failure index, which is  $p = 7$  in the reference model, is 1512s. The CPU time for the min-max bound formulation is almost ten-fold of that with the well posed  $p$ -norm failure index. The CPU time for the refined model with the min-max bound formulation is 812070s. The corresponding value of  $p$ -norm failure index with  $p = 6$  in the refined model is 10908s. The CPU time with the min-max bound formulation is 74.4 times comparing to that of the  $p$ -norm failure index. The increment of the computational cost is almost quadratic with respect to the size of the problem.

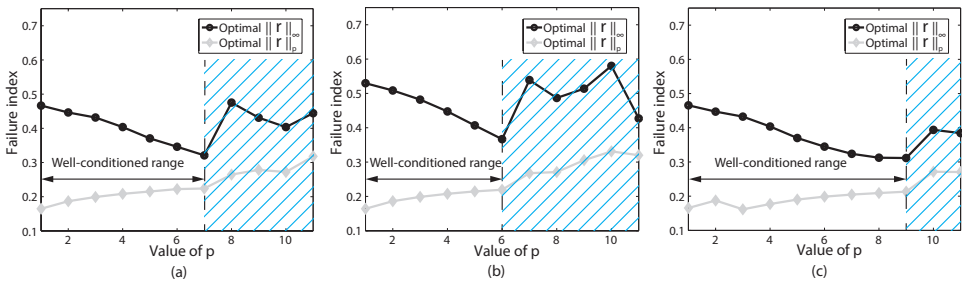


Figure 4.11:  $\|r\|_\infty$  vs  $\|r\|_p$  in three different models (a) the reference model, (b) the refined model, (c) the half model

The gaps between  $\|r\|_\infty$  (the maximum local failure index) and  $\|r\|_p$  ( $p = 1, 2, \dots, 11$ ) for the optimal designs in all of the three test cases are presented in Figure 4.11. From the three sub-figures, it can be observed that the value of  $\|r\|_p$  tends to increase consistently when the  $p$  value increases. This is due to the fact that  $\|r\|_p$  increases to the physical maximum of the local failure index (which is  $\|r\|_p$ ,  $p \rightarrow \infty$ ) with a higher  $p$  value taken. It can also be observed that  $\|r\|_\infty$  obtained in the optimal design keeps decreasing desirably when the  $p$  value increases in a certain region (referred to as the well-conditioned region) before the aforementioned numerical issues occur. Therefore, the highest  $p$  value in this well-conditioned region should be chosen to effectively reduce the maximum local failure index ( $\|r\|_\infty$ ) in strength optimization. Outside this region, the value of  $\|r\|_\infty$  obtained in the strength optimization starts to fluctuate due to the increased non-linearity.

As a result, the results in Figure 4.11 indicate that a mesh refinement actually decreases the well-conditioned range of  $p$  value while preserving symmetry with multiple locations of stress concentration allows to use higher values of  $p$ . According to the comparative analysis in Figure 4.10, the min-max bound formulation can improve the strength of the structure better than using the  $p$ -norm failure index. However, the computational cost is also more demanding comparing with the  $p$ -norm failure index for the large scale problems. Therefore, to achieve a good compromise between the strength improvement and the computational cost required, the well posed  $p$ -norm failure index is recommended to implement the strength optimization of the VSL.

## 4.5. STRENGTH OPTIMIZATION ON A L-SHAPED PLATE

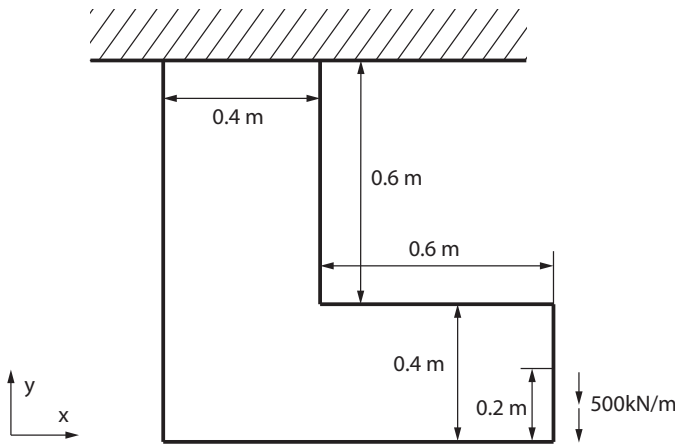


Figure 4.12: L-shaped plate

In the second numerical case, the strength optimization is implemented on an L-shaped plate subjected to a vertical load on the right edge (See Figure 4.12), which is a challenging problem due to the stress singularity at the sharp corner. The intention is to exploit the performance of the proposed method under such an extreme condition. In this case, the optimal solutions with various  $p$  values in the  $p$ -norm failure index are discussed. The mesh convergence of the optimal results for this problem with singularity issue is also studied. In addition, the optimal designs from the  $p$ -norm failure index and the min-max bound formulation are compared in terms of the maximum local failure index obtained and the CPU time cost.

The boundary condition of the model is as follows: the top edge of the plate is fixed and a distributed load of  $500\text{kN m}^{-1}$  is applied on the lower half of the right edge of the plate. The material properties of the composite laminate are the same as those in the first example in Section 4.4. The thickness of each ply is 0.6mm and the number of design layers is 6. The initial stacking sequence of the laminate of the optimization is quasi-isotropic.

#### 4.5.1. MESH-CONVERGENCE STUDY ON THE L-SHAPED PLATE

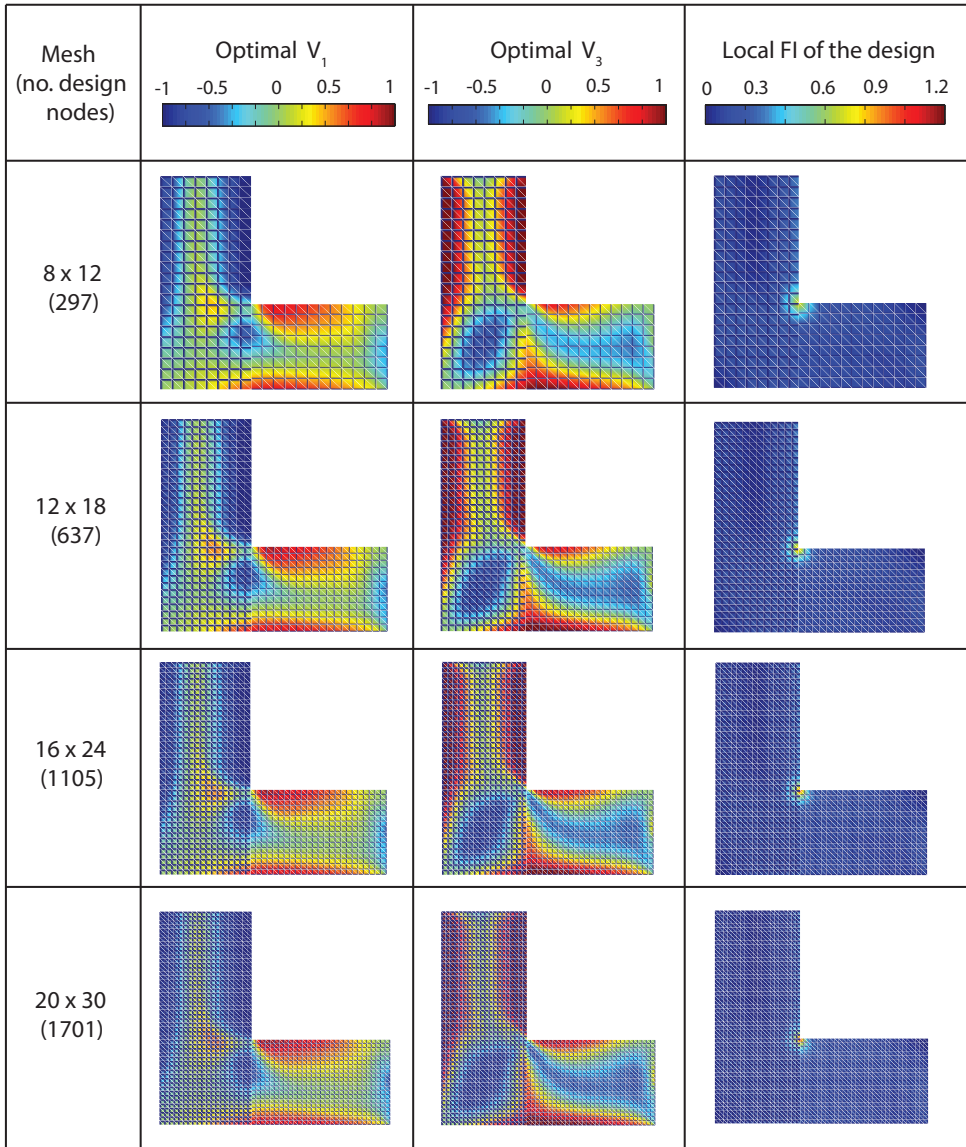


Figure 4.13: Study of the mesh convergence of the optimal results using  $p$ -norm failure index ( $p = 1$ )

In the mesh-convergence study, the numerical model is first discretized with 8 elements for the 0.4m edge, and 12 elements for the 0.6m edge. Subsequently, it is refined using  $12 \times 18$ ,  $16 \times 24$  and  $20 \times 30$  elements for the two edges, respectively. The distribution of the optimal  $V_1$ ,  $V_3$  and the corresponding failure indices for  $p = 1, 4, 6$  are computed and illustrated in Figure 4.13, 4.14, 4.15, respectively.



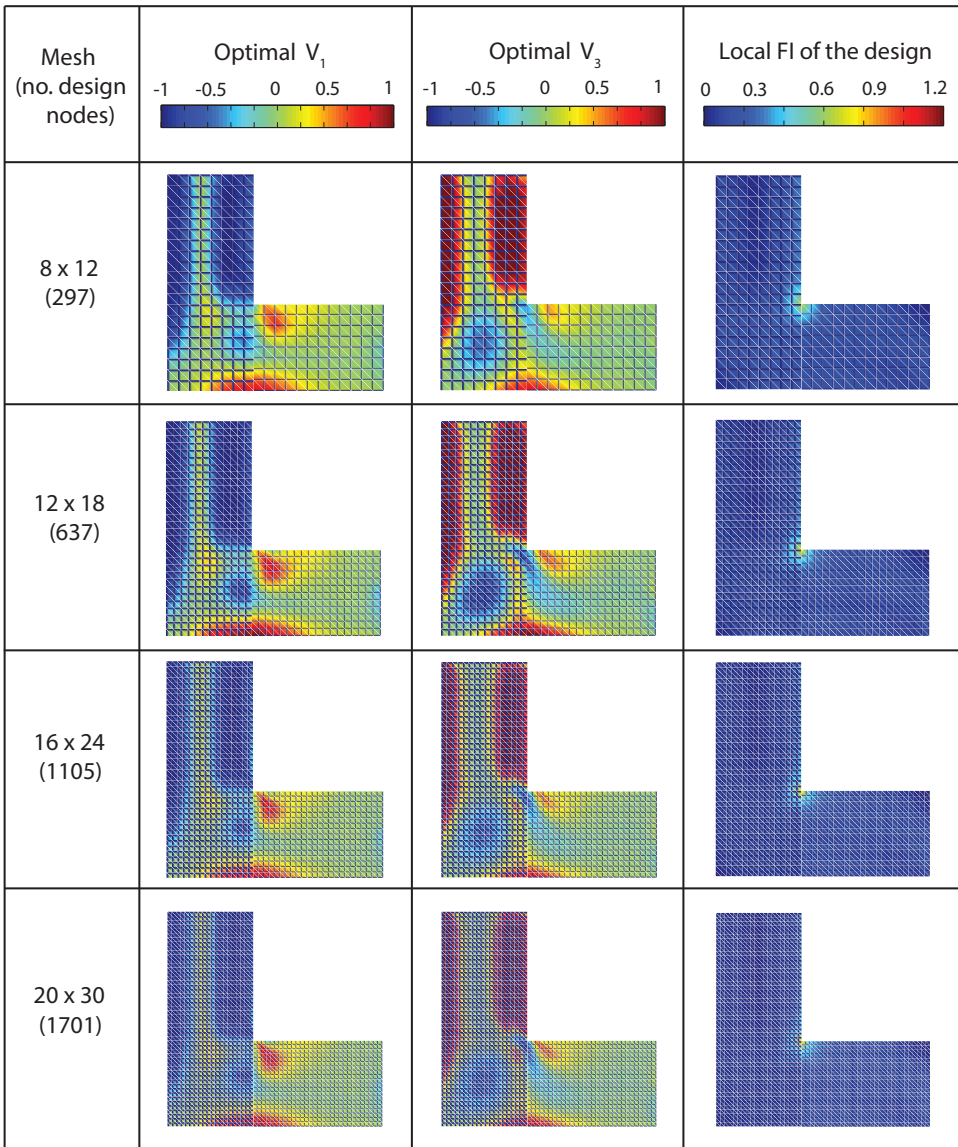


Figure 4.14: Study of the mesh convergence of the optimal results using  $p$ -norm failure index ( $p = 4$ )

As shown in the second and third columns of Figure 4.13, the distributions of  $V_1$  and  $V_3$  converge to a unique solution as the mesh of the model is refined for  $p = 1$ . The distributions of the local failure indices associated with the optimal designs also exhibit the same trend as depicted in this figure, with the maximum local failure index located at the corner of the L-shaped plate consistently. As anticipated, the maximum local value of the failure index keeps increasing in the finer mesh due to the singularity



issue. Thus, the setup for the strength optimization with  $p$ -norm failure index is demonstrated to be mesh-independent for  $p = 1$  in the L-shaped plate with stress singularity on the sharp corner, with the exception of the element where the singularity occurs (i.e., mesh-independence in the  $p$ -norm, but not in the  $p \rightarrow \infty$  case).

The numerical results for  $p = 4$  are presented in Figure 4.14. As before, the optimal dis-

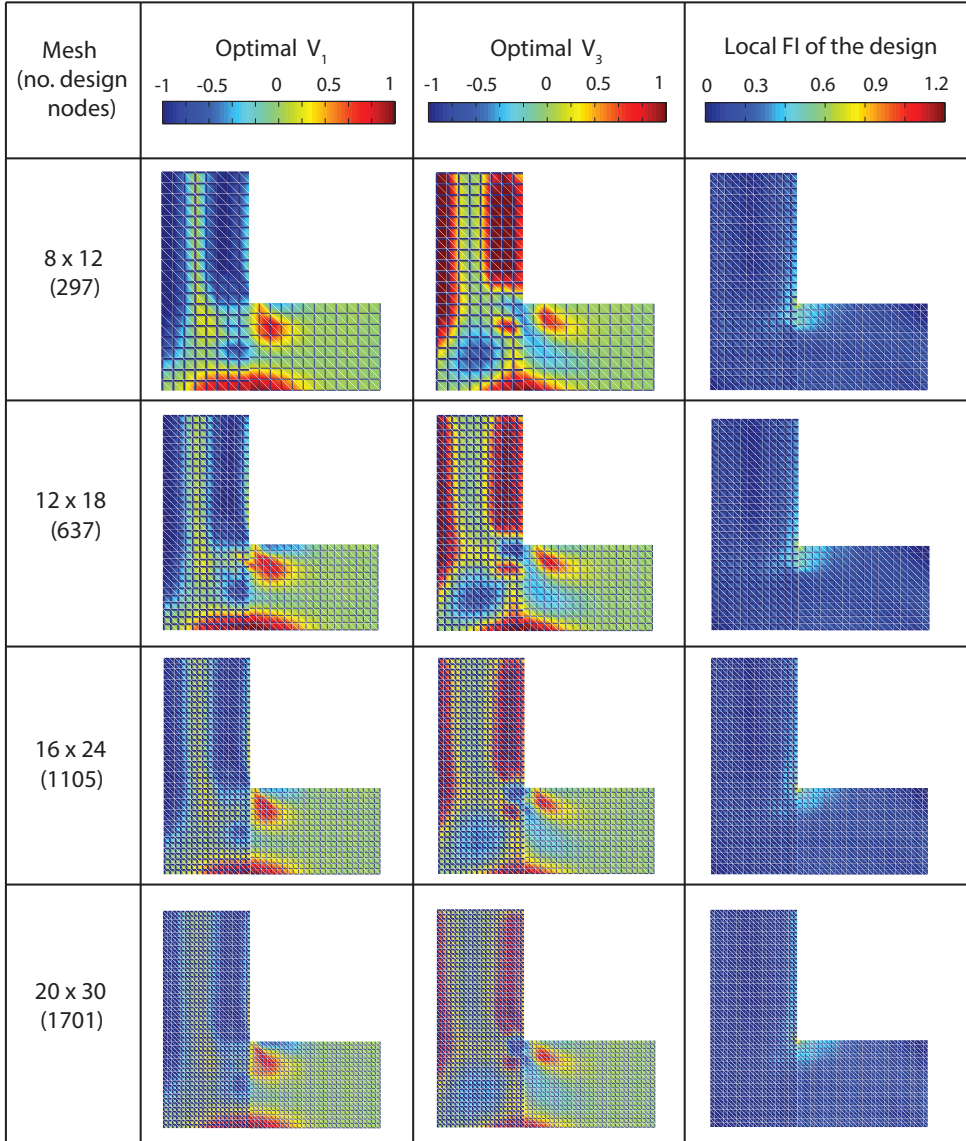


Figure 4.15: Study of the mesh convergence of the optimal results using  $p$ -norm failure index ( $p = 6$ )

tributions of  $\mathbf{V}_1$  and  $\mathbf{V}_3$  converge to a unique solution in models of different mesh sizes. The lamination parameters around the corner and the right bottom part of the L shape for  $p = 4$  are different from those with  $p = 1$ . At the corner of the plate, the  $\mathbf{V}_1$  is around 0 and  $\mathbf{V}_3$  is close to  $-1$ , which indicate that the fiber angles should lie in the  $[\pm 45^\circ]_s$  with respect to the x axis to reduce the highest stress in this region. Simultaneously, both  $\mathbf{V}_1$  and  $\mathbf{V}_3$  are nearly 0 on the right bottom part of the plate. The corresponding stacking sequence of the laminate is quasi-isotropic in order to carry the shear load on the edge. To this end, the maximum failure index in this case is obviously lower than that with  $p = 1$  for each mesh case. As a result, mesh-independence is observed again in this case and  $p = 4$  is still within the well-conditioned range, which improves the optimal design in terms of the maximum local failure index comparing with  $p = 1$ .

Figure 4.15 shows the resulting designs from  $p = 6$ . From this figure, the main features of the optimal  $\mathbf{V}_1$  and  $\mathbf{V}_3$  are in common among different mesh cases. However, discrepancy in different mesh cases can indeed be noticed as well. For instance, the distribution of  $\mathbf{V}_1$  at the corner in the  $12 \times 18$  mesh case is different from that of the other ones. Obviously, the blue region of  $\mathbf{V}_1$  and the red region of  $\mathbf{V}_3$  in the vertical section of  $20 \times 30$  case are shrunk in area comparing with the other cases. These features indicate that numerical instability already occurs when  $p = 6$  within the model including a stress singularity. In contrast to the local failure indices of  $p = 1$  and  $p = 4$ , the highest level rendered in red has completely disappeared in this case.

From the numerical results of  $p = 1, 4, 6$  in this section, the distributions of the optimal  $\mathbf{V}_1$  and  $\mathbf{V}_3$  are confirmed to converge to a unique solution with different mesh sizes. Therefore, the main conclusion of the mesh-convergence study is that the proposed method generates mesh-independent solutions desirably even in a model with singularity on stress. However, it is important to note that  $p = 6$  already leads to numerical problems in this case.

#### 4.5.2. THE OPTIMAL DESIGN FROM MIN-MAX BOUND FORMULATION

The optimal designs from the min-max bound formulation are also exploited for the L-shaped plate. The optimal  $\mathbf{V}_1$ ,  $\mathbf{V}_3$  and the corresponding distribution of local failure indices for different mesh sizes are presented in Figure 4.16. The main features of the optimal design are generally preserved as the mesh becomes denser and are similar to the design obtained from the  $p$ -norm (comparing Figure 4.15 and 4.16)

Interestingly, from the contour plots of the local failure indices in Figure 4.16, the maximum local failure index, being approximately 0.6 in the four mesh cases, is lower than those from the best designs ( $p = 6$ ) with  $p$ -norm failure index, which is around 0.8 (see Figure 4.15). Comparing the local distribution of failure indices for the min-max bound formulation with those in the  $p$ -norm cases, a noticeable feature in the local failure indices obtained in this case is that the region to reach the maximum value is larger (i.e., larger light blue region in min-max bound formulation). This indicates that the design based on the min-max bound formulation can generate a more efficient design where the internal loads are more uniformly distributed.

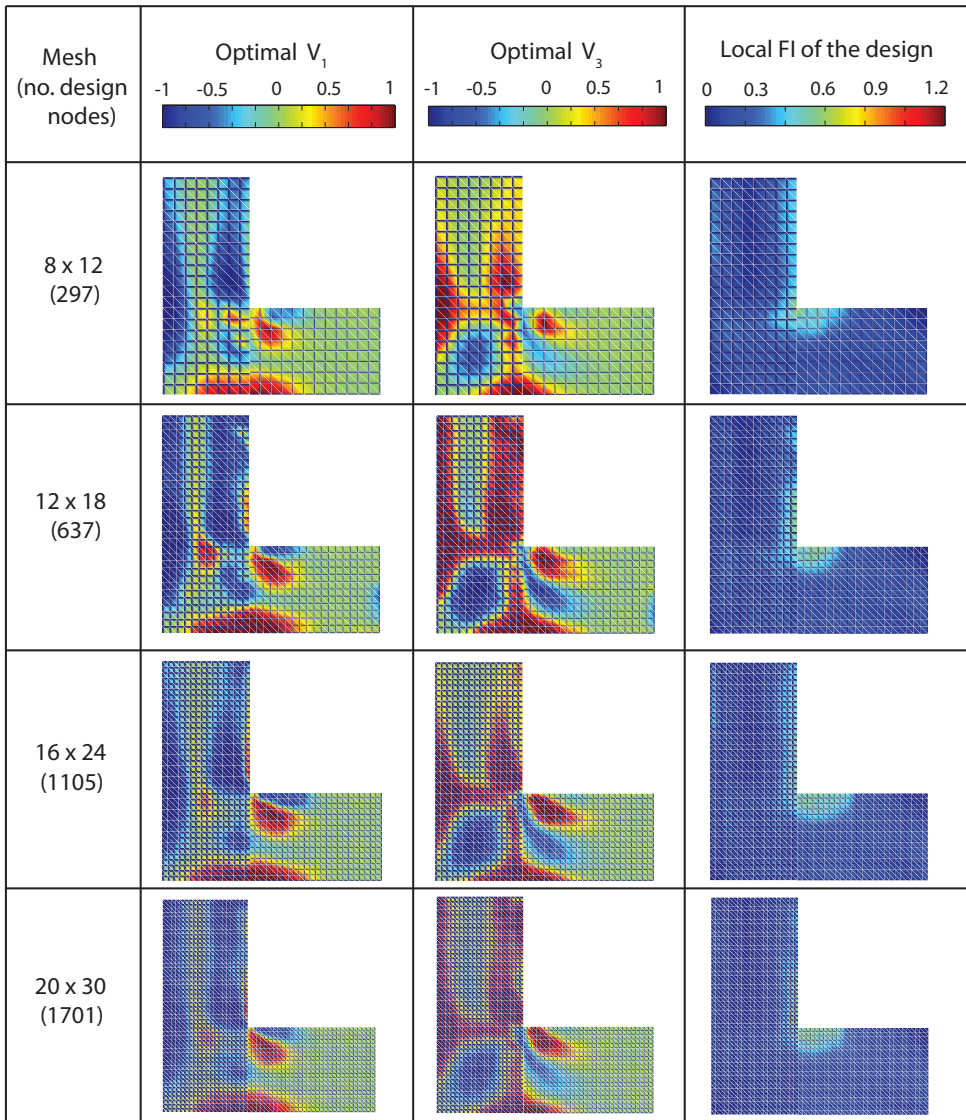


Figure 4.16: Study of the mesh convergence of the optimal results using local min-max formulation

#### 4.5.3. COMPARATIVE ANALYSIS OF THE OPTIMAL RESULTS FROM THE $p$ -NORM FAILURE INDEX AND MIN-MAX BOUND FORMULATION

In this section, the maximum local failure index and the CPU time cost obtained from the strength optimization with  $p$ -norm failure index and the min-max bound formulation are compared as depicted in Figure 4.17. The maximum local failure indices obtained with four meshes when  $p = 1, 4, 6, 8, 10$  and that from the local min-max bound

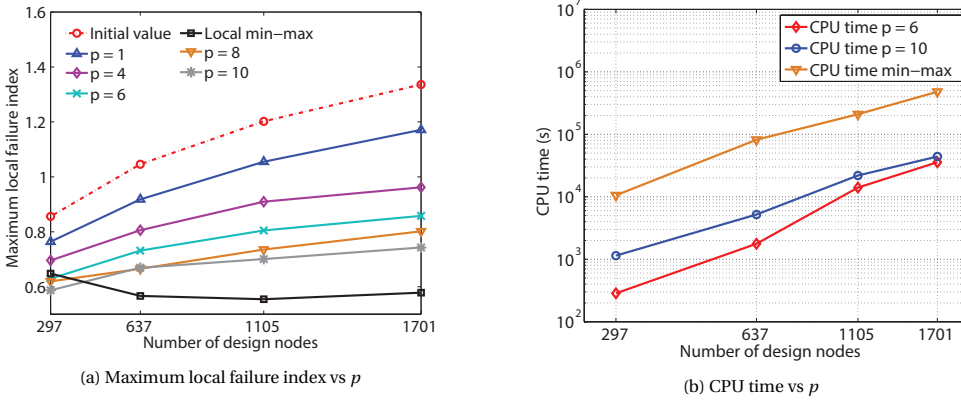


Figure 4.17: Comparison of the maximum local failure index and CPU time cost for various  $p$  value in  $p$ -norm failure index and min-max bound formulation

formulation are shown in Figure 4.17a. First of all for the initial quasi-isotropic laminate, with the mesh refinement, the maximum local failure index at the corner of the L-shaped plate keeps increasing from 0.856 to 1.336 because of the singularity issue. After the strength optimization with  $p$ -norm failure index, the maximum local failure index reduces in all of the cases to a different degree with different  $p$  value. In particular, with a higher  $p$  value, the maximum local failure index reduces further consistently as shown in the figure. With only one exception for  $p = 10$  with 637 design nodes in this figure, which overlaps with that of  $p = 8$  due to the numerical issue of  $p$ -norm failure index. However, the curve for the min-max bound formulation is decreasing from 0.648 to 0.555, as the mesh is refined from 297 design nodes to 1105 design nodes. It increases slightly to 0.578 when the number of design nodes is 1701. The remark of the results in this figure is two-fold: the min-max bound formulation is superior to the  $p$ -norm failure index in minimizing the maximum local failure index in the L-shaped plate; The  $p$ -norm formulation provides a converged design in the representative  $p$ -norm despite a lack of convergence when  $p \rightarrow \infty$ .

Eventually, the CPU time representative of the  $p$ -norm failure index and the min-max bound formulation is presented in Figure 4.17b. The slope of all these curves are roughly quadratic, identical to the conclusion in the square plate with cut-out case. In this figure, the curve for  $p = 6$  represents the relatively well-conditioned case. The curve for  $p = 10$  represents the case with a numerical issue. Clearly, the data for  $p = 6$  in the model with 1105 and 1701 design nodes is approaching that for  $p = 10$ , which indicates that numerical issues already appear slightly in the finer mesh cases. Regarding the min-max bound formulation, the computational cost is one order higher than the badly conditioned case of  $p$ -norm failure index ( $p = 10$ ). It demonstrates that the computational cost becomes a limiting factor for the min-max bound formulation applied to large-scale strength optimization of the VSL, although the min-max formulation has the potential to reduce the failure index further than the  $p$ -norm formulation.

## 4.6. CONCLUSION

In the current work, the  $p$ -norm formulation is applied in the strength optimization of the variable stiffness laminate to improve the computational efficiency. An elliptical formulation of the conservative failure envelope based on the Tsai-Wu failure criterion is employed to measure the strength of the VSL. This simplifies the Tsai-Wu failure criterion in the strength optimization. Moreover, it enables the lamination parameters to be used as the design variables in the strength optimization as the Tsai-Wu failure criterion is explicit with respect to the fiber angles, which are unknown a priori during the optimization. Thus the proposed method fits the Step 1 of the three-step optimization method for the optimal design of the variable stiffness laminate.

4

The two level approximation is applied for the  $p$ -norm failure index in this work. One important advantage of this approximation is that a firm convergence is guaranteed in every step of the inner and outer loop of the CCSA. Therefore, the number of outer loops in the CCSA can be reduced in the optimization. Hence, the computational cost to update the sensitivity of the  $p$ -norm failure index in each outer loop can also be reduced and the overall computational work can be reduced. In addition, this also contributes to the mesh-independence of the optimal results together with the 8-node serendipity element, which enhances the continuity of the stress field.

In the numerical test of a square plate with a cut-out, the effect of the  $p$  value on the optimal results in strength optimization with the  $p$ -norm failure index is studied on a reference model, a refined model and a half model. The numerical results show that  $p = 6$  is the optimum value for the  $p$ -norm failure index to reduce the maximum failure index. When  $p$  increases over 7, numerical instability and nonlinearity of the  $p$ -norm failure index are amplified. For instance, there are fluctuations in the local maximum failure index in the convergence history, the optimum local maximum failure index oscillates among different  $p$  value, the number of the outer and inner loops in the CCSA as well as the CPU time increase significantly. For each  $p$  value, the optimal lamination parameters are mesh independent. By comparing the optimal solution from the local min-max bound formulation, it confirms that the computational cost gets improved dramatically with the global aggregation method. However, a drawback of the global aggregation is that the optimal solution obtained is higher than that from the local min-max bound formulation.

In the L-shaped case, the numerical results illustrate that the strength optimization with  $p$ -norm formulation can efficiently solve numerical problems even with a stress singularity. In contrast, the computational cost for strength optimization with local min-max formulation is one order higher in this case. The optimal results confirm that the designs are essentially mesh-independent for  $p$  lower than 6. A  $p$  value higher than 6 still reduces the maximum local failure index consistently, however numerical instabilities have a detrimental effect on the smoothness of the solution. Therefore  $p$  is recommended to be lower than 6 in the extreme cases using  $p$ -norm failure index.

In future work, the formulation of the  $p$ -norm failure index can be updated to match it with the maximum local value or to make it more conservative. Consequently, it can



be used in topology optimization as objective or constraints to minimize the weight or compliance of the VSL.

## REFERENCES

- [1] A. Khani, S.T. IJsselmuiden, M.M. Abdalla, and Z. Gürdal. Design of variable stiffness panels for maximum strength using lamination parameters. *Composites Part B: Engineering*, 42(3):546 – 552, 2011. ISSN 1359-8368. doi: <https://doi.org/10.1016/j.compositesb.2010.11.005>. URL <http://www.sciencedirect.com/science/article/pii/S1359836810002131>.
- [2] Pierre Duysinx and Ole Sigmund. New developments in handling stress constraints in optimal material distribution. In *7th ALAA/USAF/NASA/ISSMO symposium on multidisciplinary analysis and optimization*, page 4906, 1998.
- [3] Chau Le, Julian Norato, Tyler Bruns, Christopher Ha, and Daniel Tortorelli. Stress-based topology optimization for continua. *Structural and Multidisciplinary Optimization*, 41(4):605–620, 2010.
- [4] Erik Holmberg, Bo Torstenfelt, and Anders Klarbring. Stress constrained topology optimization. *Structural and Multidisciplinary Optimization*, 48(1):33–47, Jul 2013. ISSN 1615-1488. doi: 10.1007/s00158-012-0880-7. URL <https://doi.org/10.1007/s00158-012-0880-7>.
- [5] Shiguang Deng and Krishnan Suresh. Multi-constrained topology optimization via the topological sensitivity. *Structural and Multidisciplinary Optimization*, 51(5): 987–1001, 2015.
- [6] Kangwon Lee, Kiso Ahn, and Jeonghoon Yoo. A novel p-norm correction method for lightweight topology optimization under maximum stress constraints. *Computers & Structures*, 171:18 – 30, 2016. ISSN 0045-7949. doi: <https://doi.org/10.1016/j.compstruc.2016.04.005>. URL <http://www.sciencedirect.com/science/article/pii/S0045794916301833>.
- [7] C.Y. Kiyono, S.L. Vatanabe, E.C.N. Silva, and J.N. Reddy. A new multi-p-norm formulation approach for stress-based topology optimization design. *Composite Structures*, 156:10 – 19, 2016. ISSN 0263-8223. doi: <https://doi.org/10.1016/j.compstruct.2016.05.058>. URL <http://www.sciencedirect.com/science/article/pii/S0263822316306419>. 70th Anniversary of Professor J. N. Reddy.
- [8] Alexander Verbart, Matthijs Langelaar, and Fred Van Keulen. A unified aggregation and relaxation approach for stress-constrained topology optimization. *Structural and Multidisciplinary Optimization*, 55(2):663–679, Feb 2017. ISSN 1615-1488. doi: 10.1007/s00158-016-1524-0. URL <https://doi.org/10.1007/s00158-016-1524-0>.
- [9] Erik Lund and Jan Stegmann. On structural optimization of composite shell structures using a discrete constitutive parametrization. *Wind Energy*, 8(1):109–124,

2005. doi: 10.1002/we.132. URL <https://onlinelibrary.wiley.com/doi/abs/10.1002/we.132>.
- [10] Erik Lund. Discrete material and thickness optimization of laminated composite structures including failure criteria. *Structural and Multidisciplinary Optimization*, pages 1–19, 2017.
- [11] J.H. Sjølund and E. Lund. Structural gradient based sizing optimization of wind turbine blades with fixed outer geometry. *Composite Structures*, 203: 725 – 739, 2018. ISSN 0263-8223. doi: <https://doi.org/10.1016/j.compstruct.2018.07.031>. URL <http://www.sciencedirect.com/science/article/pii/S0263822318306883>.
- [12] Amir M. Mirzendehtdel, Behzad Rankouhi, and Krishnan Suresh. Strength-based topology optimization for anisotropic parts. *Additive Manufacturing*, 19:104 – 113, 2018. ISSN 2214-8604. doi: <https://doi.org/10.1016/j.addma.2017.11.007>. URL <http://www.sciencedirect.com/science/article/pii/S2214860416303475>.
- [13] Samuel Tsunduka Ijsselmuiden. *Optimal design of variable stiffness composite structures using lamination parameters*. PhD thesis, Delft University of Technology, 2011.
- [14] Shahriar Setoodeh, Mostafa M. Abdalla, Samuel T. Ijsselmuiden, and Zafer Gürdal. Design of variable-stiffness composite panels for maximum buckling load. *Composite structures*, 87(1):109–117, 2009.
- [15] Samuel T. Ijsselmuiden, Mostafa M. Abdalla, and Zafer Gürdal. Optimization of variable-stiffness panels for maximum buckling load using lamination parameters. *AIAA journal*, 48(1):134–143, 2010.
- [16] JKS Dillinger, Thomas Klimmek, Mostafa M Abdalla, and Zafer Gürdal. Stiffness optimization of composite wings with aeroelastic constraints. *Journal of Aircraft*, 50(4):1159–1168, 2013.
- [17] Mostafa M. Abdalla, Shahriar Setoodeh, and Zafer Gürdal. Design of variable stiffness composite panels for maximum fundamental frequency using lamination parameters. *Composite structures*, 81(2):283–291, 2007.
- [18] Peng Hao, Xiaojie Yuan, Hongliang Liu, Bo Wang, Chen Liu, Dixiong Yang, and Shuangxi Zhan. Isogeometric buckling analysis of composite variable-stiffness panels. *Composite Structures*, 165:192 – 208, 2017. ISSN 0263-8223. doi: <https://doi.org/10.1016/j.compstruct.2017.01.016>. URL <http://www.sciencedirect.com/science/article/pii/S0263822316325466>.
- [19] Sanjay Mehrotra. On the implementation of a primal-dual interior point method. *SIAM Journal on Optimization*, 2(4):575–601, 1992.

- [20] Krister Svanberg. A class of globally convergent optimization methods based on conservative convex separable approximations. *SIAM journal on optimization*, 12(2):555–573, 2002.
- [21] Fumio Kikuchi, Masayuki Okabe, and Hidehiro Fujio. Modification of the 8-node serendipity element. *Computer methods in applied mechanics and engineering*, 179(1):91–109, 1999.
- [22] Ali Khani. *Optimum design of steered fiber composite cylinders with arbitrary cross-sections*. PhD thesis, Delft University of Technology, 2013.
- [23] Attila P. Nagy, Mostafa M. Abdalla, and Zafer Gürdal. On the variational formulation of stress constraints in isogeometric design. *Computer Methods in Applied Mechanics and Engineering*, 199(41):2687 – 2696, 2010. ISSN 0045-7825. doi: <https://doi.org/10.1016/j.cma.2010.05.012>. URL <http://www.sciencedirect.com/science/article/pii/S0045782510001611>.
- [24] Daniël M.J. Peeters, Simon Hesse, and Mostafa M. Abdalla. Stacking sequence optimisation of variable stiffness laminates with manufacturing constraints. *Composite Structures*, 125(Supplement C):596 – 604, 2015. ISSN 0263-8223. doi: <https://doi.org/10.1016/j.compstruct.2015.02.044>. URL <http://www.sciencedirect.com/science/article/pii/S0263822315001233>.
- [25] Daniël Peeters, Zhi Hong, and Mostafa Abdalla. A compliance approximation method applied to variable stiffness composite optimisation. *Structural and Multidisciplinary Optimization*, 58(5):1981–2001, Nov 2018. ISSN 1615-1488. doi: 10.1007/s00158-018-2007-2. URL <https://doi.org/10.1007/s00158-018-2007-2>.
- [26] Attila P. Nagy, Samuel T. IJsselmuiden, and Mostafa M. Abdalla. Isogeometric design of anisotropic shells: Optimal form and material distribution. *Computer Methods in Applied Mechanics and Engineering*, 264:145 – 162, 2013. ISSN 0045-7825. doi: <https://doi.org/10.1016/j.cma.2013.05.019>. URL <http://www.sciencedirect.com/science/article/pii/S0045782513001461>.
- [27] Ali Khani, Samuel T. IJsselmuiden, Mostafa M. Abdalla, and Zafer Gürdal. Design of variable stiffness panels for maximum strength using lamination parameters. *Composites Part B: Engineering*, 42(3):546–552, 2011.
- [28] P. Duysinx and M. P. Bendsøe. Topology optimization of continuum structures with local stress constraints. *International Journal for Numerical Methods in Engineering*, 43(8):1453–1478, 1998. doi: 10.1002/(SICI)1097-0207(19981230)43:8<1453::AID-NME480>3.0.CO;2-2. URL <https://onlinelibrary.wiley.com/doi/abs/10.1002/%28SICI%291097-0207%2819981230%2943%3A8%3C1453%3A%3AAID-NME480%3E3.O.CO%3B2-2>.
- [29] N. Olhoff. Multicriterion structural optimization via bound formulation and mathematical programming. *Structural optimization*, 1(1):11–17, Mar 1989. ISSN 1615-1488. doi: 10.1007/BF01743805. URL <https://doi.org/10.1007/BF01743805>.





# 5

## CONCLUSION AND FUTURE WORK

*Logic will get you from A to B. Imagination will take you everywhere.*  
逻辑会带你从A点到达B点，想象力将把你带到任何地方。

Albert Einstein

### 5.1. CONCLUSION

This research undertakes an in-depth investigation into strength optimization for lightweight structural design in two aspects: efficient strength optimization and manufacturable design of variable stiffness laminate. The first aspect intends to break through the bottleneck of computational cost required for large scale structural optimization. Two variants, in particular a local version and a global version, are developed to address the heavy computational cost from two perspectives: the local version resolves the expensive problem by developing an efficient iterative solver; whereas, the global version reformulates a massive problem into a condensed strength-oriented problem before solving it with a standard approach. Two types of material are considered in each of the two variants. The local version focuses on conventional metallic materials and the global version deals with innovative variable stiffness laminate (VSL), respectively. With regard to the optimal design of the VSL, the aim is to better enforce a manufacturing constraint on the curvature (inverse of the minimum allowable turning radius) of the fiber paths required by the automated fiber placement (AFP) in the existing three-step design procedure. This will push the novel composite laminate from the design phase forward to engineering applications, where lightweight structures with superior strength are in great demand. In this chapter, the overall research documented in this thesis is summarized.

### EFFICIENT COMPUTATIONAL METHOD FOR STRESS CONSTRAINTS

The research in Chapter 2 targets the efficiency of large scale stress constrained optimization using the previously mentioned local optimization version. An efficient iterative method is developed in order to achieve a linear relationship of computational cost with respect to the size of the problem. The conservative convex separate approximation (CCSA) framework used, as well as Mehrotra's predictor-corrector interior point method provide an efficient and robust convergence in the iterative procedure. In addition, a stress approximation modified on the basis of the fully-stressed design is proposed, which enhances the existing approximation and enables a diagonal preconditioner for the preconditioned conjugate gradient method (PCG) to solve the Schur complement of the Karush-Kuhn-Tucker (KKT) condition. In order to reduce the computational cost due to the sensitivity analysis of local stress constraints using the adjoint method repetitively, an implicit sensitivity analysis, which integrates the adjoint method and the re-analysis method together with the PCG, is developed. Thus, the sensitivity analysis is done while solving the Schur complement with the PCG. Numerical tests are conducted to verify the proposed method systematically for models composed of beam and plate elements. From the results of the optimal design, the number of iterations for the PCG, the interior point method and outer loops in the CCSA, as well as the CPU time cost for the optimization, the main findings for the newly designed method are as follows:

- In the beam cases, the computational cost of the proposed iterative system increases only linearly with respect to the size of the design problems, which is consistent with the estimation in the computational complexity analysis.
- The proposed iterative method is efficient compared with the standard approach only for large scale problems. Based on the CPU time obtained in the beam cases, the performance of the proposed iterative method is superior to the standard method only when the number of stress constraints is more than the order of 1000. Thus, the proposed iterative method is desirable only for sufficiently large scale problems.
- In the plate cases, the Lagrange multiplier obtained in the optimal solution fluctuates, which may be due to the fact that the continuity of the stress field is less than that of the Lagrange multiplier in the discrete model of the Lagrange function. Thus, a higher order element in the FEM model may be necessary in stress optimization.

### AN ENHANCED CURVATURE CONSTRAINED DESIGN METHOD FOR MANUFACTURABLE VARIABLE STIFFNESS COMPOSITE LAMINATE

In Chapter 3 a novel method is presented to enhance the enforcement of curvature constraints on fiber paths in the three-step optimization method as an extension of the existing design methodology. An inverse problem is explored to retrieve the fiber angles in Step 2 of the three-step optimization method using the optimal lamination parameters obtained in Step 1. In terms of the curvature constraints on the fiber paths, an indirect control method, which controls the curvature of fiber path through the gradient con-

straints on the lamination parameters in Step 1, is developed. Next to this, a hybrid control method, which ultimately enhances the enforcement of the curvature constraint, is developed through combining the indirect control method with the existing direct control method. The enhancement is obtained by tuning the upper bound factor of the gradient constraints in Step 1 to allow the optimal stiffness obtained with the lamination parameters to be more achievable in the inverse problem in Step 2. A parametric study is implemented systematically to validate the indirect control method, and a comparison is made in terms of the optimal compliance and the CPU time cost for the optimization between the direct, indirect and hybrid control methods. The main conclusions of this part are summarized below:

- The indirect control method is confirmed to be capable of constraining the curvature of the fiber paths, given a stringent upper bound factor  $\delta$  on the gradient constraints on the lamination parameters in Step 1.
- The optimum compliance obtained in the hybrid control method is the best out of the three methods, since the curvature constraint is properly considered in Step 1 and firmly enforced in Step 2. The optimal compliance obtained from the direct control method, which constrains the curvature of fiber paths geometrically in Step 2, is intermediate. The optimal compliance obtained with the indirect control method is the worst out of the three methods due to an over-constrained effect.
- Regarding the CPU time of the three methods, the indirect control method is the most efficient, since the number of gradient constraints on the lamination parameters is only one per element regardless of the number of the design layers. The CPU time for the hybrid control method is moderately higher than that of the indirect control method due to the steering constraints imposed for each layer of each element in Step 2. The computational cost for the direct control method is the most expensive out of the three methods for two reasons: (i) optimization in Step 1 takes more iterations in the absence of gradient constraints on the lamination parameters; (ii) the inverse problem in Step 2 takes more iterations to converge as the lamination parameters obtained in Step 1 are more difficult to match with the steering constraints.
- The hybrid control method is to be preferred when the curvature of fiber paths is constrained in the three-step optimization method, i.e., the minimum compliance can be obtained at an intermediate computational cost.

#### EFFICIENT STRENGTH OPTIMIZATION OF VARIABLE STIFFNESS LAMINATE

In Chapter 4, a global failure index, which is also called the  $p$ -norm failure index based on the  $p$ -norm aggregation, is applied in the strength optimization of the VSL to set up the previously mentioned global version method. The main focus of this part is to accelerate strength optimization with the lamination parameters in Step 1 of the three-step optimization method. In order to ensure the validity of the Tsai-Wu failure criterion with respect to the lamination parameters, an elliptical formulation of the conservative failure envelope is employed. The two level approximation, formulated in terms of the in-plane

stiffness matrix and the lamination parameters respectively, is applied for the  $p$ -norm failure index to guarantee a strict conservativeness and convexity of the sub-problem. The algorithms to address the KKT condition and the optimization framework are identical to those in Chapter 2. With the setup as such, a robust and efficient method to solve the strength optimization of the VSL is achieved in three ways. First, the size of the optimization problem, i.e., the number of constraints for the KKT condition, is condensed effectively by aggregating the local failure indices into a single  $p$ -norm failure index. Second, the computational cost of the sensitivity analysis is decreased significantly by solving the adjoint system for the  $p$ -norm failure index only once. Third, an efficient and robust convergence is achieved in every step of the inner and outer loop of the CCSA due to the two layer approximation, the predictor-corrector interior point method and the optimization framework.

The local version of the strength optimization using the min-max bound formulation is also implemented and compared with the results obtained from the  $p$ -norm failure index. The concluding remarks for this chapter are as follows:

5

- The  $p$  value needs to be properly chosen for the  $p$ -norm failure index. From the numerical tests, numerical instability and nonlinearity of the  $p$ -norm failure index disturbs the convergence of the optimization as the  $p$  value is beyond the well-conditioned range. For the cases analyzed in the present work, the best value of  $p$  is 6 for a good compromise between the achievable optimal design and numerical issues.
- The proposed method is robust, which provides mesh-convergent optimum design in a model even with stress singularity, such as the L-shaped plate. One reason is due to the fact that the  $p$ -norm failure index is discretized consistently with the FEM discretization. In addition, a higher order element (i.e., the 8-node serendipity element) is employed in this work, based on the experience in Chapter 2 to increase the continuity of the stress field.
- The min-max bound formulation can optimize the strength of the VSL better than the  $p$ -norm failure index. Whereas, the latter is far less costly comparing with the min-max bound formulation. As a result, the  $p$ -norm failure index is more suited to large-scale strength-oriented optimization.

## 5.2. FUTURE WORK

The current research can lead to various interesting studies in structural optimization in the future. Four specific points are brought forward in the section for future work. First of all, further improvement in the efficient iterative method presented in Chapter 2 is necessary for the plate cases, in order to achieve the linear relationship in the computational cost with respect to the size of the problem. Currently, the Lagrange multipliers obtained in the optimal solution are slightly fluctuating and not reaching the high values associated with active stress constraints. This is due to the fact that the order of the continuity of the stress constraint is lower than that of the Lagrange multiplier in the discrete form of the Lagrange function. To improve the continuity of stress constraint,

elements with a higher order polynomial in the FEM model (Tessler [1]) should be chosen for the stress and its sensitivity calculation. Another option is to use isogeometric analysis (IGA), where the order of the basis function from the non-uniform rational basis spline (NURBS) is easier to elevate through  $p$  refinement (Da Veiga et al. [2]). Additionally, in order to avoid the mesh dependency in the stress sensitivity, this is recommended to be implemented in the continuous form consistently in the governing equation (Wang et al. [3]) before discretization in the FEM. Once the issues on the Lagrange multiplier and the mesh dependency of the stress sensitivity are addressed, the proposed iterative method may achieve the efficiency expected in the plate cases.

Another promising possibility to boost the efficiency of large scale stress constrained optimization problems is to build an efficient iterative solver based on the multigrid method. Not only can this be used as an efficient solver for the partial differential equation (Notay [4]), but also acts as an efficient preconditioner for the PCG (Liu et al. [5]). The fundamental idea of the multigrid method, as an efficient solver, is to reduce the computational cost through correcting the short-wavelength errors of iterative solvers, such as Jacobi and Gauss-Seidel method, in coarser meshes. To this end, it can be applied in the sensitivity analysis with the adjoint method for a large number of constraints or to solve the Schur complement in the optimization (Kočvara and Mohammed [6]). Whereas, for the multigrid preconditioner, this is developed to accelerate the convergence rate of the conjugate gradient method through combining the paradigm of the multigrid method in the iteration (Tatebe [7]). It has been demonstrated as a promising preconditioner in topology optimization (Amir et al. [8]). Hence, relevant research can lead to an efficient solver for large scale stress constrained optimization as well.

For constraining the curvature of the fiber paths of the VSL, a valuable research to be carried out is to account for this factor in Step 3 of the current three-step optimization method, namely the fiber paths reconstruction step with the streamline analogy. As this is not considered in the current method, the risk is that the fiber paths achieved at the end of Step 3 may still violate the curvature limitation albeit it is controlled in both Step 1 and Step 2. Additionally, the proposed method in this research need to be extended to the general 3D cases using shell elements, where bending is also involved. In that case, at least two more out-of-plane lamination parameters are to be constrained at each design point for a symmetric and balanced laminate. Corresponding numerical tests need to be implemented thereafter for different applications, such as optimization of strength, buckling, vibration, aeroelasticity or more complex nonlinear behaviours etc.

Finally, regarding the strength optimization of the VSL with  $p$ -norm failure index, this can be further enhanced by combining scaling and clustering techniques, which allows the  $p$ -norm failure index to match the maximum of the local failure indices. In that case, the enhanced  $p$ -norm failure index can be imposed either as the objective or the constraint in the optimization of the VSL, which is more suited to engineering practice. Not only the stiffness of the VSL can be tailored, but also the optimum topology can be obtained through topology optimization for various purposes, with strength considered concisely in the setup. In addition, as the failure mechanisms of composite laminates are diverse due to the associated complex fabrication, different failure criteria should be explored, and in the meanwhile validated with respect to the lamination parameters for

the VSL, in order to allow more failure mechanisms to be considered for different cases in the optimization.

With the above research successfully completed in the future, strength optimization or optimization in general will be accomplished efficiently for large scale structural design.

## REFERENCES

- [1] Alexander Tessler. A higher-order plate theory with ideal finite element suitability. *Computer Methods in Applied Mechanics and Engineering*, 85(2):183 – 205, 1991. ISSN 0045-7825. doi: [https://doi.org/10.1016/0045-7825\(91\)90132-P](https://doi.org/10.1016/0045-7825(91)90132-P). URL <http://www.sciencedirect.com/science/article/pii/004578259190132P>.
- [2] L. Beirao Da Veiga, Annalisa Buffa, Judith Rivas, and Giancarlo Sangalli. Some estimates for h–p–k-refinement in isogeometric analysis. *Numerische Mathematik*, 118(2):271–305, 2011.
- [3] Zhenpei Wang, Mostafa Abdalla, and Sergio Turteltaub. Normalization approaches for the descent search direction in isogeometric shape optimization. *Computer-Aided Design*, 82:68 – 78, 2017. ISSN 0010-4485. doi: <https://doi.org/10.1016/j.cad.2016.06.002>. URL <http://www.sciencedirect.com/science/article/pii/S0010448516300513>. Isogeometric Design and Analysis.
- [4] Yvan Notay. An aggregation-based algebraic multigrid method. *Electronic transactions on numerical analysis*, 37(6):123–146, 2010.
- [5] C. Liu, X. Zheng, and C.H. Sung. Preconditioned multigrid methods for unsteady incompressible flows. *Journal of Computational physics*, 139(1):35–57, 1998.
- [6] M. Kočvara and S. Mohammed. Primal-dual interior point multigrid method for topology optimization. *SIAM Journal on Scientific Computing*, 38(5):B685–B709, 2016. doi: 10.1137/15M1044126. URL <https://doi.org/10.1137/15M1044126>.
- [7] Osamu Tatebe. The multigrid preconditioned conjugate gradient method. Technical report, NASA Langley Technical Report Server, 1993.
- [8] Oded Amir, Niels Aage, and Boyan S. Lazarov. On multigrid-cg for efficient topology optimization. *Structural and Multidisciplinary Optimization*, 49(5):815–829, May 2014. ISSN 1615-1488. doi: 10.1007/s00158-013-1015-5. URL <https://doi.org/10.1007/s00158-013-1015-5>.

# ACKNOWLEDGEMENTS

It is my honor to take the chance to write this acknowledgement enclosed with the dissertation. The PhD stage is a challenging but nice experience for me, which dates back to September 1, 2014. This journey, which lasts five years, five months and 20 days, enriched me with many things to learn (technically, physically, and psychologically), to explore (mostly research, but also including inter-personal stuff), to experience (parties, traveling and conferences) and many people to interact with (warm-hearted and impassive, positive and passive, productive and inefficient, interesting and dull etc.). Everything that happened motivates me to find a better person in myself. I will deliver my sincere gratitude to all the people that helped, encouraged, accompanied me in the meanwhile.

I will acknowledge my first daily supervisor **Dr. Mostafa M. Abdalla**, who is intelligent and enthusiastic about numerical methods in computational mechanics, composite structures and optimization etc. Thank you for guiding me into the gate of research in the first two and a half years of my PhD. Your excellent technical skills and proactive attitude keep me enthusiastic in exploration. Also, thanks to my supervisor **Dr. Sergio Turteltaub** for the numerous discussion in the next two and a half years. Your knowledge in computational mechanics, skills in organizing numerical results and writing techniques for the scientific manuscript are excellent. Moreover, I am impressed by your conscientious in the quality control of the work, generally without time limitation. Thanks to my promoter, **Prof. Chiara Bisagni**, for the yearly meetings to check my progress and actively help to resolve the bottlenecks of my PhD. It is important to have your support and your feedback on my work.

Additionally, I would like to acknowledge my gratitude to **Daniël Peeters** for two years of collaboration until the end of my PhD. It is a lot of help to share your code for angle retrieval and fiber path reconstruction, which saves me from developing these from stretch again. Thank you for always being ready for the discussions about the numerical results and the quick feedback to my manuscript. I saw what being disciplined and responsible mean from you. Thanks to **Prof. Sybrand van der Zwaag** for encouraging me at my very frustrating time by checking my introduction and conclusion. Your optimistic attitude and great efficiency are very inspiring to me. Also, thanks to **Emeritus Prof. Alan Rothwell** for checking the summary of my thesis. It is really a memorable discussion about the feedback the whole morning in your office. I wish you great health and happiness! Thanks to **Mr. Cees Timmers** and **Dr. Mirjam Snellen** for their suggestions in my PhD. You do show your great professional skills and expertise in coaching people. Thanks to previous PhD students in our group **Ke Liang, Yujie Guo, Weiling Zheng** for always being ready to talk to me remotely in China when I feel struggling. It is very important to have your support.



Next, I would like to recognize my office mates **Jayaprakash Krishnasamy (J.P.)** and **Jaco Brandsen**. It is a great time to work with you together in the same office for five years. I really like the nice discussions with you about research, jobs, culture, sports, movies and so on. I will never forget the discussion with J.P. on the Galerkin method just out of curiosity. It is of great help to discuss the job hunting experience with Jaco. Thanks to both of you for sharing my feelings over the years. I think I can not finish my PhD without your accompany. I also like to thank everybody in my research group **Christos, Roeland, Laura, Jan Hol, Boyang Chen, Saullo, Julien, Jurij, Sathiskumar, Xiaopeng Ai, Lan Yang, Yuqian Tu, Jiayao Zhang, Ang Li, Mario, Edgars, Antonio, Eddy, George, Tito, Marta, Javier, Natalia, Kevin van Dooren, Jens, Paul, Ines, Niels, Darwin, Tigran, Yasir, Bas, Luc, Andres, Meryem, Duo Zou, Giorgio, Carlo, Kevin Wils, Jinghua Tang**. It is nice to talk with you about the interesting stories and have lunch together. Especially for **Mario**, thank you for checking my status and providing suggestions to me every now and then. Thanks to **J.P., Jaco, Jens** and **Giorgio** for helping me with my cover letter. Thanks to **Kevin** and **Eva** for helping in the Dutch version summary. I turned to be more optimistic, open-minded and considerate by interacting with you guys.

Thanks to my professors in my master stage: **Prof. Jun Huang** and **Prof. Yuanming Xu** for your instructions in my master, which led my way to a PhD. Also, thanks for your suggestions for my research and life every time we met in Beijing when I went back home during the Spring Festival. You all helped to remove my anxiety, which made it easier for me to focus on my research.

I also appreciate the previous PhDs in our research group: **Samuel T. IJsselmuiden** and **Attila Nagy**. Not only because of your well-written thesis but also for your willingness to share. It is really kind of you to provide me the prompt reply and explain everything in detail through email even when we never met each other.

Thank my fellows coming to Delft in the same year: **Xiang Fu, Jian Fang, Yue Zhao, Yazhou Yang, Jiapeng Yin, Yamin Huang, Linying Chen, Zenan Yang, Rong Zhang, Qingxi Li, Jinyu Tang, Meixia Shan, Haiyan Lu, Xing Chang, Jie Cai, Qu Hu, Xiao Liang, Xiao Lin, Wenhua Qu**. Thanks to the talks about research and life, and the parties we had before. Many thanks to **Jiao Chen, Fei Xu, Meng Wang, Yin Chen, Tian Zhang, Ding Ding, Peiyang Luo, KaiKai Pan, Shuaiqiang Liu, Hao Yu, Riming Wang, Dan Cheng, Zhirui Zong, Xuan Zheng, Yan Liu, Youwei Wang, Shuo Li** for the dinners and board games together. Also, many thanks to all of my roommates in the five years: **Shuai Yuan, Pengling Wang, Haigong, Kai Liu, Liangfu Wei, Xinyu Zhou, Xinmiao Du, Congbiao Sui, Maolong Lyu, Xiaojuan Zhang**. It is really nice to share the same apartment with you. I know more about taking care of other people from you. Especially for Kai Liu, your cooking skill and proactive attitude is really impressive.

Thanks to my badminton coaches: **Patrick, Nicky, Indra, Jan-Willem** for teaching me about how to train myself both physically and psychologically. I will train more for agility in the future. Also thanks to my friends on the badminton court: **Fuqi Liang, Tingkai Kuo, Yanbo Wang, Lizuo Xin, Qiyao Peng, Jie Ren, Xuan Tao, Kailun Yang, Zhe Li, Xiujie Shan, Roel, Zaiyang Zhou**. You make the games more exciting and enjoyable. It is really nice to discuss the skills and other interesting things with you after the game.

Thanks to the alumnus/alumni of Beihang University in Delft: **Zi'an Qin, Ziqiao Huang, Jun Wu, Jingtang Liao, Changgong Zhang, Wandong Wang, Anqi Fu, Yuzhe Xiao**, especially to **Xuerui Wang** and **Sihao Sun** for your encouragement. It is really nice to have parties and talks to you. You always have a lot of innovative ideas. I always feel that the time goes faster with you.

Also, thanks to the friends I met in the conferences and symposium: **Liang Xia, Yingjun Wang, Lyu Zhao, Jie Gao, Qi Wang, Long Wu, Yaolu Liu, Feiyu Geng, Zhijun Wang, Jian Zhang, Yong Zhang, Lidan Zhang, Dianlei Feng, Xin Huang, Ying Zhao, Yuxin Zhou**. I have a very good time to meet you every time. The nice presentation and posters of your work makes the tedious research very attractive.

I also appreciate the ones, with whom I had a good time but are not mentioned in the acknowledgement. You make me more clear about what kind of person I want to be and what role I am going to play. I will be positive and confident towards other people and the world in the future as you did to me.

I would like to gratitude China Scholarship Council for sponsoring my PhD project. This helps me fulfill my dream of studying in Europe, where I meet a lot of excellent researchers and experience different cultures.

Thanks to **my grandparents** (姥姥, 爷爷, 奶奶) for taking care of me and providing me everything I want in my childhood. Thanks to **my aunts** and **uncles** for inviting me to have nice food every time I go back home and providing help to my family when I am away during my studies all these years. It enables me to focus on my work.

Finally, I would like to acknowledge my deepest gratitude to **my parents**, who support my study unconditionally every step of my way. Thank you for always providing the best environment to me, understanding me no matter what happened and bringing me up with a lot of hard work. After so many years, I realized that what I get from you is, in fact, the best if I look around. I would like to say "thank you very much, I love you".

Best wishes to everybody mentioned above, and you who are reading this thesis.

Zhi Hong  
13-01-2020  
Delft, the Netherlands



# A

## APPENDIX

### A.1. FEASIBILITY OF THE INDIRECT CONTROL METHOD

In this appendix, the feasibility of the indirect control method is tested systematically by changing the value of the upper bound factor  $\delta$ , the minimum allowable turning radius  $r_{\min}$  and the number of design layers in the angle retrieval step  $n_d$ . Discrete values in the following ranges are used:  $r_{\min} \in [0.4, 2.0]$  m,  $\delta \in [0.04, 0.14]$  and  $n_d = 1, \dots, 6$ . The problem solved is the same as the one described in test case 1 with the same material properties and thicknesses; the only difference are the values of  $\delta$ ,  $r_{\min}$  and  $n_d$ . Hence, the upper bound used in Step 1 for each case is according to Eqs. (3.38) and (3.39).

To determine whether a design obtained from the indirect control method is actually feasible or not, the curvature constraint is verified a posteriori, i.e., the smallest curvature found by searching all local values of the curvature of the design obtained after Step 2 and the corresponding Step 3 are compared to the minimum allowable turning radius. The upper bounds in Eqs.(3.38) and (3.39) depend on both  $r_{\min}$  and  $\delta$  (for a given thickness), hence it is convenient to present the results in two distinct formats, namely feasible/infeasible regions as a function of  $\delta$  for one fixed value of  $r_{\min}$  and feasible/infeasible regions as a function of  $r_{\min}$  for one fixed value of  $\delta$ . In both formats the results are given for various values of  $n_d$ .

#### A.1.1. FEASIBLE/INFEASIBLE RANGE FOR DISTINCT UPPER BOUND FACTORS $\delta$ IN INDIRECT CONTROL METHOD

The range of the upper bound factor  $\delta$ , where the minimum turning radius can be constrained with the indirect control method is illustrated in Figure A.1 for  $r_{\min} = 0.8$  m for distinct values of the number of design layers  $n_d$ . From the figure, it can be observed that, for example, for  $n_d = 6$  design layers and for a minimum turning radius of  $r_{\min} = 0.8$  m, the smallest turning radius is below the critical value when  $\delta = 0.1$  (infeasible) but

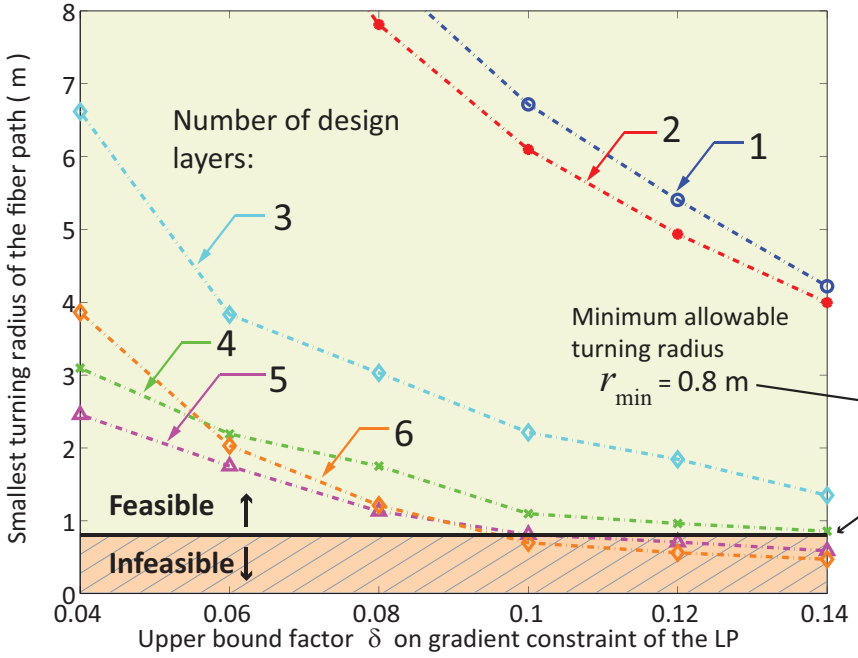


Figure A.1: Smallest layer-wise turning radius found in designs for test case 1 obtained using the indirect control method as a function of the upper bound factor  $\delta$  and for distinct numbers of design layers  $n_d$ . The feasible and infeasible designs are separated by the line corresponding to the minimum allowable turning radius  $r_{\min} = 0.8$  m.

it is above when  $\delta = 0.08$  (feasible). As expected, the results indicate that the smallest turning radius decreases as  $\delta$  increases since the curvature constraint is progressively relaxed. However, the smallest turning radius in a design does not vary monotonically as a function of the number of design layers, which reflects the non-uniqueness of the angle retrieval process (inverse problem).

It can be observed from the figure that the designs obtained with only 1 or 2 design layers ( $n_d = 1, 2$ ) are clearly within the admissible design region, although the corresponding designs tend to have relatively small curvatures (large radius of curvature). As the number of design layers increases, so does the curvature (i.e., the smallest radius of curvature decreases) and eventually the design may become infeasible.

### A.1.2. FEASIBLE/INFEASIBLE RANGE FOR DISTINCT MINIMUM TURNING RADIUS $r_{\min}$ IN INDIRECT CONTROL METHOD

The range of values of the minimum turning radius  $r_{\min}$  such that the design can be constrained with the indirect control method is illustrated in Figure A.2 for  $\delta = 0.05$  m

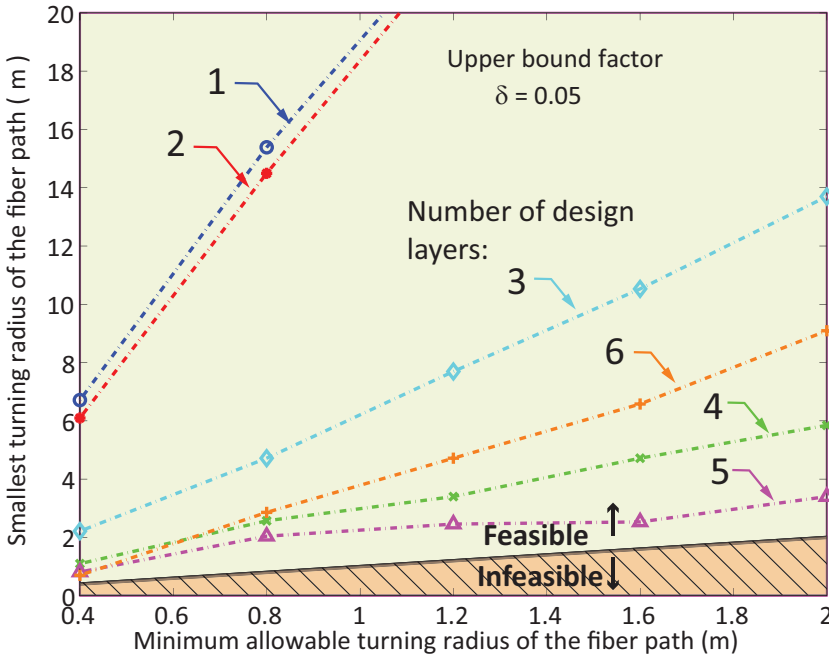


Figure A.2: Indirect control method: Feasible and infeasible designs for a given upper bound factor  $\delta = 0.05$  for test case 1 as a function of the minimum allowable turning radius  $r_{\min}$  for distinct values of the number of design layer during the angle retrieval step. The optimal lamination parameters are obtained in Step 1 with gradient constraints scaled by  $\delta = 0.05$  and the smallest turning radius is the one recovered from Step 2 in at least one of the layers without steering constraints. The straight line separating the feasible and infeasible domains corresponds to points where the smallest turning radius in a design coincides with the minimum allowable turning radius.

for distinct values of the number of design layers  $n_d$ . As may be observed from the figure, it turns out that, for all values considered, a feasible design can be obtained. This reflects that the value  $\delta = 0.05$  is sufficiently small to generate feasible designs. The corresponding design, however, has relatively small curvature (i.e., limited steering), which indicates that imposing the curvature constraint indirectly via the gradient of the lamination parameters is plausible but at the expense of severely limiting the design capacity.



# CURRICULUM VITÆ

Zhi Hong was born on February 20 1989 in Chaoyang, Liaoning Province, China. Grown up in a warm family, with diligent and kind-hearted parents, he enjoyed the happiness in the childhood.

For the bachelor, he intended to study architecture, which is his dream major. However, he majored in aircraft design at Shenyang Aerospace University in 2007, following the spirit of design, but also based on the opportunity he got. From there, he found great interests in structural mechanics. The achievement in this stage includes: Third Prize in National 'Innovation Cup' Aircraft Design Competition, Provincial Recognition Award in National 'Zhou Peiyuan' Mechanics Competition. In 2011, he finished his bachelor as a distinguished undergraduate student.



To aim higher in education, he moved to Beihang University in the master stage. He worked on buckling optimization of a grid-stiffened structure using a genetic algorithm there. Rather than only focusing on the research, he also involved in extracurricular activities, like graduate student union in the university. His interest in mechanics and optimization motivated him to explore more about theories in structural optimization.

In 2014, he started to work on efficient strength optimization of variable stiffness laminate in Aerospace Structures and Computational Mechanics group, Delft University of Technology. In the first two and a half years of the PhD training, he worked with Dr. Mostafa Abdalla on developing an efficient algorithm for the strength optimization problem. After Dr. Abdalla's sudden leave from the group, he started a 'pre-doc' mode on the research. Throughout half a year of intensive study and reflection, he became an independent researcher. Together with the collaboration with Dr. Sergio Turteltaub and Dr. Daniël Peeters, the thesis is completed in five years and 40 days. His research interests include: scientific computing methods, computational solid mechanics, composite structures and convex optimization.

According to his experience, the most important characters for research are to be resilient, optimistic, flexible, open-minded and efficient. In the meanwhile, the skills on proposing ideas, problem solving and decision making, scientific writing and collaborating with other people are of great importance. For the next move, he aims to work on something innovative but more applicable to create value and contribute to society.